UNIVERSITÀ
DEGLI STUDI
DI TORINO

Gypsum physical mechanical characterization and influence on geological risks in quarry environment.

PhD Thesis

Doctoral School of Sciences and Innovative Technologies
Department of Earth Sciences
University of Turin

PhD Candidate: Chiara Caselle

Supervisor:
Prof. Sabrina Bonetto   University of Turin

Co-Supervisors:
Prof. Cesare Comina   University of Turin
Prof. Daniele Costanzo   Polytechnic of Turin
Prof. Anna Ramon Tarragona   UPC (Barcelona)

Reviewers:
Prof. Patrick Baud   University of Strasbourg
Prof. Eduardo Alonso Pérez de Ágreda   UPC (Barcelona)

Turin, 2020

Abstract

The present PhD Thesis proposes an overview of the mechanical behaviour of gypsum rock in response to the principal physical parameters that may affect the stability of underground excavations.

The bi-hydrated phase of calcium-sulphate system (gypsum mineral) is a widely used material in several industrial fields, mainly related to building industries. Hence, the exploitation of gypsum rocks, by both open-pit and underground quarries, is diffuse all over the world and the excavation of underground drifts requires specific attention to the mechanical characterisation.

The wide range of gypsum facies observed all over the world suggests the importance of a facies-specific mechanical characterisation. Gypsum is, indeed, present in nature as constitutive mineral of rocks with a wide range of textural, microstructural and compositional features. The Thesis focuses on the analysis of "branching selenite", a typical gypsum facies that is present in most of the Upper Miocene evaporites of the Mediterranean Basin. This rock facies is commonly exploited either in open pit or underground quarries and has a specific relevance for stratigraphic and ore body reconstructions for mining, because it is associated to a geological "key layer". Nevertheless, a specific mechanical characterisation is not available in literature and is therefore worth of investigation.

Unlike synthetic gypsum, natural gypsum rock may present heterogeneous features, even within a single facies, that complicate the mechanical characterisation. For this reason, the Thesis proposes a detailed characterisation of the material from the textural, microstructural and compositional point of view, in order to describe and quantify the material heterogeneity. The results of this analysis were compared with the outputs of a series of mechanical tests, with the aim to quantify the effect of the heterogeneity on the material response. In addition, some specific tests were directed to the investigation of the influence of the layering on the crack coalescence and failure propagation in the material.

The drifts of underground gypsum quarries are often located below the static level of the groundwater table, requiring a continuous water pumping to allow for the accessibility of the drifts themselves. The presence of water (or elevate humidity conditions) in the rock mass may significantly weaken the mechanical strength of gypsum rock, affecting the general stability. In addition, the loading conditions that are applied on gypsum pillars remain constant for long times (i.e. the entire duration of the active excavation and also after the end of exploitation, for several decades). The time-dependent response (i.e. creep deformation and failure) becomes therefore a fundamental variable for the stability assessment in the long-term.

For these reasons, a large part of the Thesis was dedicated to the investigation of the influence of water and to the analysis of creep response in branching selenite gypsum. The results highlighted the existence of a weakening mechanism based on

the progressive dissolution of gypsum along the grain boundaries and the mineral cleavage that tends to decrease the strength of the rock and to enhance the creep response.

Acknowledgements

List of Contents

Chapter 1

Introduction

1.1 Field of interest

The increasing demand of gypsum as raw material in a wide range of industrial fields (e.g. building engineering, clinical applications, agriculture and production of paints) implies its extensive exploitation by both open-pit and underground quarries all over the world. Gypsum applications mainly involve the construction industries. It is, indeed, a main component of stucco, cements and wallboard products. Besides these uses, gypsum is implied in the production of paints, as a soil conditioner/fertilizer, in the food industries and in several clinical applications as regenerative material for bone defects, dental plaster or as a delivery vehicle for pharmaceutical agents (Van Driessche et al., 2019). Following the US Geological Survey on Mineral Commodity (February 2019), approximately 160 million tons of gypsum were exploited through mining activities worldwide during 2018 (Table 1.1).

Table 1.1 Worldwide mine-production and reserves of gypsum following the US Geological Survey on Mineral Commodity (^{e} Estimated; NA Not available)

	Mine production		Reserves
	2017	2018^e	
United States	20,700	21,000	700,000
Algeria	2,200	2,200	NA
Argentina	1,500	1,500	NA
Australia	1,400	1,400	NA
Brazil	3,400	3,400	340,000
Canada	1,700	1,700	450,000
China	15,500	16,000	NA
Egypt	2,200	2,200	NA
France	4,200	4,200	NA
Germany	3,100	3,100	NA
India	2,700	2,700	36,000
Iran	16,000	16,000	1,600
Japan	4,700	4,700	NA
Mexico	5,400	5,400	NA
Oman	5,500	5,500	4,900
Pakistan	2,000	2,000	NA
Russia	4,000	4,000	NA
Saudi Arabia	3,150	3,200	NA
Spain	7,000	7,000	NA
Thailand	9,250	9,300	NA
Turkey	9,000	9,000	200,000
Other countries	16,100	21,000	NA
World total (rounded)	141,000	150,000	Large

The stability assessment of these world-wide diffuse mining sites requires a detailed knowledge of mechanical response of gypsum as natural rock. Unlike synthetic gypsum, natural gypsum rock may present heterogeneous features, even within a single facies, that complicate the mechanical characterization. In the common practice of underground excavation, the lack of a specific focus on the relationship between gypsum geological variability and strength parameters often leads to ignore important information for the mechanical characterization of the ore deposits, in detriment of both safety and productivity. In addition, the frequent presence of water or elevate humidity conditions in the underground drifts, particularly if coupled with the time factor, induces a deleterious effect on the mechanical properties that, if neglected, may create serious risk scenarios (e.g. roof collapses or pillar failure).

The record of accidents in gypsum underground drifts is well-documented all over the world. Currently, failure in gypsum quarries in China are the primary hazards in non-metal mining sites, causing personal injuries and damages to the infrastructures (e.g. road damages, cracking and collapses in adjacent residential areas and agricultural lands or ground subsidence –Xia et al., 2019). As instance, Figure 1.1 reports the images of some of the damages produced by a wide ground collapse occurred in Xingtai gypsum mines (China) in 2005 (Wang et al., 2008).

Figure 1.1 Damages produced by a large ground collapse occurred in Xingtai gypsum mines (China) in 2005: (a) collapse of surface buildings; (b) inclination and failure of surface land; (c) failure on surface land; (d) vertical dislocation through surface infrastructures (Wang et al. 2008)

In absence of adequate planning for the recovering, also the end of the active exploitation may create dangerous scenarios in abandoned gypsum drifts. The long-term stability may be affected by the aging of gypsum due to the high relative humidity in the underground environments. In addition, the end of the exploitation may be accompanied by the interruption of dewatering operations (e.g. pumping), bringing to the groundwater flooding of the drifts. This may trigger alteration and dissolution phenomena with a general reduction of the stability of the quarries (e.g. Auvray et al. 2004 in France; Castellanza et al. 2010 in Italian Alps; Sadeghiamirshahidi and Vitton 2019 in Michigan, USA – Figure 1.2).
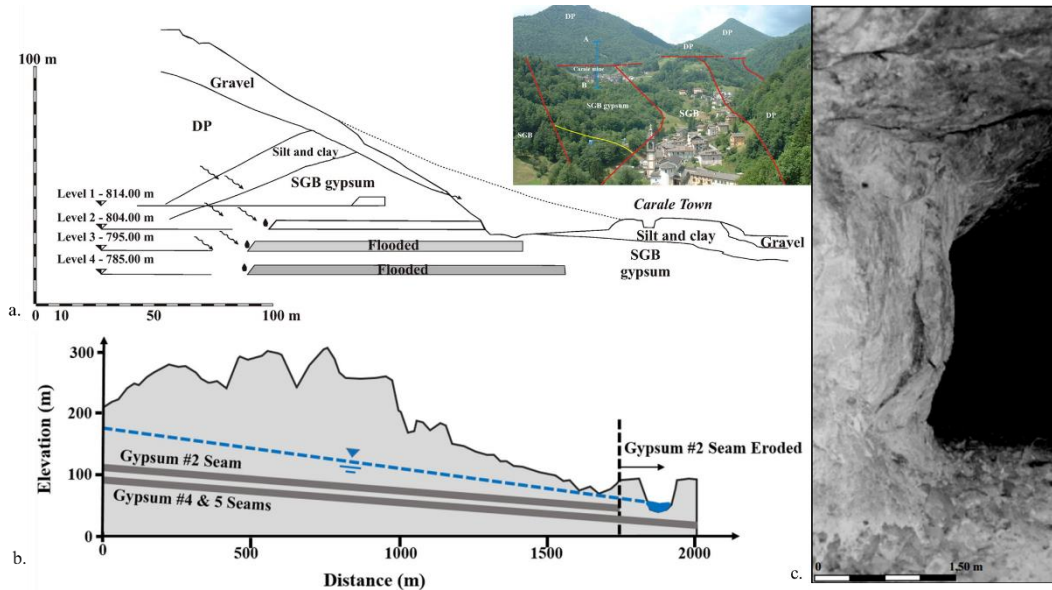
Figure 1.2 a. Abandoned flooded gypsum quarry in Italian Alps (Castellanza et al. 2010) b. Abandoned flooded gypsum quarry in Michigan, USA (Sadeghiamirshahidi and Vitton 2019) c. Effect of aging of the mechanical features on a gypsum pillar in an abandoned gypsum quarry in France (Auvray, 2003)

1.2 Aims of the Thesis

The present PhD Thesis aims to propose a comprehensive evaluation of the physical/chemical parameters that may influence the mechanical response of gypsum rock. The recently described gypsum facies named branching selenite (Lugli et al., 2010) was chosen as testing material. It is, indeed, a gypsum facies present in most of the Upper Miocene evaporites of the Mediterranean Basin and has a scientific and economic relevance because it is associated to a specific layer (reported in geological literature as "key layer"). It is consequently very useful for both stratigraphic studies and ore body reconstructions for mining. Its geological features define a strongly heterogeneous and anisotropic rock facies. As well as other gypsum facies, it is commonly exploited either in open pit or underground quarries. Mining tunnels through this material can reach lengths of tens of kilometers and both underground and surface stability have to be assured. Nevertheless, despite its strategical importance, detailed mechanical characterization for this specific facies is not available in literature and is therefore worth of investigation.

With this general objective, the following four detailed goals were pursued:

- The evaluation of the dependence of the bulk strength of gypsum on the geological variability, quantified in terms of grain size distribution, microstructure, porosity, mineralogical composition and anisotropy orientation.
- The assessment of the time-dependent strain and failure features of the material

- The analysis of the role of water and relative humidity on the mechanical response
- The investigation of the mechanisms involved in the strain accommodation and crack coalescence processes of gypsum rock in dependence to all these considered factors.

1.3 Contents and organization of the Thesis

The thesis is organized in nine Chapters.

After the present introduction, **Chapter 2** proposes a literature review about the main physical and mechanical properties of gypsum mineral and gypsum rocks, with a focus on the influence of water on the mechanical response, both in the short-term and long-term regimes.

Chapter 3 proposes an overview of the geological, hydrogeological and exploitation framework of the test site, with a specific insight on the macroscopic features of the gypsum that is object of this study (branching selenite facies).

Chapter 4 illustrates the results of a detailed analysis of this material, in terms of textural, microstructural and compositional features.

Chapter 5 concentrates on the short-term mechanical response of branching selenite gypsum, tested with direct and indirect methods (i.e. Uniaxial Compressive Test, Point Load Test, Ultrasonic Pulse Velocity). The results, highlighting the variability of material strength, were interpreted and discussed in the light of the physical/chemical heterogeneity quantified in Chapter 4.

A specific insight on the processes of crack coalescence and strain accommodation is provided in **Chapter 6**. This Chapter considers the influence of the layering orientation and the effect of the confining pressure on the deformative processes that the rock suffers during compression.

Chapter 7 introduces the water saturation and the time-dependent response in the experimental investigation, also proposing a micro-mechanical analysis of the tested samples.

A further insight on the influence of the relative humidity on the mechanical behaviour is presented in **Chapter 8**. The Chapter also illustrates an experimental investigation on the long-term deformation of gypsum under the application of low axial stresses (i.e. in the stress range expected in the quarry test sites).

Eventually, **Chapter 9** offers a contextualization of the described results in the framework of underground excavation, discussing the scale effect and drawing some general conclusions.

1.4 List of papers and conference papers published during the period of PhD

Caselle C., Bonetto S., Costanzo D., Crack coalescence and strain accommodation in gypsum rock, Frattura ed Integrità Strutturale, *under revision*

Caselle C., Bonetto S., Comina C., Stocco S., 2020. GPR surveys for the prevention of karst risk in underground gypsum quarries, Tunnelling and Underground Space Technology 95. https://doi.org/10.1016/j.tust.2019.103137

Caselle, C., Umili, G., Bonetto, S., Costanzo, D., Ferrero, A.M., 2020. Evolution of Local Strains under Uniaxial Compression in an Anisotropic Gypsum Sample, Lecture Notes in Civil Engineering 40, pp. 454-461

Caselle C., Bonetto S., Comina C., 2019, Comparison of laboratory and field electrical resistivity measurements of a gypsum rock for mining prospection applications, International Journal of Mining Science and Technology, 29(6), pp. 841-849. https://doi.org/10.1016/j.ijmst.2019.09.002

Caselle C., Bonetto S., Vagnon F., Costanzo D., 2019. Dependence of Macro Mechanical Behaviour of Gypsum Rock on Micro-scale Grain-Size Distribution. Géotechnique Letters 9(4), 290-298. https://doi.org/10.1680/jgele.18.00206

Caselle, C., Bonetto, S., Colombero, C., Comina, C., 2019. Mechanical properties of microcrystalline branching selenite gypsum samples and influence of constituting factors. Journal of Rock Mechanics and Geotechnical Engineering, 11(2), 228-241. https://doi.org/10.1016/j.jrmge.2018.09.003

Caselle, C., Umili, G., Bonetto, S., Ferrero, A.M., 2019. Application of DIC analysis method to the study of failure initiation in gypsum rocks. Géotechnique Letters 9(1), 35–45. https://doi.org/10.1680/jgele.18.00156

Caselle, C., Penone, A., Bonetto, S., 2018. Preliminary mechanical characterisation of gypsum rock using UCS and Point Load Test correlation. Geoingegneria Ambientale e Mineraria 153, 60–67.

Caselle, C., Bonetto, S., Vagnon, F., Costanzo, D., 2018. Preliminary results of gypsum mechanical characterization, in: Geomechanics and Geodynamics of Rock Masses. Presented at the EUROCK - ISRM Symposium 2018, pp. 1123–1128.

Chapter 2

Gypsum mineral and gypsum rock: physical and mechanical properties

The stability assessment of gypsum quarries, both underground and open pit, requires an extensive knowledge of the mechanical properties of this rock material. The investigation of short-term and long-term response, besides an attention to the effects of water dissolution and weathering processes, are fundamental for a reliable characterization of the quarry sites.

In the present Chapter, the main physical and crystallographic features of gypsum mineral are summarized. The Chapter then reviews the principal literature data about mechanical properties of gypsum rock, focusing on the influence of water, on the mechanisms of crack coalescence and strain accommodation and on the creep behaviour.

2.1 Gypsum mineral

Gypsum ($CaSO_4 \cdot 2H_2O$) is the bi-hydrate phase of the calcium sulphate system. The system includes two farther crystallographic species: the hemi-hydrate phase (bassanite – $CaSO_4 \cdot 0.5H_2O$) and the anhydrous phase (anhydrite – $CaSO_4$). The chemical reactions of hydration or de-hydration of the calcium sulphate phases may spontaneously occur depending on temperature and pressure, following the curves shown in Figure 2.1. The Figure defines the stability conditions of each phase in different pressure ranges. In the common practice, the crystallographic structure of gypsum is considered stable and not-susceptible of dehydration for temperatures not higher than 40°C (~ 313°K), to completely exclude the possibility of a partial loss of water molecules.
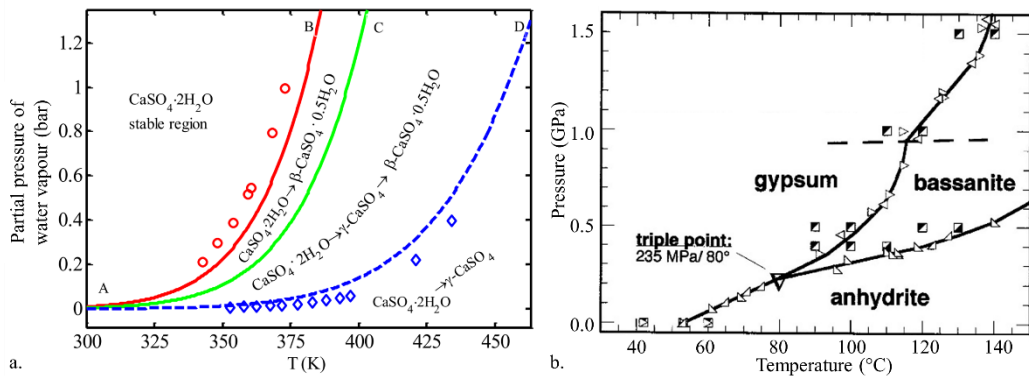
Figure 2.1 a. Results of thermodynamic calculations about the $CaSO_4 – H_2O$ system proposed by Tang et al., 2019 b. Pressure-temperature phase diagram of Calcium Sulphate by Mirwald, 2008

In the crystallographic structure of gypsum (Figure 2.2a), the presence of water molecules defines a layering in parallel direction to (010) plane. The layering consists of pairs of two adjacent sheets of Ca^{2+} ions and $(SO_4)^{2-}$ ions (in tetrahedral structure). Two water molecules join the successive pairs of sheets through hydrogen bonds, connecting water-oxygens with tetrahedrons-oxygens. As a result, gypsum crystals show a perfect (010) cleavage, clearly visible in the SEM micrograph in Figure 2.2b. The micrograph reproduces a gypsum crystal in the common euhedral form of gypsum, defined as *selenite*. The crystal well exemplifies also another typical feature of selenite gypsum, i.e. the contact twin on (100) crystallographic plane, commonly described as 'swallow tail' or 'arrowhead'.
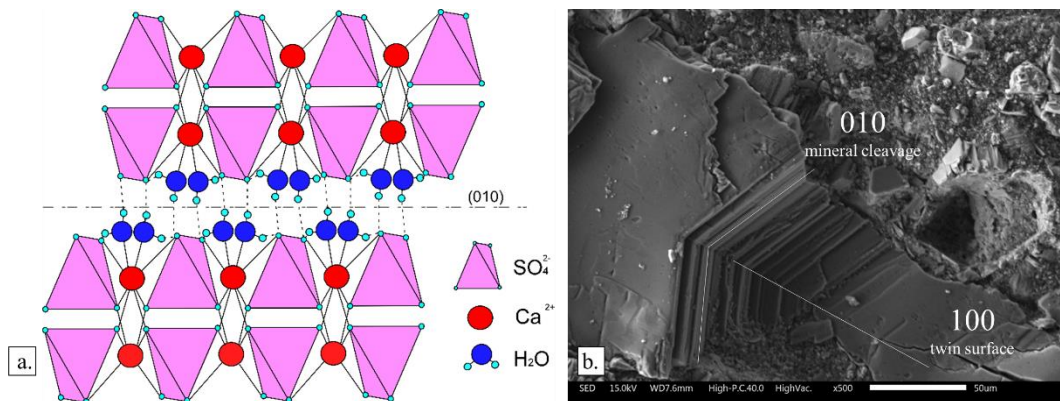
Figure 2.2 a. Crystallographic structure of gypsum. b. Selenite gypsum crystal, with the perfect mineral cleavage on the (010) crystallographic direction and the contact twin on the (100) crystallographic plane

The low force of the hydrogen bonds connecting the Ca-SO$_4$ layers in the gypsum structure controls some of the principal physical features of gypsum, *in primis* the low hardness (i.e. 2 in the Mohs scale of hardness).

The layered crystallographic structure of gypsum has also been identified as one of the reasons of the plastic strain behaviour of the mineral. Craker and Schiller, 1962 reported on an experimental investigation of long-term deformation of single gypsum crystals. They found high deformability in parallel direction to the (010) crystallographic plane (Figure 2.3), despite a sudden break-up in perpendicular direction. In the authors' interpretation, the weakness of the hydrogen bonding of water molecules implies an easier formation of reticular defects along the 010 plane than in the other crystallographic directions, where molecules are connected through the stronger ionic bond. Therefore, the formation and sliding of dislocations (i.e. linear disposition of reticular defects) and the consequent plastic deformation results easier along the water layers than in the calcium-sulphate structure.
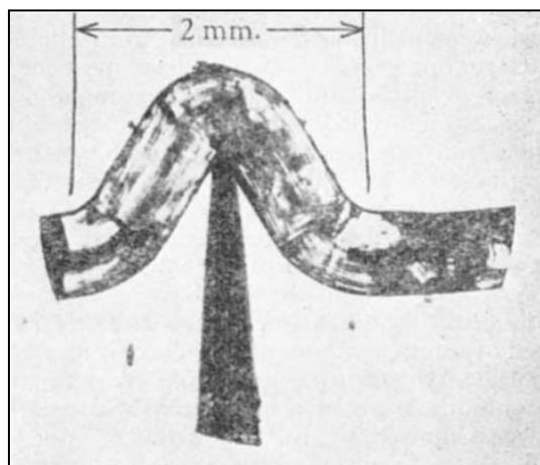
Figure 2.3 Gypsum crystal deformed along the (010) crystallographic plane (Craker and Schiller, 1962)

The influence of water on the gypsum properties does not only involve the water molecules within the mineral structure, but also the effect of external water. Gypsum has, indeed, a very high solubility in fresh water (0.015 mol/kg H_2O, i.e. about 100 times than calcite solubility in water). As shown in Figure 2.4a, a rise in temperature increases the gypsum solubility, with a maximum around 40°C. The presence of other salts in the solution can additionally affect the dissolution rate of gypsum, e.g. NaCl in solution enhances the solubility of gypsum (Figure 2.4b), while $CaCl_2$ reduces it.
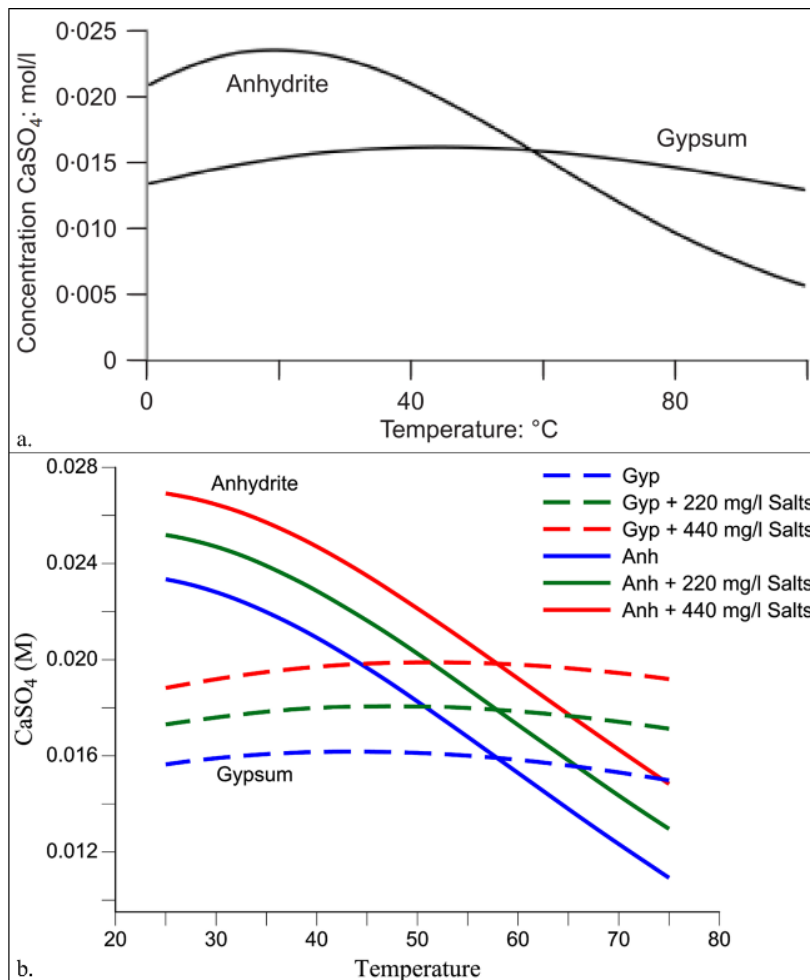
Figure 2.4 a. Solubility curves of gypsum and anhydrite in water with temperature (Ramon and Alonso, 2013) b. Evolution of calcium sulphate solubility curves with different concentrations of NaCl (Ramon and Alonso, 2018)

The dissolution process of gypsum in water is well-documented in the scientific literature for its implications on the stability of underground voids, the development of karst phenomena and the worsening of mechanical properties.

At the microscale, the water dissolution produces structures that have been investigated with different techniques by several authors (e.g. SEM by Yu et al., 2016, micro-computed tomography by Meng et al., 2018). Yu et al., 2016 highlighted a particular feature of gypsum dissolution structures, describing a process of crystal splitting along the weak structural surfaces (i.e. gypsum cleavage) (Figure 2.5). This structure was related by the authors to the experimental evidence that dissolution on (010) crystallographic faces has a general higher rate than in other crystallographic directions (Fan and Teng, 2007).
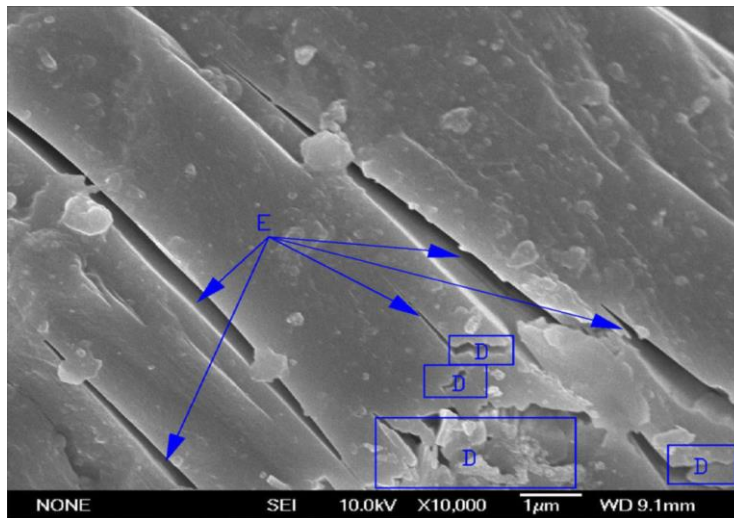
Figure 2.5 Damage of gypsum crystals after water dissolution. D areas represent rupture and fragmentation structures, whereas E arrows show the splitting of gypsum along the mineral cleavage (Yu et al., 2016)

2.2 Mechanical properties of gypsum rock

Gypsum is present in nature as constitutive mineral of rocks with a wide range of textural, microstructural and compositional features. The sizes of gypsum crystals can vary from few microns to several meters. Porosity is generally low, ranging between less than 1% up to 10%. Gypsum rocks, with a predominant presence of gypsum, may contain, in lower percentages, other minerals, varying in reason of the depositional environment. Specific features of gypsum rocks in terms of grain size, texture, microstructure, composition and depositional environment may be described as 'facies'.

The most common depositional environments for gypsum, as well as for other evaporite rocks, include marginal, shallow or deep basins where the rate of water evaporation is greater than the total water inflow, bringing to the concentration and precipitation of residual mineral.

In marine-marginal sabkhas (i.e. arid region salt marshes), gypsum crystals may precipitate in the pores of soils in the upper phreatic and vadose zones. Most of these

gypsum rocks are then dehydrated, creating irregular nodules and layers of hemi-hydrate or anhydrite. The change of humidity and temperature conditions may bring to the re-hydration of part of the rock, forming a gypsum facies that is typically defined as 'microcrystalline' or 'alabastrine' gypsum, i.e. a fine-grained massive facies formed by the replacement of anhydrite (Schreiber and Tabakh, 2000).

In shallow-water subaqueous environments, gypsum crystalizes in independent clusters, crusts or undulated beds. These gypsum facies are very similar in thicknesses, morphologies and chemistries to the gypsum beds that are easily observable in modern Salinas (Schreiber and Tabakh, 2000).

In deeper water environments, gypsum rock may have different features depending on the sedimentary conditions. For instance, it is possible to find:

- gypsum facies with well-marked current structures, in comparatively shallow environments;
- finely laminated and continuous gypsum facies, deposed in the deeper areas of the basins;
- massive selenite gypsum facies, with pluricentimetric gypsum crystal with a well-formed selenitic shape;
- resedimented gypsum facies, with sizes of arenites or rudites and all the usual features of non-evaporites resedimented deposits.

The importance of a facies-based mechanical characterization of gypsum rock was often suggested in the scientific literature, as confirmed by the review presented in paragraph 2.2.1. The following paragraphs describe different risk scenarios connected with underground drift and tunneling excavations in gypsum and sulphate-rich rocks, proposing a literature review of the experimental researches that try to address each of these topics.

2.2.1 Mechanical strength of gypsum rocks in different facies

Several studies were accomplished on the comparison of mechanical properties of different gypsum facies. Papadopoulos et al. (1994) compared the mechanical properties of alabastrine, medium-grained and coarse-grained Neogene gypsum from Crete, recognizing the strong influence of formation mechanisms and depositional environments. Yılmaz and Sendır (2002) analyzed the mechanical response of a pure alabastrine gypsum type from the Sivas Basin (Turkey), whereas mechanical properties of porphyric and alabastrine gypsum types from the same basin were compared in Yilmaz (2007). At the nanoscale, Chen et al. (2010) investigated the influence on the elastic properties of different geometrical configurations of gypsum crystals (needle aggregates vs randomly oriented) in synthetic samples.

Table 2.1 presents a collection of literature data about mechanical strength of gypsum under uniaxial compression. It clearly shows a wide range of strength that cannot be

completely explained only by the porosity variability. The data suggest the influence of other controlling factors, e.g. the difference in facies, with consequent differences in terms of grain size, porosity, mineralogical content and depositional processes.

Table 2.1 UCS and porosity values of gypsum samples in different facies.

Reference	Gypsum Facies	UCS [MPa]	Porosity [%]
Singh and Eksi, 1987	undefined	25.9 – 33.4	0.92 – 2.92
Papadopoulos et al., 1994	Alabastrine gypsum	12	
	Medium-grained gypsum	4.6	
	Coarse-grained gypsum	4.9	
Yılmaz and Sendır, 2002	Pure alabastrine gypsum	15.04 - 30.0	
Moiriat et al., 2006	Water saturated saccharoid gypsum grain size > 1mm	13.7	15.5
	Water saturated saccharoid gypsum 0.1 mm < grain size < 1mm	16.9	3.5
	Water saturated saccharoid gypsum grain size < 0.1mm	23.5	4.6
Bonetto 2006	Fine grained gypsum	11.1 – 15.5	
	Coarse grained gypsum	5.7 – 11.7	
Yilmaz, 2007	Pure alabastrine gypsum	28 – 36.2	
	Porphyritic gypsum	16.2 – 19.7	
Castellanza et al., 2010	Gypsum facies from an Upper Triassic sabkha	16	
Liang et al., 2012	Xishan gypsum deposit of Taiyuan with random presence of band structures of pure calcium sulphate	13.4 – 15.6	
Heidari et al., 2012	Gypsum facies from the Early Miocene	3.8 – 30	

	Gachsaran Formation (Iran), with peculiar crystalline-gypsum and micrite layers and veins		
Salih and Mohammed, 2017	Gypsum rock that locally contains marl or clay impurities within cracks.	20	

2.2.2 Weathering and worsening effect of water

Gypsum underground quarries are often located below the groundwater table and, during the active exploitation, dewatering operations (e.g. pumping) are often required. Despite the water-pumping, relative humidity can remain high in the underground drifts and residual water can persist in the rock porosity, creating conditions of partial saturation. At the end of the exploitation, the interruption of pumping operations brings to the re-establishment of the initial water level and to the modification of the saturation conditions in the drift pillars.

The sensitivity of mechanical response on the relative humidity and the water saturation becomes, therefore, a primary element in the long-term stability assessment of gypsum pillars. Moreover, the long-term permanence of gypsum in water (particularly if in presence of a flow, with continuous renovation of fresh water) may trigger dissolution processes, inducing variations in the rock microstructure and additional worsening of mechanical strength.

Several research groups focused on the influence of weathering and worsening effect of water on the physical and mechanical properties of gypsum rocks.

Auvray et al., 2004 proposed a study of the aging of gypsum pillars in abandoned underground mines. They considered two mining sites, with two different gypsum facies (a saccharide gypsum facies, with 1 mm crystals and regular bedding of 1 cm, and a microcrystalline gypsum facies, with grain size lower than 1 mm and absence of any particular orientation). With a SEM-BSE morphological analyses, they investigated samples drilled at increasing depth within the pillars (Figure 2.6a). The external portions of the pillars, being more exposed to the humid atmosphere of the drifts, showed higher evidences of dissolution and corrosion processes, while the centre (Figure 2.6a-7) seemed to be almost undisturbed. In agreement with these observations, the authors measured a general decrease of physical properties (e.g. density, porosity, velocity of seismic waves) from the centre to the surface of the pillars (Figure 2.6b).
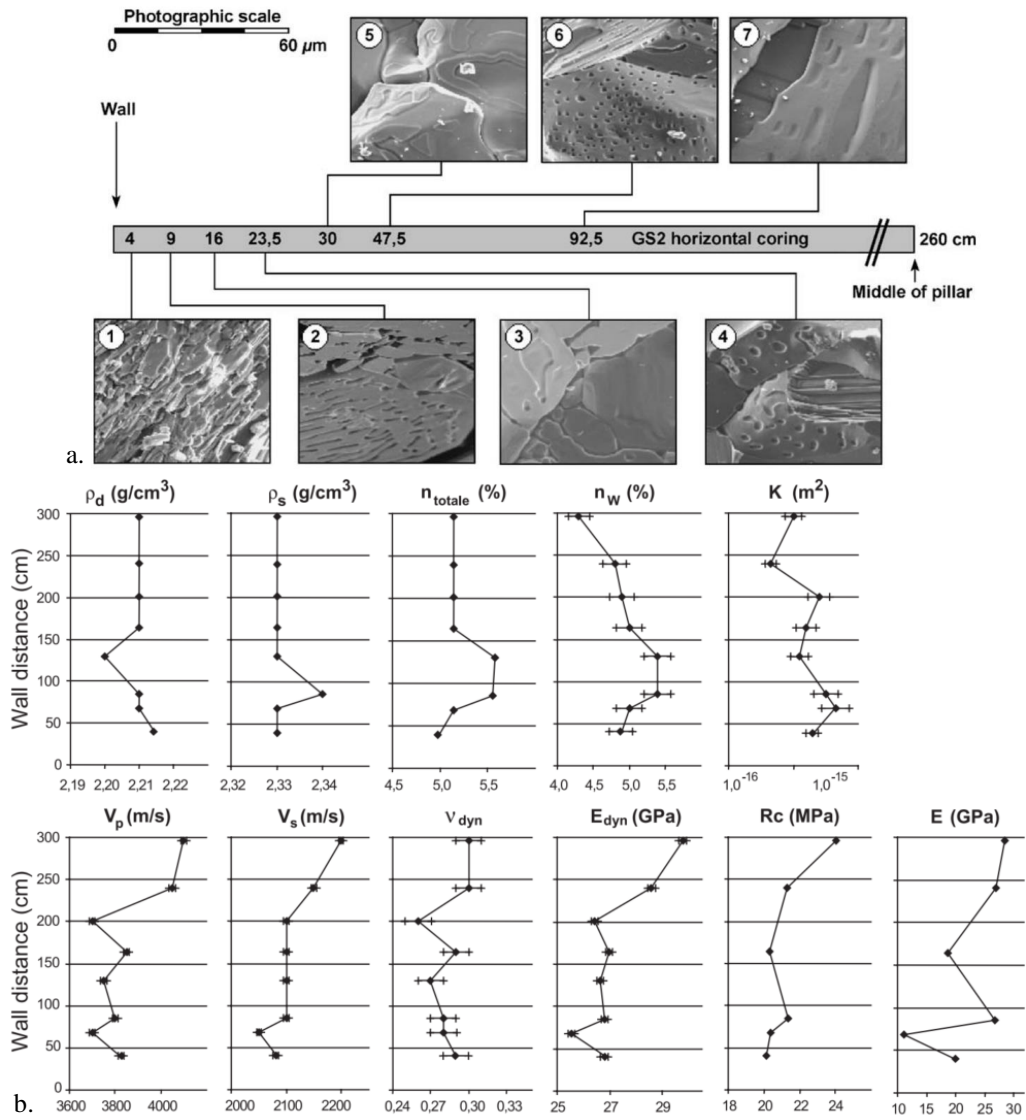
Figure 2.6 SEM micrographs on a core sample drilled in a gypsum pillar b. Evolution of physical parameter with the distance from the pillar wall (Auvray et al., 2004)

Yilmaz, 2010 described a set of experiments on gypsum samples from a massive gypsum facies of the Hafik formation in Sivas basin (Turkey), with gypsum content close to 100%. The experimental investigation underlined a clear reduction of UCS and Young modulus in consequence to the increase of water content (Figure 2.7a-b – the saturation corresponds to a water content of about 8.5-9%). The results suggested that not only a strength decrease of about 50% can be appreciated going from dry to completely saturated conditions, but also that even a very small increase in water content (1–2%) can cause a considerable worsening of strength features of

the rock. An additional information is included in the graph in Figure 2.7c: the worsening of strength in response to water saturation increases with the increasing time of immersion in water, suggesting the involvement of water-dissolution processes.
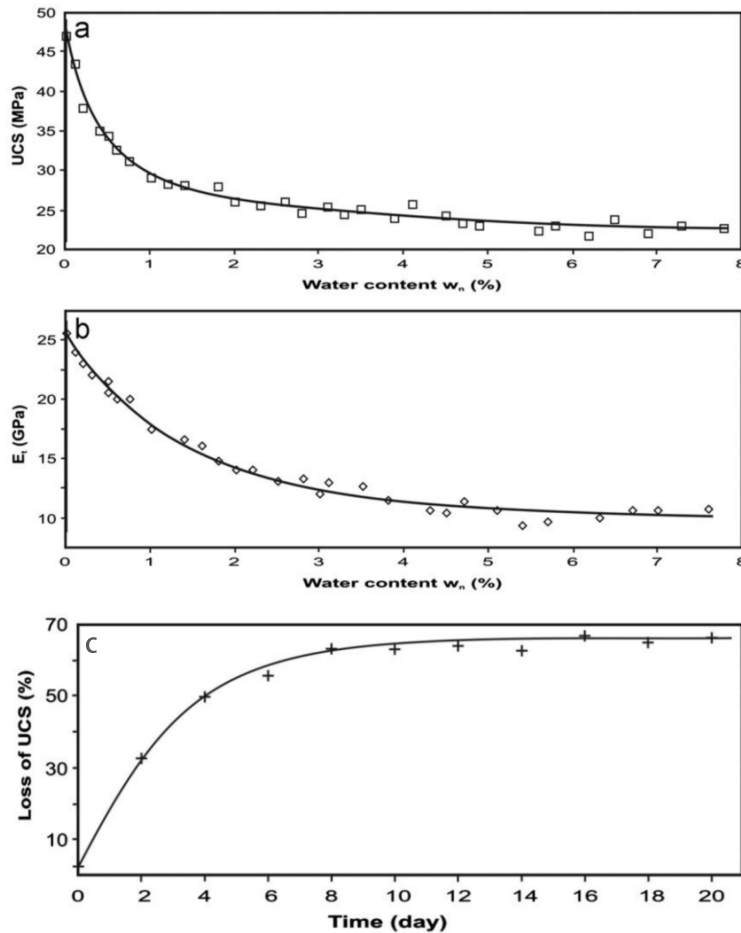
Figure 2.7 a. Decrease of UCS of gypsum samples with increasing water content. b. Worsening of elastic modulus of gypsum samples with the increase of water content (the saturation corresponds to a water content of about 8.5-9%) c. Loss of strength of gypsum with the increasing of time of immersion in water (Yilmaz, 2010)

A similar worsening of mechanical properties of gypsum with water was observed by Castellanza et al., 2008. Their study was performed on Triassic gypsum from Northeastern Italian Alps, deposed in arid costal settings (sabkha). The dissolution effect was evaluated for different times of immersion in flowing water, up to the almost complete dissolution of the sample (Figure 2.8a). The consequent strength and stiffness degradation is clearly evident from the graphs in Figure 2.8b-c. Based on these experimental results, Castellanza et al., 2010 reported on the stability

assessment of an abandoned underground gypsum quarry, proposing an evaluation of pillars stability based on the deteriorating effect of water.
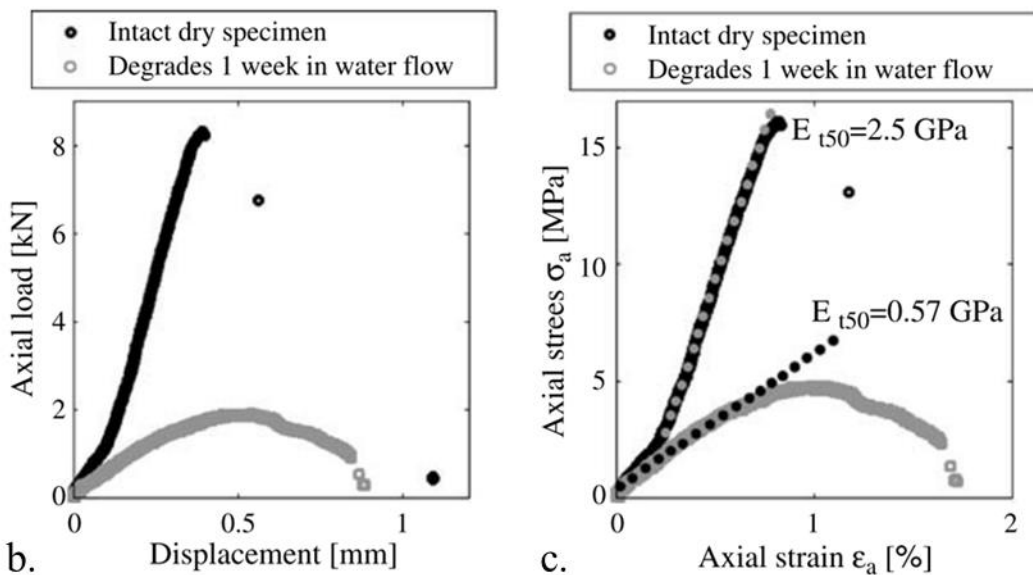
Figure 2.8 a. Gypsum samples after increasing times of immersion in flowing water. b. Stress-displacement curves of specimens in undisturbed conditions and after one week of immersion in flowing water. c. Young modules in the two considered conditions (Castellanza et al., 2008)

The experimental investigation reported by Liang et al., 2012 introduced an additional element. They considered the presence of NaCl in different concentrations in the soaking brine and the influence of temperature variations. Their results showed a weakening of gypsum strength of 27% and 37% for a brine with 50% NaCl concentration and temperatures of 40°C and 70°C respectively. The weakening

exponentially increases (up to 62% and 90%) for 100% NaCl concentration of the brine.

The study by Salih and Mohammed, 2017 suggested that also the application of a confinement pressure during the immersion of samples in water is an element that enhances the gypsum dissolution and the deterioration of mechanical properties. Their results, summarized in Figure 2.9, refer to uniaxial compression tests performed on samples previously soaked in water for different times and under different confining pressures.
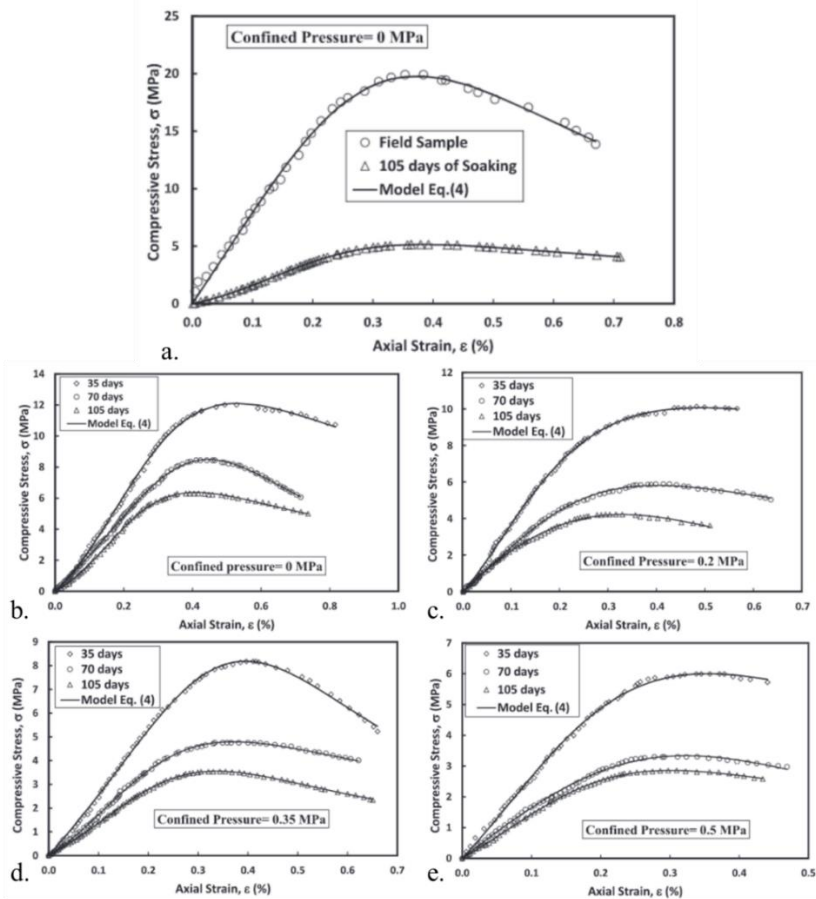
Figure 2.9 a. Stress-strain curves of uniaxial compression tests on gypsum samples in undisturbed conditions and after a 105 days soaking. b-d Stress-strain curves of uniaxial compression tests on gypsum samples after soaking of 35, 70 and 105 days with confining pressures of 0, 0.2, 0.35 and 0.5 MPa respectively (Salih and Mohammed, 2017)

Zhu et al., 2019 proposed a multiscale investigation of the phenomenon. The mechanical data about the worsening of mechanical strength of gypsum rock immersed in water for increasing time intervals (Figure 2.10 a-d) were accompanied by a SEM investigation of the microstructures produced in the rock by the water

(Figure 2.10 d-g). The authors suggested that the deterioration of mechanical properties depends on the change in internal microstructure that, with the continuous increase of immersion time, sees the destroying of connections between the rock particles through the hydrolysing and weakening of crystal bonds at the tip of microcracks. In additions, the presence of water in the microcracks exerts a pressure on the crack walls, making difficult to close them, and has a lubrication action that reduces the rock friction.
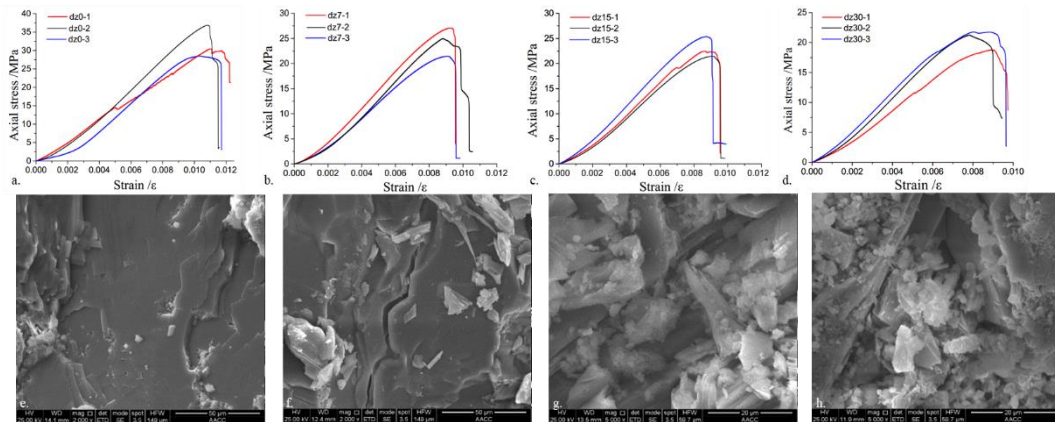
Figure 2.10 a-d. Stress – strain curves of gypsum samples in natural state (a) and after immersion in water for 7 days (b), 15 days (c) and 30 days (d). e-f. SEM images of the correspondent samples before the mechanical test (Zhu et al. 2019)

2.2.3 Failure coalescence and plastic behaviour

The microscale mechanisms controlling the failure coalescence and strain accommodation processes in synthetic and natural gypsum samples have for long time interested the scientific world.

A wide literature is available on the processes of failure coalescence in synthetic gypsum that was often used as good rock-model material for the similarity of behaviour with brittle rocks. This kind of synthetic material (a specific mixtures of gypsum powder, water and other components, e.g. celite, with a mean porosity of 30%) offers the advantages of a good repeatability of the results and the possibility to easily prepare a high number of samples. Shen et al., 1995 and Bobet and Einstein, 1998 proposed the investigation of fracture initiation and propagation monitored by a microscope connected to a video recorder during mechanical tests (in uniaxial or biaxial compression). The initial samples included two flaws, with different orientations and relative positions, and the tests were performed with displacement control, that is more likely to produce stable fracture propagation. Sagong and Bobet, 2002 introduced the complication of multiple initial flaws (up to 16). Wong and Einstein, 2009a and Wong and Einstein, 2009b followed a multiscale approach to investigate and compare the crack coalescence in synthetic samples of gypsum and

natural samples of Carrara marble. The macroscopic study of photographical images acquired with a high-speed camera during the uniaxial tests was enriched with the comparison with pre- and post-failure analyses at SEM and ESEM. The results underlined the difference in cracking mechanisms between a natural rock material (Figure 2.11 a-c) and the synthetic rock-like model (Figure 2.11 b-d).
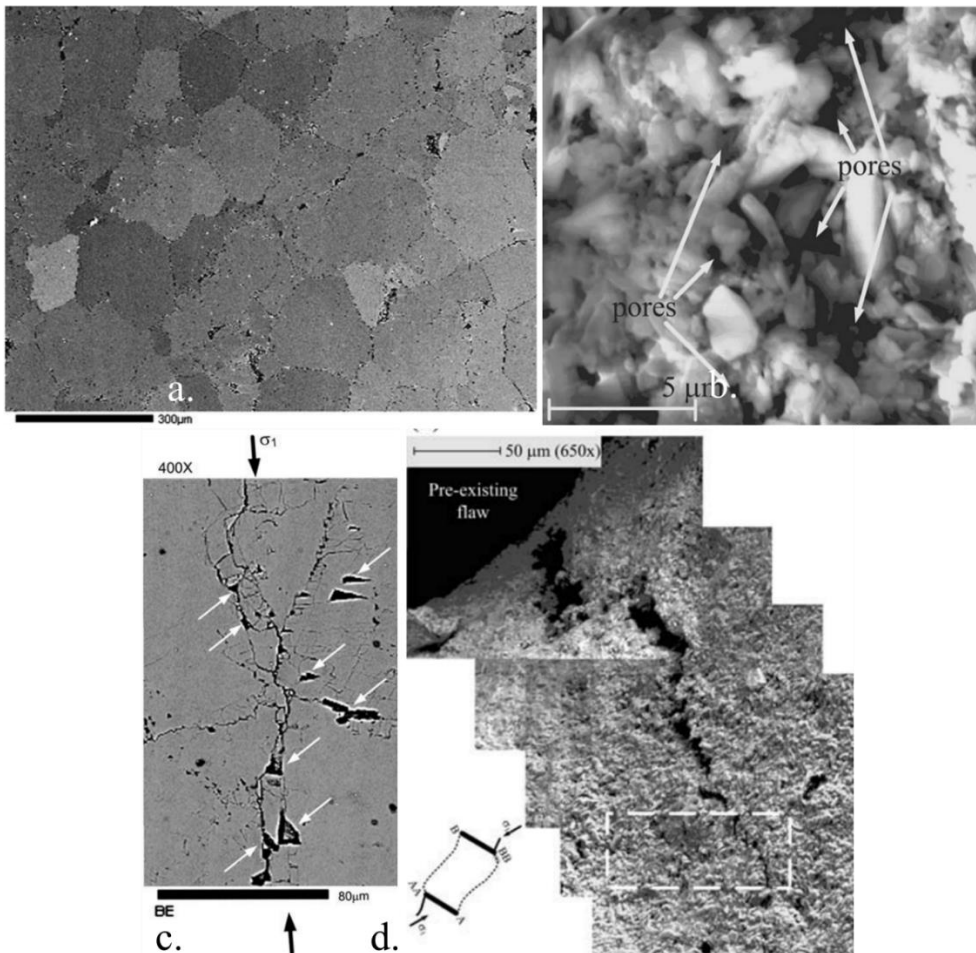
Figure 2.11 a. SEM micrograph of Carrara marble sample before the test b. ESEM micrograph of synthetic gypsum sample before the test c. Typical crack in Carrara marble sample after the mechanical test d Typical crack in synthetic gypsum sample after the mechanical test (Wong and Einstein 2009b)

Bing et al., 2018 proposed a set of numerical simulations with distinct element code (UDEC) using as reference material the synthetic gypsum samples investigated in the cited literature. The simulations involved uniaxial compression tests on specimens with pre-existing flaws with varying inclination angles (0°–90°) and lengths (10–30 mm). Results (Figure 2.12) show a decrease in peak strength for the

intermediate values of dip angle (30°–60°). This strength decrease is more accentuated for higher lengths of the flaws.
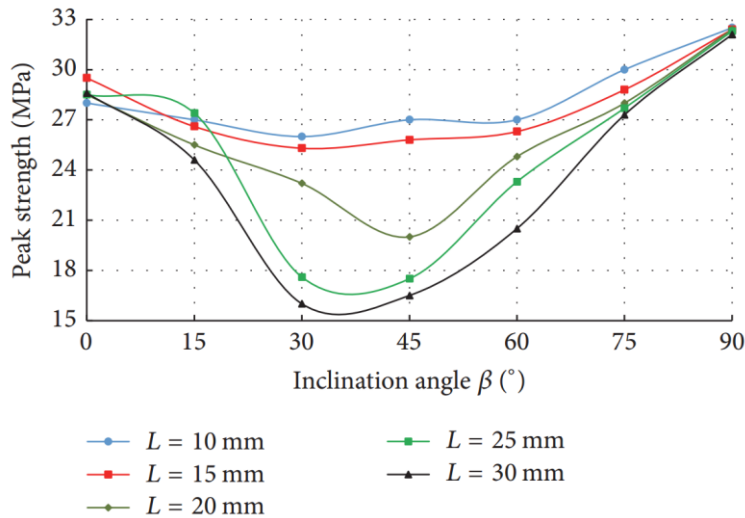
Figure 2.12 Trend of simulated uniaxial peak strengths of gypsum samples with initial flaws with inclination angles ranging between 0° and 90° and lengths between 10 and 30 mm (Bing et al. 2018)

Recently, Čebašek and Frühwirt, 2018 investigated the behaviour of synthetic gypsum samples with different orientations of pre-existing flaws under a static compressive load level (i.e. creep), aiming to understand the microcracking processes and predicting the timing of final failure of a rock-like material. Basing on the results, they described the time-dependent cracking mechanism as a progressive material degradation, with the initiation and growth of cracks at the small scale and the following coalesce to form large-scale fractures and fault zones, bringing to the sample collapse.

The scientific contributions about the processes of crack coalescence and strain accommodation in natural gypsum rocks are less frequent. The topic has been mainly approached with microstructural analyses and acoustic emission (AE) data. However, a wide range of stress conditions was contemplated in the test settings (e.g. torsional shear strain, triaxial compression), allowing for a description of transition from brittle to plastic strain regimes.

Zucali et al., 2010 proposed a quantitative microstructural study on natural gypsum samples (gypsum content >99%) experimentally deformed in torsion at a confining pressure of 300 MPa, investigating a range of shear strains from 0 to 4.82 and a range of temperatures from 70 to 90°C. Their results underlined the presence of a plastic deformation recorded by gypsum for the entire range of shear strain, from the initial to highest values. In the investigated range of strain and temperature, they observed a behaviour of gypsum completely characterized by the coexistence of brittle and

plastic deformation. Only by increasing the temperature above 90°C, they could observe a clear brittle to plastic transition.

A detailed analysis of the material response under triaxial compression was proposed by Brantut et al. 2011. They investigated the behaviour of Volterra gypsum (a highly-pure fine-grained alabastrine facies of gypsum rock) in triaxial compression, under a range of confining pressure from 2 to 90 MPa, at room temperature and 90°C. Through the integration of mechanical data, microstructures and acoustic emissions, they proposed an interpretation of the modality of strain accommodation in the rock. The stress-strain curves presented in the contribution (Figure 2.13a) are characterized by small stress drops (from 0.5 to 6 MPa in amplitude). This kind of behaviour coexists also with the ductile deformation and the strain hardening. Based on microstructural observations, the authors suggested a correspondence between the stress drops and the generation, in the rock, of shear bands formed by microcracks and kinked grains (an example of kinked grain is shown in Figure 2.13b). They observed that this shear banding process produces acoustic energy at elevated temperature but is silent at room temperature. They suggested, therefore, the possible existence of a process of dynamic stress drops generation (i.e. an earthquake mechanism) at elevate temperatures, driven by a micro-plasticity process (i.e. kinking of the grains).
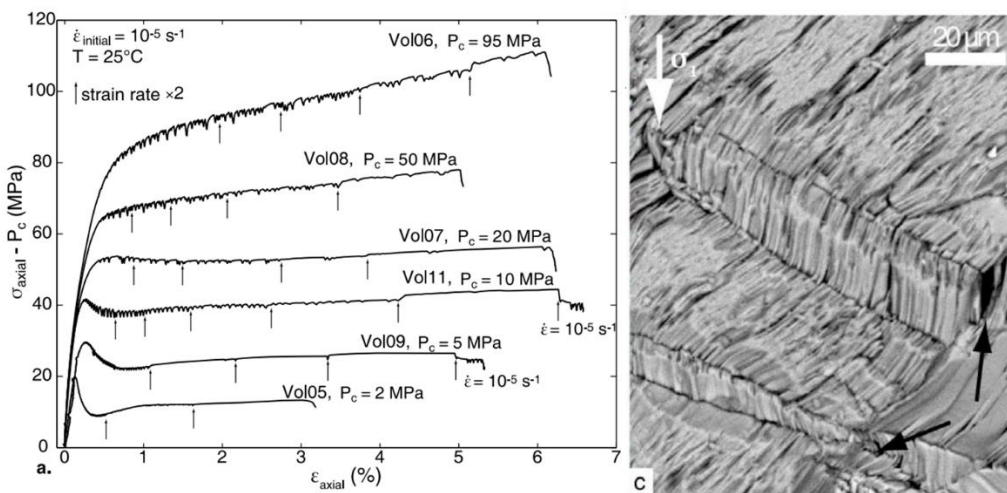
Figure 2.13 a. Stress-strain curves from triaxial tests at room temperature (small arrows indicate when strain rate was increased by a factor of 2). b. Microstructural evidence of a kinking deformation on a gypsum grain in a sample deformed at Pc = 50 MPa. The black arrows indicate crack opening at the edges of the kinked grain (Brantut et al. 2011)

Also Lacidogna et al., 2019 investigated the behaviour of acoustic emissions in gypsum rocks. They proposed a study of the relation between snap-back instability, fracture coalescence and energy emission in natural gypsum samples under compression. Their results highlighted the absence of direct correspondence between

fracture energy and acoustic emission. They suggested, on the other hand, a relation between acoustic energy and snap-back instability (i.e. the catastrophic drop in the load carrying capacity that occurs in correspondence of a sudden crack propagation in brittle materials). Their experimental investigation showed a clear difference in AE records on tests performed with constant stress rate (i.e. with a sudden collapse of the sample after the peak strength) and with constant strain rate (i.e. with a gradual advancement of stress and strain after the peak strength). In the first case, the sample collapse (i.e. snap-back instability) corresponds to a hit in cumulative AE energy that is not present in the second case (i.e. strain controlled conditions), suggesting the total dissipation of energy for the creation of the new fracture surfaces.

2.2.4 Time-dependent behaviour

The underground gypsum quarries are generally exploited by room-and-pillar methods, with pillars supporting the action of a static load for long times (i.e. the life-time of the active quarry exploitation). If the rock is not interested by a rapid unstable failure under high stresses, a time-dependent deformation or a creep damage under the action of long-term stress can however take place. The creep damage could also be delayed behind the active mining exploitation for several years or even decades, suggesting an additional element of interest in the study of creep process in gypsum rock.

The existence of a time-dependent deformation under the application of a constant load have been recognized and described for all the rock materials. However, in the hard-brittle rocks, the achievement of high creep strain rates is usually subjected to conditions of elevate temperatures or high pressures. On the other hand, a creep deformation is often observed in soft rocks at room temperature and under pressure conditions normally encountered in engineering structures (Roy and Rao, 2015).

Figure 2.14 offers a schematic representation of the typical creep curves in rock materials. After the initial phase of instantaneous elastic strain, two kinds of strain-time paths can be described, depending on the level of applied stress. If the stress is close to the peak stress (Curve 1), the material shows an initial phase with decreasing strain rate (primary or transient creep), followed by a phase of stable strain rate (secondary or steady-state creep). After a certain interval of stability, the strain rate starts to gradually increase, driving the sample to the creep failure (tertiary or accelerate creep). If the stress is significantly lower than the failure stress (Curve 2), the transient creep takes more time to stabilize on the steady-state conditions. In these stress ranges, the steady-state conditions may not be replaced by an acceleration of strain rate and the curve may settle on an asymptotic value.
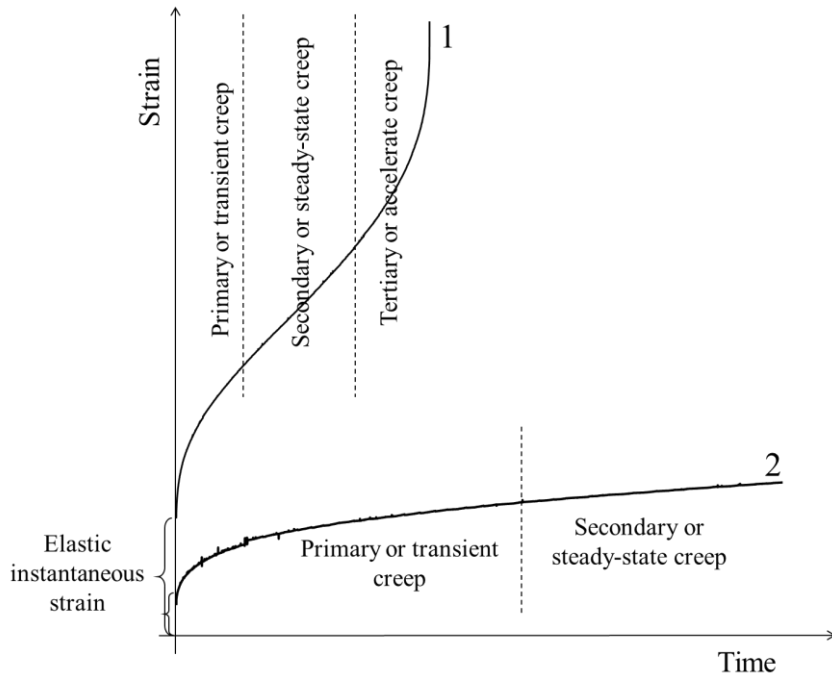
Figure 2.14 Typical axial strain-time curves for creep deformation. 1. Stress level close to the failure stress. 2. Low or intermediate stress level compared to the failure stress.

The mechanisms involved in the creep strain of gypsum rocks and the effect of water and relative humidity in the creep process are quite complex and include the interaction of several mechanisms.

De Meer and Spiers (1995, 1997, 1999) described a comprehensive experimental investigation of creep behaviour of reconstructed granular gypsum samples, focusing on the assessment of the importance of pressure solution. Their experimental program included hydrostatic and uniaxial compaction tests on samples with particle size ranging from 15 to 280 μm, with an investigation of different conditions of fluid saturation (i.e. dry, oil, water oversaturated in gypsum, NaCl+gypsum water solution). The water-saturated samples were tested under both chemically closed (i.e. undrained) and open (i.e. flow through, with continuous renew of water and possibility to remove any dissolved material) conditions. The presented results included the following evidences:

- dry and oil saturated materials showed little or no creep where samples flooded with saturated gypsum solution creeped significantly
- a 10 to 30 times increase in compaction creep rate was observed in the flow-through tests with respect to chemically closed-system (Figure 2.15a)
- the absolute creep rates obtained with NaCl were up to 50 times faster than in NaCl-free conditions (Figure 2.15b).

The authors accompanied the mechanical data with the microstructural analysis of the deformed material, highlighting the presence of indentation, truncation and overgrowth microstructures in the creeped samples (e.g. Figure 2.15c).

All these experimental evidences brought the authors to propose a creep model based on a mechanism of pressure solution along the grain boundaries. However, they observed that the creep was slower than what could be expected basing on a classical pressure solution model. They suggested, therefore, the presence of a rate-limiting mechanism, with opposite action, that they recognized as the precipitation of new gypsum on the pore walls (Figure 2.15d).
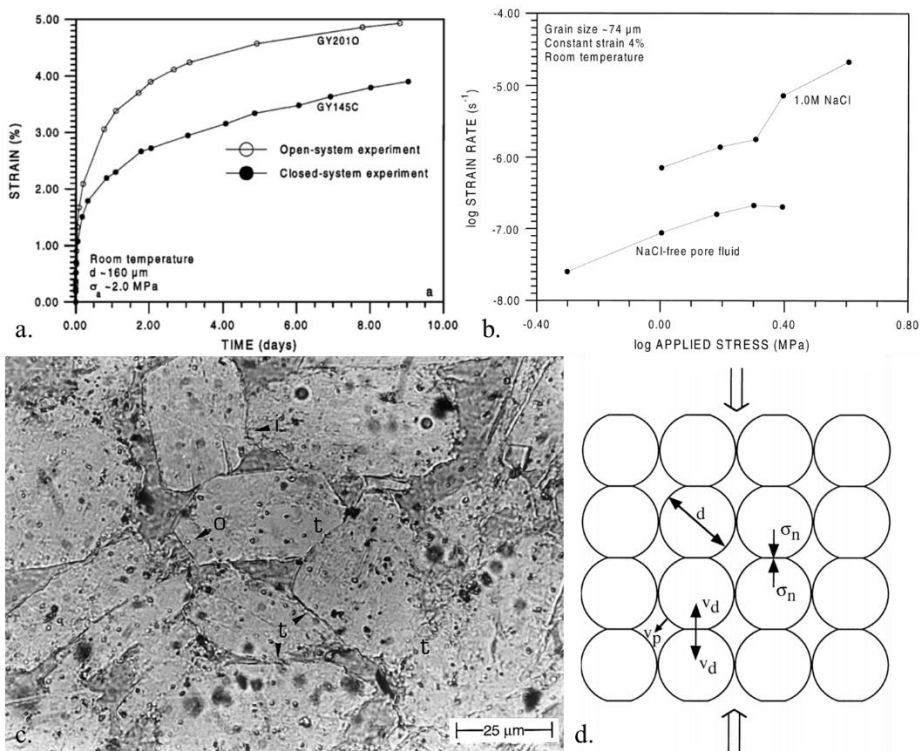
Figure 2.15 a. Comparison of uniaxial creep tests in water under chemically open and close conditions respectively (De Meer and Spiers, 1997) b. Comparison of strain rate data of creep in water with and without NaCl (De Meer and Spiers, 1999) c. Optical microscope micrograph of gypsum at the end of the creep test with evidences of indentation (i), truncation (t) and gypsum overgrowth (o) (De Meer and Spiers, 1999) d. Schematic representation of the creep model proposed by the authors. In the scheme, σ_n is the normal stress across grain-to-grain contacts, and v_d and v_p are the velocities of dissolution and precipitation, respectively. (De Meer and Spiers, 1999)

Hoxha et al., 2005, 2006 proposed a wide experimental analysis and modelling contribution about creep behaviour of natural gypsum rock (considering an orogenic gypsum rock facies, with porosity lower than 3% and a gypsum content higher than 99%). They focused especially on the role of relative humidity, evaluating the

influence of this parameter in short-term triaxial tests and in creep tests. Creep behaviour was evaluated with three types of test configurations:

- under uniaxial compression and constant relative humidity
- under step-wise uniaxial compression and step-wise relative humidity
- under step-wise triaxial compression on samples with natural water content.

In the results of short-term triaxial compression tests, the authors did not observe a clear control of relative humidity on the mechanical behaviour (maybe hidden by the material variability). However, they registered a clear dependence of creep strain rate on this parameter. In additions, the experimental results showed the presence of an intensive time-dependent and humidity-dependent dilatancy, that the authors considered as an indication of a damage-like mechanism, even if not directly related to the growth of new cracks.

Based on the experimental data, the authors suggested that the influence of relative humidity was not limited to the only lowering of creep activation energy. They proposed that, during the creep, the water molecules in the humid atmosphere form a water film along the crystal contacts, making easier the relative sliding. According to the authors, the water films should be enhanced by the intra-crystalline water molecules of gypsum that, when the material is stressed, tend to migrate from their sites to the pores of the rock.

Additional experimental data about creep tests on saccharoid gypsum in saturated conditions are reported in Moiriat et al., 2006. The authors measured the time-dependent deformation of gypsum with different grain sizes under uniaxial compression. Results highlighted the achievement of accelerated creep conditions for applied stresses higher than 35% of the uniaxial short-term strength (Figure 2.16). These results were used in Nedjar and Le Roy, 2013 to propose a constitutive model of long-term behavior of gypsum rock. The proposed model includes the presence of a damage mechanism active from the very first phases of creep tests in a viscoelastic framework.
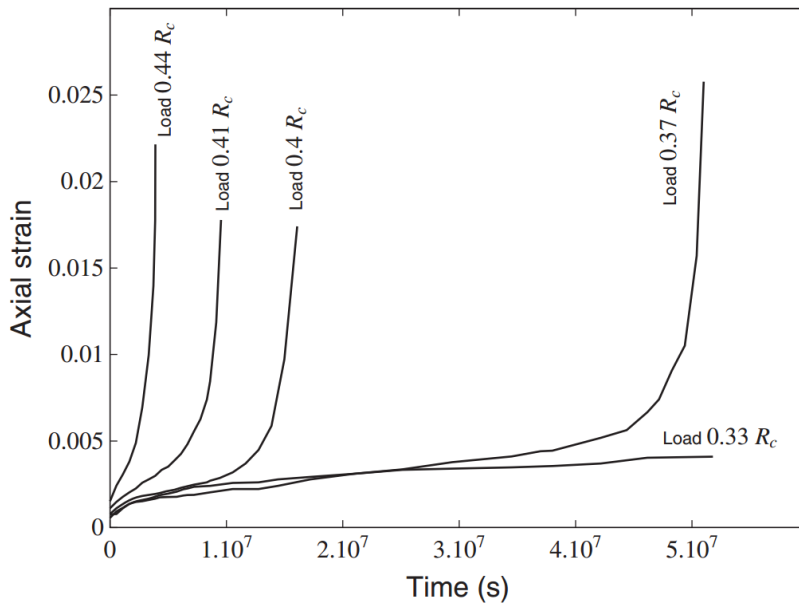
Figure 2.16 Experimental data on creep in saturated gypsum samples (Moiriat et al., 2006)

A recent experimental investigation (Liu et al., 2019) reported on the results of short-term uniaxial compression tests and long term step-wise creep tests on prismatic gypsum samples (Figure 2.17). The experimental investigation refers to a marine gypsum facies with grain size ranging between 1 and 5 mm and gypsum content higher than 75%. The described results, exemplified in Figure 2.17, include the registration of the longitudinal wave velocity for the entire duration of the tests. The results show an anomalous increase of wave velocity during the creep test before the sub-critical instability (Figure 2.17b). This anomalous trend is considered by the authors as the evidence of a phase of reduction of microcrack events that allows for the accumulation of energy then used for the failure of specimen.

It is worthwhile to notice that, testing the material in dry conditions, the authors registered a value of creep failure strength greater than the uniaxial compression short-term strength.
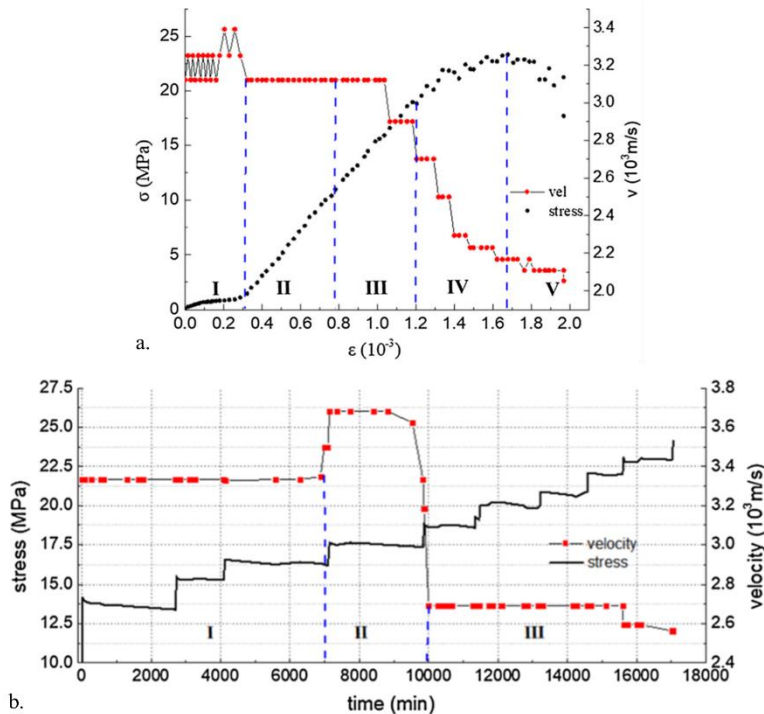
Figure 2.17 a. Stress and longitudinal wave velocity against strain during a uniaxial compression test on a prismatic gypsum sample b. Stress and longitudinal wave velocity data in time during a step-creep test on gypsum (Liu et al., 2019)

2.2.5 Swelling behaviour of sulphate-rich deposits

As already mentioned, gypsum bodies may be associated with other evaporitic rocks. This association may be primary, due to the precipitation of different evaporitic minerals under the same sedimentary conditions, or consequent to the gypsum dehydration that may occur both synsedimentary or after the burial. When gypsum is buried, indeed, the temperature rises, bringing to the loss of crystallization water and to the replacement of gypsum with hemi-hydrate and/or anhydrite. Hence, gypsum rock bodies are often associated with irregular volumes of anhydrite rocks.

Sulphate-rich formations, with gypsum and anhydrite minerals, may generate, in presence of a water circulation, the development of severe expansions when are involved in underground excavation (e.g. Alonso et al., 2013; Ramon et al., 2017). The rock expansion may affect the functionality and stability of engineering infrastructures in tunnels and underground drifts, causing great displacements at not-confined surfaces and important swelling pressures against structural elements. The problem of these expansion mechanisms is complicated by the sudden occurrence and uncertain evolution in time, without any apparent stabilisation of swelling pressures and deformations over time. Similar sulphate-related expansions have also been observed in civil infrastructures (e.g. bridge pillars and buildings) founded in

sulphate-rich deposits, causing the generation of heaves and structural damages (Alonso and Ramon, 2013; Alonso et al., 2015; Ramon and Alonso, 2013, 2018).

Ramon and Alonso 2013 proposed an interpretation model of this phenomenon that is summarized in the scheme in Figure 2.18. The water, circulating in the open fissures of the rock, dissolves part of the available anhydrite mineral, becoming oversaturated in sulphate and calcium ions. From this oversaturated water solution, new gypsum crystals precipitate, growing on the boundaries of the rock fissure. In absence of well-open pre-existing fissures, the crystal growth itself may induce an enlargement of the cracks, favouring an additional water circulation in the rock body.

This crystallization of new gypsum crystals generates the volume increase of the rock, bringing to the displacement and swelling pressures registered on the infrastructures.
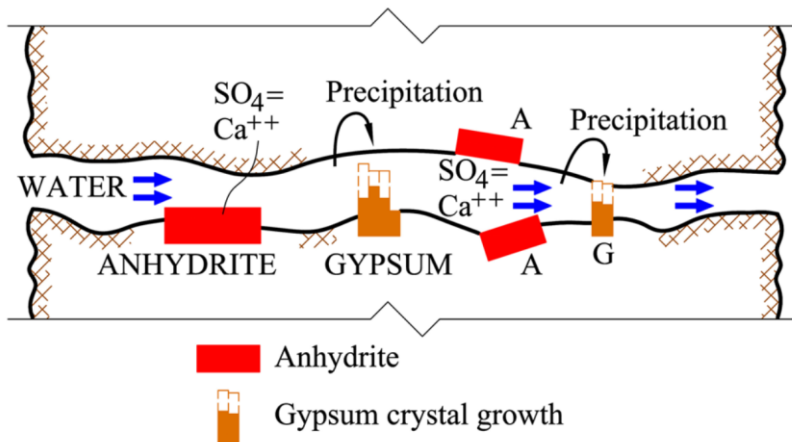
Figure 2.18 Schematic representation of the mechanism proposed to explain the severe expansion observed in sulphate-rich rocks (Ramon et al., 2017)

Recently, Ramon and Alonso 2018 suggested the importance of an additional element (i.e. the rock microstructure) in controlling this expansion mechanism. The contribution proposes a comparison between two different cases of expansion in infrastructures founded in anhydrite rocks.

In the first case (more completely described in Alonso and Ramon 2013 and Ramon and Alonso 2013), the registered entity and rate of heave are more significant. In this case, the rock is an anhydrite claystone, with a dominant clay matrix (Figure 2.19a). This microstructure implies that a large specific surface of anhydrite is exposed to the water dissolution. In addition, the easy fissuration of the clay matrix facilitates the access of water.

In the second case, the measured heave-rate is slower. In this case, the rock shows the aspect of a massive anhydrite, with high values of measured anhydrite content (up to 100%). This rock is very impervious, leaving small anhydrite surface area exposed to circulating water.

The authors concluded, therefore, that the massive nature of the anhydrite in the second case, reducing the surface exposed to water circulation, was one of the causes of the lower rate of heave.
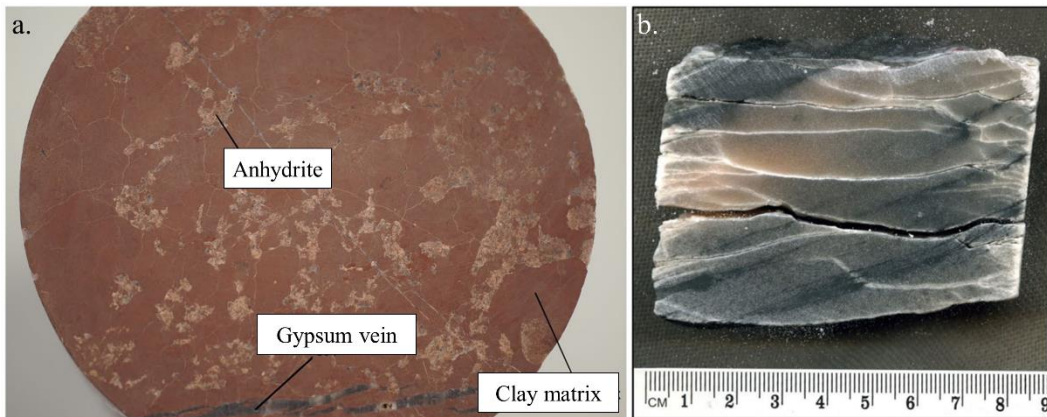
Figure 2. 19 Anhydrite rocks responsible of expansion phenomena. a. Red claystone with anhydrite aggregates and gypsum veins b. Massive anhydrite (Ramon and Alonso, 2018)

Chapter 3

Geological, geotechnical, hydrogeological framework and tested material

The Earth's geological history records several giant evaporitic events, during which big marine basins were interested by extreme climatic conditions, allowing for the precipitation of enormous masses of salt, gypsum and other evaporitic minerals (e.g. the infra-Cambrian of the Middle-East, the Permian of eastern Europe). Among the others, the Messinian Salinity Crisis of the Mediterranean is probably one of the most famous and controversial events, because of its recent age and the entity of precipitate rocks, despite the very short duration.

The present Chapter proposes a brief review of the most relevant literature studies about the Messinian Salinity Crisis, with a focus on the range of observed gypsum facies and a zoom on the geological setting of Monferrato area. The geotechnical and hydrogeological framework of gypsum quarries in Monferrato area is then provided. The Chapter closes with a description of the peculiar structure of branching selenite gypsum, specific object of the experimental study presented in this Thesis.

3.1 Messinian Salinity Crisis and gypsum deposits in the Mediterranean area

The Messinian Salinity Crisis is an important evaporitic event that involved the Mediterranean Basin during the Upper Miocene. It brought to the deposition of enormous volumes of evaporitic sediments (at least 10^6 km^3) in a relatively short period of time (640kyr) (Rouchy and Caruso, 2006). Evaporitic sediments were observed and exhaustively described in several onshore locations in Italy, Spain, Greece and Cyprus (Figure 3.1a). The knowledge of the sediments of the deeper parts of the basin, sited in correspondence of the present-day offshore Mediterranean Sea, is more unprecise and mainly due to indirect measures. A series of offshore seismic survey campaigns in the '50-'70s allowed for the identification of the persistent presence of three low-velocity seismic units (defined as Messinian Trilogy) all over the Mediterranean basin (Figure 3.1b). These units are classically interpreted as three evaporitic intervals, defined as Upper Evaporite Unit, Salt Unit and Lower Evaporite Unit, from the top to the bottom. Drilled samples, only available for the Upper Evaporites, mainly contain anhydrite, halite and marls.
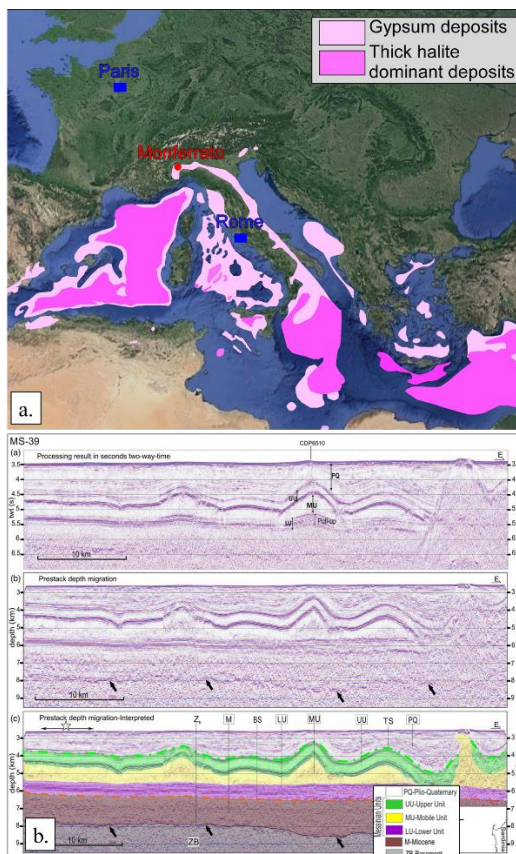
Figure 3.1 a. Geographical distribution of evaporitic sediments in the Mediterranean basin (Rouchy and Caruso, 2006, modified). b. Off-shore seismic data from the Sardo-Provencal basin interpreted as Messinian Trilogy (Dal Cin et al., 2016).

A largely accepted stratigraphic model to describe the deposits of the Messinian Salinity Crisis was proposed by CIESM (Commission Internationale pour l'Exploration Scientifique de la mer Méditerranée) in 2008 (CIESM, 2008). The model follows the idea that different sedimentary records can be deposed in the same time interval but in different paleo-oceanographic environments. Three kinds of Messinian sub-basins (with their correspondent paleo-oceanographic environments) are therefore described in the Mediterranean area: peripheral or marginal sub-basins, including both shallow-water (0–200 m) and relatively deep-water (300–1000 m), and deep or central sub-basins (>1000 m) in the offshore domain (Figure 3.2a).

The model, synthetized in Figure 3.2b, divides the Crisis in three stages.

The **first stage** (5.971-5.60Myr) includes the onset of the Crisis, with the first deposition of gypsum sediments in the marginal basins. These sediments are characterized by the rhythmical alternation of massive several-meters gypsum beds with thinner shale layers (Primary Lower Gypsum Unit). This rhythmicity is attributed to the influence of astronomical parameters (i.e. orbital variations), controlling the alternation of drier versus more humid conditions. Each gypsum-shale pair represents a 'stratigraphic cycle' and can be considered as time-equivalent, corresponding to a deposition time of 20kyr. This offers a reliable method of relative chronology. A clear stratigraphic marker in Primary Lower Gypsum Unit all over the Mediterranean basin is the synchro comparison of Branching Selenite facies in correspondence of the 6th stratigraphic cycle from the onset of the Crisis.

In deeper and intermediated basins, the stratigraphic record of this first stage is characterized by dolostones and/or anoxic shales.

Primary Lower Gypsum Unit and the equivalent deep-environment anoxic shales are interrupted by an important erosional surface defined as MES (Messinian Erosional Surface).

The **second stage** (5.60-5.55Myr) corresponds to the resedimentation of the Primary Lower Gypsum Unit as a chaotic body (Resedimented Lower Gypsum) in the deeper basins.

Eventually, the **third stage** (5.55-5.33Myr) includes the deposition of hypo-haline sediments in the so-called "Lago-Mare" facies.
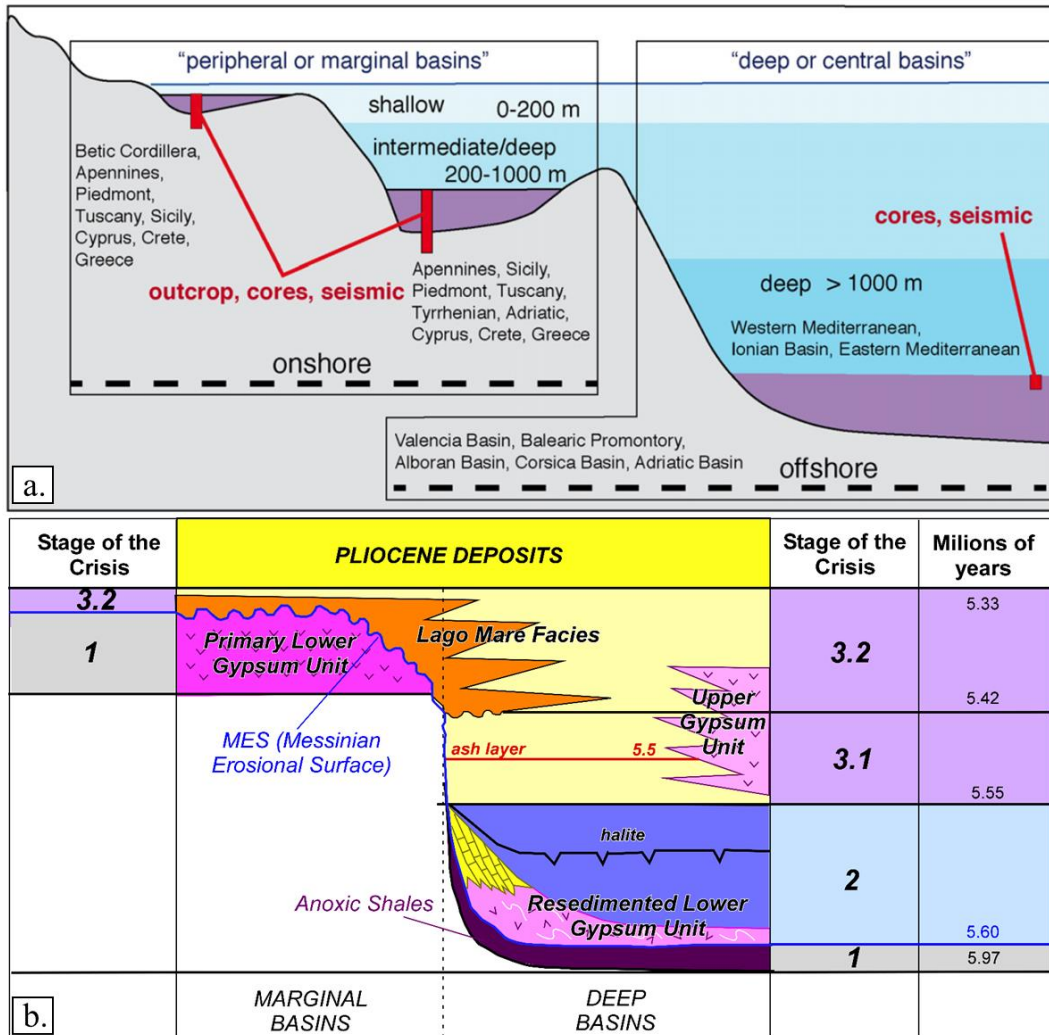
Figure 3.2 a. Schematic classification of the Messinian sub-basins in the Mediterranean (Roveri et al., 2014) b. Three-stages interpretation model of the Messinian Salinity Crisis (CIESM, 2008)

The complex geological framework controlling the Messinian Salinity Crisis implies a high variability in gypsum facies all over the Mediterranean basin. In particular, in the sedimentary record of the first stage of the Crisis, Lugli et al., 2010 recognized the presence of at least 6 different facies that are briefly described in the follow.

The *giant and massive selenite* (Figure 3.3a) consists of twinned gypsum crystals (arrow-head or swallow-tail) with average size of several centimeters. The peculiar organization of these crystals was successfully used to determine the strata polarity, because the vertical growth direction of the crystals is subperpendicular to the stratification.

The *banded selenite* (Figure 3.3b) or grass-like selenite consists of relatively small vertical crystals, less than 10 cm in thickness, separated by thin few-millimeter thick carbonate laminae.

The *branching selenite* (Figure 3.3c) has been variously described as "nodular and lenticular selenite" or "wavy, needle-like selenite layers" (in Sicily) or "hemi-radial to radial selenite" (in Spain). It consists of clear selenite gypsum crystals, with length varying from some millimeters up to few centimeters, having long axes inclined or oriented horizontally. These crystals are grouped into decimeter-large irregular nodules and lenses separated by thin fine-grained carbonate or gypsum laminae. The rock organization reveals clusters of these gypsum nodules, grouped in branches projecting outward from an initial nucleation zone into a fine-grained matrix. These branches are widely spaced and very broad so that the nucleation points are not always visible. The matrix surrounding the branches may consist mostly of gypsum or mudstone with fine-grained gypsum.

As previously mentioned, this facies only appears from the 6th cycle of the Crisis and consequently allows for an easy identification of all over the Mediterranean basin. For this reason, it is considered as a key sedimentological level and is reported in literature with the name of "Sturani Key Bed" (SKB) (Dela Pierre et al., 2011).

The *displacive selenite* consists of lenticular or twinned gypsum crystals with a typical horizontal growth direction ("flat-laying"). This facies is commonly present at the top of selenite beds, along the contact with the overlaying shale layers.

The *gypsarenite* and *gypsrudite* (Figure 3.3d) are clastic deposits recognized throughout the selenite successions of the Primary Lower Gypsum Unit. This facies is present in thin layers in the more marginal portions of the successions. In most of the cases, the selenite clasts are only slightly corroded, suggesting local erosion and re-deposition as a consequence of floods at the basin margins.
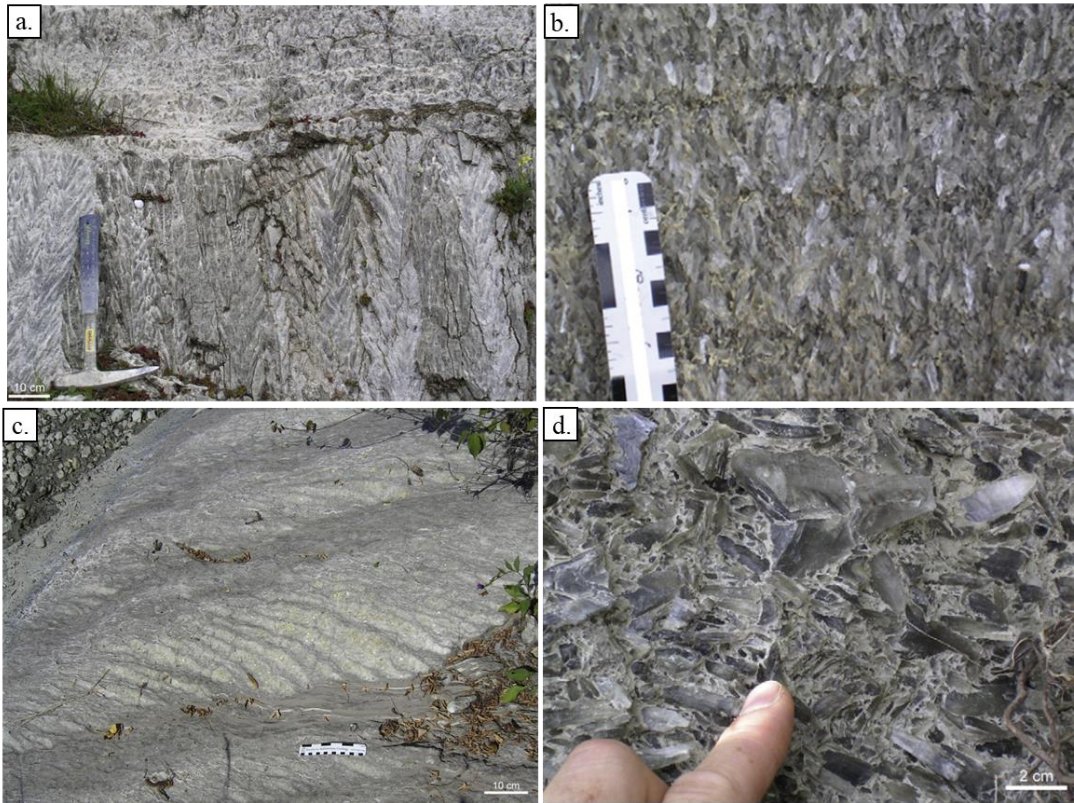
Figure 3.3 Examples of gypsum facies recognized in the Primary Lower Gypsum Unit all over the Mediterranean basin: a. Massive selenite b. Banded selenite c. Branching selenite d. Gypsrudite (Lugli et al. 2010)

3.2 Gypsum deposits in the Monferrato Domain

As cited in Figure 3.2a, during the Messinian Salinity Crisis, Piedmont was occupied by a 'shallow peripheral' sub-basin, defined as Tertiary Piedmont Basin (TPB). The complex sedimentary Tertiary Piedmont Basin occupied, indeed, large areas of Piedmont from the Upper Eocene to the end of Miocene. The geological literature classically divides this Basin in 5 tectono-stratigraphic domains (Torino Hill, Monferrato, Langhe, High-Monferrato and Borbera Grue - Clari et al., 1995; Piana and Polino, 1995). In this framework, thick gypsum deposits of the Messinian Salinity Crisis were observed and described (Figure 3.4).
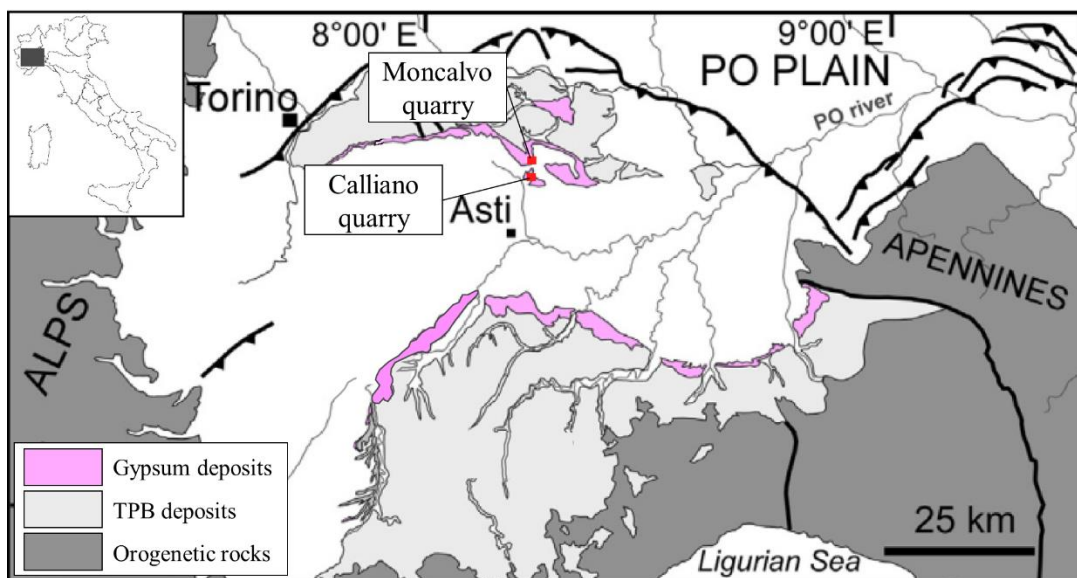
Figure 3.4 Areal distribution of Messinian gypsum deposits in Piedmont and geographical location of the test sites

In particular, the stratigraphic succession of Monferrato geological domain, sited in the northern part of the TPB and object of this study, is synthetized in the stratigraphic column in Figure 3.5. The described succession starts with the S.Agata Fossili Marls, a deep-sea marl unit. Based on bio-stratigraphic and cycle-stratigraphic data, the onset of Salinity Crisis was identified within this geological unit, and specifically two cycles under the base of gypsum sediments.

The following geological unit includes a thick evaporitic succession that counts 13 gypsum – marl cycles (for a total of 15 cycles, including the two marl cycles in the S.Agata Fossili Unit). This evaporitic succession corresponds to the Primary Lower Gypsum (PLG) Unit.

The first three gypsum cycles consist of thick massive selenite beds, with mean thickness of 10 m. Gypsum is mainly massive selenite, consisting of twinned crystals vertically oriented with sizes between 3 and 10 cm. The interlayer marl levels have a mean thickness of 2-3 m. The upper surfaces of marl levels are usually irregular, due to the presence of conic structures, interpreted as load structures due to the nucleation of gypsum crystals in a not-yet lithified marl sediment.

The fourth cycle (the 6th from the onset of the Crisis) corresponds to the appearance of branching selenite facies. It is a thick gypsum layer (about 10 m) of microcrystalline gypsum (mean size of the crystals of 1 mm). It is mainly composed by gypsum in branching selenite facies, but the presence of cumulate gypsum and clastic gypsum can sometimes be observed. This layer is recognized as the stratigraphic key level "Sturani Key Bed" (SKB) (Dela Pierre et al., 2011). Over the SKB, finer interbedded

layers of gypsum and marl are present, referred as "higher evaporitic cycles" (Dela Pierre et al., 2016).

This primary succession is locally re-deposited as RLG (Resedimented Lower Gypsum). In different areas of Monferrato, the presence of big volumes of resedimented evaporitic succession have been observed within the so-called 'Complesso Caotico della Valle Versa'.

The top of both PLG and RLG is sealed by river and lagoon sediments ('Lago-Mare Facies') and deep-sea Pliocenic sediments that close the stratigraphic column.
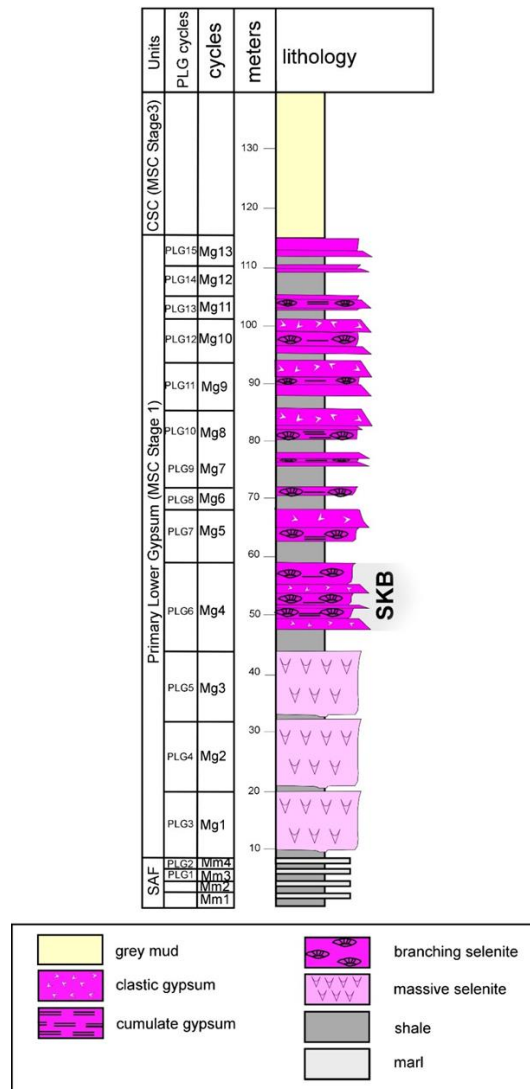
Figure 3.5 Stratigraphic succession of the Monferrato area (Dela Pierre et al., 2016)

3.3 Quarry sites and geotechnical setting

Gypsum bodies in the Monferrato area have been extensively exploited in the last decades for commercial purposes by both open pit and underground quarries.

Two main exploitation methods for underground quarries have been traditionally used: drill and blast methods and road header. The first method was mostly associated to Resedimented Gypsum units, with more inhomogeneous, non-linear and smaller orebodies that make difficult the exploitation with a road header. The resulting quarries have drifts that intersect each other orthogonally, leaving in place square pillars. On the other hand, gypsum from the Primary Lower Gypsum Unit creates a bedded and regular orebody that was usually exploited with continuous mining machinery.

Moncalvo and Calliano Quarries, where the material object of this study comes from, are two classical examples of quarries exploited in Primary Lower Gypsum Unit. The orebody, in coherence with the stratigraphic column in Figure 3.5, consists of four gypsum layers, each about ten meters thick, divided by marl layers a few meters thick.

Nowadays, the exploitation is active in the first two layers (in Calliano) or three layers (in Moncalcvo) from the top, while the macrocrystalline gypsum layer in the lower stratigraphic position is not in use. The quarries are therefore organized in two (in Calliano) or three (in Moncalvo) underground levels.

As said, the excavation work proceeds using continuous mining machinery, represented by a road header. The drifts do not intersect each other orthogonally as in a blasting exploitation, but take a "lozenge pattern", with a "rooms and rib pillars" exploitation planning (Figure 3.6a) (Bonetto et al., 2008).

The excavation faces are smooth, with a regular surfaces and average sizes of 6m x 6m, with rounded corners and a slight convexity. The advancement of the road header machine produces residual "waves" in the lateral walls of the drifts (Figure 3.6b). Their amplitude (about 0.4 m) corresponds to the material exploited in each machine step.
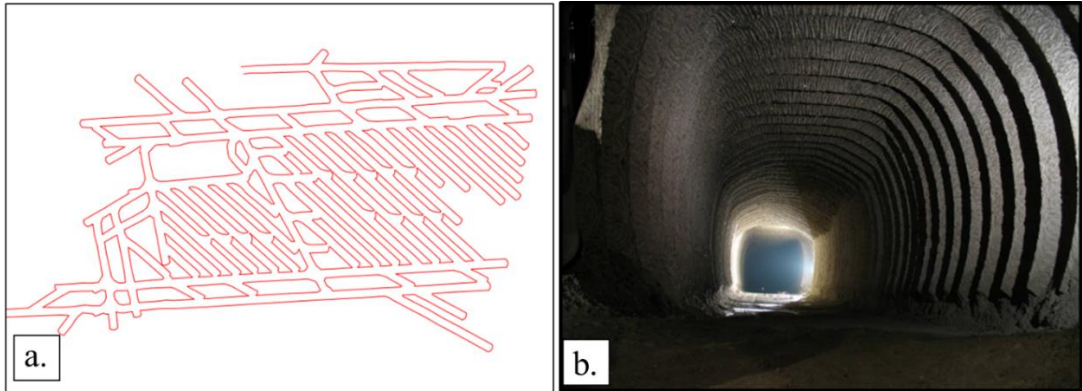
Figure 3.6 a. Lozenge drilling pattern for the excavation of gypsum with road header b. Regular profile of the drilling drifts, with the "waves" produced by the machine advancement on the lateral walls.

In the studied area, the stratification lay nearly horizontal and drifts run completely into the gypsum layers. The maximum stress on walls and pillars (i.e. the vertical stress created by the geostatic load of the overlaying deposits) is therefore perpendicular to the main sedimentary discontinuities. The branching selenite gypsum (specific object of this study) lays at maximum depths of 50 – 60 m and the overlying material mainly consists of marls and clays. Figure 3.7a reports the consequent stress distribution before the excavation of the drifts.

The opening of the drifts generates a disturbance in the orientation of the principal stresses and an increase of axial stresses insisting on the pillar-walls, as shown in Figure 3.7b-c. The Figure, showing the stress distribution estimated in the framework of quarry planning, suggests stress levels of 4-5 MPa in correspondence of the pillar-walls.
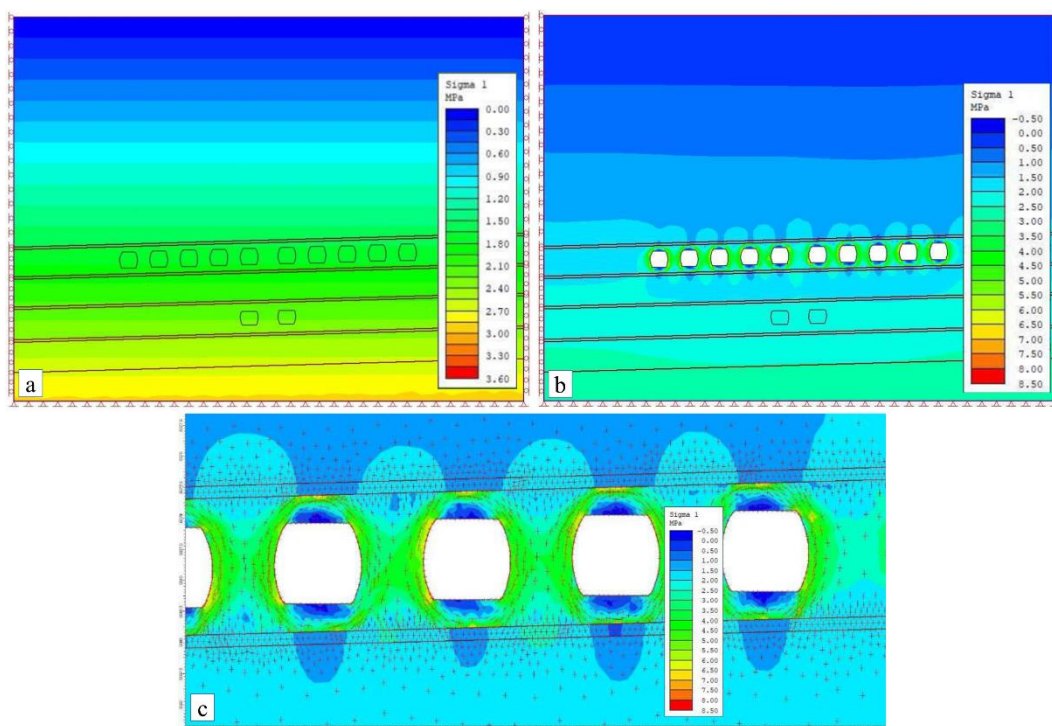
Figure 3.7 a. Distribution of the maximum principal stresses (σ_1) before the drifts excavation. b. Distribution of maximum principal stresses (σ_1) after the drifts excavation. c. Detail of distribution and directions of the principal stresses in correspondence of the drifts (Geostudio, 2018)

3.4 Hydro-geological framework

Several evidences of karst phenomena have been recognized in the gypsum beds of Monferrato area. The water circulation in gypsum rock can be schematized as proposed in Figure 3.8a. The karst system is controlled by the presence of pre-existing fracturing (with a mean sub-vertical orientation) and by the sub-horizontal stratigraphic discontinuities, separating gypsum and marls. The permeability contrast of these stratigraphic discontinuities favours the water circulation within the gypsum body and the consequent dissolution processes, leading to the development of the karst conduits and cavities.

Even if the stratigraphic characteristics are similar in the areas of the Moncalvo and Calliano quarries, significant differences in the structural assessment imply complete different hydrogeological scenarios. Vigna et al., 2017 proposed two main circulation models to describe the hydrogeological situations in the Monferrato area. The two models were described in the underground quarries of Moncalvo and Calliano, since the presence of an underground excavation offers a good observatory.

In the Moncalvo quarry (Figure 3.8b) the gypsum sequence is relatively compact. Both superficial waters and rising fluids, following sets of fractures in the upper and

lower rocks (aquitards), recharge the karst circuits, creating an underground water circulation within isolated main conduits and caves. In this quarry, the karst problem assumed a particular relevance since 15th of February 2005, when the incidental intersection of a karst circuit during mining works caused an inrush of 60000 m^3 of water mixed with mud. The inrush brought to the complete flooding of the lower quarry tunnels (Bonetto and Fornaro, 2005; Bonetto et al., 2008; Vigna et al., 2010). A big "camera" (a few hundred m^3) was found in contact with the drift where the inrush had happened. From this "camera", 850 m of cave passages, characterized by typical phreatic morphologies, were observed.

A completely different hydrogeological situation can be found in Calliano quarry (Figure 3.8d), where gypsum beds are characterized by a much more intense fracturing, with numerous small karst conduits and water-bearing fractures. Calliano is a classic example of "dispersive karst circulation system", an extensively fractured and karstified aquifer with very good interconnection among fractures and karst conduits. The features of this kind of acquifer bring to create a water table level that is similar to a classic piezometric surface in porous aquifers.
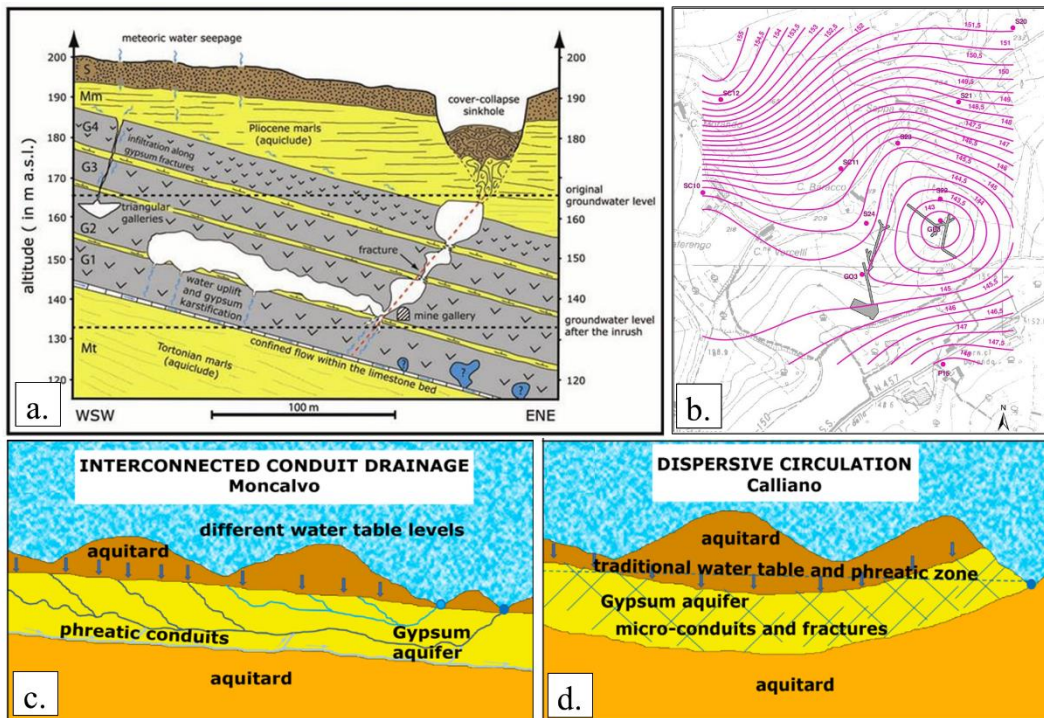
Figure 3.8 Scheme of the karst circuit characteristics in the gypsum body (Vigna et al., 2010; Bonetto et al., 2008) (b) Depression of potentiometric surface due to the pumping operations in Calliano quarry (Vigna et al., 2017) (c) and (d) Conceptual models for karst circulation in gypsum (modified by Vigna et al., 2017): (c) Interconnected conduit drainage karst system, recognized in Moncalvo quarry. (d) Dispersive karst circulation system, recognized in Calliano quarry

In both the quarry environments, the presence of a karst aquifer requires the intervention of de-watering operations to permit the accessibility to the underground drifts. Long-term pumping operations are therefore included in the exploitation plans of both the quarries. The effect of this pumping in correspondence of Calliano quarry, monitored by Vigna et al. 2017, returned a depression of potentiometric surface that is perfectly similar to what could be expected in a porous aquifer (Figure 3.8b). This evidence confirms the good interconnection of this kind of karst aquifer, with water completely permeating the gypsum rock.

3.5 Tested material: Branching Selenite Gypsum Facies

The relevant thickness and lateral continuity of Sturani Key Bed all over the Mediterranean basin implies the economic interest in the quarry exploitation of branching selenite gypsum facies. As said, in the Monferrato area, this facies has been object of open pit and underground exploitation for several decades and active exploitation is still ongoing in underground environment.

However, despite the high lateral continuity of the layer, this gypsum facies is strongly heterogeneous in terms of textural and compositional features. At the macroscale, the rock appears to be organized in lenticular bodies of selenite gypsum ('branches') surrounded by layers of finer material with various thicknesses (Figure 3.9a). The presence and spatial distribution of these layers contributes to create the anisotropy of the rock. This anisotropy is evident at the rock-mass scale (macroscale), as well as at the sample scale (mesoscale), with specific key features that are periodically reproduced at the different observation scales. At the mesoscale, indeed, the rock anisotropy is defined by decimeter-large irregular nodules and lenses of selenite crystals with major axes slightly inclined or horizontally oriented (Figure 3.9b-3.9c). Thin anastomosed fine-grained laminae separate the nodules. The laminae have thickness ranging among several millimetres (usually with prevalent carbonate or gypsum fine crystals) and very tiny films (typically constituted by prevalent clay and terrigenous minerals).

Figure 3.9 a. Excavation face in a gypsum underground quarry in Monferrato (NW Italy). It is evident the typical structure of the branching selenite gypsum, with branches of coarse material surrounded by anastomosed fine layers. b. Core sample of branching selenite gypsum, with nodules of coarser gypsum crystals surrounded by thin fine-grained laminae. c. Hand sample, with a more detailed scale, with nodules of coarse gypsum crystals surrounded by thin fine-grained laminae

The branching selenite samples investigated in this study were obtained from the quarries sites of Calliano and Moncalco and from a survey campaign of 17 drillings in the evaporitic succession of the Monferrato area. Core drilling was performed in vertical direction, i.e. perpendicularly to the sub-horizontal stratification and to the main sedimentary discontinuities. Drilling cores were described and sampled to obtain core pieces with suitable geometrical features for the mechanical tests.

All the samples show features that allow for the attribution to the branching selenite facies. However, the meso-textural appearance of samples is strongly heterogeneous. Figure 3.10 shows the range of variability, from samples with evident macroporosities and branching structure clearly marked by colour and differential erosion (in the left of the Figure) to compact and more uniform samples, with branching structure only identified by a change in grain size or slight differences in colour (on the right).

Figure 3.10 Samples of branching selenite gypsum, underlining the mesoscopic heterogeneity of the material

Based on meso-textural features, two material groups were defined (denominated, for sake of simplicity, A-type and B-type, Figure 3.11). A-type samples are greyish, with a well-compacted appearance. Their branching selenite structure is macroscopically only identified by the differences in grain size. B-type samples are more yellow-brownish and the layering of the branching selenite structure is thin and well evident for the brownish colour and the differential erosion.

Figure 3.11 Macroscopic appearance of A-type (a) and B-type (b) gypsum samples

This two material groups do not include the complete range of variability of the rock: samples with intermediate characteristics cannot be satisfactorily described by any of these categories. "A-type" and "B-type" features describe, indeed, the "extreme" characteristics of the rock (end-members).

In the present Thesis, this distinction in A-type and B-type gypsum is used as a trace in the physical-chemical and mechanical characterization of the material. Chapter 4, in particular, proposes a textural, microstructural and compositional description of the features of A-type and B-type gypsum.

Chapter 4

Physical-Chemical Characterization of Branching Selenite Gypsum

The strong heterogeneity of branching selenite gypsum in terms of textural and compositional features was schematized in Chapter 3 in two material groups based on mesoscale appearance. The better-quality A-type samples are greyish, more homogeneous and with a well-compacted appearance. Their branching selenite structure is macroscopically only identified by the differences in grain size or slight changes in colour. B-type samples, on the other hand, are more yellow-brownish and the layering of the branching selenite structure is thin and well evident for the brownish colour and the differential erosion. These two groups may be considered as 'end-members', since represent the "extreme" features of the material heterogeneity.

The present Chapter aims to deepen the definition of these two material end-members, proposing a detailed characterization of the physical-chemical properties of the facies, focusing on the texture, the porosity and the mineralogical composition. After a description of the methodologies applied for the characterization, a presentation and a discussion of the results are provided.

4.1 Methodologies

4.1.1 Grain size distribution

The size distribution of crystals and grains in the rock (i.e. grain size distribution) was estimated for a number of representative samples by means of an image analysis method at the microscale. This technique has been successfully used in the last decades since facilitates rapid and semi-automated access to grain dimensions (e.g. Heilbronner and Keulen, 2006; Jutzeler et al., 2012; Buscombe, 2013).

Photographical images of the thin sections were acquired with an optical microscope (Figure 4.1a). At least three pictures of different portions for each section were processed and analysed, to take into account the material variability and therefore increase the representativeness and reliability of results.

The image processing consists of three steps:

- The application of a colour threshold for a preliminary and automatic grain delineation (Figure 4.1b). Aside from the grain boundaries, the colour threshold excludes the rock porosity and the finest material (too fine to be characterized with optical microscope)
- A process of manual retracing of grains edges (Figure 4.1c) (for improving manual delineation, the colour image was converted into grayscale intensity image)
- The automatic calculation of particle areas using the open source ImageJ code (Schneider et al., 2012).

The frequency distribution of the particle grain sizes calculated from the areas values was attained using the ASTM standard size classes. The total number of particles in each class was recalculated to the correspondent weight. Computing the percentage of passing material for each size class, grain size distribution curves were obtained (Figure 4.1d) and D10, D50 and UC (Uniformity Coefficient) were defined for each sample.
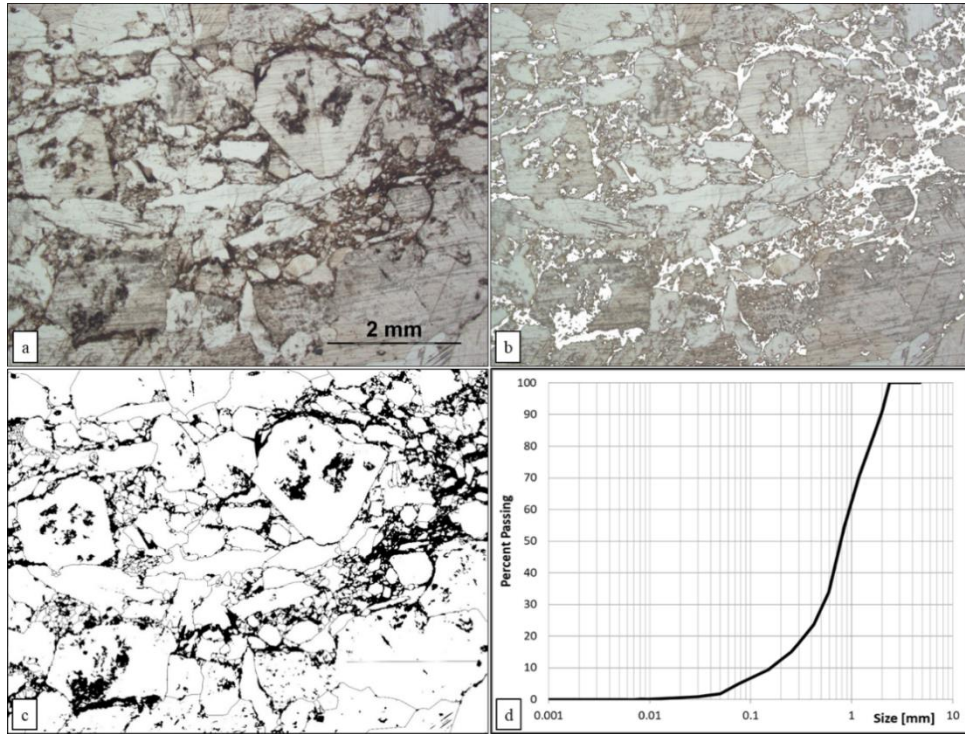
Figure 4.1 Processing flow performed on thin section images of Sample S58C9 for the determination of the grain size distribution. a. Thin section micrograph acquired with the optical microscope. b. Application of a threshold filter to perform a first automatic delineation of the grains. c. Grayscale image after manual delineation of grains. d. Resulting grain size distribution curve

4.1.2 Porosity and Microstructure

A rigorous quantification of the material porosity was performed with the Helium Pycnometer, a high precision instrument for the measurement of the solid volume of specimens. The porosity of cylindrical specimens was obtained as the ratio between the solid volume and the geometrical volume retrieved by height and diameter (measured with calibre).

Besides the measure of open porosity obtained with Helium Pycnometer, the material characterization included two additional methodologies (SEM and MIP) aimed to the description of position, size and nature of the pores.

A method of image analysis with SEM images in backscattered electrons (BSE) was used for a first description of pores and cracks, creating a map of the location of the porosity. With the BSE acquisition mode, the images identify an intensity that depends on the average atomic number Z of the target. Since atomic number of pores is zero, the images show high grey-scale contrast between "pores" and "rock". Although some three-dimensionality is sacrificed, with the simple application of a threshold, it is possible to distinguish the "pore" pixels from the "rock" pixels.

To obtain representative information, image reproduction of the entire sections were obtained by juxtaposition of more detailed pictures (Figure 4.2a). Constant magnification and resolution were used for the acquisition of the images. The elaboration was performed with the software ImageJ, with the following processing flow:

- Application of a Filter to reduce the noise (Median Filter with Radius of 2.0 pixel) (Figure 4.2b)
- Application of a threshold, automatically determined through the Otsu algorithm (Figure 4.2c)
- Delineation of the interested area and count of total pixels
- Count of black pixels (pores) in the interested area (Figure 4.2d).

The ratio among total pixels and black pixels returns the value of total porosity of the thin section.
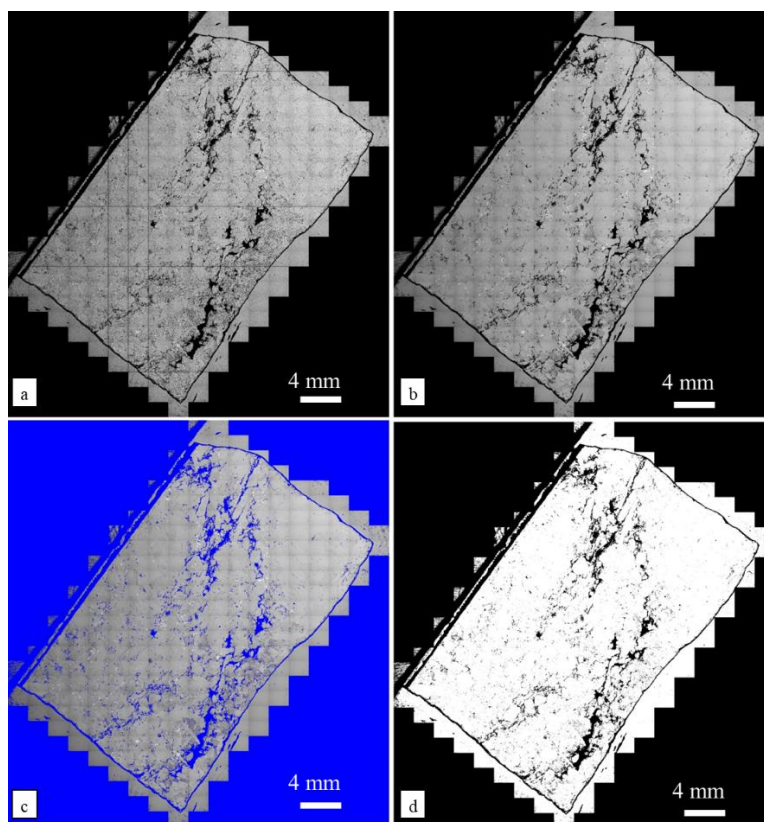
Figure 4.2 Processing flow of SEM image of Sample S58C9 for the determination of the porosity. a. Image of the entire thin section obtained through the juxtaposition of photographical images acquired with back-scattered SEM. b. Application of the median filter to the reduction of the noise c. Application of a threshold, automatically determined through the Otsu algorithm. d. Final black and white image, where black pixels are pores and white pixels are the surrounding rock.

A more detailed and quantitative study of the size and nature of the pores was performed with the combination of MIP (Mercury Intrusion Porosimetry) and SEM in Secondary Electron (SE) acquisition mode.

MIP is an extremely useful characterization technique for porous materials. Pores between 500 μm and 3.5 nm can be fully investigated (Giesche, 2006; Romero and Simms, 2008). 1 cm^3 specimens (Figure 4.3a), previously over-dried with a freeze-drying process, are introduced in the void camera of the instrument. Mercury injections, following increasing pressure steps, bring to the progressive saturation of pores with decreasing entrance diameter (i.e. throat size). A well-known mathematical correlation (Washburn formula) is largely accepted for the calculation of correspondent throat sizes for each pressure step. High precision volume measurements of intruded mercury are performed throughout the test in order to quantify the volume of porosity correspondent to each throat size. Results are presented in terms of derivative of porosity index '*e*' against the throat pore size, in logarithmic scale.

SEM-SE offers a morphological description of rock pores. Slices of rock samples with mean sizes of 20x30 mm and mean thickness of 5 mm were cut with a circular saw. Their conductivity was enhanced with the application of a Carbon metallization to the sample surface (Figure 4.3b). Thanks to the high depth of field of SEM instrument, highly detailed morphological images of the shape and the geometrical features of rock pores were obtained. EDS (Energy Dispersive X-Ray Spectroscopy) analyses were performed pointwise on the samples to associate chemical information to the morphological images.
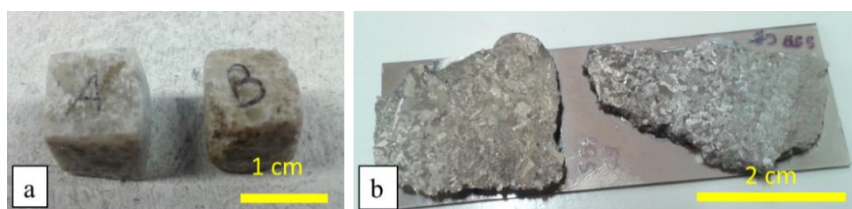
Figure 4.3 a. Specimens for the MIP test. b. Rock slices with carbon metalization prepared for the SEM observations

4.1.3 Mineralogical Composition

The percentage of gypsum mass out of the total mass of the rock was measured through the thermogravimetric method (Porta, 1998). The method bases on the thermal-induced dehydration of gypsum rock. Considering a total conversion of gypsum in anhydrite around a temperature of 200°C and knowing that the total amount of crystal water is 20.91% of the gypsum weight, the percentage of gypsum content can be calculated through the measure of weight variations during the heating.

Once quantified the mean percentage of gypsum mineral in the rock, the nature of non-gypsum minerals was assessed with two different methodologies: SEM-EDS (Energy Dispersive X-Ray Spettroscopy) and XRPD (X-Ray Powder Diffraction). For the XRPD analyses, 0.5 g of material were reduced in size with a mortar and diluted in water, creating a solution with a concertation lower than gypsum solubility (2 g/l). After 24 hours, the solution was filtered and the solid residual portion was deposited for the RX analysis, in order to study the insoluble minerals without the interference of gypsum spectrum.

These powder samples were also analysed with a specific procedure for the characterization of clay minerals. XRPD analyses were repeated before and after the application of treatments with organic fluids (i.e. glycol) and by heating (350°C and 500°C). The behaviour of the clay groups (Illite, Vermiculite and Smectite) in response to these treatments is different, allowing for a determination of the right group.

Smectite clay minerals may be recognized through the peculiar swelling process (i.e. the reversible absorption of molecules in the interlayer spaces of the clay structure). The swelling may occur in presence of water but also with several polar organic liquids, such as glycol. In pure smectitic clays, the glycol saturation brings to an expansion of the d_{001} spacing (i.e. the perpendicular direction to the basal plane), up to 17Å. With the heating treatments, the interlayer molecules are expelled: at a temperature of 350°C, smectite clays loose most of their interlayer molecules, with a resulting d_{001} spacing of about 10Å.

Conversely, pure illitic and vermiculitic clays are inert to the treatments, with unchanging values of d_{001} spacing of 10Å and 14Å respectively.

The clay analysis was accomplished with the Python open-source code PYXRD, implementing a matrix algorithm specifically developed for the analysis of X-ray diffraction of disordered lamellar structures. The software performs a probability analysis on the XRPD data, returning modelled curves to compare with the measured data and the correspondent percentages of each clay family.

4.2 Results

4.2.1   Grain Size Distribution

Figure 4.4 shows six representative micrographs of A-type and B-type gypsum samples, observed with an optical microscope in reflected light.

A-type samples show the dominant presence of a matrix of small crystals (mean size of 0.1 mm). These small crystals concentrate along layers, elongated in the direction of the anisotropy, wrapping oval lenses with 1-2 mm crystals. Some of the gypsum crystals into these lenses show an elongated shape, with maximum lengths of 9-10 mm, underlying the anisotropy (Figure 4.4c). In this configuration, crystals are perfectly in contact, without empty spaces. This is mainly due to the poor sorting of the grain size and the consequent presence of fine crystals (<0.5 mm) in the voids among coarser grains.

Conversely, in B-type samples, the grain size seems to be more homogeneous, resulting in a clast-supported texture. The fine-grained gypsum crystals seem to be replaced by clays or other phyllosilicate minerals, sometimes organized in thin films. Fractures surfaces may occur along these films (Figure 4.4e). In addition, the images show a less compact structure, with void spaces among the crystals. The local presence of lenses of crystals with average size almost twice than the grain size in the other sections (e.g. Figure 4.4f) completes the range of material variability.
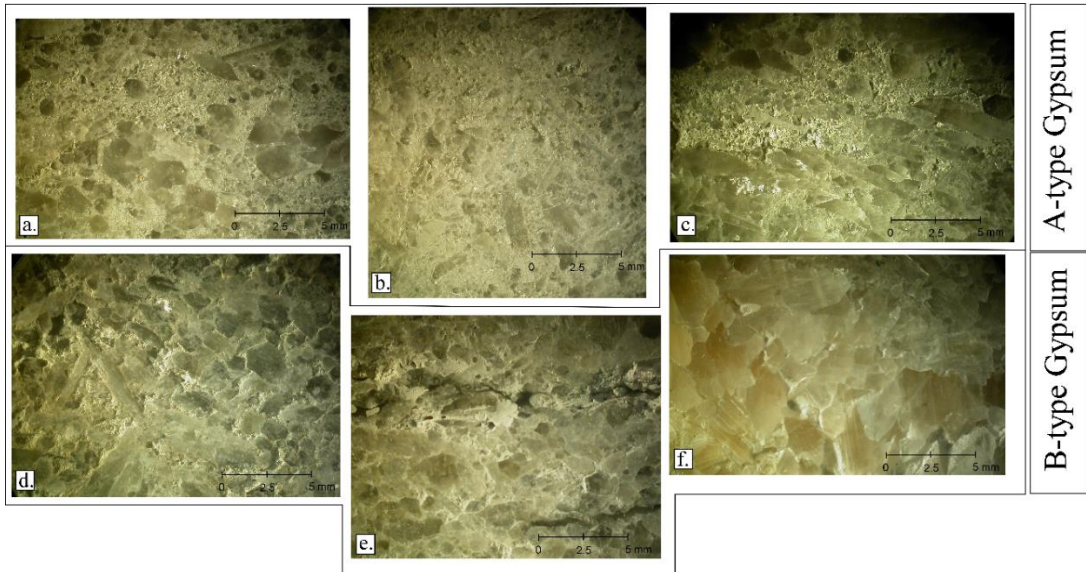
Figure 4.4 A-type and B-type micrographs (optical microscope in reflected light)

The grain size distribution curves (Figure 4.5) confirm a clear distinction among A-type and B-type gypsum samples: A-type curves describe a finer material, with high

percentages of crystals in the finest size classes, while B-type curves are coarser, with absence of material finer than 0.4-0.5 mm.

The dip-angle of the curves is also different, confirming a higher size homogeneity in B-type samples, while A-type gypsum has a general lower Uniformity Coefficient (UC).

Results of the grain size coefficients (D10, D50 and UC) are summarized in Table 4.1 that reports the maximum and minimum values for the entire dataset and the threshold values that divide the A-type and the B-type distribution curves.

Table 4.1 Maximum values, minimum values and thresholds between A-type and B-type materials for D10, D50 and Uniformity Coefficient

	D10	**D50**	**UC**
Maximum	0.85	1.5	1.97
Minimum	0.06	0.3	8.33
Threshold	0.3	1	4
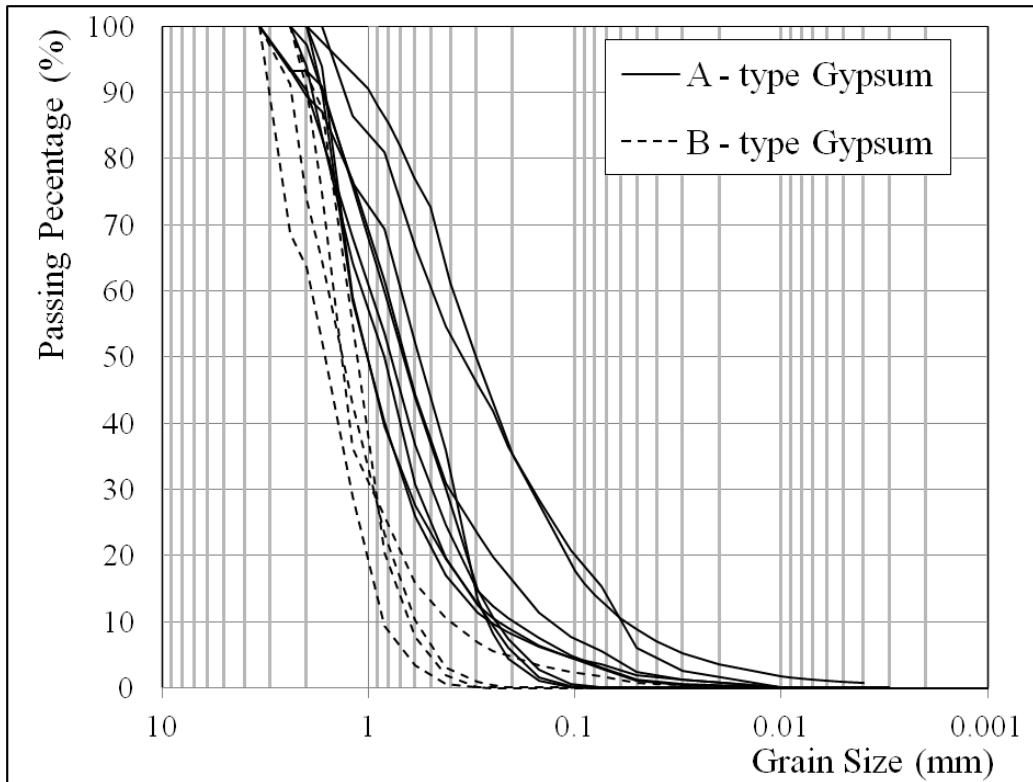
Figure 4.5 Grain size distribution curves of A-type and B-type gypsum samples

4.2.2   Porosity and Microstructure

The porosity of a group of 77 cylindrical samples of A-type gypsum[1] (diameter: 20 mm – length: 40 mm) was measured with Helium Pycnometer technique, assessing a range of porosity between 3% and 10%, with a mean value between 5% and 6%. The range of variability in the measured parameter is quite high, despite the low spatial distribution of the considered samples (coming all from the same vertical drilling core).

The measurements of Helium Pycnometer porosity on B-type gypsum samples registered higher values, with maximum reaching 15%.

SEM-BSE porosity maps of three representative samples are reported in Figure 4.6. The maps refer to A-type and B-type end-member samples and to a sample with intermediate characteristics (Figure 4.6a, 4.6b and 4.6c respectively). In general, a preferential distribution of pores along the fine-grained layers (underlined with black lines) was observed. However, clear differences between the samples can be highlighted.

A-type samples present a diffuse and fine porosity. Fine-grained layers, mainly consisting of equigranular grains (i.e. gypsum, calcite, feldspar or quartz), occupy large areas of the rock and contain the majority of the pores. The absence of a clear colour differentiation among coarse-grained nodules and fine-grained layers suggests a mean compositional homogeneity between these two elements of the branching structure.

On the other hand, B-type samples show a net distinction between fine layers and coarser nodules. The fine layers consist of very thin films of clays and other phyllosilicate materials, with a clear planar shape. These layers, for the low thickness and the compact organization, can only host fine pores, in low quantity. Conversely, the coarse-grained lenses host coarser and more abundant pores.

The dataset includes also samples with hybrid characteristics, as the example in Figure 4.6c that shows the presence of both fine-grained layers of equigranular grains and thin films with phyllosilicate minerals.

---

[1] These samples will be the object of the experimental results described in Chapter 7
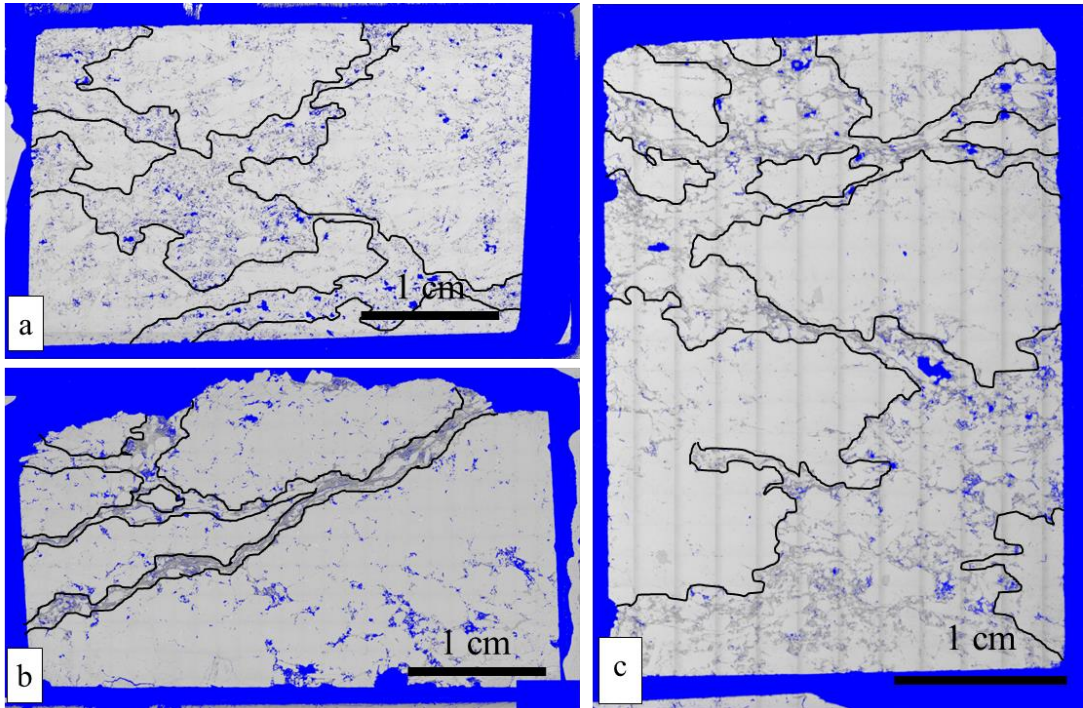
Figure 4.6 SEM-BSE micrographs of the thin section of end-member samples (A-type in Figure a and B-type in Figure b) and of a sample with intermediate characteristics (c). In blue, the pixels identified as pores.

Two representative specimens of A-type and B-type gypsum were investigated with the MIP and SEM-SE techniques in order to describe size and shape of the respective porosities.

Figure 4.7a shows the MIP results for the two samples. Results can be described as follows:

- <0.1 µm – No pores were detected neither for sample A and for sample B
- $0.1 - 1$ µm – Both sample A and sample B show an increasing concentration of porosity towards coarser pore sizes, even if in sample B the growth is not uniform, but characterized by a multi-modal distribution.
- $1 - 6$ µm – High pore concentration for both sample A and sample B. Sample A has its absolute maximum between 1 and 2 µm. Again, sample B pore distribution is multi-modal.
- $6 - 20$ µm – Maximum concentration of porosity for sample B, while sample A has almost zero porosity in this size class.
- $11 - 100$ µm – Neither sample A and sample B have significant pore concentrations in this size range

- \> 100 µm – Both sample A and sample B show an increase of measured porosity in this interval, suggesting the presence of big pores, maybe even bigger then higher resolution of the method (500 µm).

The principal differences are, therefore, the porosity peak between 6 and 11 µm in sample B, which does not have an analogous in sample A, and the multi-modal pore size distribution of sample B.
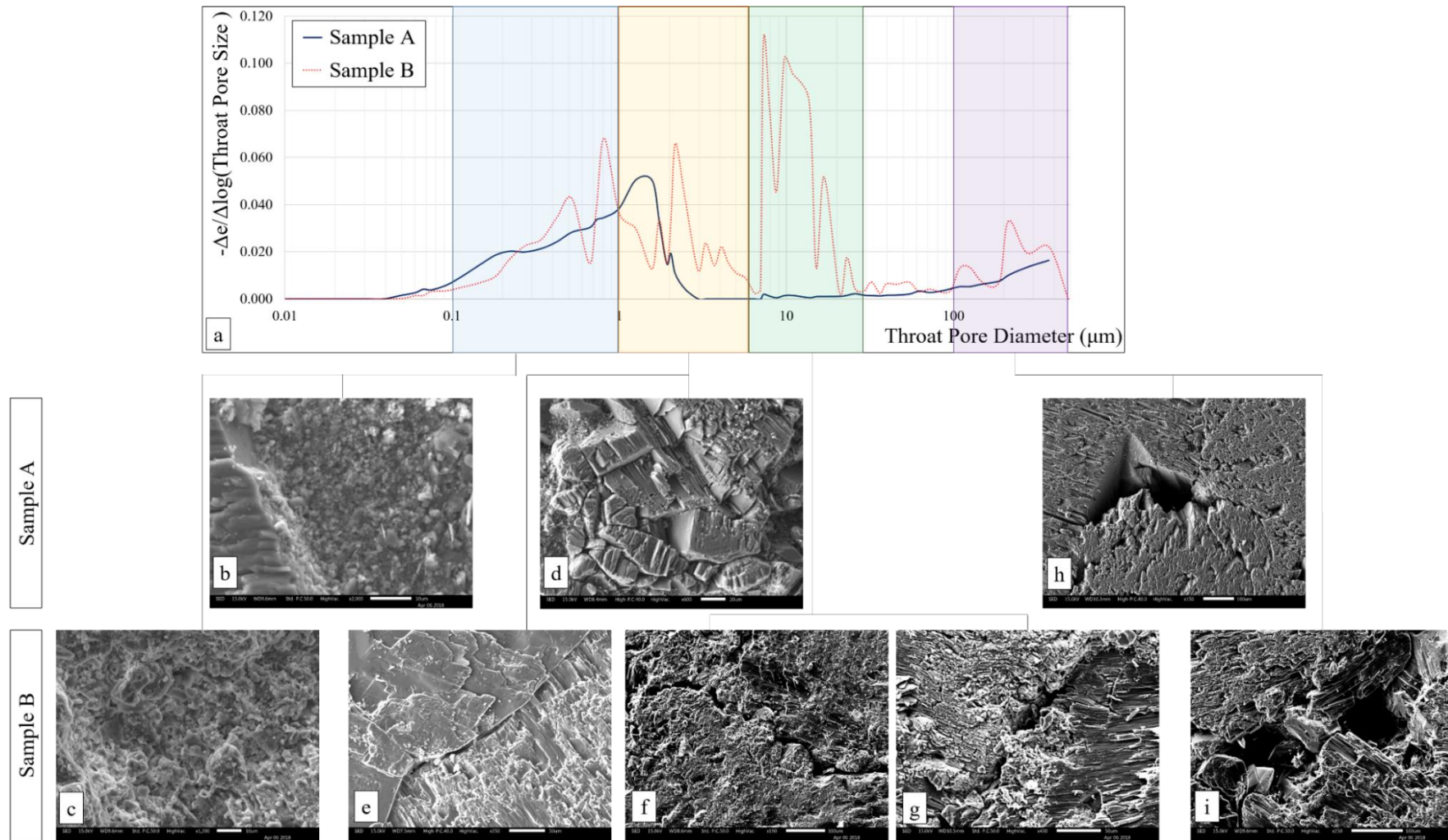
Figure 4.7 a. Results of the MIP tests on representative samples of A-type and B-type gypsum. b. and c. SEM micrographs of the pores in the interval between 0.1 and 1 μm for A-type and B-type samples respectively. d. and e. Contact between the grains in sample A and sample B respectively. f. and g. Cracks and opening along the grain contacts in B-type sample. h. and i. Examples of pores bigger than 100 μm in sample A and sample B respectively.

SEM morphological micrographs in Figures 4.7b-4.7c suggest an association between the first pore-size class (smaller than 1 μm) and the finest grain-size class of the rock (smaller than 3-4 μm).

This grain-size class mainly consists of non-gypsum minerals. EDS spectra (e.g. Figure 4.8b) indicate the predominant presence of Ca and Mg, with the additional presence of K, Si and Al. EDS analysis on these very fine materials cannot be reliably associated to a single particle, but returns a general composition. These materials can be, therefore, considered as a dolomitic plus terrigenous cement of the rock.

An image threshold filter was applied on the micrographs to quantify the size of the pores (Figure 4.8a-4.8c). The resulting frequency distribution (Figure 4.8d) shows that the mean pore size is compatible with the first pore-size class in the MIP results (0.1 – 1 μm).

The features of this dolomitic plus terrigenous matrix are similar for the A-type and the B-type samples. The grain and pore sizes, in general, are similar, even if slightly coarser in sample B.
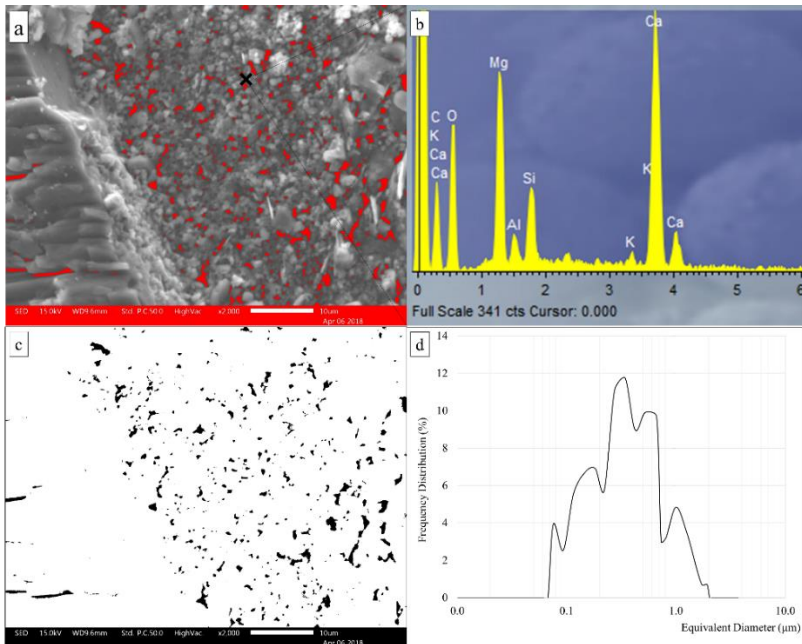
Figure 4.8 a. Micrograph representing the finest matrix of the rock. b. EDS spectrum, showing the presence of dolomite and clay minerals. c. Pore distribution obtained with an image processing of Figure 4.8a. d. Frequency distribution of pores in Figure 4.8c.

The second pore-size range recognized in Figure 4.7a (1-6 μm) can be associated to the void spaces at the contact between gypsum crystals. This kind of porosity can be found in both the gypsum typologies.

The following pore-size class (6-20 μm) can be explained considering that gypsum crystals in B-type samples are not always well adherent and open spaces and cracks are visible along the grain boundaries. The opening of these contacts was measured on the micrographs (e.g. Figure 4.9), returning a range between 10 and 20 μm.
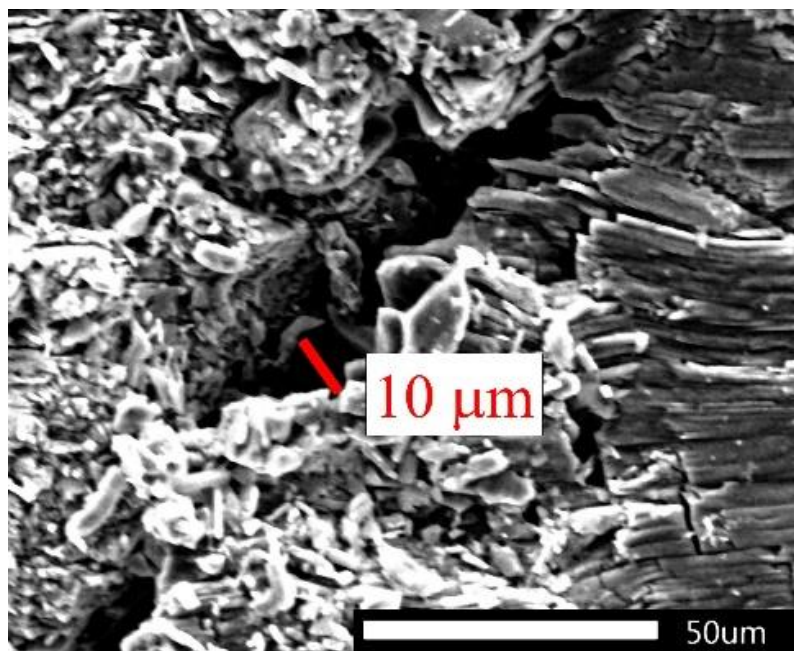
Figure 4.9 Opening of cracks along the grain boundaries in B-type sample.

Eventually, big pores (larger than 100 μm) were recognized in SEM images of both the samples, even if their presence is more frequent and evident in B-type gypsum. The confirmation of their being pores of the material and not an effect of the sample preparation is given by the presence in them of groups of acicular crystals of hydrothermal minerals (Figure 4.10). The EDS analysis showed, for these crystals, a concentration in Sulphur and Strontium. Hence, their precipitation is probably connected with the circulation of sulphur-oversaturated fluids in the pores of the material.
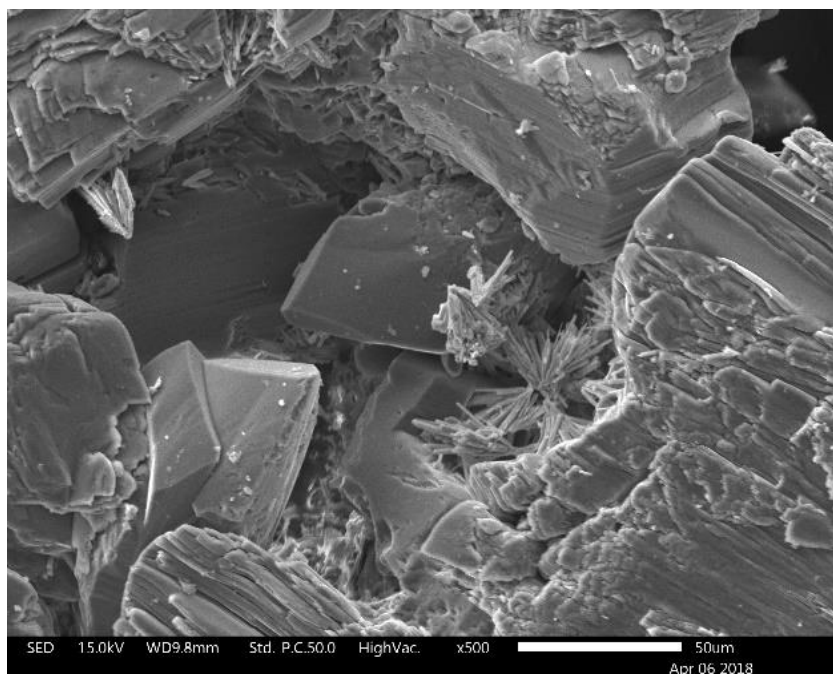
Figure 4.10 Morphology of big holes in B-type sample, with presence of acicular crystals of Celestine (Strontium Sulphate).

Table 4.2 proposes a summary of porosities obtained from the different techniques for A-type and B-type samples. Despite some differences in the results (reflecting the variability of the material), the three methodologies underline the clear difference between A-type and B-type gypsum.

Table 4.2 Ranges of porosity measured with the different methodologies for A-type and B-type gypsum.

Methodology	A-type	B-type
He Pycnometer	0.03 – 0.09	0.07 – 0.15
SEM	0.02 – 0.07	0.03 – 0.10
MIP	0.04	0.08

4.2.3   Mineralogical Composition

Figure 4.11 shows the results of gypsum content measurements on 20 analyzed samples. The graph shows gypsum percentages ranging between 77% and 97%. Within this range, the B-type samples tend to concentrate in the lower part of the distribution (with gypsum contents lower than 90%). Some outliers can be however observed, as the last sample (number 20), with a concentrations near to 100%.
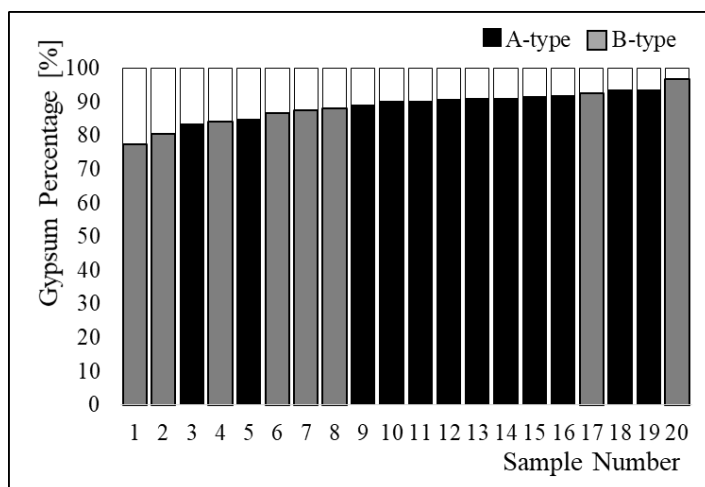
Figure 4.11 Results of gypsum content measurements, sorted in ascending order.

Figure 4.12 shows the results of XRPD analyses on the non-gypsum portions of the material (on both A-type and B-type samples). As can be seen, the predominant presence of calcite is a common feature in all the samples. Aside for calcite, the analysed powder samples contain quartz, feldspar minerals, dolomite, some additional sulphate minerals (Magnesium and Sodium-Aluminium sulphates) and clay minerals.
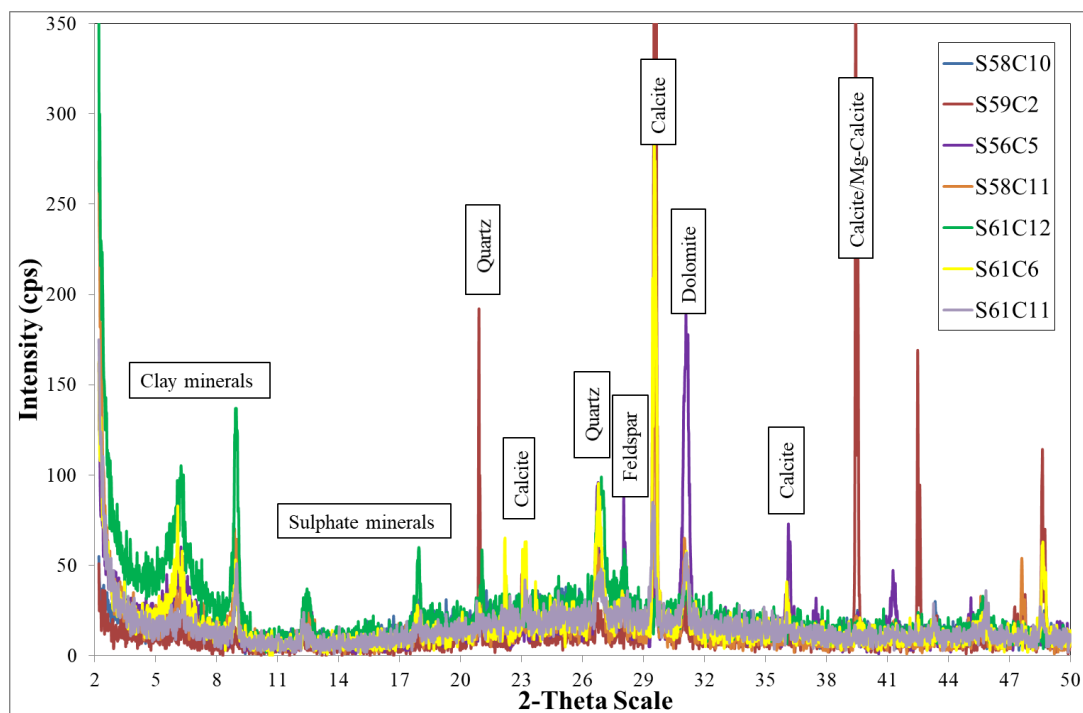
Figure 4.12 XRPD analyses on the non-gypsum fraction

Compositional maps from SEM-EDS offer a localization of these mineralogical phases in the structure of the gypsum rock. Figure 4.13 proposes two representative situations of the general features of the material.

Figure 4.13a-b reproduces a large portions of rock. The lenses of gypsum crystals (in green-blue, in the upper and lower parts of the image) are locally bordered by a rim of calcite (in green). They are separated by layers of finer-grained material. The yellow-brown colour of these layers derives from the coexistence of Si (yellow), K (fuchsia), Al (orange) and Mg (violet), suggesting a main terrigenous composition (i.e. clay minerals, feldspars and quartz). These layers represent weakness horizons in the structure of the rock, as it is confirmed by the presence of a sub-horizontal crack.

Figure 4.13c-d, proposing a zoom on the fine-grained layers, suggests that the matrix is not only composed by terrigenous minerals, but that it also includes the presence of a dolomitic cement. In the map, portions with prevalence of elements connected with terrigenous minerals (Si, Al, Mg K, represented in light blue/green colours) intersect with portions with prevalence of Ca and Mg. The presence of dolomite mineral is also confirmed by several punctual EDS analyses, that returned the record of Ca and Mg in similar proportions.
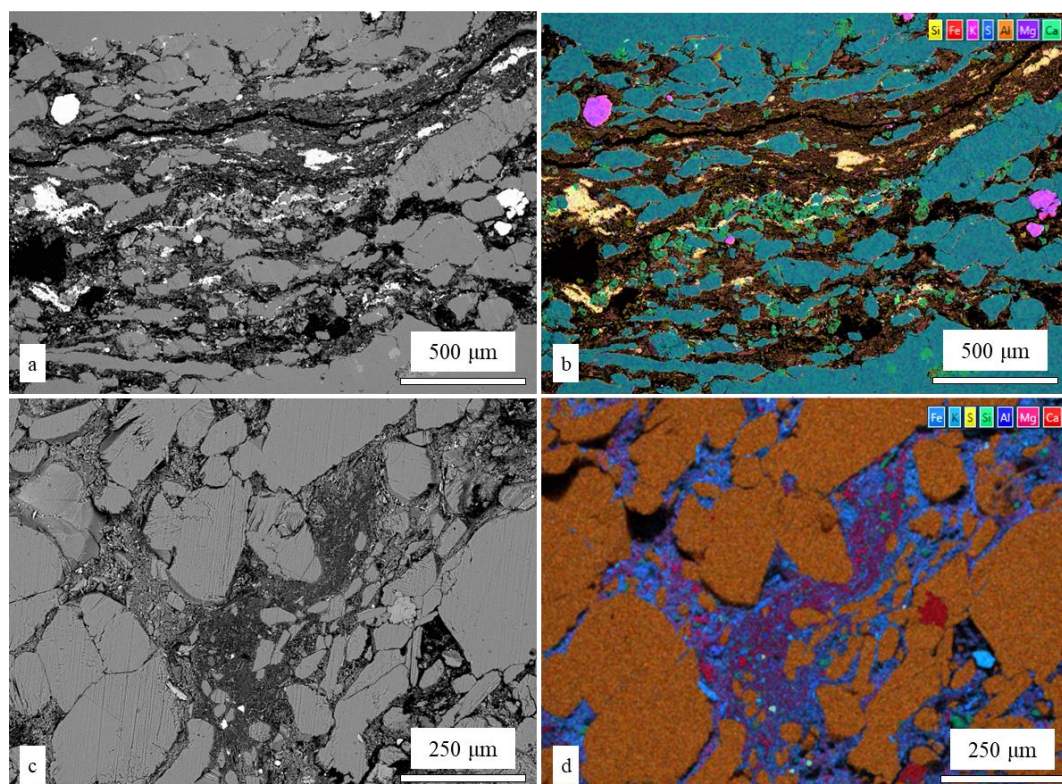
Figure 4. 13 a. and b. SEM-BSE micrograph and SEM-EDS compositional map of a large portion of rock, representing the typical features of the branching selenite structure. c. and d. SEM-BSE micrograph and SEM-EDS compositional map of a detail on the fine-grained portions. Both the scenes refer to A-type samples

As confirmed by the XRPD analyses, the terrigenous portions of the rock are largely composed by clay minerals. The results of semi-quantitative analyses of clays (Figure 4.14) suggest the coexistence of different clay groups. The Figure reports the results of the analyses on three samples (reflecting the range of variability of the results) in natural conditions and after the glycol and thermal (T=350°C) treatments. In the entire dataset, the predominant clay family is the Illite, as confirmed by the height of the peak at $2\theta = 8.9°$ (i.e. $d_{hkl}=9.8\text{Å}$). This peak is already present in the natural samples and seems to be inert to the treatments. However, the data suggest the presence of other clay groups. All the samples in natural state register a large peak with $2\theta =5°- 6°$ (i.e. $d_{hkl}\simeq14\text{Å}$). After the treatment of glycolation, part of this peak has a movement to the left (to lower values of 2θ and higher values of d_{hkl}), testifying a process of swelling (i.e. Smectite clay minerals). The last step (thermal treatment, T=350°C) brings to a general collapse of these peaks on the peak of Illite. The modelling is not able, however, to reproduce the absence of a complete collapse of Smectite/Vermiculite groups on the Illite and this brings to the absence of a perfect correspondence between measured and modelled curves.
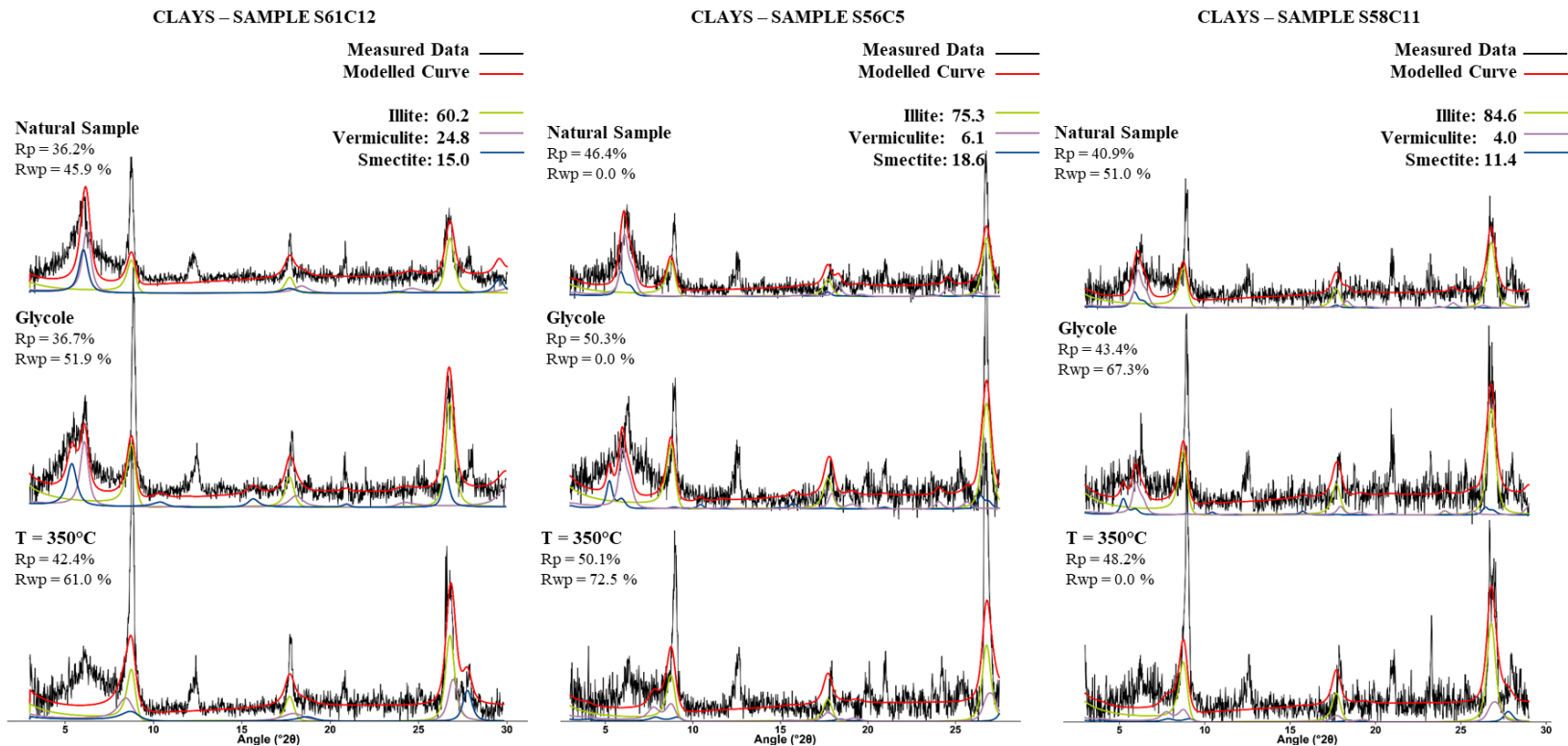
Figure 4.14 Results of clay analysis on three representative samples

4.3 Discussion

The described results on the textural, microstructural and compositional features of branching selenite gypsum confirm the high heterogeneity of this rock facies. The first recognized heterogeneity involves the grain size distribution of the samples. It is possible to relate this heterogeneity at the mesoscale with the structure of the rock at the macroscale. As discussed in Chapter 3, at the rock-mass scale, the branching selenite facies is organized with big branches of coarse material (mainly gypsum) surrounded by layers of finer material, with a more complex mineralogical composition. Similarly, these layers are organized, in themselves, with a structure of branches and surrounding finer layers and this structure is periodically repeated in the rock up to the micro-scale. As a consequence, the distribution of textural and compositional features in the rock-mass is not homogenous. Depending on the position of the sample in the rock structure (i.e. within the coarser branches or in the matrix, with higher or lower concentration of coarser lenses), the grain size, as well as the porosity and the mineralogical composition, is different.

The two material groups (A-type and B-type), described in Chapter 3 at the mesoscale, are here confirmed with microstructural and chemical analyses. The distinguish features of A-type and B-type materials are summarized in Table 4.3.

Table 4.3 Distinguish features of A-type and B-type material groups

	A - type	**B - type**
D10	< 0.3 mm	> 0.3 mm
D50	< 1 mm	> 1 mm
Uniformity Coefficient	> 4	< 4
Branching layers	Mainly composed of equigranular minerals	Very thin films mainly composed of clay minerals
Porosity	3% - 9%	7% - 15%
Pore size distribution	Absence of pores in the range $10 – 20$ μm	Presence of pores in the range $10 – 20$ μm (i.e. cracks along the grain boundaries)
Gypsum Content	$> 90\%$	$< 90\%$ (or $> 97\%$)

In particular, the key elements that distinguish the two groups are:

- The texture, with a coarser and highly sorted grain size distribution in B-type gypsum, and different features of the fine layers (thicker and mainly

> composed of equigranular minerals in A-type and very thin films of phyllosilicate minerals in B-type)
> - The gypsum content (either very high or low in the B-type gypsum)
> - The microstructure, that sees the presence of microcracks and structures related to fluid circulation in B-type material.

These elements suggest the existence of a primary variability, mainly in terms of texture and composition (i.e. the consequence of the branched structure of the deposit) that was enhanced by the circulation of fluids. The coarser materials, with a higher primary porosity, facilitate a preferential permeation of the circulating fluids. The water, due to the long permanence in the pores, starts a process of gypsum solution, enlarging the pre-existing pores and dissolving the material along the crystal boundaries.

The distribution of A-type and B-type material in the orebodies is, therefore, controlled by the hydrogeological setting of the area. As described in Chapter 3, indeed, the water circulation within the gypsum bodies follows different organizations. The hydrogeological setting of Calliano area (with karst water completely saturating the gypsum orebody instead to be localized in karst conduits as in Moncalvo area) facilitates the triggering of dissolution phenomena in the rock. Hence, a wider distribution of B-type gypsum in the orebody is associated to this kind of hydrogeological setting.

As will be discussed in Chapter 5, the material heterogeneity here observed influences the mechanical response of the rock. Hence, the material sampling (number, size and distribution of chosen samples) recovers a fundamental role in the characterization of the orebody. If the samples selected for the mechanical characterization are not representative of the real features and variability of the orebody, the results of mechanical tests will not reproduce the real features of the rock, despite a perfect execution of mechanical tests.

Chapter 5

Short-term mechanical response

The heterogeneity of branching selenite gypsum in terms of textural, compositional and microstructural features described in Chapter 4 opens the issue of the variability of mechanical response. The classification of the rock in two classes (A-type gypsum, with finer grain size and lower porosity, and B-type gypsum, with coarser grain size, higher clay content and evidences of dissolution structures) defines two well-distinct end-members that are useful in the material characterization.

The alternative presence of A-type and B-type gypsum in the orebody requires a specific focus on the relationship between gypsum geological variability and strength parameters. The lack of this kind of analysis would lead, in everyday practice of underground excavation, to ignore important information for the mechanical characterization of the ore deposits.

For this reason, the present Chapter proposes a mechanical characterization of the short-term uniaxial response of branching selenite gypsum, following this two material classes as guideline to address the topic of the microstructural, compositional and textural influence. In the final section, the additional analysis of the role of each physical-chemical parameter aims to overcome the duality of the material classes division and to propose a more complete interpretation.

5.1 Introduction

The influence of textural and compositional features of rock materials on the mechanical response has been observed and described in several rock types. In particular, several authors reported on the importance of the porosity, often considered as the principal factor controlling the rock strength (e.g. Atapour and Mortazavi, 2018; Baud et al., 2017; Palchik, 1999; Ulusay et al., 1994). However, also the grain-size distribution has been observed to be an important aspect driving the mechanical response. This was observed in limestone (Fredrich et al., 1990; Handin and Hager, 1957), sandstone (Atapour and Mortazavi, 2018; Cheung et al., 2012; Klein et al., 2001; Singh, 1988), marbles (Olsson, 1974), anhydrite (Skinner, 1959), dolomite (Hatzor and Palchik, 1998, 1997) and igneous rocks (Eberhardt et al., 1999). Larger grains and longer grain boundaries, resulting in longer weakness surfaces, increase the Griffith crack length, driving a worsening of mechanical properties (Eberhardt et al., 1999; Fredrich et al., 1990; Wong et al., 1996). Moreover, an increase in crystals size is associated with an increase in intra-granular reticular defects: the dislocation density, usually higher in bigger crystals, decreases the intra-crystalline strength.

The assessment of geomechanical strength that is necessary in various engineering issues, including the selection of appropriate excavation techniques and the stability analysis of underground voids, is often approached with the Uniaxial Compressive Strength (UCS) test. UCS test is, indeed, one of the most widely used testing methodologies in the geomechanical characterization of rock materials.

Hence, the present Chapter addresses the mechanical characterization of branching selenite gypsum with a series of UCS tests on cylindrical samples. Results confirm the large variability of mechanical response related to the described high geological heterogeneity.

In everyday practice, the strength characterization with UCS test (usually performed on a small number of samples for the expensiveness and the necessity of accurate sample preparation) may be insufficient to completely describe the rock heterogeneity. The possibility to complement the UCS data with a larger number of cheaper and more expeditious tests would result in a larger data set without significant cost increase. For similar reasons, cheaper and faster methodologies, providing alternative physical and mechanical parameters potentially related with

UCS, have been proposed by various authors (among others, Hatherly et al., 2005; Lawrence et al., 2013; Sharma and Singh, 2008).

The simplest method to provide an expeditious index of the rock mechanical strength is the Point Load Test (PLT). This technique is economic and quick; it does not require any specimen preparation and can be possibly carried out directly on site. By contrast, deformation cannot be controlled during the test. The resulting PLT Strength Index I_{S50} can be potentially correlated with UCS (ISRM 1985, ASTM 1995, ASTM 2007). Different authors focused on rock-type dependent I_{S50}-UCS relationships and conversion factors (Basu and Kamran, 2010; Bieniawski, 1975; Broch and Franklin, 1972; Chau and Wong, 1996; Çobanoğlu and Çelik, 2008; Fener et al., 2005; Hardy, 1997; Heidari et al., 2012; JahanGer and Ahmed 2013; Kahraman et al., 2005; Kahraman and Gunaydin, 2009; Li and Wong, 2013; Salah et al., 2014; Singh et al., 2012; Tsiambaos and Sabatakakis, 2004).

Beside destructive methods, non-destructive ultrasonic tests can be used to indirectly assess the rock mechanical properties, by correlations between Ultrasonic Pulse Velocity (UPV) and elastic or strength parameters (Butel et al., 2014; Hatherly et al., 2005; McNally, 1990; Oyler et al., 2010; Vasconcelos et al., 2008; Yasar and Erdogan, 2004). In particular, UPV-UCS correlations were recently established for different rock types in several studies (Butel et al., 2014; Colombero et al., 2016; Karaman and Kesimal, 2015; Vasanelli et al., 2017; Vasconcelos et al., 2008; Wang and Li, 2015; Zel et al., 2015).

This Chapter proposes, therefore, in addition to the mechanical characterization with the most established technique (UCS), an integration with faster and cheaper methodologies (PLT and UPV) in order to obtain appropriate correlations and a reliable technical characterization for branching selenite gypsum.

5.2 Samples
The mechanical characterization described in the present Chapter was performed on 84 core samples in branching selenite facies drilled in the Monferrato area. Since the axial direction of the cores is perpendicular to the stratigraphic anisotropy, UCS test, PLT and UPV measurements, performed in the axial direction of the cores, simulate the stress conditions of pillars and walls in underground quarries. Cores were made available from a private company and the related diameter (80 mm) was out of our control. After parallel cutting of the edges with a circular saw (perpendicularly to core axis), sample lengths were in the range between 200 mm and 500 mm. Samples were inspected to verify the absence of macro-cracks and prepared for testing following ASTM 4543-01 standard requirements. Number and sizes of the cores tested for mechanical characterization (UCS, PLT and UPV) are summarized in

Table 5.1. The sampling procedure is shown in Figure 5.1. All the tests discussed in this Chapter were performed in dry conditions.

Table 5.1 Number of samples tested with the described methodologies and sizes of the specimens.

Test	N° of samples	Spicemen sizes	N° of common samples
UPV	67	200-500 x 80 mm	UCS-UPV: 15
Point Load	55 (85 specimens)	30-70 x 80 mm	UCS-PLT: 13
UCS - *constant strain rate*	18	160-280 x 80 mm	
UCS - *constant stress rate*	9	160-280 x 80 mm	
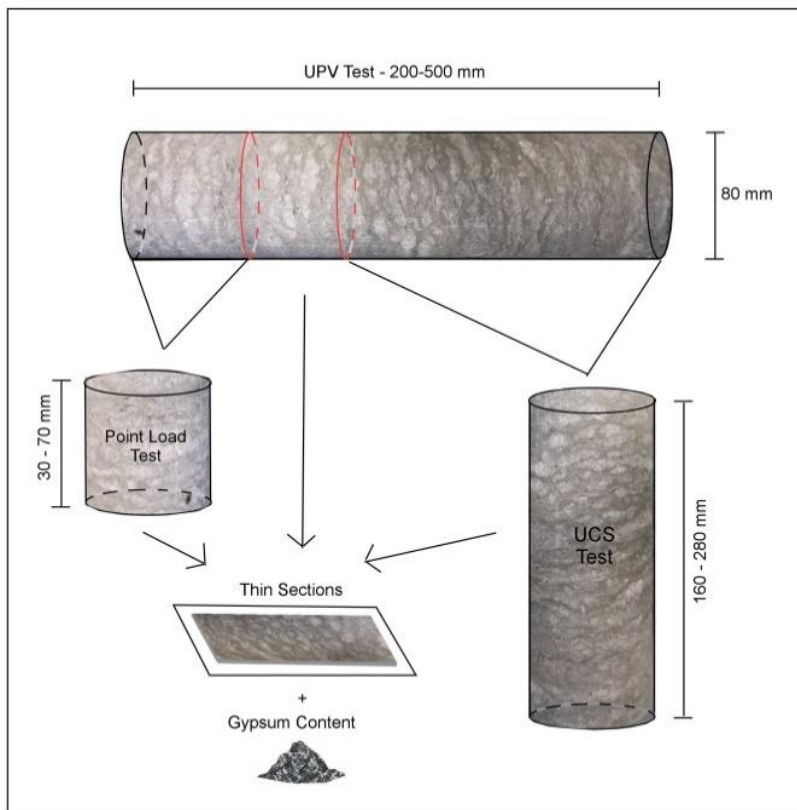
Figure 5.1 Schematic representation of sample extraction from the long cores and preparation according to geometrical requirements.

Even if all the cores were tested with the non-destructive UPV technique, only 67 measurements are discussed in the following; the results of the remaining 17 cores were excluded due to the high standard deviation among the measurements.

In some cases, the total core length was higher than the standard requirements for UCS and PLT tests. Therefore, cores were further cut in shorter samples, allowing for the execution of multiple PLT tests.

Since the textural and compositional analyses presented in Chapter 4 were carried out on the remaining parts of the samples, the results can be reliably associated with the mechanical measures discussed hereafter.

5.3 Methodologies
5.3.1 UCS tests
Unconfined compression tests were performed following ASTM D 3148 - 02 and UNI EN 1926-2007 standard requirements. A loading frame (Figure 5.2) applied an increasing axial load up to sample failure. Both constant stress-rate and constant strain-rate tests were performed. In the first configuration, only the maximum strength value was recorded, without strain measurement. In the second configuration, a constant strain rate (specified in Table 5.2) was applied by means of a servo-controlled system; axial displacement was monitored throughout the test and the material behavior after the peak load was also recorded. For some of the test, additional measures of local strains were performed with electrical resistance strain gauges (in both axial and lateral direction – Figure 5.2a) or with linear variable differential transformers (LVDTs) measuring the central 2/3 of the sample height (Figure 5.2b).

Uniaxial Compressive Strength, UCS, and tangent Young's Modulus, E, were evaluated for each specimen. Additionally, for the samples with axial and lateral strain gauges, the value of Poisson Ratio is also provided.

Table 5.2 Samples sizes, physical parameters, method used for the measure of strain and applied strain rate

Sample Name	Strain Measure System	Strain Rate	Height	Diameter	Bulk specific weight	Gypsum Content
		s^{-1}	mm	mm	kN/m^3	%
S61 C6	LVDT	3E-05	158.42	78.73	22	91.02
S56 C5	LVDT	1E-05	158.55	78.76	22.1	83.52
S61 C11	LVDT	1E-05	160.07	78.64	22	84.78
POA	LVDT	1E-05	199.8	99.3	22.23	90.83
S61 C12	LVDT	1E-05	163.36	78.66	21.3	93.55
S58 C7	Strain Gauge	3E-06	177	77.3		
S58 C6	Strain Gauge	3E-06	160	78		
S58 C9	Strain Gauge		173	78.6	22.1	88.97
S58 C4	Strain Gauge	4E-06	134	77		

S58 C12	Strain Gauge	3E-06	176	77.9		
S59 C2	Strain Gauge	3E-06	175	77.2		
S58 C11	---	3E-06	175	78	21.9	87.43
S58 C13	---	2.5E-06	213	79		
S59C1s	---	1E-05	127	78	21.60	
S59C2b	---	1E-05	131	77.3	22.10	
S59C2s	---	1E-05	122	77.2	21.57	
S59Cs	---	1E-05	119	77.3	21.07	
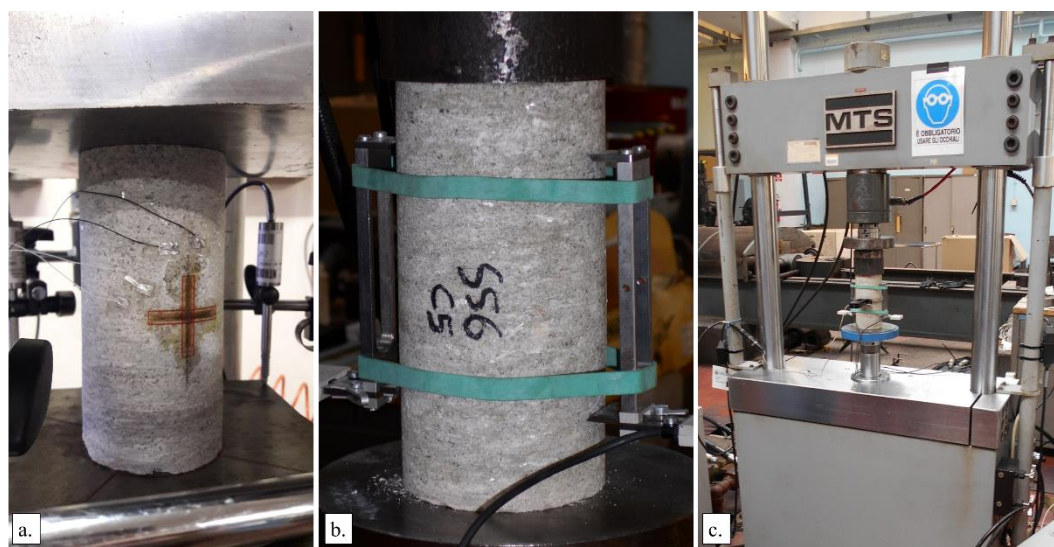
Figure 5.2 a. Uniaxial Compression Test with measure of local strains with electrical strain gauges. b. Uniaxial Compression Test with measure of axial strains with LVDTs. c. General view of the loading press during the UCS test

5.3.2 Point Load Test

Gypsum samples were loaded in the PLT apparatus (Figure 5.3) between two conical steel points, according to the Suggested Method for Determining Point Load Strength (ISRM 1985; ASTM 2007). In test conditions involving core specimens tested along the axial direction, the sample geometric requirements follow:

$$0.3 \emptyset < H < \emptyset \qquad (5.1)$$

For this reason, the cores were cut in smaller samples, with lengths between 30 mm and 70 mm (Figure 5.1).

The Point Load Index I_S is defined as the ratio between the applied force at failure (P) and the equivalent diameter of the core (D_e):

$$I_S = \frac{P}{D_e{}^2} \qquad\qquad (5.2)$$

where:

$$D_e{}^2 = \frac{4H\text{Ø}}{\pi} \qquad\qquad (5.3)$$

where Ø is the diameter and H is the height.

Due to the influence of the sample diameter on I_S, a normalized value referred to an equivalent sample with diameter of 50 mm (I_{S50}) is used:

$$I_{S50} = \left(\frac{D_e}{50}\right)^{0.45} \cdot I_S \qquad\qquad (5.4)$$

This parameter has been determined for all the cores sampled.

Figure 5.3 a. Point Load test equipment. b. Detail of sample failure under the application of the punctual load with the conical points

5.3.3 UPV Test

UPV measurements were performed with an ultrasonic pulse generator (Pundit – Proceq) which provides emission and acquisition (at a sampling frequency of 2 MHz) of P waves by means of two cylindrical transducers having a nominal frequency of 54 kHz (Figure 5.4).
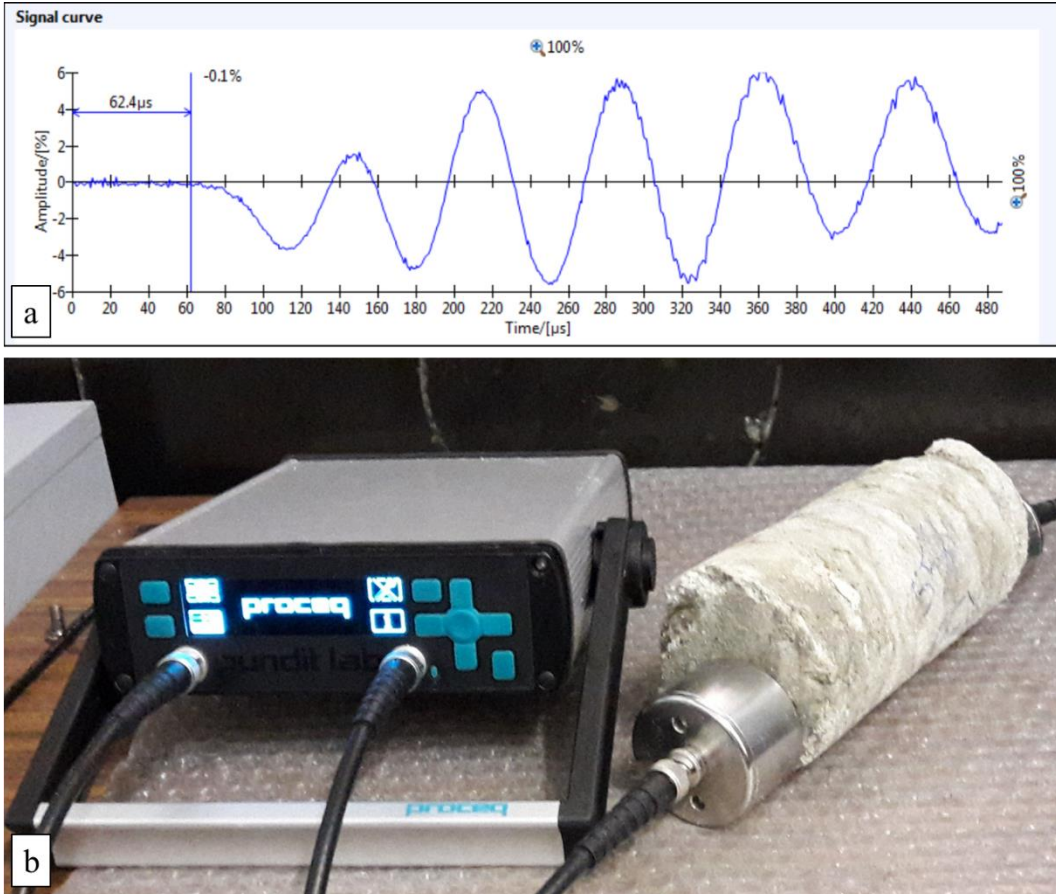
Figure 5.4 a. Output of the recorded P-wave curves b. Pundit – Proceq equipment used for the measure of UPV in the samples

Measurements were conducted following the standard requirements for laboratory determination of pulse velocities (ASTM, 2008). Particularly, the sample height H (between 200 and 500 mm) respected the standard relationship with the core diametr Ø (80 mm) and the average grain size d, following:

$$H \leq 5\varnothing \qquad (5.5)$$

$$H \geq 10d \qquad (5.6)$$

Branching selenite gypsum is a fine-grained rock having a maximum grain size of about 10 mm, thus H largely respected Equation 5.6.

Given the relatively low nominal frequency of the transducers some discrepancies from the standard arose with the core diameters Ø, considering:

$$\varnothing \geq 5\lambda \geq 15d \qquad (5.7)$$

where λ is the pulse wavelength, defined as:

$$\lambda = \frac{UPV}{f} \qquad (5.8)$$

Considering a mean UPV of 2000 m/s, the expected wavelength λ is 37 mm. As a consequence, samples with diameter of 80 mm could not fully satisfy Equation 5.7, but it was at least ensured to have measurements on samples respecting Ø>2λ.

10 UPV acquisitions were repeated on each sample. Manual picking of the first arrival times was performed on each recorded trace, to obtain the time of travel within the investigated core. Determination of the P-wave velocity was then straightforward since travel distances (core height) were known. Final UPV values for each sample were averaged over the 10 measurements.

5.4 Results
5.4.1   UCS test
Figure 5.5 shows the results of UCS tests. As for the following Figures, the measures are associated with A-type or B-type gypsum groups basing on the observation of macroscopic features of the samples.
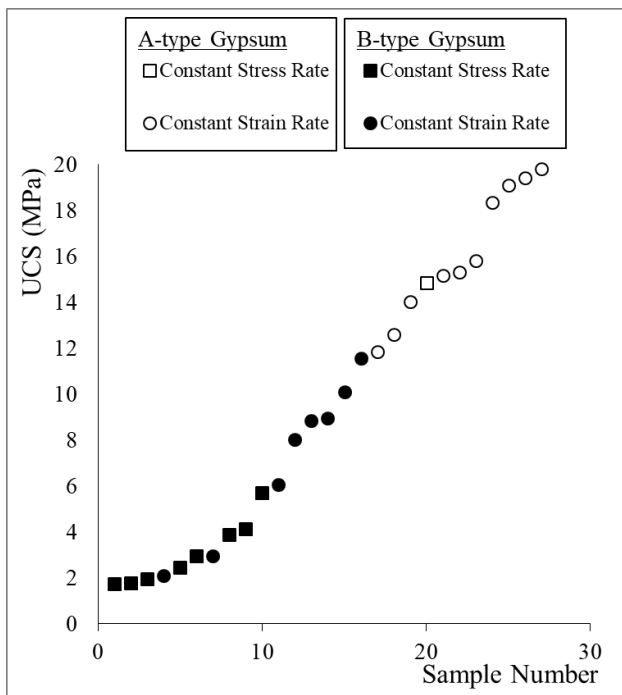
Figure 5.5 UCS values determined on 23 samples from unconfined compressional tests, sorted in ascending order.

The UCS values are sorted in ascending order, from low to high values, to allow for a progressive visualization of the distribution of the measured parameters. UCS ranges between 1.73 MPa and 19.81 MPa and a clear distinction between the two material groups can be set at 12 MPa.

The complete stress-strain curves obtained in constant strain-rate test conditions are reported in Figure 5.6. The related elastic parameters are summarized in Table 5.3. Table 5.3 also lists the available porosity data from helium pycnometer, the grain-size distribution indexes (D10, D50 and UC) and material class (A- or B-type).

Table 5.3 Strength results of uniaxial tests and, when available, values of elastic moduli, values of grain-size distribution indexes (D10, D50 and UC), porosity from helium pycnometer and gypsum class (A-type or B-type)

Sample Name	UCS	E	υ	D10	D50	UC	n	Gypsum Type
	MPa	GPa		mm	mm		%	
S61 C6	19.81	13.49	---	0.06	0.3	6.67	3.46	A
S56 C5	19.1	11.87	---	0.06	0.32	8.33	3.14	A
S61 C11	16.4	11.19	---	0.26	1	4.62	5.64	A
POA	15.17	18.87	---	0.14	0.65	5.71	4.04	A
S61 C12	12.61	6.76	---	0.2	0.8	5	2.31	A
S58 C7	18.35	6.68	0.24	0.11	0.21	0.25	---	A
S58 C6	15.3	7.61	0.33	---	---	---	---	A
S58 C9	14.04	14.47	0.29	0.22	0.85	4.77	7.11	A
S58 C4	11.57	2.86	0.37	---	---	---	---	B
S58 C12	10.1	1.71	0.42	---	---	---	---	B
S59 C2	2.12	0.80	0.33	0.17	0.7	5	11.4	B
S58 C11	8.02	---	---	0.4	1.3	3.75	3.71	B
S58 C13	11.84	---	---	---	---	---	---	A
S59C1s	8.95	---	---	---	---	---	---	B
S59C2b	8.86	---	---	---	---	---	---	B
S59C2s	6.07	---	---	---	---	---	---	B
S59Cs	2.96	---	---	---	---	---	---	B

To allow for a comparison among the different experimental curves, Figure 5.6 reports the axial strains measured from the piston movement during the test (and not the measures of local displacements from strain gauges, that were not available for all the samples).

The results highlight a clear distinction among A-type and B-type samples in terms of both strength and stiffness. An arbitrary strength limit can be assumed around 12

MPa. B-type samples show a lower stiffness: the strain registered in correspondence of the peak strength are up to twice the correspondent values in A-type material.
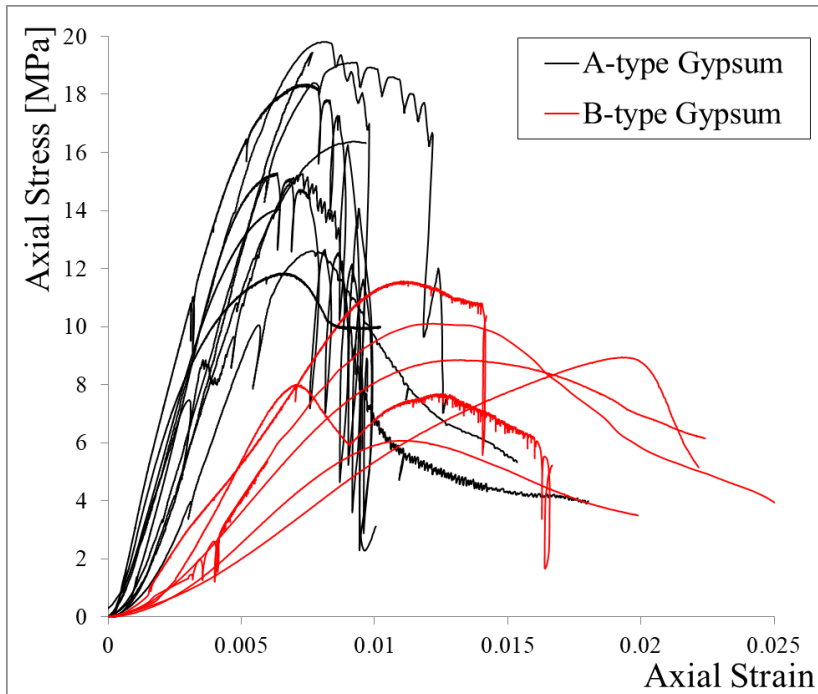
Figure 5.6 Results of UCS tests.

In correspondence of the peak load, visible failures were not often observable on the sample surface. The growth of the first macroscopic cracks began during the loss of load in the post-peak phases.

In A-type samples, cracks progressively propagated until the coalescence of a well-defined failure surface, with an angle of 60°. In most cases, the specimen did not reach a final collapse, but an internal cohesion was maintained even after failure (Figure 5.7a).

B-type samples, with lower strength, did not often develop a well-defined failure surface. Conversely, sub-horizontal breaking surfaces that follow the rock anisotropy and seem to develop along the fine films separating different gypsum lenses were often observed (Figure 5.7b).

Figure 5.7 a. A-type sample at the end of the test b. B-type sample at end of the test.

5.4.2 Point Load Test

Obtained I_{S50} values of all the 85 tested specimens are reported in Figure 5.8 in ascending order. I_{S50} values distribute quite homogeneously over a wide interval (0.02 MPa – 1.20 MPa). The average I_{S50} computed on the whole dataset is 0.56 MPa.

The distinction in the two material groups (A-type and B-type) defines three areas of the graphs:

- with I_{S50} < 0.40 MPa, a clear prevalence of B-type samples is observed
- between I_{S50} = 0.40 and I_{S50} = 0.80 MPa, the data register a transition from the prevalence of B-type to the prevalence of A-type
- with I_{S50} >0.80 MPa, the values are mainly associated with A-type specimens.
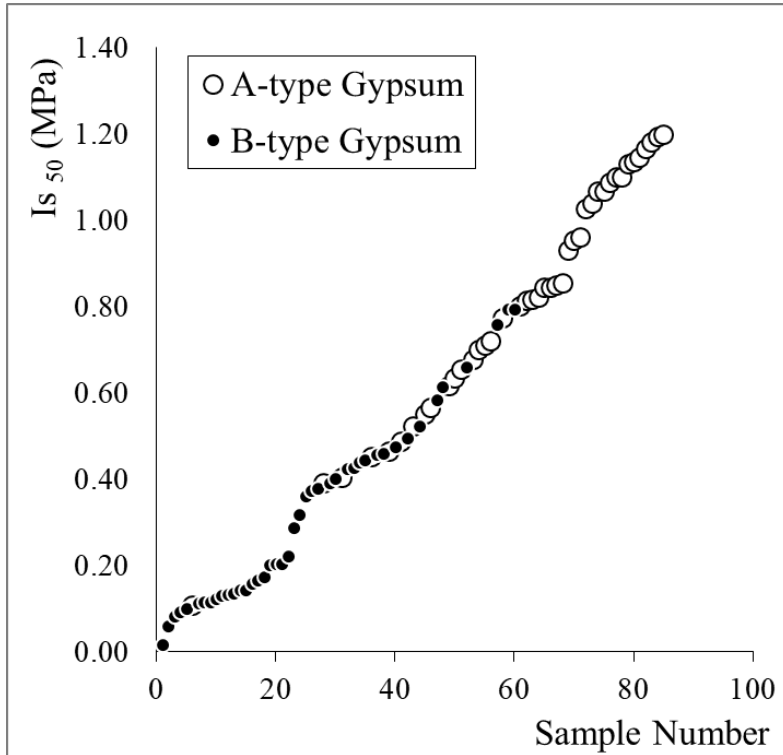
Figure 5.8 Is$_{50}$ values determined on A-type and B-type samples from Point Load Test, sorted in ascending order.

Macroscopic observation on post-failure samples highlighted systematic differences between samples of A-type and B-type material groups. In the first case, samples often broke in several scraps, with failure surfaces developed not only in vertical direction, but also sub-horizontally, following the weakness surfaces of the rock anisotropies (Figure 5.9a). In the second case, samples generally broke in two parts, with a clear sub-vertical failure surface (Figure 5.9b).

Figure 5.9 a. After-failure rock fragments of B-type samples. b. After-failure rock fragments of A-type samples.

5.4.3 UPV test

Average UPV values obtained on the 67 samples are reported in Figure 5.10. Results are sorted in ascending order and categorized in A-type and B-type groups. Measurements spread out in a wide range, with a minimum of 745 m/s and a maximum of 4813 m/s. The average velocity of the whole dataset is 2198 m/s. In correspondence of this mean value, it is possible to establish a limit between the values referred to A-type or B-type gypsum samples respectively in the higher and in the lower part of the distribution.
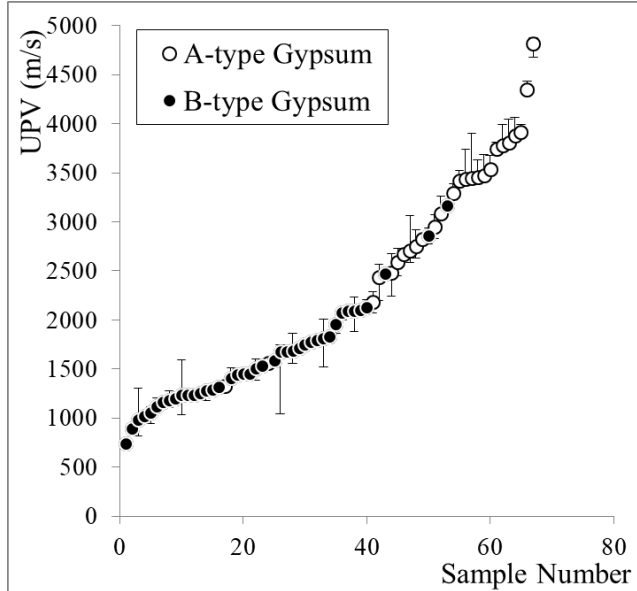
Figure 5.10 Average UPV measurements on samples in A-type and B-type groups, sorted in ascending order.
The vertical black bars show the maximum-minimum range of the ten measurements performed on each sample.

When the Young's Modulus E and Poisson's Ratio υ were available from local measures of axial and radial strains in the UCS tests (see Table 5.3), P-wave velocities (V_P) were retrieved for a direct comparison with the UPV results, following

$$V_p = \sqrt{\frac{K + 4/3\mu}{\rho}} \qquad (5.9)$$

where $K = \dfrac{E}{3\,(1-2\upsilon)}$ is the bulk modulus, $\mu = \dfrac{E}{2\,(1+\upsilon)}$ is the shear modulus and ρ is the material density.

In general, results show a good correspondence between measured UPV and calculated V_P (Figure 5.11).
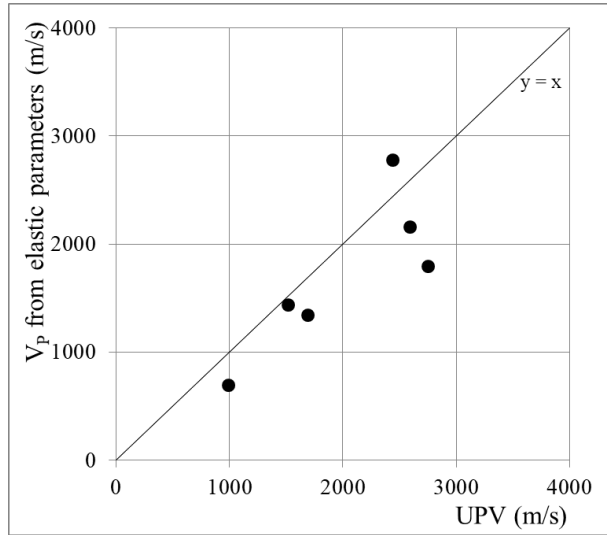
Figure 5.11 Comparison among Vp retrieved from elastic parameters and from the UPV measurements.

5.5 Discussion of the results

5.5.1 Dependence of mechanical behaviour from geological features

The presence in B-type gypsum of microcracks, detachments along the grain boundaries and others dissolution structures (recognized in Chapter 4 as one of the characterizing elements of this gypsum-type) is probably one of the principal causes of the clear distinction in strength responses between the two material groups. However, the range of variability of strength parameters is not completely described by the A-type – B-type dichotomy and other elements should be considered.

The correlation of UCS with grain-size indexes (D10 and D60 indexes) describes a quite defined inverse linear trend (Figure 5.12a-b). The three lines in the graph refers to the best-fit curve and to a deviation of +/-3 MPa. The majority of the points fits this interval, suggesting a confidence degree for the linear trend.

Conversely, the sorting of the material (i.e. the Uniformity Coefficient, D60/D10, Figure 5.12c) defines a direct linear relation with the UCS, suggesting that poor-sorted materials, with a variety of grain sizes, achieve a more efficient organization and higher rock compactness, resulting in an higher strength.

The dependence of the mechanical behaviour on the grain size distribution is usually related to intra-granular strain mechanisms (i.e. the higher concentration of dislocations in coarser grains reduces the strength) and to crack mechanisms (i.e. Griffith theory). Coarser grains reduce the rock failure threshold due to their internal lower strength and the creation of longer weakness surfaces along the contacts between grains. An increase in finer-grained material, even if the number of grain-contacts increases, may be considered as a strengthening element due to the short length of these contacts and their random orientation, which inhibit surface coalescence (Eberhardt et al., 1999; Fredrich et al., 1990).
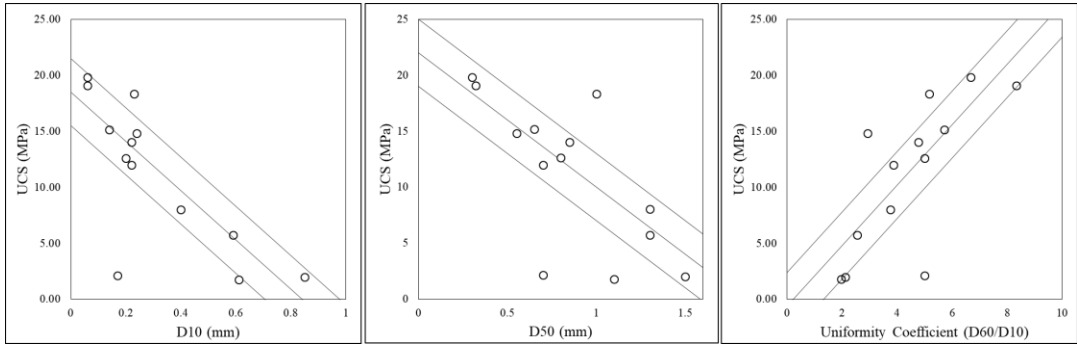
Figure 5.12 Relationship and linear regressions among UCS and D10 (a), UCS and D50 (b) and UCS and Uniformity Coefficient (UC) (c). The lines in the graphs represent the trend line (central line) and a deviation of +/-3 MPa

As commented in Chapter 4, in branching selenite structure the poor sorting of the material (i.e. high variety of grain sizes) is usually due to the abundance of thin-grained layers, mainly composed by equigranular minerals. Conversely, in samples with higher grain-size homogeneity, these layers are substituted by thin films of clays and other phyllosilicate materials. The shape (not equigranular, but thin and planar) and the low strength of these minerals contribute to the formation of significant weakness surfaces, introducing an additional cause of weakening of the bulk strength of the rock.

Figure 5.13 shows the relationship between strength and porosity. Even if a general direct linear trend can be proposed, the data dispersion is very high. As described in Chapter 4, pores tend to be more easily hosted along the fine-grained layers with equigranular minerals, whereas structures with big lenses of gypsum crystals and thin films with phyllosilicate minerals more difficultly accommodate porosity. Therefore, the strengthening effect due to decrease in porosity is probably partially masked by this change in microstructure.
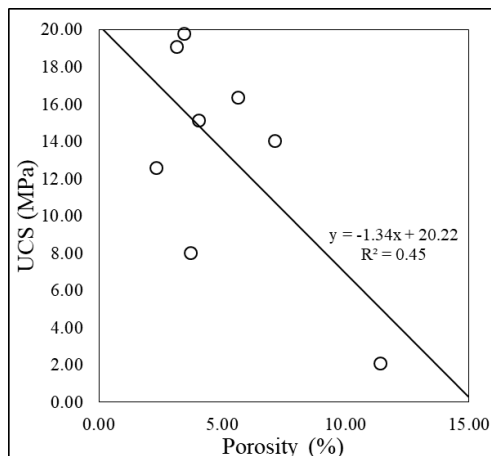
Figure 5.13 Relationship and linear regression between UCS and porosity

In Figure 5.14, all the gypsum content data are compared with the corresponding UCS values, obtained either directly from the uniaxial tests or from Is_{50} and UPV values (using the relationships that will be proposed in paragraph 5.5.2). The data register a general increase of strength with the increase of gypsum content. Figure 5.14 proposes an exponential regression to describe the trend of the data, with a confidence range of +/- 3% of gypsum content. The confidence range includes the majority of the points, with only three points out of the trend.

$$UCS = 5E\text{-}6 \; e^{\,0.161 \, gc(\%)}$$
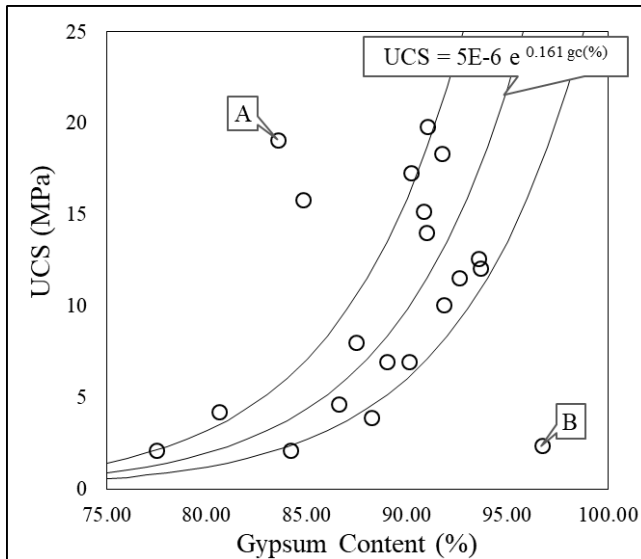
Figure 5.14 Relationship and exponential regression between UCS and gypsum content. The three curves represent the best fit equation and a confidence range of +/-3% gypsum content. The outliers points named A and B can be justified in reason of their anomalous grain size distributions (respectively higher and lower than the average).

These outlier data can be, however, explained in the light of the textural features. Sample correspondent to point B, having the highest gypsum percentage of the dataset (96.7%), registered extremely low strength values by both PLT and UPV measurements. This anomalous behaviour may be related to the grain size, that is coarse and locally almost twice than the one observed in the other samples. As mentioned above, bigger grains and longer intergranular grain boundaries promote the formation of failure surfaces at the grain contacts, resulting in an average reduction of strength.

Conversely, sample correspondent to point A, with high UCS and low gypsum content, has very fine grain size and shows the presence a good interlocking among the crystals, with a very compact structure, that increases the material strength.

5.5.2   Correlation between mechanical parameters

Correlations between UCS values and PLT and UPV measurements have been attempted. For these analyses, only one PLT result for each original core was considered. I_{S50}-UCS and UPV-UCS relationships are shown in Figure 5.15. The best

fitting was obtained with exponential regression for Is_{50}-UCS data (with a R^2 coefficient of 0.89) and with linear regressions for UPV-UCS data (R^2=0.78).
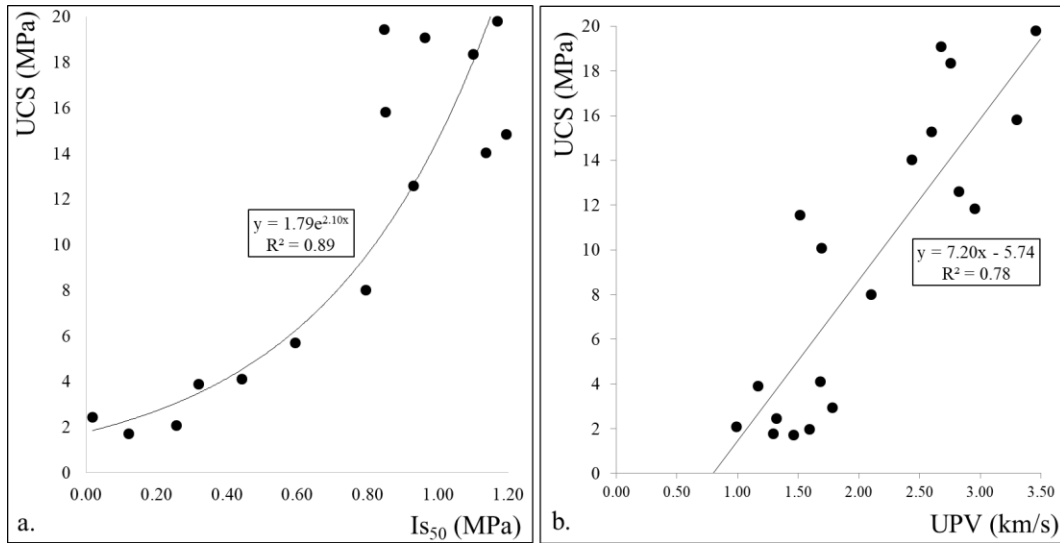
Figure 5.15 I_{S50}-UCS (a) and UPV-UCS (b) relation, with the best fitting regression curves.

The exponential shape of the relationship between Is_{50} and UCS, with a strength-dependent increase of the correlation factor, is in agreement with previous observations on weak rocks (Kahraman et al., 2005; Palchik and Hatzor, 2004; Sabatakakis et al., 2008).

Chapter 6

Influence of material anisotropy on fracture coalescence and mechanisms of strain accommodation

As described in Chapters 3 and 4, the texture of branching selenite gypsum is strongly anisotropic. At the rock-mass scale, this anisotropy is defined by the presence of big branches of clear selenite gypsum that seem to be projected outward from an initial nucleation zone into a fine-grained gypsiferous matrix (Lugli et al., 2010). The orientation of these branches follows, in average, the strike of the gypsum beds. However, their dip direction is not regular, because they are almost vertical at the nucleation point and tends to became horizontal towards the peripheral portions.

The irregular orientation of gypsum branches also influences the anisotropy at the sample-scale, identified by the gypsum nodules and surrounding fine-grained layers. As discussed in Chapter 5, the presence and features of these layers (i.e. levels of equigranular grains or thin films of phyllosilicate minerals) strictly controls the

strength and stiffness of the rock. If the angle of anisotropy deviates from the horizontal, the weakening effect of these layers may be enhanced. The orientation of pre-existing weakness planes in rock materials, indeed, often influences the mechanisms of crack coalescence and strain accommodation.

The present Chapter aims, therefore, to propose an investigation on the mechanisms involved in strain accommodation and crack coalescence of branching selenite gypsum, focusing on the influence of anisotropy orientation and on the increase of confining pressure. Since, due to its better mechanical properties, A-type gypsum shows a better definition of the failure surface, this topic is addressed only focusing on A-type gypsum samples. This gypsum typology guarantees, indeed, a higher test repeatability and comparability among the results, avoiding the presence of unexpected microcracks observed in B-type gypsum.

6.1 Introduction

Measuring and quantifying crack coalescence and strain localization during laboratory tests are important and challenging research topics in rock mechanics. Several techniques have been adopted for this purpose (e.g. optical and electronic microscopy, radiographic analysis, ultrasonic and acoustic techniques, multiple stress and strain local measurements, digital image correlation, x- ray tomography). In particular, Digital Image Correlation (DIC), providing strain values on a grid on the entire surface of the sample for the entire duration of the test, is an innovative technique with large applications in mechanical engineering (Blaber et al., 2015; Chu et al., 1985; Peters and Ranson, 1982; Vend Roux and Knauss, 1998).

In rock mechanics research field, many attempts to apply DIC technique during loading tests were made, e.g. Ferrero and Migliazza, 2009 on marl subjected to uniaxial compression tests, Nguyen et al., 2011 on tuff subjected to plane-strain compression tests, Zhang et al., 2012 on sandstone under indentation, Stirling et al., 2013 on sandstone subjected to Brazilian tests, Yang et al., 2015 on granite subjected to uniaxial traction tests, Vitone et al., 2013 on fissured clays under plane-strain compression.

However, this methodology cannot be directly applied to more complex loading conditions, when the sample is inserted in a visual opaque structure for the application of a confining pressure. The analysis of rock deformation mechanisms in triaxial loading conditions cannot be performed with DIC analysis. In this framework, a largely used methodology is the analysis of the post-test microstructures on thin sections. The application of this methodology to gypsum rock was proposed by Brantut et al., 2011 and Zucali et al., 2010.

The present Chapter aims to investigate the mechanisms involved in the strain accommodation and crack coalescence of gypsum under uniaxial and triaxial

compression. The mechanical data are associated to a multiscale analysis of the effects induced on the material by the compression. The open-source DIC software Ncorr (Blaber et al., 2015) is used for the analysis of uniaxially loaded prismatic samples with different anisotropy orientations. The evolution of strain and failure structures with the increase of confining pressure is evaluated by testing the mechanical response of cylindrical samples under triaxial compression and performing a microstructural analysis of post-failure samples. The resulting strain maps and microstructures' images are analysed and described to propose a reconstruction of the process of crack coalescence based on the textural features of the material.

Different sample shapes were adopted for the different tests (prismatic for uniaxial and cylindrical for triaxial), based on the tests necessities and on the method used for the investigation of failure mechanisms. Despite the difficulty to directly relate the mechanical results on samples with different shapes, the results provide a useful comparison of the strain accommodation structures in the rock.

The Chapter opens with a three-dimensional description of the material anisotropy. A description of the testing methodologies is then provided, followed by a presentation and discussion of the results of mechanical tests and of the analysis of failure coalescence and strain accommodation.

6.2 Anisotropy at the sample scale

At the sample scale, the anisotropic structure of branching selenite is defined in two-dimensional and in one-dimensional spaces: a planar anisotropy is described by the gypsum nodules and the surrounding layers of carbonate and clay minerals and a linear preferential orientation is created by the elongation of gypsum crystals and nodules themselves.

The outcrop of the planar anisotropy can be observed on the samples faces, as shown in Figure 6.1, representing the eight prismatic samples prepared for the compression tests with DIC analysis. The Figure proposes an estimation of the angles, including a range of variability, aimed to quantify and describe the irregularity of the planes. Among the eight prepared samples, only seven were analysed. Sample 2, indeed, broke during the pre-loading operations of the UCS tests and was therefore excluded from the discussion. The remaining samples can be divided in three groups, basing on the orientation of the planar anisotropy:

- Horizontal anisotropy (*Sample* 1 – *Sample* 6)
- Intermediate angles, between 30° and 60° (*Sample* 3 – *Sample* 4 – *Sample* 7)
- Vertical anisotropy (*Sample* 5 – *Sample* 8).
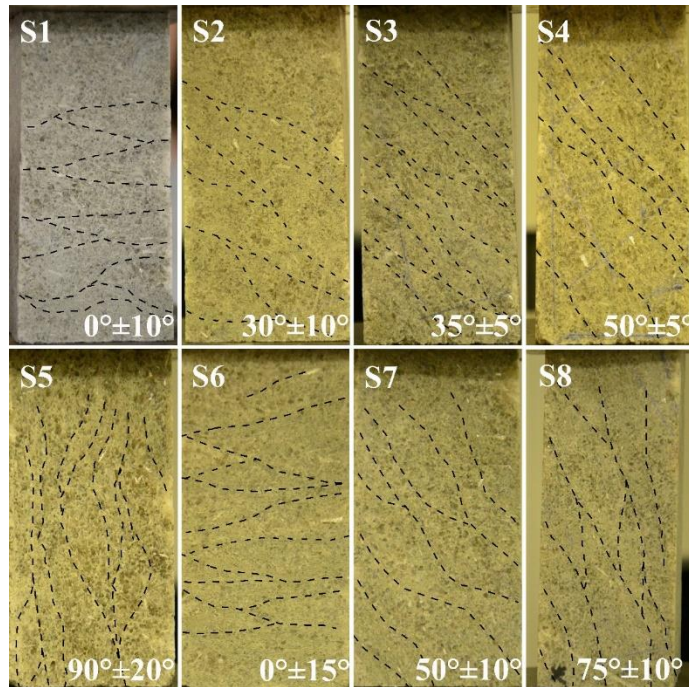
Figure 6.1 Dip angles of the anisotropy planes in the prismatic samples tested under with uniaxial compression

To appreciate the one-dimensional lineation, a three-dimensional view of the samples has to be considered. With this aim, Figure 6.2 proposes the photographical images of two perpendicular faces of the seven samples at the end of the compression tests. The Figure also includes a schematic representation of the principal textural elements that can be recognized on the samples surfaces (i.e. oriented gypsum crystals and nodules).

Thanks to this three-dimensional point of view, samples with horizontal anisotropy (*Sample* 1 and *Sample* 6) show a preferential orientation of elongated crystals in parallel direction to the face in the right of the picture. This preferential orientation defines the one-dimensional lineation of the material.

Something similar can also be observed on the right faces of samples with vertical anisotropy (*Sample* 5 and *Sample* 8). In these samples, the right face corresponds to the strata surface, being oriented parallel to the orientation of the layering planes. In these cases, the orientation of crystals, despite some dispersion, underlines a preferential vertical orientation, particularly well-defined in *Sample* 8.

In *Samples* 3, 4 and 7 (intermediate angle group), the three-dimensional visualization creates an apparent horizontal orientation of the planar anisotropy on the right faces. However, this is only the effect of the intersection of the anisotropy planes with the

vertical face of the samples, but the real dip angle has to be measured on the left faces.
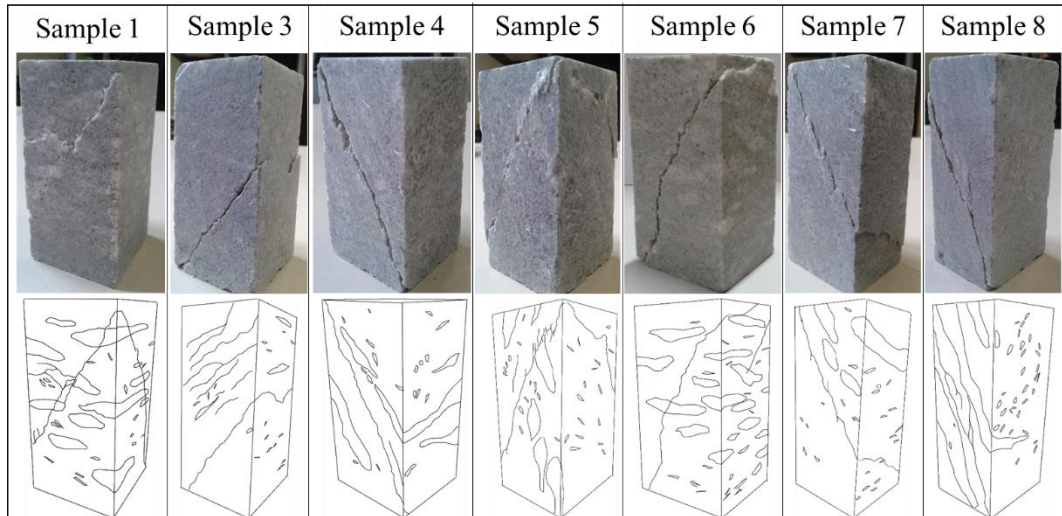
Figure 6.2 Prismatic samples at the end of the Uniaxial Compression Test and schematic representations of the orientation of principal nodules and elongated gypsum crystals in the samples.

6.3 Testing methodologies
6.3.1 Uniaxial tests and DIC analysis

The uniaxial tests were performed with a GDS Instruments Medium Pressure Triaxial Apparatus (MPTA): it was adapted to work without the triaxial cell, therefore functioning by applying only the axial compression to the sample, leaving it visible. Samples were loaded uniaxially up to the failure with a constant displacement rate of 0.06 mm/min (0.03 mm/min for *Sample* 1). The same rate was maintained also after the peak stress, in order to study the post-peak behaviour. Axial displacements of the entire sample (total displacements) were measured during the tests.

Uniform samples sizes of 100x50x50 mm were adopted. The upper and lower faces were polished to obtain smooth and parallel planes. The prismatic shape, with four free flat faces of similar sizes, was preferred to the cylindrical one to facilitate, during the test, the acquisition of the photographical images without perspective effects. The choice to have four axial faces with similar sizes instead to enhance one dimension, as in the usual procedure of DIC analysis, was aimed to study two different sides of the sample, in order to describe the strain distribution in its three-dimensionality.

Videos (frame rate: 24 frames/s, with resolution of 1920x1080 and focal length of 20 mm) were acquired throughout the test with two digital cameras (a Nikon D7000

and a Sony NEX-5N). Two adjacent and perpendicular faces were analysed in order to have a complete description of the deformation and failure (Figure 6.3).
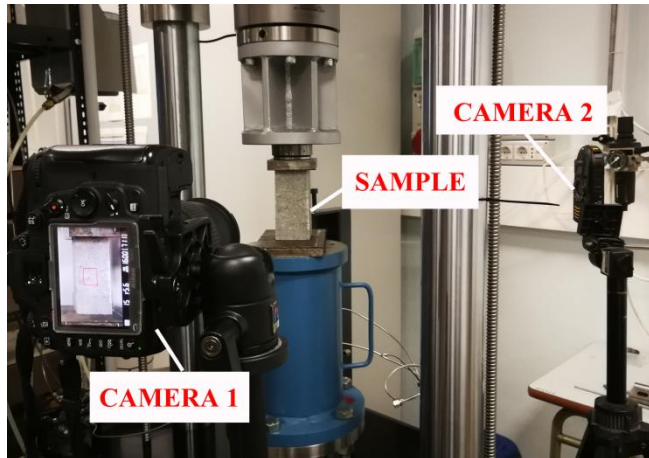
Figure 6.3 Setting of the uniaxial test equipment and of the two cameras acquiring videos.

Ncorr v.1.2.2 software (Blaber et al., 2015), implementing Digital Image Correlation (DIC) algorithms, was used to process frames (we chose to extract from each video a frame every 5 seconds). The software is able to estimate displacement and strain of a sample under deformation using image processing techniques. The method consists in comparing each progressive image with the reference one (shot before the test beginning). The software subdivides the image in small areas (pixel subsets) and verifies their positions with respect to the first image. The result is a grid with displacement data of each subset with respect to the reference image (displacement field). Thanks to the assignment of a scale factor, estimated with a graphical procedure as the ratio between a certain length measured on the image (expressed in pixel) and the corresponding length measured in real world (expressed in millimetre), displacement data are converted into the actual unit of measurement of the sample. Strain calculation is then performed using the strain window algorithm proposed by Pan et al., 2009. The method is based on a pointwise local least squares fitting technique. The sample is divided in squared areas containing a finite number of discrete points (i.e., strain calculation window). The strain calculation windows should be small enough so that the displacement distributions inside them can be approximated as planes. With a linear least square minimization, the parameters of those planes can be assessed and used to compute the Green-Lagrangian strains.

6.3.2 Triaxial tests and microstructural investigation

Triaxial tests were performed with the same GDS MPTA machine used for the uniaxial compression. An isotropic phase brought to the desired conditions of pressure in the oil cell. The axial stress was then increased with a constant displacement rate of 0.03 mm/min. The axial strains were measured throughout the

test with a sensor registering the axial displacement of the piston. In addition, the volumetric strain path was retrieved considering the changes of oil volume in the cell with respect to the initial volume of the sample.

Tests were performed on seven cylindrical samples with diameter of 50 mm and height of 100 mm with horizontal direction of the anisotropy planes. Hereafter, they will be referred to following the letter assignation in Figure 6.4. The upper and lower faces were polished and rectified in order to obtain flat and parallel surfaces.

Figure 6.4 Cylindrical samples for the triaxial test (denominated with alphabetic letters from a to g)

The DIC procedure is not suitable for the analysis of samples in triaxial stress conditions, because the presence of the oil cell inhibits the acquisition of photographic images during the test. For this reason, the strain accommodation mechanisms were described with a multiscale approach at the end of the test. After a macroscopic description, samples were cut and thin sections were obtained for three representative samples. Optical microscope and SEM (Scanner Electron Microscope) observations were performed in order to describe the deformative and failure features.

6.4 Results of mechanical tests
6.4.1 Dependence of uniaxial response on the anisotropy orientation
Figure 6.5 shows the results of uniaxial strength compressive tests on the seven samples. The graph divides the results in horizontal (0°), vertical (80°- 90°) and intermediate (30° - 60°) dip-angles of the anisotropy. The higher strength values are registered in correspondence of horizontal and vertical anisotropy planes. However, the most significant variation among the curves is the change in strain behavior. Samples with horizontal anisotropy show a long post-peak softening phase with the presence of little stress drops. On the other hand, samples with vertical anisotropy reach the collapse just after the peak. Moreover, the Young Modulus is significantly higher, with lower axial strain in correspondence of the peak point. An intermediate behaviour is manifested by the samples with intermediate anisotropy angles: their curves show a soft deformation until the strength peak and in the initial part of the post-peak. This is however suddenly interrupted with an abrupt loss of strength, in

some way corresponding with the first stress drop in the samples with horizontal anisotropy.
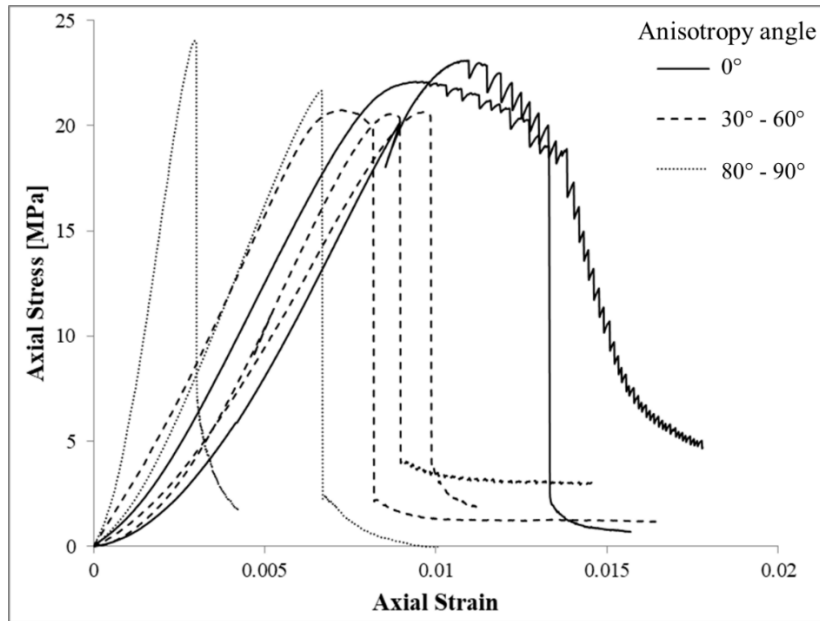
Figure 6.5 Stress-strain curves of samples with low, intermediate or high anisotropy angle.

Figure 6.6 summarizes the uniaxial strength values in function of the anisotropy dip angle ranges. The impossibility to assign a univocal value of angle, due to the natural irregularity of the anisotropy surfaces, is represented in the graph through the horizontal error bars.

The graph confirms the clear dependence of strength on the anisotropy orientation: horizontal and vertical anisotropy angles return the higher strength values, while intermediate angles are associated to a strength decrease, suggesting a parabolic trend. The curve in Figure 6.6 is only qualitative, aiming to underline the trend but not to propose a mathematical relationship, since the quantification of anisotropy dip angle is an interpretation and data are presented as ranges and not as precise numbers.
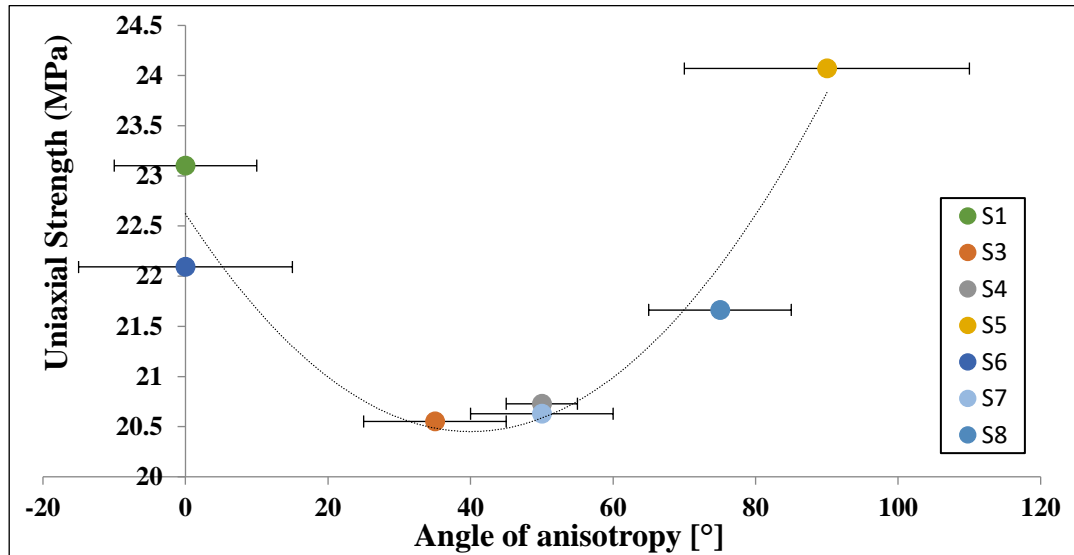
Figure 6.6 Distribution of uniaxial strength values in function of the dip angle of the anisotropy.

6.4.2 Mechanical response in triaxial conditions

Figure 6.7 shows the results of the performed triaxial tests. The confining pressures and the maximum differential stresses reached during the tests are summarized in Table 6.1.

Table 6.1 Summary of results of triaxial tests

Sample Name	Confining Pressure [MPa]	Maximum Differential Stress [MPa]
a	1	15.32
b	2	18.42
c	4	18.21
d	4	24.72
e	6	25.13
f	6	29.26
g	8	32.54

The stress-strain curves in Figure 6.7a underline a change of behaviour from the clear softening of *Sample* a to a more hardening kind of deformation in *Sample* g, with the assessment of a stable value of stress that does not decrease until the end of the test (at a final strain of 6%). It has to be noticed that even the introduction of a little confining pressure (e.g. 1 MPa in *Sample* a) brings to the duplication of the axial strain with respect to the unconfined tests (e.g. Figure 6.5).

The peak stress data are reported in the p-q graph in Figure 6.7b and in the Mohr circles representation in Figure 6.8. Both representations suggest a linear best-fit trend of the failure envelope. As will be shown in Chapter 7, this linear trend is only verified for low values of confining pressure (i.e. pressure lower than 10 MPa). For

higher values of confining pressure, indeed, a decreasing friction angle will be observed. However, in these tensional range, a friction angle in the range between φ = 30° and φ = 34° can be considered.
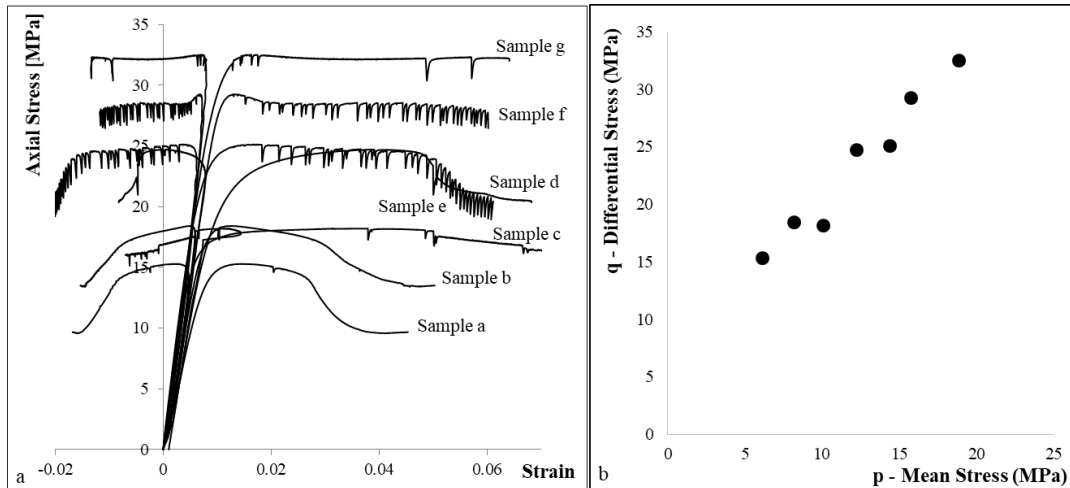
Figure 6.7 Axial and volumetric strains curves of triaxial tests. b. Plot of the maximum strengths in the p-q graph.
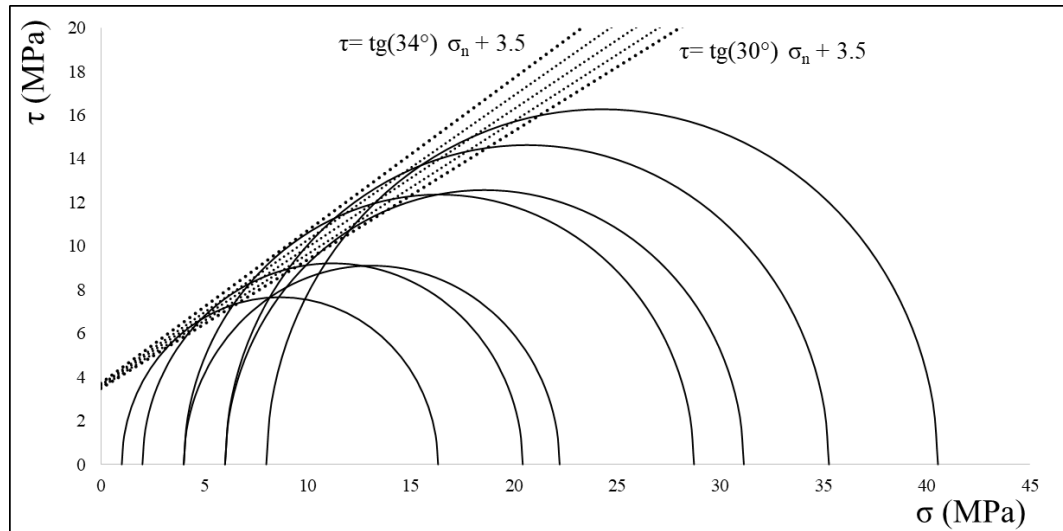
Figure 6.8 Mohr circles and failure envelope

Figure 6.9 shows the macroscopic features of the seven samples at the end of the triaxial tests. They are ordered (from *Sample* a to *Sample* g) following the increasing confining pressure. To each photographic image, we associated a schematic representation of the sample shape and fracturing. The Figure suggests a gradual transition (from lower to higher pressures) from a structure characterized by a single, localized failure surface (*Samples* a, b, d), to the presence of a more diffuse

fracturing, with conjugate surfaces (*Samples* c, e, f), to the total absence of visible fracturing coupled with a barrel shape of the sample (*Sample* g). Until one principal failure surface is visible, a constant angle with the main loading direction can be observed. In *Samples* a, b, d and e (but also in the samples from uniaxial test) an angle α with the horizontal surface of about 60° was measured. This angle is coherent with the friction angle evaluated from the failure envelope, following

$\alpha = \varphi/2 + \pi/4$.
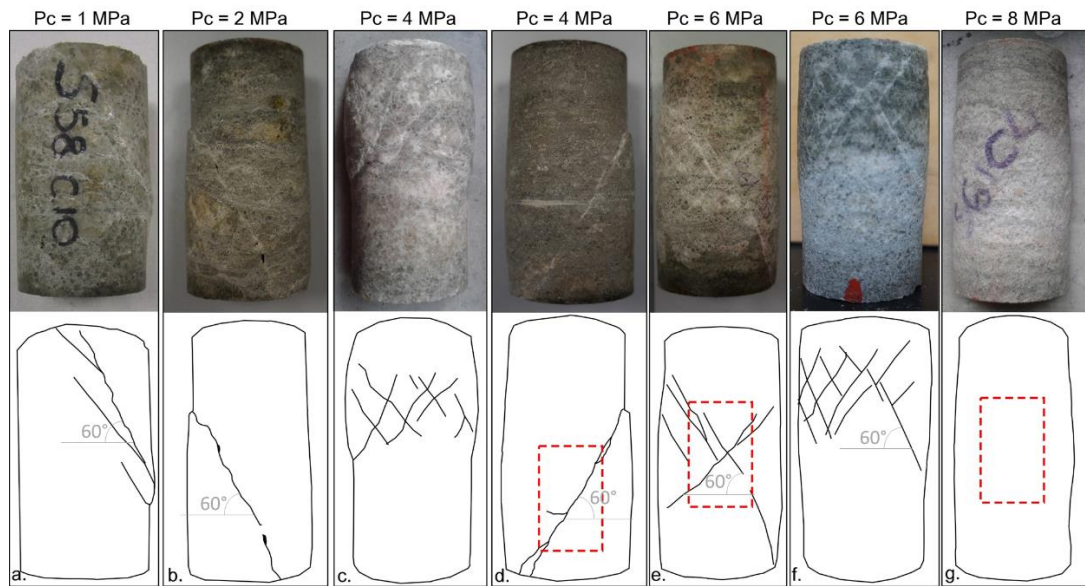
Figure 6.9 Photographic images and schematic representations of samples at the end of the test.

6.5 Fracture coalescence and strain accommodation
6.5.1 Reliability of DIC analysis results

Results of DIC analysis on uniaxial tests were computed to obtained displacement and strain evolution-paths for different positions on the sample surfaces. The results allow for a qualitative evaluation of DIC reliability. As an example, this paragraph reports the results obtained on *Sample* 4, proposing a discussion of the obtained curves.

Figure 6.10 shows the DIC load-displacement curves of points along a line straddling the fracture. Each curve refers to a specific point on the face: displacement values obtained for each frame are associated to the load registered from the load cell at the correspondent time from the beginning of the test.

Curves are compared with the total displacements measured from the machine. Since the considered line is in the half of the axial length of the sample, the total displacements were divided by 2.

The comparison shows a very good agreement between the curves.
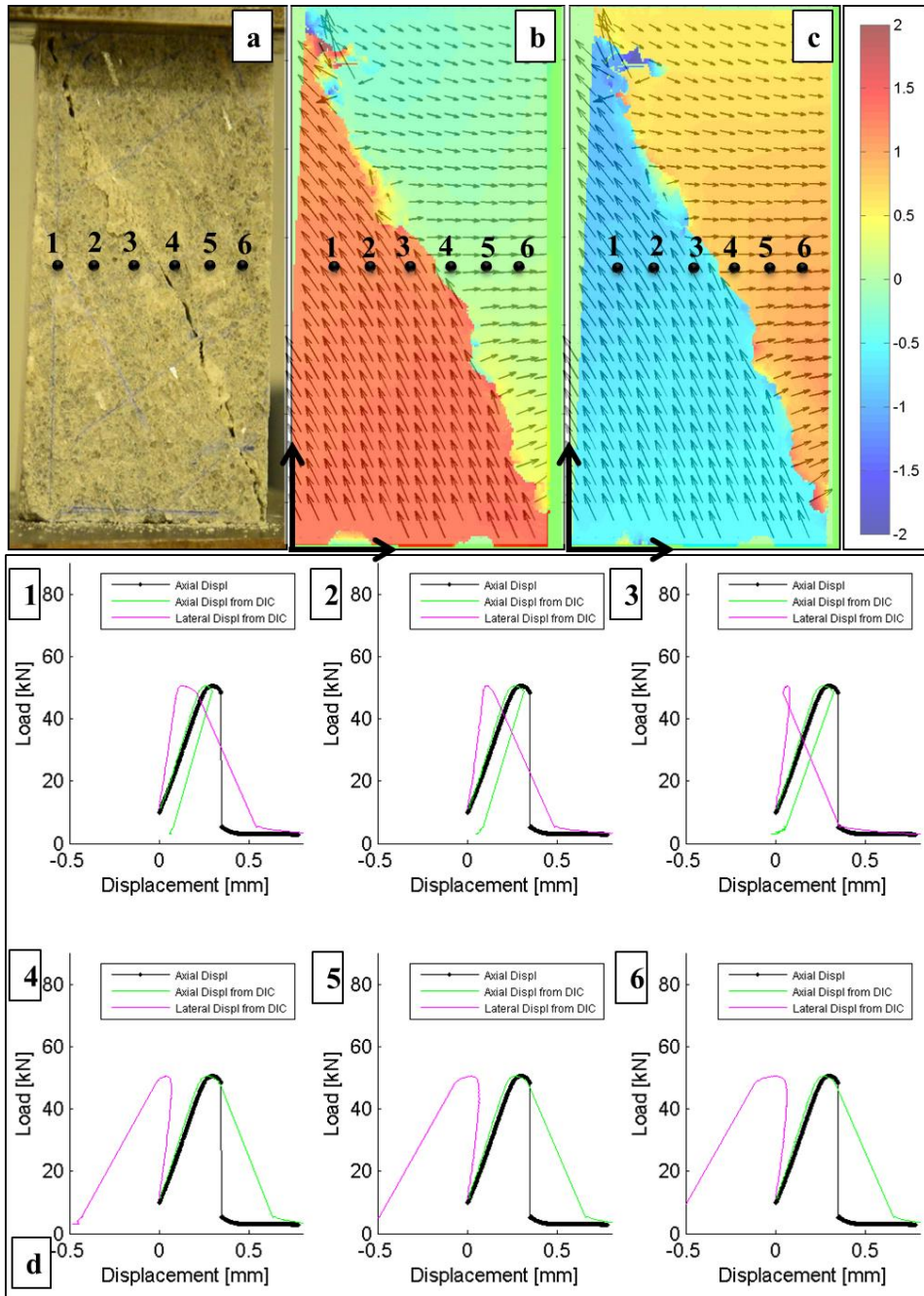
Figure 6.10 a. Macroscopic appearance of Sample 4 at the end of the uniaxial compression test. b. Colour map of axial displacement and displacement vectors at the end of the test. c. Colour map of lateral displacement and displacement vectors at the end of the test. d. Comparison of the load-displacement curve measured from the load system (black curve) and the axial and lateral displacement curves obtained with the DIC analysis for the six points shown in Figures 6.10a, b and c.

Values of displacement from DIC analysis are vectors with concordant versus with the axes of Figures 6.10b and 6.10c. Since the load is applied with a piston from below, during the elastic phase axial displacements are positive (upward), while the lateral displacements are almost zero. Figure 6.11, showing the same load-displacement curves in a single graph, helps in reading the data. During the elastic phase, all the curves of displacement from DIC are equivalent. When the onset is reached (i.e. when the linear elastic conditions are lost), the curves of lateral displacement start to diversify, highlighting the opening of tensional fractures. Indeed, points on the left (1, 2, 3) move to the left, while points on the right (4, 5, 6) move to the right. Only after reaching the peak, the curves of axial displacement start to separate, with the upper part, represented by points 4, 5 and 6, showing a negative displacement (downward). This suggests the beginning of a relative sliding movement.
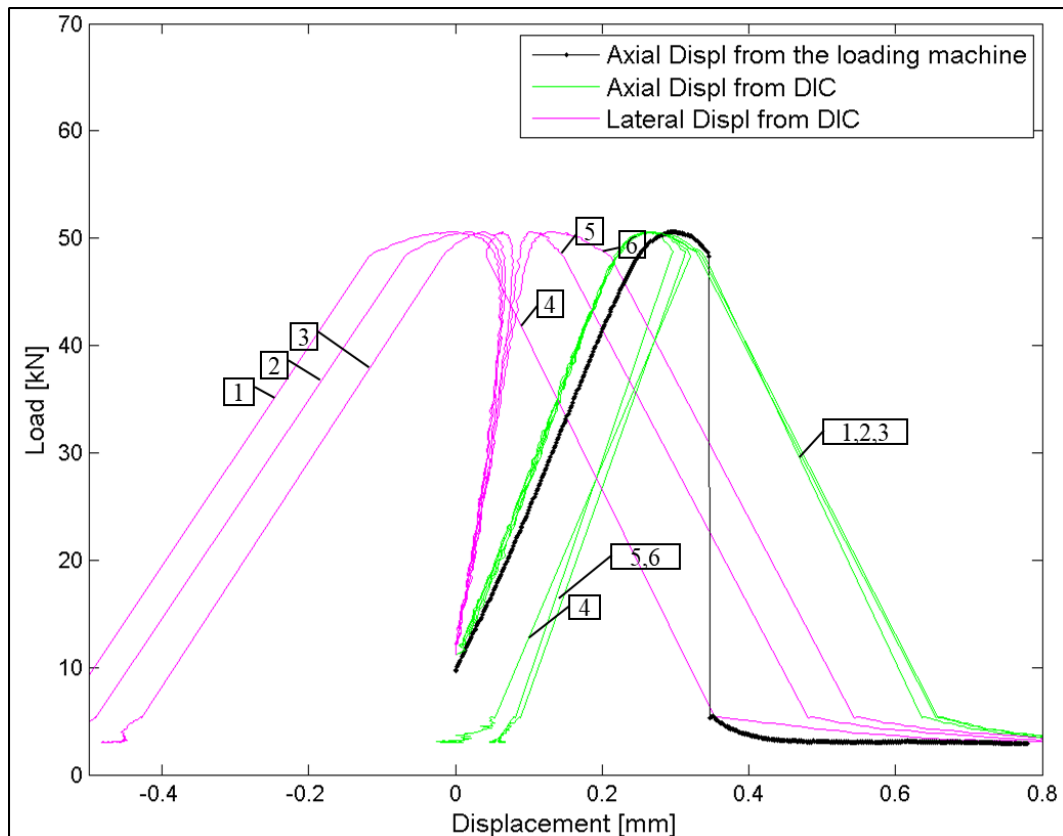
Figure 6. 11 Comparison of load vs displacement curves showed in Figure 6.10d. The numbers refers to the points in Figures 6.10 a, b and c

The computation of strains, including a process of differentiation, is highly sensitive to noise. The resulting load-strain curves are, indeed, noisier and less well-defined than the displacement ones.
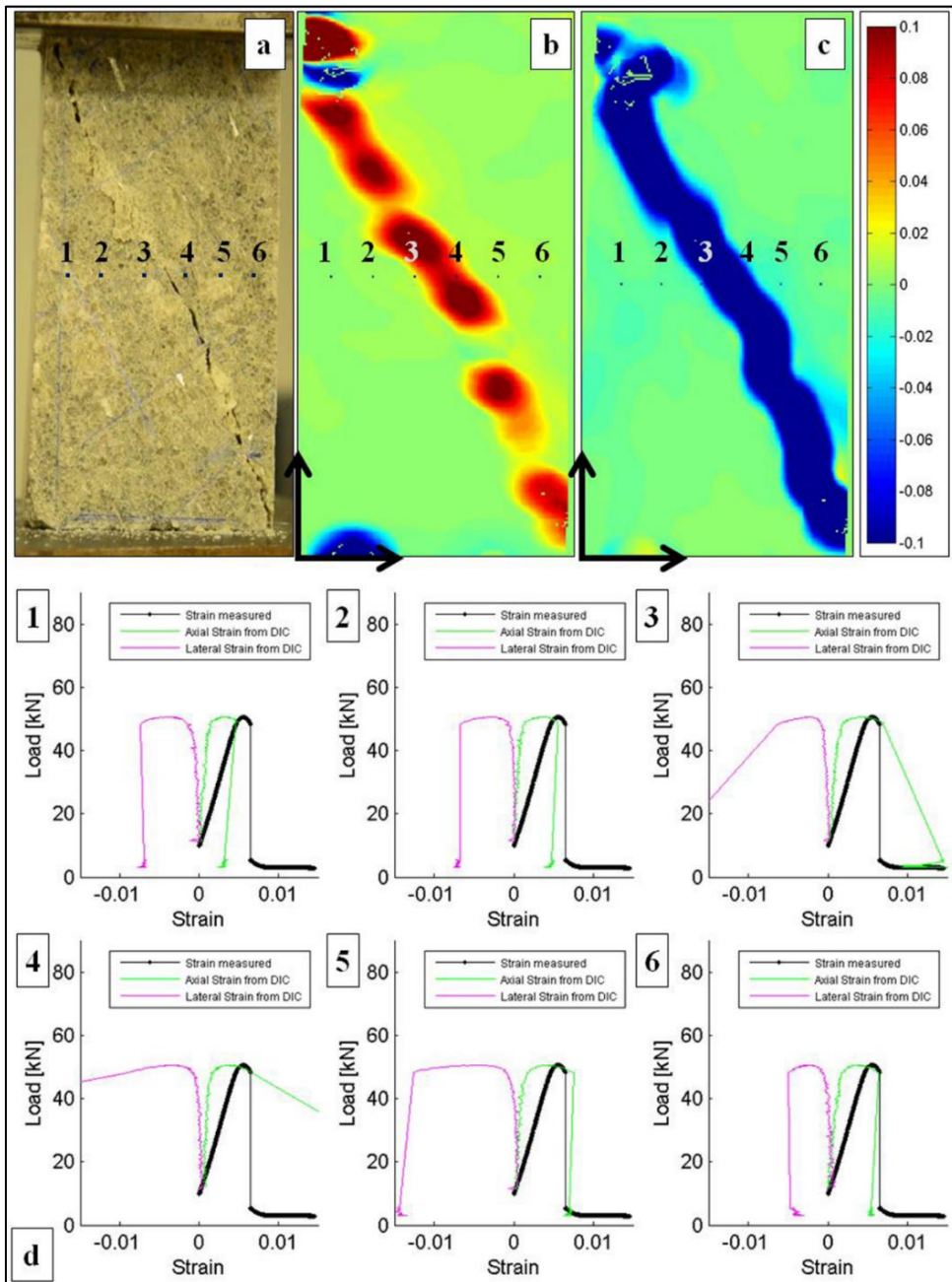
Figure 6.12 a. Macroscopic appearance of Sample 4 at the end of the uniaxial compression test. b. Map of axial strains at the end of the test. c. Map of lateral strains at the end of the test. d. Comparison of the load vs strain curve measured from the load system (black curve) and the axial and lateral strain curves obtained from the DIC analysis for the six points showed in b and c.

Figures 6.12 and 6.13 show the load vs local strain curves referred to the same horizontal line straddling the fracture analysed in Figure 6.10.

99

The linear elastic loading phase, characterized by small axial and radial strains, is followed by a significant strain acceleration, both in axial and lateral directions, starting from the onset point. No evident differences among the curves are recognized before the peak strength. Nevertheless, after the peak, points 3, 4 and 5 (nearer to the fracture surface) show higher strains, leading to the collapse of the sample. In particular, point 5, even if in Figures 6.12b and 6.12c seems to be out from the failure area, shows high lateral deformations before the collapse, suggesting the evolution, during the test, of a larger shear zone than the final failure surface.

During the loss of load and the correspondent coalescence of failure surface, points 3 and 4 show a sudden increase of strain, while the other points, further from the failure area, show an almost vertical trend. The failure happens, therefore, without any important strains far from the fracture.

After the failure, in almost all the curves, it is possible to recognize a decrease of strain, due to the elastic relaxation of the material.
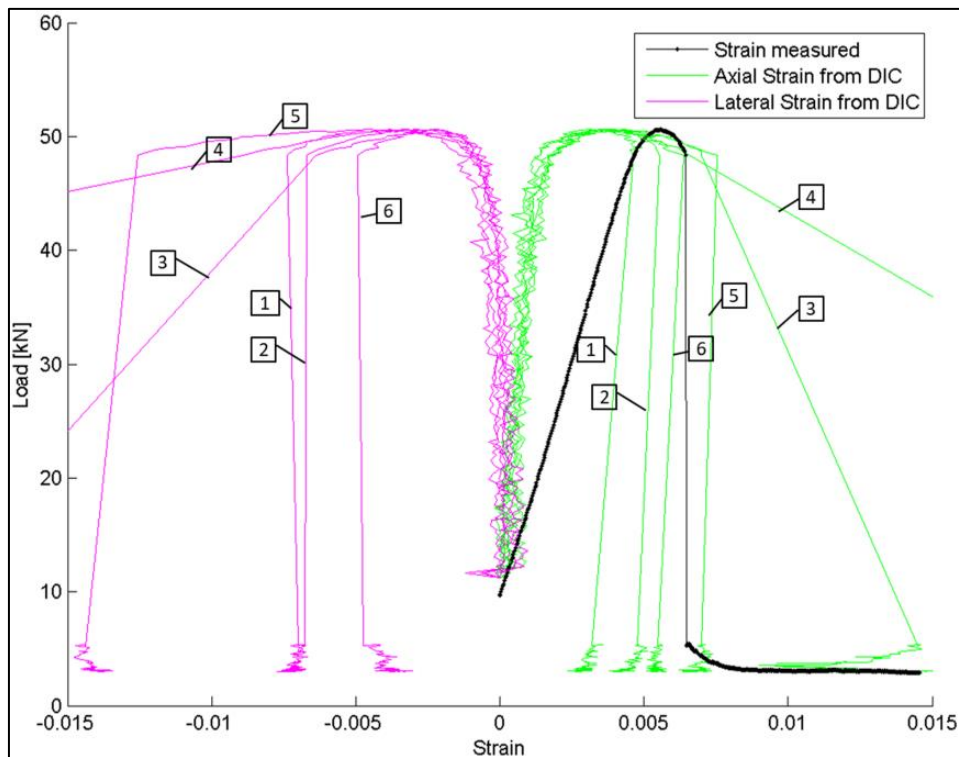
Figure 6.13 Comparison of load vs strain curves of uniaxial compression test in Sample 4 from the loading system (black curve) and from the DIC analysis in the points reported in Figure 6.12a, b and c.

In terms of qualitative description of strain evolution, results of DIC analysis seem, therefore, to be reliable for the good coherency with mechanical data and macroscopic appearance of the sample at the end of the test.

6.5.2 DIC analysis and material anisotropy

Figures 6.14, 6.15 and 6.16 show the evolution of maps of axial and horizontal strains during the progress of the uniaxial test for samples with intermediate, vertical and horizontal anisotropy angles respectively. The strain maps refer to two perpendicular faces of the prismatic samples. Data are represented in terms of 3D graphs oriented as the real samples, with the axial load direction corresponding to the z-axis. A uniform colour scale is chosen to facilitate the comparison. In the representation, compressive strains are considered as positive, while extensive strains are negative.

In all the Figures, the strain maps refer to the following moments of the test:

- the elastic part of the stress-strain curve (point A)
- the onset point, when the elastic conditions are interrupted and the strain rate starts to increase (point B)
- the strength peak (point C in Figure 6.14 and 6.16 and point E in Figure 6.15).
- the post-peak phase (points D-E in Figure 6.14 and points D-G in Figure 6.16)
- the end of the test, after the sharp loss of strength that leads to the real rupture of the sample.

From the naked eye observation of photographical images, no evidences of cracks can be recognized in correspondence of point C (peak strength) on the surface of any of the samples.

Figure 6.14, referring to *Sample* 4, can be considered as a representative example of the features of all the samples with intermediate anisotropy angles.

During the elastic phase (point A), strains in the maps are homogeneously distributed. When the onset is reached (point B), we start to recognize the intensification of axial strains in the high-left corner of the left face. This strain localization in the corner, at the contact with the loading frame, is probably controlled by the prismatic shape of the sample.

In correspondence of the peak point (point C), the maps show a band of strain localization, oriented as the sample anisotropy (50°). During the short post-peak phase, the strain localization increases along this band that maintains the angle of 50° until point E.

However, when the stress-strain curve registers the loss of load leading to the rupture of the sample, the complete coalescence of the fracture is reached following the failure angle of 60°, consistent with the rest of material.

The discrepancy between these two phases of fracture coalescence can also be macroscopically recognized in the post-failure sample (Figures 6.14b-c), where the

crack surface has different orientations in the upper (around 50-55°) and in lower part (60°).

Figure 6.14 Results of DIC analysis on Sample 4: a. Stress-strain curve. b. Post-test sample. c. Schematic representation of failure surface and anisotropic elements. d. Evolution of maps of axial strains during the test. e. Evolution of horizontal strains during the test

102

As already said, in the samples with vertical anisotropy, the stress-strain curves register the absence of a softening post-peak phase, because the loss of stress immediately follows the strength peak. For this reason, Figure 6.15 (referring to *Sample* 5) proposes an analysis of the pre-peak instants instead of the strain maps in the post-peak phase. Since the entity of registered strains for this sample is largely lower than in the others, the limits of the colour scale of Figures 6.15d and 6.15e are set on 1/4 than in the other Figures.

The maps of axial strains in Figure 6.15d are not particularly informative, because until point F (with the actual coalescence of the failure surface), the strain concentrations do not identify any coherent path.

On the other hand, maps of lateral extensional strains (Figure 6.15e), describing the development of tensional cracks, contain more interesting information on the failure evolution. Maps in points C, D and E, describing the instants before the sample rupture, see the presence and evolution of "points" of strain localization on the left face (i.e. where the planes of the anisotropy outcrop). These strain localizations are sub-vertical in average, but have random orientations, probably following the high variability of the anisotropy planes in this sample (see Figure 6.1). However, the coalescence of these tensional cracks soon brings to the sudden collapse of the sample, with the formation of failure surface in point F.
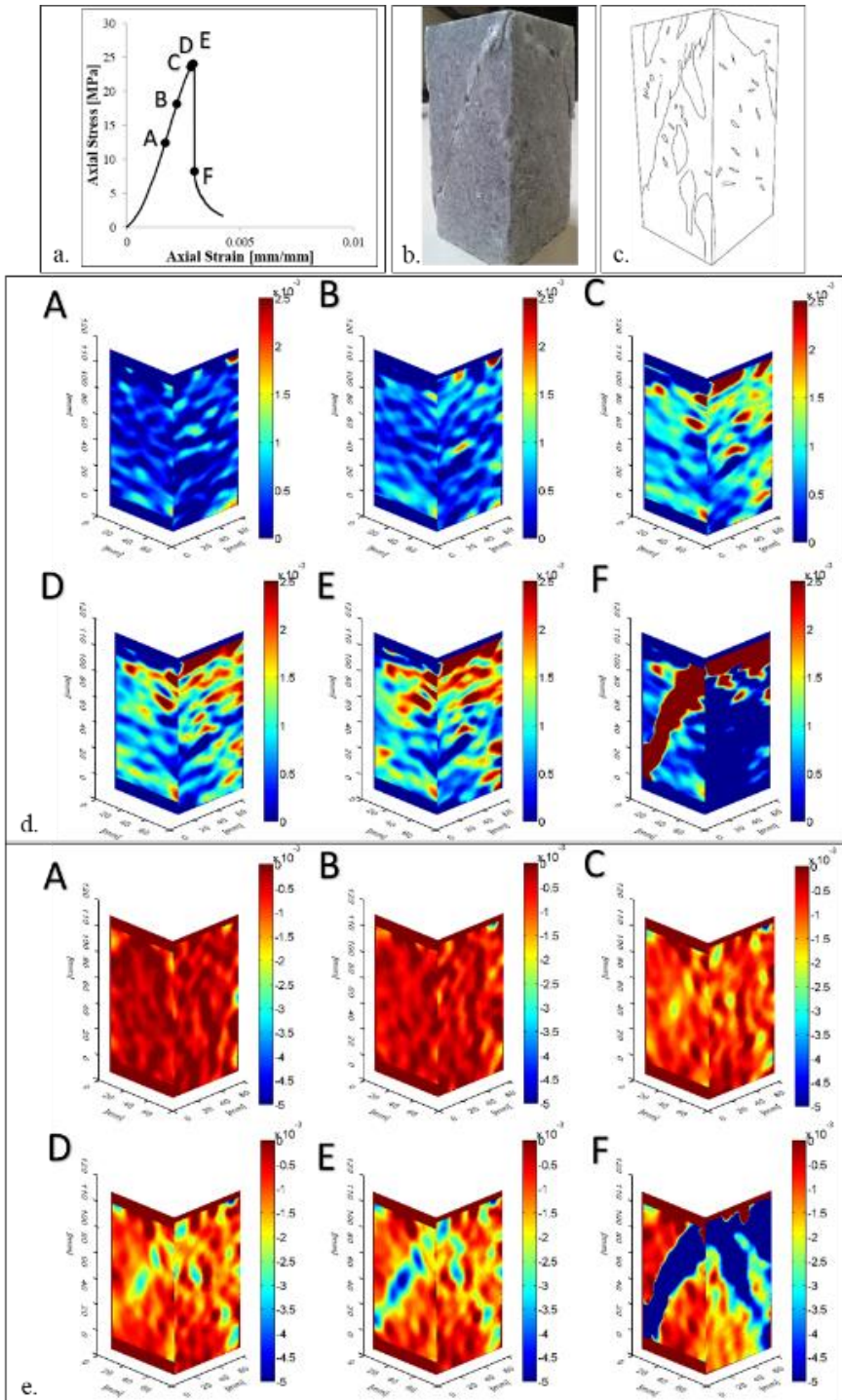
Figure 6. 15 Results of DIC analysis on Sample 5: a. Stress-strain curve. b. Post-test sample. c. Schematic representation of failure surface and anisotropic elements. d. Evolution of maps of axial strains during the test. e. Evolution of horizontal strains during the test

104

Contrary to samples with vertical anisotropy, samples with horizontal anisotropy have long post-peak softening phases. For this reason, Figure 6.16, describing the strain evolution of *Sample* 6 (horizontal anisotropy), includes four strain maps in this part of the curve (points D, E, F and G).

The initial part of the strain evolution is similar to the previous samples: homogeneous strains are observed during the elastic phase, and the first strain intensification can be recognized in correspondence of the onset point (point B), in terms of axial strains in the lowest part of the right face.

This strain intensification is enhanced when the strength peak is reached (point C). At this point, also the horizontal deformation shows a concentration of high strains, delineating the first evidences of two conjugated alignments. Similar evidences can be found on the left face only after the peak, at point D.

The following evolution of the sample continues to be characterized by a higher deformation on the right face than on the left face. However, the deformation on the right face does not bring to the complete failure of the sample, as shown by the stress-strain curve: the small stress drops are quickly recovered, maintaining a constant stress/strain ratio. The significant increase of strain concentration on this face is insufficient to reach the failure of the sample.

On the other hand, when on the left face the alignment of horizontal strains covers the entire sample surface (Figure 6.16e-point G), the sample fails, with an important stress drop (point H) and the clear formation of a well-defined failure surface. The direction of the final failure is therefore aligned with the linear anisotropy of the material.

The creation of a coherent failure surface able to suddenly reduce the rock strength is allowed only in the direction parallel to the crystals elongation. The preferential orientation of gypsum crystals inhibits the coalescence of the strain concentrations located on the right face, where a real failure surface cannot be created.
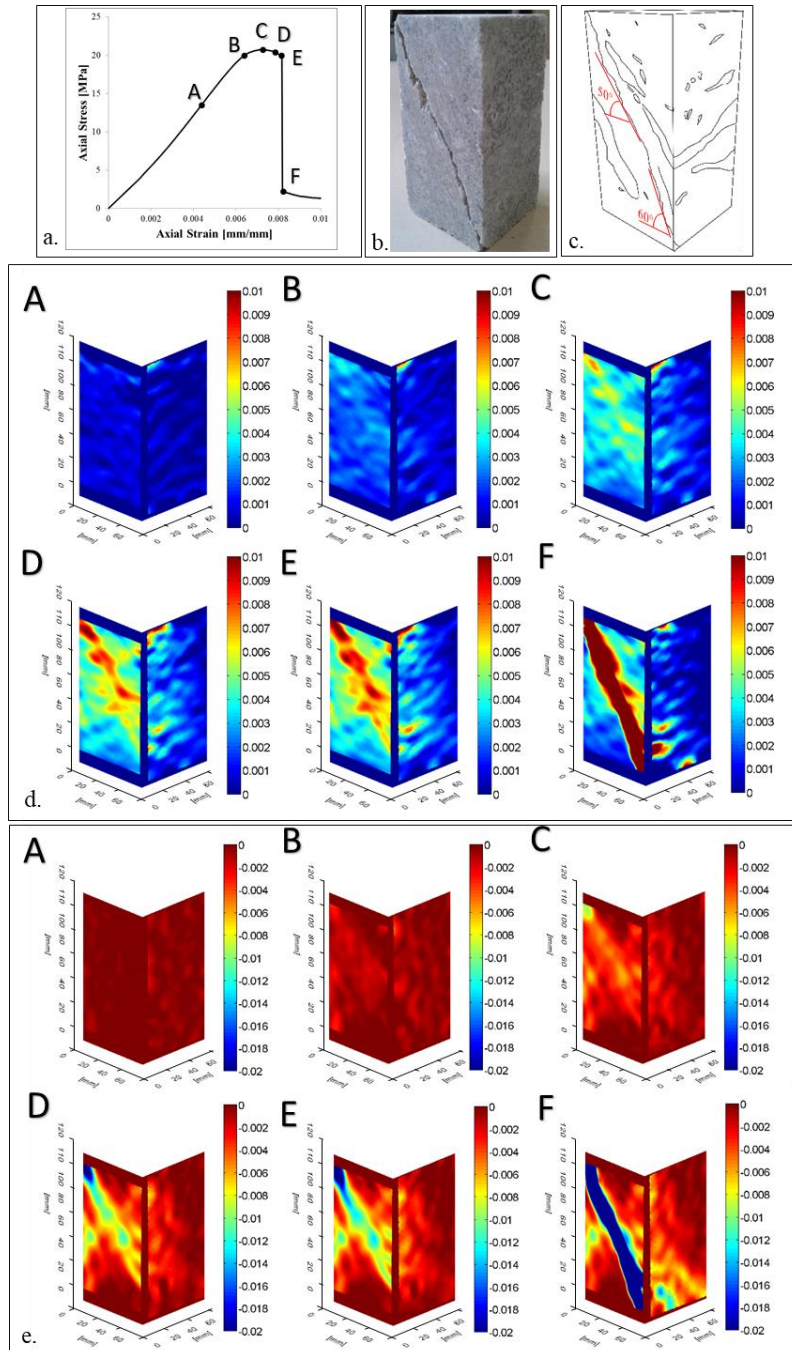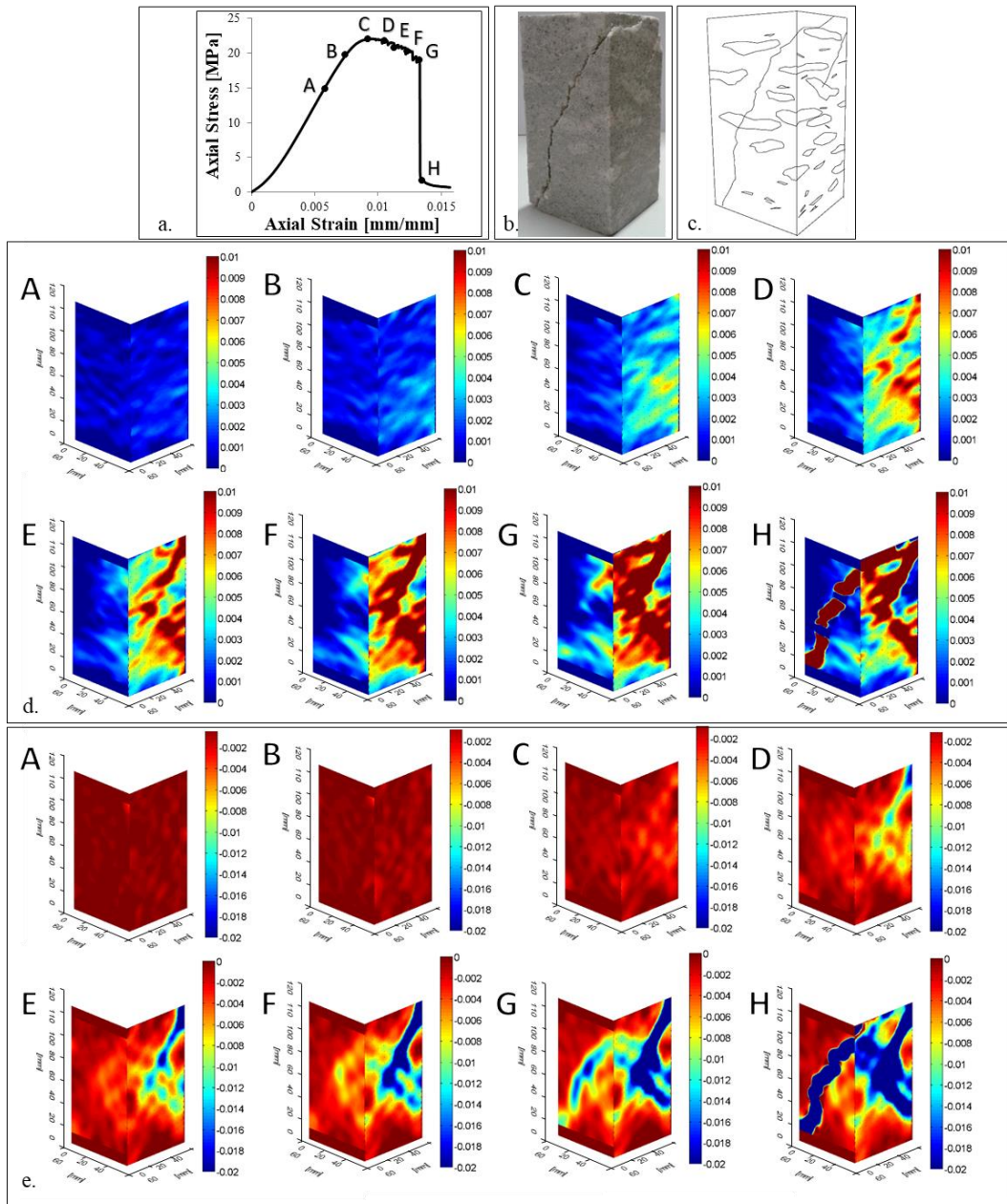
Figure 6.16 Results of DIC analysis on Sample 6: a. Stress-strain curve. b. Post-test sample. c. Schematic representation of failure surface and anisotropic elements. d. Evolution of maps of axial strains during the test. e. Evolution of horizontal strains during the test

Axial deformation maps in Figure 6.16d, in correspondence of points F-G-H, clearly show the presence of a horizontal concentration of strains in the lower right part of the left face. This element, better highlighted in Figure 6.17a, is concord with the texture of the material. The photographic image of the post-failure sample (Figure

6.17b) shows, indeed, a structure (fine layer surrounding a nodule of gypsum crystals) in the same position of this strain concentration.

Something similar can be recognized in the analysis of *Sample* 1 (Figure 6.17c-d). In this case, the map of axial strains describes, in addition to the failure surface, the presence of a sub-horizontal crack that reproduces the shape and orientation of the layering of the rock. In the same position, the post-failure sample shows the presence of a sub-horizontal crack (Figure 6.17d), suggesting a process of failure along the horizontal anisotropy.
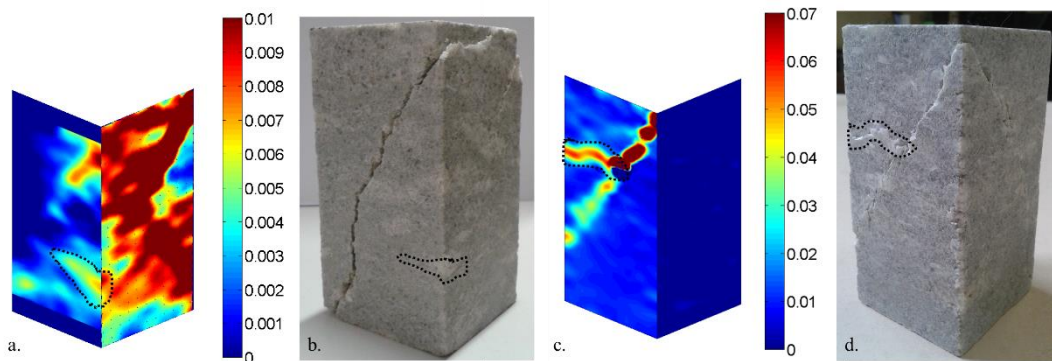
Figure 6.17 Correspondence of strain concentrations with the textures and structures of the samples a-b Final map of axial strains and corresponding photographic image of Sample 6 c-d Final map of axial strains and corresponding photographic image of Sample 1

A texture/structure control of the deformation and failure is evident for all the analysed samples. The position and orientation of nodules and gypsum crystals always influences the position and orientation of the first strain localizations and the process of crack coalescence.

6.5.3 DIC analysis and failure coalescence by step-wise unstable crack growth

As already noticed, several stress drops characterize the post-peak stress-strain behaviour of samples with horizontal anisotropy (both in uniaxial and triaxial loading conditions). This kind of behaviour was analysed considering the DIC results on *Sample* 1. This sample was deformed with a slower strain rate, allowing for a more detailed analysis of the results. For the present application, the elaboration was started at a strain of 0.8% (i.e. in correspondence of the onset point), to avoid the noise produced by the elastic deformation phase and focalize the analysis on the failure coalescence.

Figure 6.18 shows the maps of lateral strains obtained with DIC analysis in correspondence of the stress drops. Each line of the Figure reports three images before and three images after the drop. The stress-strain graphs show the correspondent position of the drops.

The image shows a step-wise propagation of the crack coalescence: in each line, a sudden advancement of the failure is registered in correspondence of the stress drop. The three images before the drop and after the drop are almost identical and only at the moment of the drop itself the failure coalescence has a new step.

This kind of behaviour is consistent for all the duration of the strain softening, suggesting a mechanism of stepping-coalescence of the failure surface.

Figure 6.18d refers to the biggest stress drop registered. It marks a change in the curve slope, starting a phase of faster strength degradation. This crucial point of the stress-strain path corresponds to the complete development of the failure surface that, in the last step in Figure 6.18d, connects the two sides of the sample.
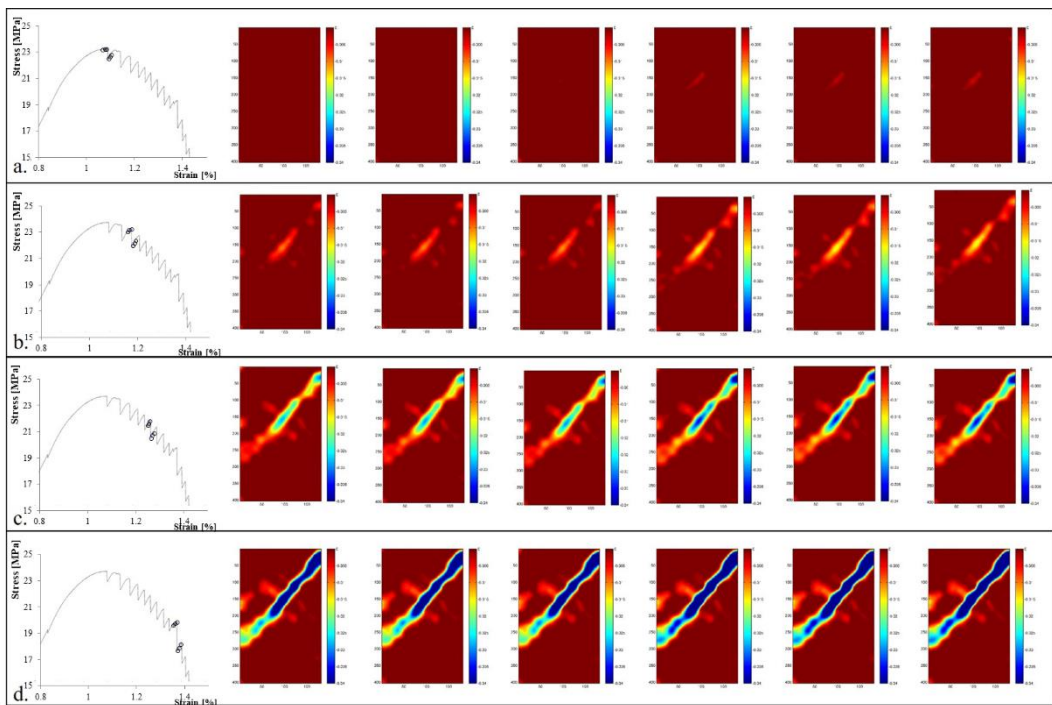
Figure 6.18 Step-wise failure coalescence registered with DIC analysis. Each line reports six maps of lateral strains. The position of the maps is shown by the dots in the stress-strain graphs a. First stress drop, with the first evidence of a crack. b. Accretion of the failure surface. c. Coalescence of two failure edges in the upper part of the sample. d. Complete coalescence of the failure on the entire surface of the sample.

6.5.4 Evolution of microstructures with the confining pressure

As already said, the evolution of strain accommodation in triaxial samples could not be performed with DIC analysis for the visual inaccessibility of the samples during the tests. The analysis was therefore performed with the microstructural analysis of post-test samples.

Three thin sections were obtained from the central portions of *Samples* d, e and g (dashed rectangles in Figure 6.9). These samples were selected with the aim to represent the three typologies of deformation observed in the post-test triaxial samples at the macroscale: single fracture, diffuse conjugate fracturing and absence of fracturing with barrel shape (corresponding to confining pressures of 4, 6 and 8 MPa respectively).
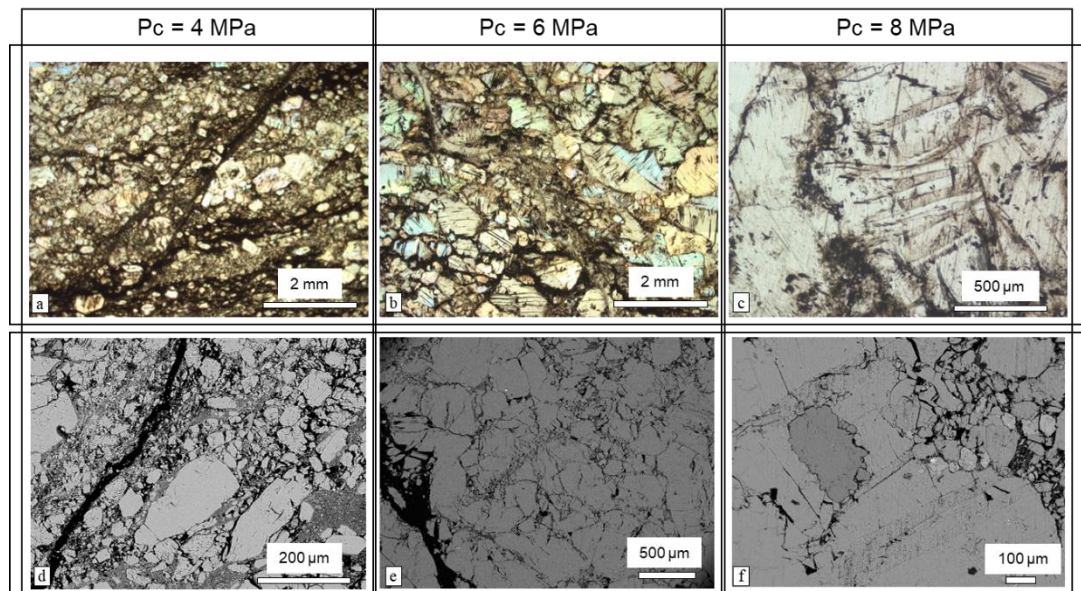
Figure 6.19 a. Failure surface in Sample d at optical microscope. b. Failure surface in Sample e at optical microscope. c. Intra-crystalline plastic deformation in Sample g at optical microscope. d. Failure surface in Sample d at SEM. e. Failure surface and conjugate structure in Sample e at SEM. c. Intra-crystalline deformation in Sample g at SEM.

The analysis of the microstructures confirms that the introduction of a confining pressure does not inhibit the possibility of a failure coalescence. Up to a confining pressure of 6 MPa, a clear failure surface is recognizable in the samples, not only at the mesoscale, but also at the microscale. The images in Figure 6.19 show a summary of the most significant features in both optical microscope and SEM. Both *Sample* d and *Sample* e (Pc = 4 MPa and Pc = 6 MPa respectively) show the clear presence of an open failure (Figure 6.19a-b-d-e). From the SEM imaging of *Sample* e, however,

the further presence of an incipient structure, oriented as a conjugate, can be identified (Figure 6.19e).

At a microscopic insight, the failure surfaces appear to be accompanied by a larger deformation area, consisting of crashed grains, as highlighted in the micrograph in Figure 6.20c. The phenomenon of grain crashing, however, is not only localized along the failure surface, but also interests other portions of the rock. As instance, Figure 6.20a shows an intense crashing phenomenon on a gypsum crystal that has a left edge that gradually turns into fine-grained crashed gypsum. Similar evidences characterize several portions of the samples and seem to be particularly concentrated in the finer layers of the rock, in accordance with the sub-horizontal cracks observed in the uniaxial samples (see Figure 6.17).

Besides the presence of brittle deformation (explicated in form of failure surface), the sample deformed at Pc = 4 MPa shows some evidences of a plastic intra-crystalline deformation (e.g. Figure 6.20b).
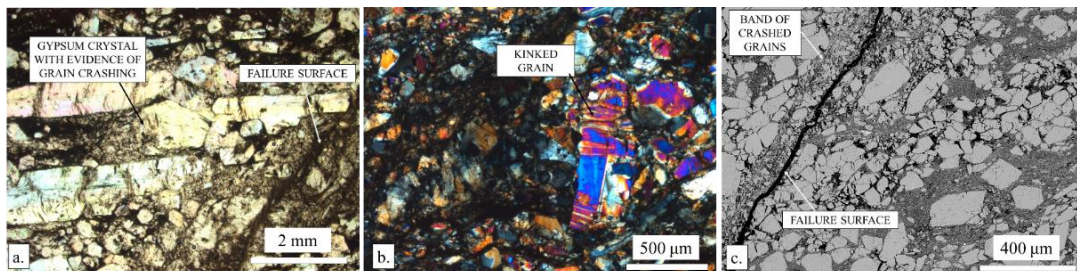
Figure 6.20 Micrographs of Sample d (Pc = 4 MPa) a. Failure surface and evidences of grain crashing at optical microscope in reflected light. b. Kinked grain, in optical microscope with crossed nicols. c. Failure surface, observed at the SEM.

At Pc = 6 MPa (*Sample* e), the brittle regime is still the principal mode of strain accommodation, with the presence of a well-defined failure surface (Figure 6.21a). However, as shown in Figure 6.19e, the thin section reveals the additional presence of a conjugate structure. The central part of this structure (Figure 6.21b) consists of a diffuse fracturing that creates a zone of crashed grains. This central band is accompanied by a larger area of fracturing that helps in the accommodation of the relative displacement of the upper and the lower portions of material.

In this sample, the presence of intra-crystalline plastic structures becomes more evident. As shown in Figure 6.21c, the crystals appear to be deformed for the effect of a kink folding, i.e. a folding mechanism with straight limbs and pointed hinges that is usually associated to materials with a fine, regular layering. In the present framework, the regular layering corresponds to the mineral cleavage along the (010)

crystallographic direction. As described in Chapter 2, this cleavage reproduces the sandwiched crystallographic structure of gypsum, with an alternation of sheets of Ca^{2+} and $(SO_4)^{2-}$ ions and double-sheets of water molecules. The weakness of the water-water chemical bonds favours the formation of the mineral cleavage.
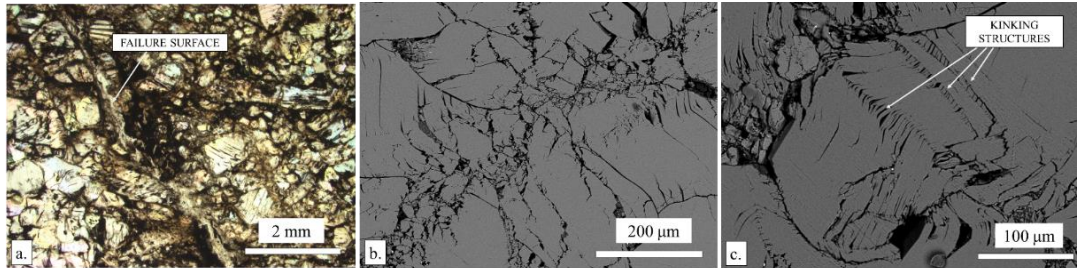
Figure 6.21 Micrographs of Sample e (Pc = 6 MPa) a. Failure surface, observed at optical microscope in reflected light. b. Shear band oriented as a conjugate, observed at the SEM c. Kinked grain at the SEM

In *Sample* g (Pc = 8 MPa), the presence of kinked grains becomes the principal effect of strain accommodation. Even if the evidences of brittle deformation can be still recognized in form of a diffuse fracturing, the microscope analysis confirms the absence of a failure surface in this sample. The kinking structures involve the majority of big gypsum crystals (Figure 6.22a-b). It is possible to notice, however, a preferential concentration of these structures on gypsum crystals oriented in vertical direction (i.e. with the cleavage planes parallel to the principal stress σ1). This confirms the connection between the kinking and the mineral cleavage.
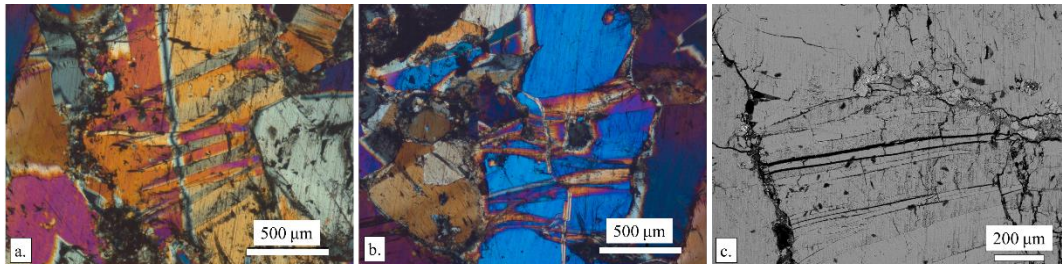
Figure 6.22 Micrographs of Sample g (Pc = 8 MPa) a. Kinked grain, in optical microscope with crossed nicols. b. The presence, in the middle of the gypsum crystal, of a quartz grain, intensifies the complexity of the kinking structures (optical microscope with crossed nicols) c. Gypsum crystal with kinking structure and sharp cracks along the kink borders, observed at the SEM.

The presence of kinked grains can be easily recognized with the optical microscope at crossed nicols, since the change in orientation of the crystal implies a change in the interference colour and in the other mineralogical features (e.g. relief). These differences may suggest a phenomenon of phase transition (e.g. dehydration) due to the effect of compression. In order to verify this hypothesis, a punctual analysis with micro-raman spectroscopy was performed on the main gypsum crystals and on the

kinked bands. The results (Figure 6.23) show perfect homology of phase, excluding the possibility of a compression-induced dehydration process.
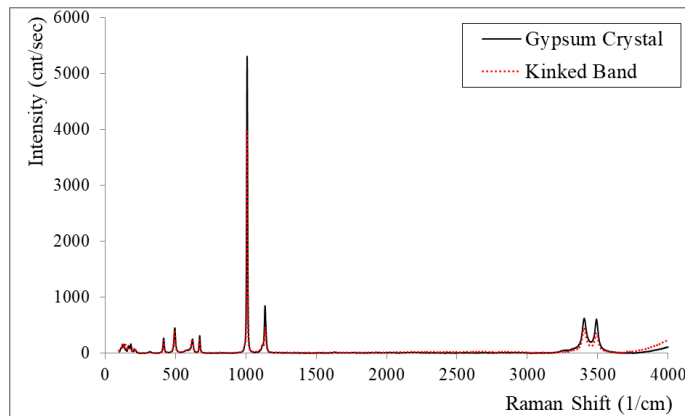
Figure 6. 23 Micro-raman spectra for gypsum crystals and kinked bands

Brantut et al., 2011, who observed similar structures in triaxially loaded samples of Volterra gypsum, suggested that the kinking mechanism is a hardening mechanism: after a certain amount of strain, the energy needed to further deform a specific grain becomes larger than the energy needed to start to deform a new grain. This is coherent with the transition of behaviour from strain softening to strain hardening observed in the mechanical tests.

As a confirmation of this idea, Figure 6.22c proposes the SEM micrograph of a kinked grain with sharp cracks along the boundaries of the kink bands. This evidence seems to suggest that each gypsum crystal can accommodate with plastic kinking only a certain amount of strain. The further increase of deformation on that specific grain brings to failure. If the kinking process exploits the weak chemical bonding among water molecules of the crystallographic structure, the failure of the crystals necessarily implies the involvement of the salt structure (ionic bond between Ca^{2+} and $(SO_4)^{2-}$ ions), requiring an higher level of energy.

6.6 Discussion of the results

Results of DIC analysis showed the strict control of textural properties and, in particular, of the anisotropic layering on the strain accommodation and crack coalescence of branching selenite gypsum. With a layering orientation perpendicular to the axial applied stress (i.e. horizontal anisotropy), the presence of strain localizations or even cracks was recognized along the fine-grained layers, despite their unfavourable orientation to failure coalescence. On the other hand, intermediate angles of anisotropy, being orientated almost parallel to the final angle of crack, were

observed to facilitate the failure coalescence, reducing the bulk strength of the material.

The investigation of two perpendicular faces of the prismatic samples allowed for a three-dimensional description of strain evolution, particularly important for the non-homogeneous and anisotropic character of the material. This approach allowed to describe, in samples with horizontal anisotropy, the easier failure propagation in parallel direction to the linear preferential orientation defined by the gypsum crystals and nodules.

In addition, the DIC results highlighted, in the samples with horizontal anisotropy, the presence of a stepping coalescence of the failure surface, that well relates with the record of stress drops in the stress-strain curves, suggesting the existence of a step-wise unstable crack growth.

A similar stress-drop unstable post-peak behaviour was registered also in presence of a lateral confinement. Considering also the stability of failure angle (i.e. about 60° despite the increase in confining pressure) a substantial similarity of crack mechanism can be imagined.

However, a wide increase in axial strain was registered in the mechanical tests with the introduction of a confining pressure. This can be explained considering the appearance of an intra-crystalline plastic strain mechanisms (i.e. the "kinking" of the grains). The effect of the lateral confinement seems, therefore, to activate plastic mechanisms that dissipate the energy that would otherwise be used to coalesce new cracks. With the increase of confining pressure, the plastic mechanisms became energetically more advantageous, while the possibility to open and coalesce tensional cracks is disadvantaged.

Chapter 7

Time dependent behaviour and water saturation

In underground quarry environments, static loading conditions act on the gypsum pillars for the entire duration of the active exploitation. Depending on the recovery plan, the axial load may be maintained also after the end of the exploitation operations, for several decades. The short-term strength of the rock, evaluated in Chapters 5 and 6, can only be referred to the possibility of a failure in consequence to the sudden application of the axial load. The assessment of stability conditions in the short-term does not preclude the possibility of deformation or even failure in the long-term.

In addition, as already introduced, the drifts of gypsum quarries are often located below the static level of the groundwater table, requiring a continuous water pumping

to allow for the accessibility of the drifts themselves. The end of the quarry activity will coincide with the interruption of the de-watering operations and the re-assessment of the original level of water table. Water will saturate the gypsum body, filling the connected porosity of the rock and influencing the general stability of the quarry.

For these reasons, the present Chapter aims to investigate the mechanical response of branching selenite gypsum in time-dependent regime, also considering the influence of water saturation. As for Chapter 6, with the aim to minimize the sample variability and to favour the test repeatability, only A-type gypsum was considered and the homogeneity among the samples was assured as much as possible.

7.1 Introduction

The existence of a time-dependent sub-critical cracking process, alternative to the classical fracturing propagation due to the application of stress, has been observed for all rock types (Brantut et al., 2013). This kind of time-dependent behaviour may allow the rock to deform and fail at stress levels lower than the peak ones, as exemplified by the phenomenon of creep (i.e. the deformation over time, and possible failure of samples, under the application of a prolonged constant stress lower than the peak strength). An high sensitivity of creep strain rates and failure times to environmental conditions (e.g. differential stress, confining pressure, temperature and pore fluid composition) have been observed by many authors (e.g. Brantut et al., 2013, 2012; Gasc-Barbier et al., 2004; Heap et al., 2009). In particular, salt rocks are particularly sensitive to the influence of water. In gypsum, not only the creep response (e.g. de Meer and Spiers, 1999, 1997, 1995) but also the time-independent strength (e.g. Liang et al., 2012; Yilmaz, 2010; Zhu et al., 2019) have often been observed to depend on the presence of water.

The present Chapter aims to propose a description of the influence of water on the mechanical response of branching selenite gypsum, distinguishing between the general effects of a saturating fluid (e.g. internal pore pressure, which could also be observed with a non-reactive fluid such as oil) and the water-gypsum chemical interactions. Hence, tests are performed in dry, kerdane-saturated (i.e. oil-saturated) and water-saturated conditions. The investigation includes uniaxial compression tests, uniaxial creep tests and conventional triaxial tests. The mechanical results are accompanied by microstructural data on the effects induced in the rock by the mechanical compression, aiming to propose a description of the mechanisms involved in the gypsum deformation process.

7.2 Tested Samples

Mechanical tests were performed on a group of 77 cylindrical specimens (height: 40 mm; diameter: 20 mm), re-sampled from two bigger core pieces. The original cores, in coherence with the tested material described in Chapter 5, have a diameter of 80

mm and macroscopic features typical of A-type material. Both the core pieces come from the same axial drilling. The geometrical proximity assures, therefore, a certain textural and compositional homogeneity.

Helium-Pycnometer porosity was measured for all the 77 specimens. The complete dataset of measured and derived physical properties (i.e. sizes, dry mass, He-pycnometer volume, solid density, bulk density, porosity) can be found in the Annex 7.1. Porosity and bulk density values are summarized in Figure 7.1. The measured porosity ranges between 3.35% and 9.82%. The Figure also provides an evaluation of mineralogical composition in terms of ratio among porosity and bulk density (that, if the open porosity is neglected, only depends on the solid density). The existence of a good linear trend, with low dispersion, confirms the good compositional homogeneity of the dataset.
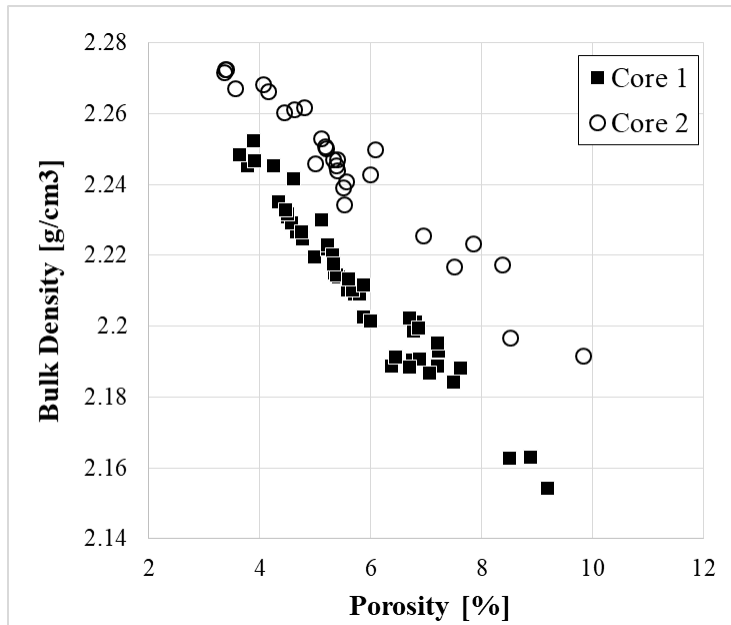
Figure 7.1 Measurements of porosity against bulk density in the 77 samples. The low dispersion of the data suggests a good compositional homogeneity of samples from Core 1 and Core 2 respectively.

7.2.1 Water saturation

Due to the high solubility of gypsum, the stability of testing conditions and the long-term equilibrium are difficult to be assured for water saturation. The very fast dissolution rates of samples saturated with distilled water suggested to look for less aggressive water solutions. A first attempt was made with commercial water (i.e. Volvic water), which known salt concentration could be useful to have repeatable test conditions. However, also in this case, the dissolution rate (monitored through the measure of electrical conductivity of the water containing the samples) was very high: the electrical conductivity increased by a factor 10 in 2 days. Therefore, a

specific saturation process with a gypsum-oversaturated solution was tested. Distilled water was enriched with gypsum powder and gypsum waste samples were left in the solution for long times (i.e. up to several months), monitoring the electrical conductivity. After 10 days, a stable value of 1.8 mS/cm was obtained. This solution, a priori at equilibrium, was then used to saturate the samples. Samples were left in water for a period of at least two weeks. The conductivity, monitored throughout the saturation period, remained stable at 1.8 mS/cm.

To legitimate the use of this solution for the mechanical tests, Figure 7.2 proposes the comparison of curves from uniaxial compression tests on gypsum samples saturated in Volvic water and in gypsum over-saturated solution respectively. The substantial analogy between the results confirms that the effect of the two kinds of water can be considered equivalent. Therefore, all the tests reported henceforth are performed with the gypsum-saturated water solution.
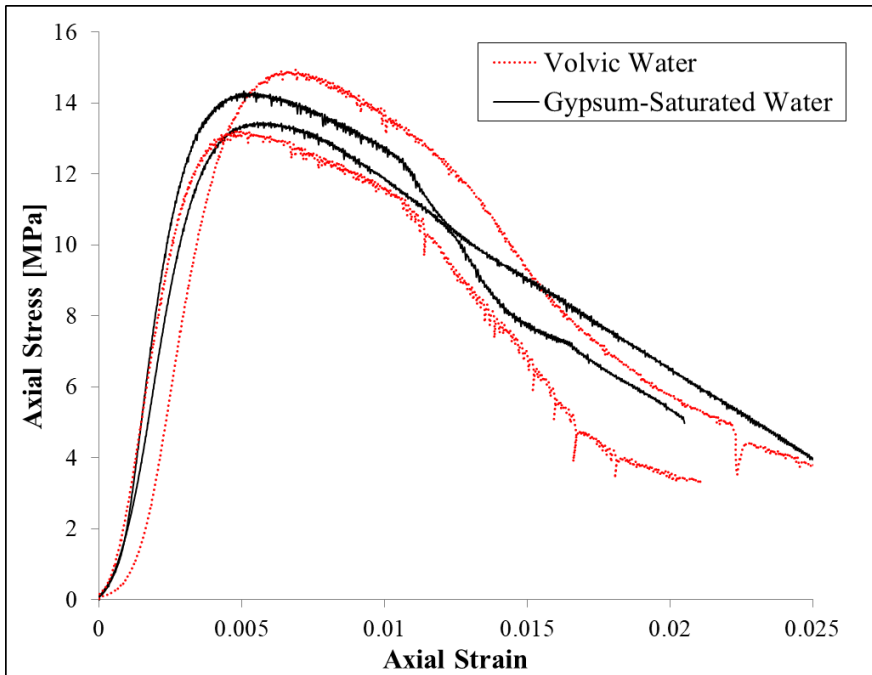
Figure 7.2 Comparison of results of uniaxial compression tests on samples saturated with Volvic water and with gypsum over-saturated solution respectively. The similarity among the curves legitimate the use of gypsum over-saturated solution for the mechanical characterization.

7.2.2. Kerdane saturation

As said, the proposed experimental program also includes the compression of oil-saturated samples, aiming to exploit the inert reaction between gypsum and an a-polar fluid. Despite the absence of a dissolution process, the saturation with Kerdane (i.e. a bright-yellow de-aromatised oil) produced an intense red colouration on the surface of the samples (Figure 7.3a). This red colouration was particularly

concentrated along the thin-grained layers of the branching selenite structure and could not be completely eliminated by the simple environmental-conditions evaporations, as testify by Figure 7.3b (after a period of about one month). In order to understand the reasons for this colouration, SEM-EDS compositional maps were performed in correspondence of the most intense red-colouration areas (Figure 7.3c). In coherence with the analyses presented in Chapter 4, the resulting maps show the presence of big crystals (in Figure 7.3c, Gypsum in green, Celestine in orange and finer carbonate minerals in blue) surrounded by a finer matrix, with a main siliceous composition (in red in the map in Figure 7.3c). The red colouration areas in the macroscopic samples are in correspondence of this siliceous matrix of the rock. A punctual analysis of small grains composing this fine siliceous material returned a composition of Si, Al, Mg, Na and minor K and Fe (e.g. Figure 7.3c), that can be associated to a multi-layered clay mineral. Since, as documented in Chapter 4, the clay minerals in branching selenite gypsum may contain a certain percentage of Smectite (i.e. swelling clay), the red colouration can be considered as the effect of the absorption of Kerdane oil in the swelling structure. Known that the collapse temperature of swelling clay minerals is 350°C, the Kerdane-saturated sample was heated in oven at this temperature. At the end of the heating treatment, the red portions of the sample turned to black, confirming an expulsion of the red/Kerdane due to the collapse of the clay structure. The high temperature had also the obvious side effect to dehydrate gypsum crystals, that turned into white anhydrite minerals (Figure 7.3e).
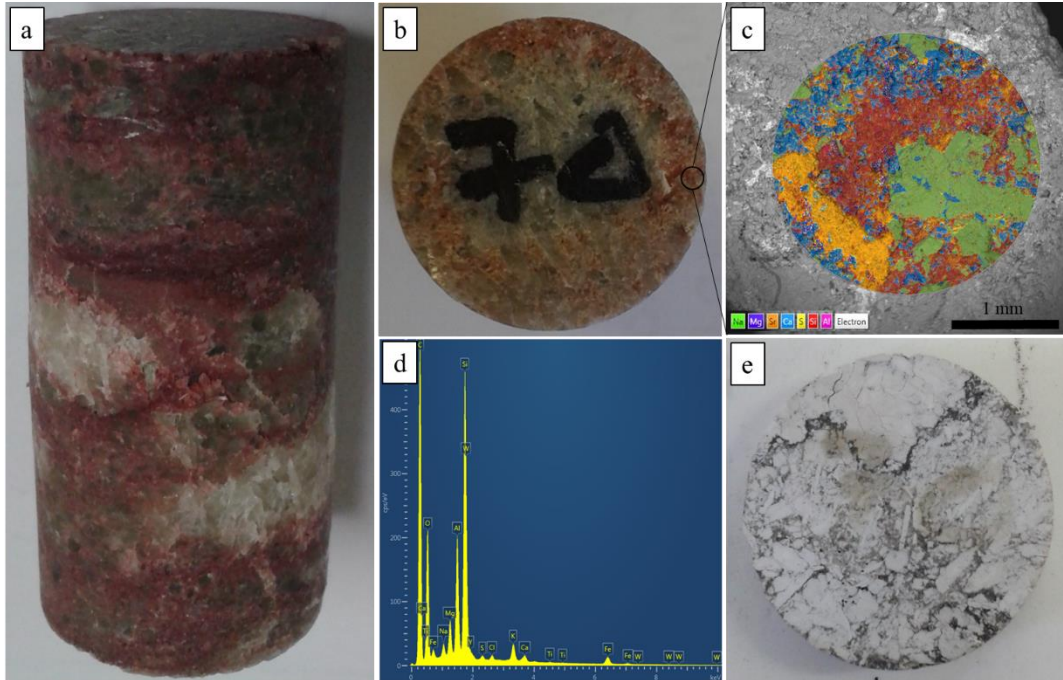
Figure 7.3 a. Red colouration of Kerdane-saturated gypsum sample immediately after the compression test. b. Red colouration of Kerdane-saturated gypsum sample after one month c. SEM-EDS compositional map of red portions. The green portions correspond to gypsum (Ca + S), the orange portions to celestine (Sr + S), blue crystals are carbonate minerals (mainly Ca), while red portions are the thin-grained matrix of the rock (corresponding to main Si and Al, with minor S, Sr and N) d. Punctual SEM-EDS analysis of red portions. e. Kerdane-saturated gypsum sample in Figure 7.3b after heating at temperature of 350°C

7.3 Testing methodologies
7.3.1 Uniaxial loading conditions

Uniaxial tests were performed with a servo-controlled mechanical press. Axial displacements were measured throughout the test with an LVDT sensor. Strain rates in a range between 10^{-4} and 10^{-8} s^{-1} were used in order to investigate the time-dependent behaviour of the material.

To complete the information about the time-dependent strain response, a series of creep tests was additionally performed, with the same servo-controlled mechanical press, imposing the constant stress conditions over time as zero stress-rate.

Due to the considerable variability registered in uniaxial strength, the stress level of the creep tests was established on the basis of stress-strain curve shape. Traditional uniaxial strength tests were performed under strain-rate control until the end of the linear elastic portion of the curve (i.e. onset point). Tests were then stopped, imposing the stress values correspondent to the onset point as constant stress.

As shown in Figure 7.4, both step-wise creep tests and 'complete' creep tests were performed. In the former, an initial lower stress level was chosen. In each step, stress

was maintained constant until the observation of steady-state conditions. At the end of each step, stress was increased by 1 MPa, until the failure of the sample. In the latter, the chosen stress was maintained constant until the acceleration of strain rate leaded to the creep failure.
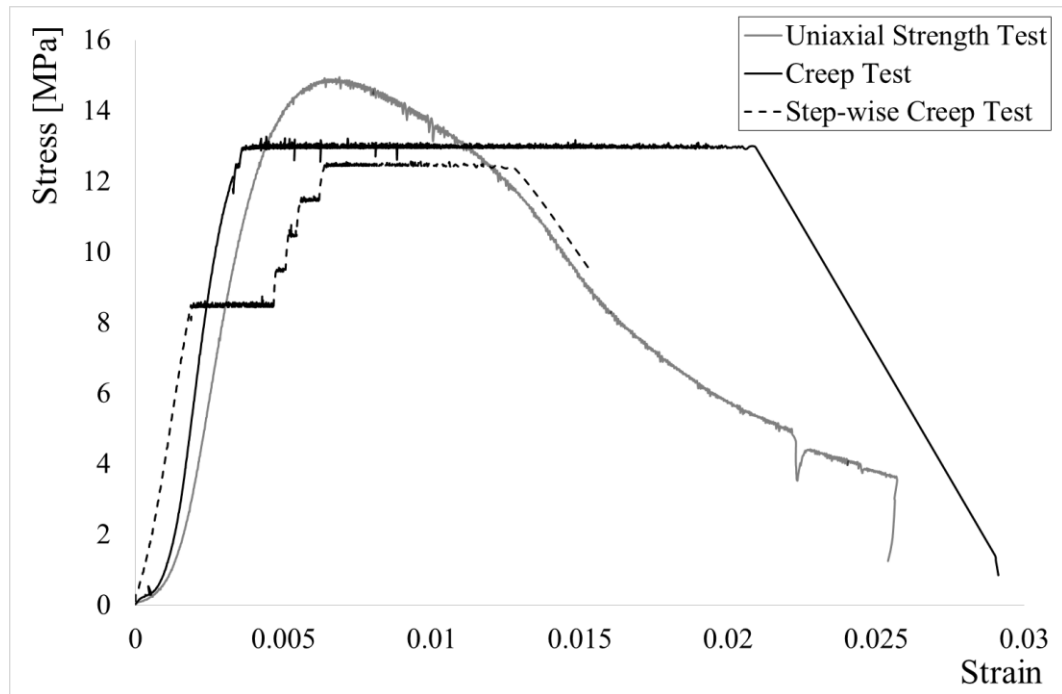
Figure 7.4 Comparison of typical stress-strain paths of uniaxial strength tests, "complete" creep tests and step-wise creep tests.

As previously mentioned, tests were performed in dry and saturated conditions. Dry conditions were obtained keeping the samples in vacuum at a temperature of 40°C before the test. Saturated tests (both Kerdane-saturated and water-saturated) were performed after a saturation period of at least two weeks. The saturation was then maintained throughout the test, performed within a recipient filled with the saturating fluid, as shown in Figure 7.5.
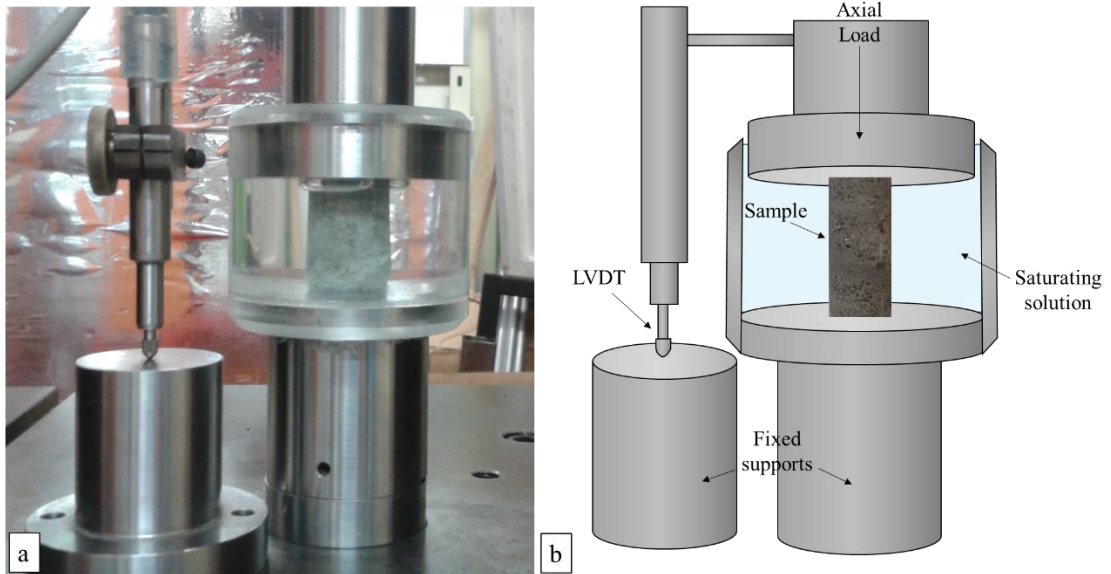
Figure 7.5 Photographical image (a) and scheme (b) of the uniaxial tests set-up

7.3.2 Triaxial loading conditions

Triaxial tests were conducted in a servo-controlled triaxial cell. The tests started with the initial imposition of the confining pressure with hydrostatic loading path. The axial stress was then increased with a constant strain rate of $10^{-5}s^{-1}$. Axial displacement, axial load and confining pressure were registered throughout the tests. Additionally, information about the volumetric strain was obtained by comparing the initial volume of the sample with the in-continuum measure of the changes of oil volume in the cell.

The gypsum over-saturated water solution is unsuitable to be used in the drainage water circuit of a triaxial cell, for the possibility of gypsum precipitation in the pipes and serious damages to the machine. Therefore, the water influence on the triaxial mechanical response was tested in undrained conditions with partially de-saturated samples.

Samples were initially saturated with the gypsum-water solution. Then, before the tests, the to-be-tested sample was removed from the receipt of the water solution and water was allowed to evaporate. The weight of the sample was constantly monitored until a quantity of about 25% of the total water in the pores was evaporated. At that moment (with a water saturation of 75%), the sample was introduced in the equipment for the triaxial test. In this way, the development of over-pressure conditions in the undrained triaxial cell should be inhibit, since the volumetric compression of the material is lower than the available 25%.

The correspondence of mechanical conditions of samples with 100% saturation and 75% saturation was verified in the uniaxial test. As shown in Figure 7.6, stress-strain curves are comparable. However, if the de-saturation percentage becomes too high (e.g. 50%), the correspondence of mechanical behaviour could not be completely assured.
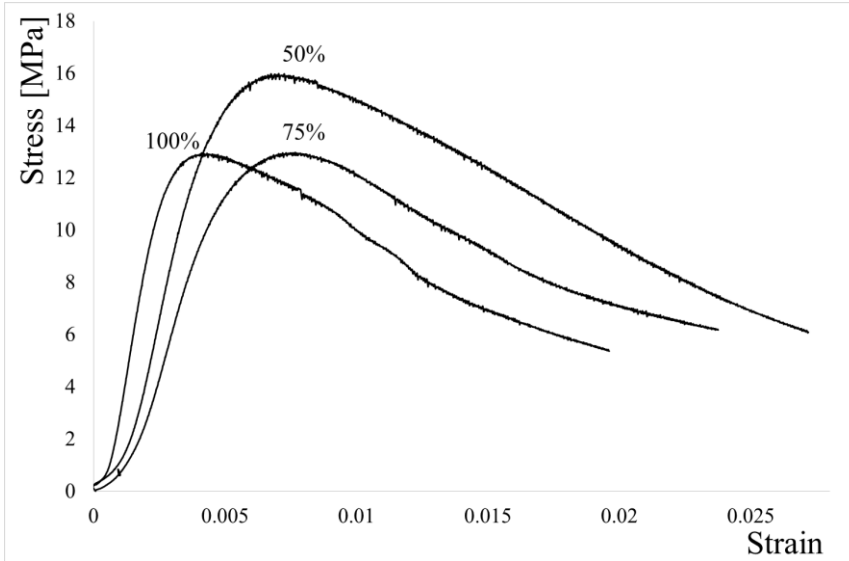
Figure 7.6 Stress-strain curves of uniaxial compression tests under 100%, 75% and 50% saturation conditions.

7.4 Experimental Results
7.4.1   Uniaxial loading conditions
Figure 7.7a shows representative stress-strain curves of dry, water-saturated and oil-saturated uniaxial tests with standard strain rate ($10^{-5}s^{-1}$). The graph attests a strength decrease of about 50% from dry to water-saturated conditions (i.e. from 25 MPa to 12 MPa), while the oil-saturated samples are in a strength range that is intermediate between dry and water-saturated (around 20 MPa). The strain value in correspondence of the peak strength remains unchanged in the different tests (about 0.4%). As a consequence, a clear decrease in Young Modulus follows the water saturation and, to a lesser extent, the oil saturation.

Aside from the strength differences, the most evident change can be observed in the post-peak phase of the stress-strain curves. In dry conditions, in coherence with the behaviour described in Chapter 6, the post-peak deformation is driven by frequent stress drops. The stress losses are, however, quickly recovered and the general trend of the post-peak describes a well-defined softening curve. Despite the difference in strength, the stress-strain curves of Kerdane-saturated samples are similar to dry tests, with several stress drops and a sharp softening. On the other hand, this kind of unstable stress-drop behaviour is not observed in water-saturated samples, where the softening trend is continuous. In addition, the strain softening in water-saturated

samples is slower, with a longer phase of stress stability (or slow stress decrease) after the peak strength.

The totality of dry and water-saturated uniaxial tests is summarized in Figure 7.7b, where strength results are plotted against porosity. The graph defines an inverse linear trend in water-saturated conditions, with a general decrease of strength with the increasing porosity. On the other hand, strength-porosity trend for dry samples is less clear. Considering that all the dry samples reported in Figure 7.7b come from Core 1 (i.e. have a good compositional homogeneity, following Figure 7.1), the high dispersion of strength values should be imputed to other factors (e.g. grain size or typology and orientation of branching layering, as discussed in Chapters 5 and 6).
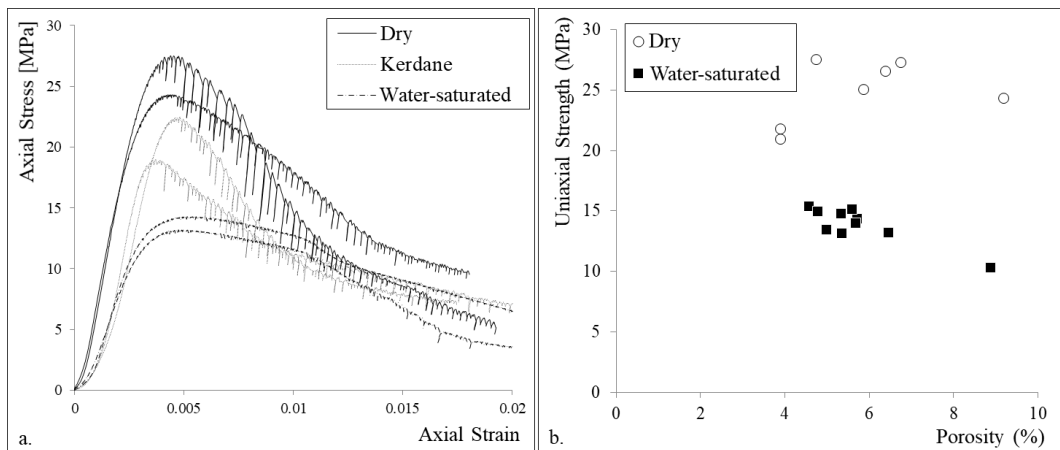
Figure 7.7 a. Stress-strain curves of uniaxial compression tests in dry, oil-saturated and water-saturated conditions. b. Peak strength against porosity of uniaxial tests in dry and water-saturated conditions

The effect of strain rate on the stress-strain curves is evaluated in Figure 7.8 that shows the results of oil-saturated and water-saturated uniaxial tests with strain rates ranging between 10^{-4} and 10^{-8} s^{-1}.

In oil-saturated conditions (Figure 7.8a) the change of strain rate does not imply significant variations in the stress-strain behaviour: strength range, softening behaviour and stress-drops in the post peak remain substantially unchanged in all the curves.

On the other hand, the decrease of strain rate has a significant influence on the results of water-saturated tests (Figure 7.8b). Strain rates of 10^{-7} and 10^{-8} s^{-1} result in a decrease in peak strength and, particularly, in the loss of the clear softening behaviour recoded in all the other test conditions. When the tests were stopped (measured strain higher than 1.5%), no evidence of strength decrease in the post-peak had yet been registered.
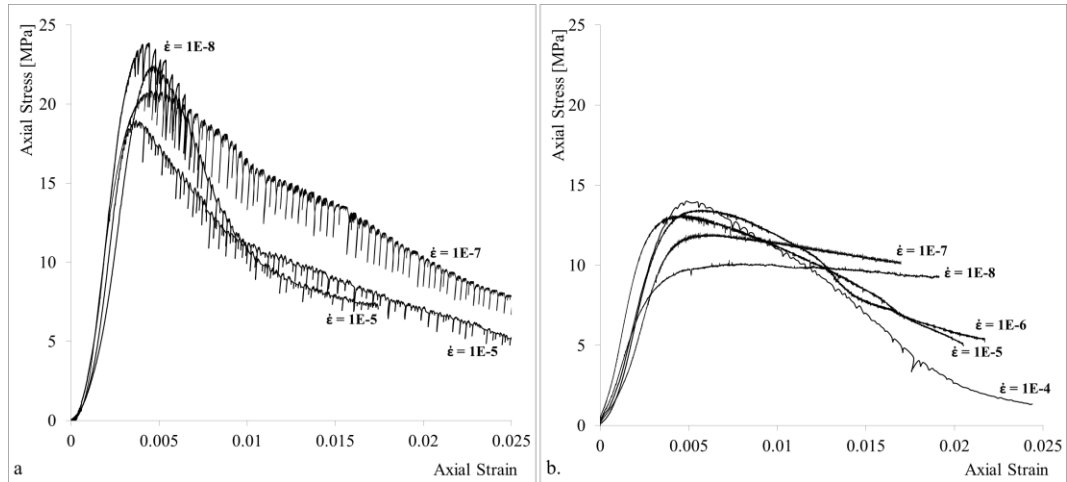
Figure 7.8 Strain rate effect on gypsum samples saturated in Kerdane (a) and in water (b) tested in uniaxial compression

A similar dependence of time-dependent behaviour on the saturation conditions can be observed in the results of creep tests. Figure 7.9 shows the time-strain curves of step-wise creep tests in dry, oil-saturated and water-saturated conditions. The stress applied in each step is reported on the Figure. The graph highlights the clear difference in strain rate of dry and kerdane samples, on one side, and water-saturated sample, on the other side. The formers show a substantial absence of creep deformation. The almost totality of measured strain is registered in the first few seconds of each step (i.e. immediately after the application of the stress). This absence of creep is still observed in the last step before the collapse (i.e. with an applied stress less than 1 MPa lower than the material strength). Water-saturated sample, on the other hand, shows a quite elevate strain rate already in the first step. The measured strain-rate increases in each step, up to the accelerated conditions and the final failure of the sample.
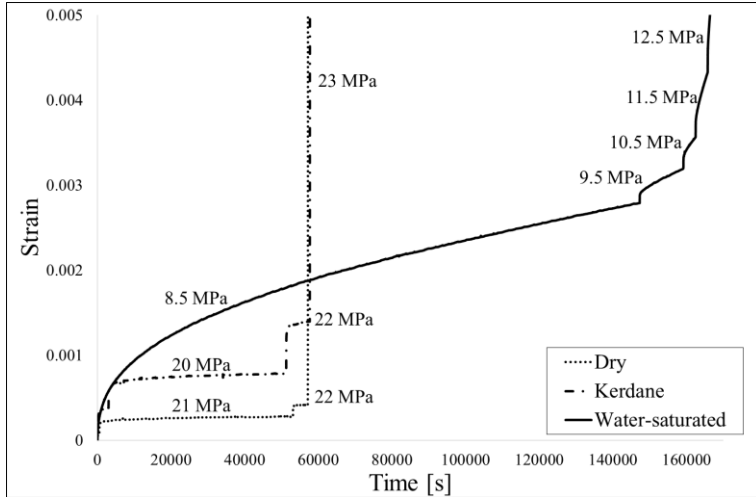
Figure 7.9 Results of step-wise creep tests in dry, oil-saturated and water-saturated conditions

Figure 7.10 summarizes the comparison of all the performed step-wise creep tests. The final strain rates registered in each step are plotted against the correspondent stresses. The graph testifies a good repeatability in the data of water-saturated creep. Despite the sample variability and the consequent horizontal translation (i.e. strength differences), the three data series align regularly along parallel lines. Again, oil-saturated and dry samples stand out for their lower strain rate. At the final step before sample collapse, their strain rate is more than two orders of magnitude lower than the equivalent measure in water-saturated samples.
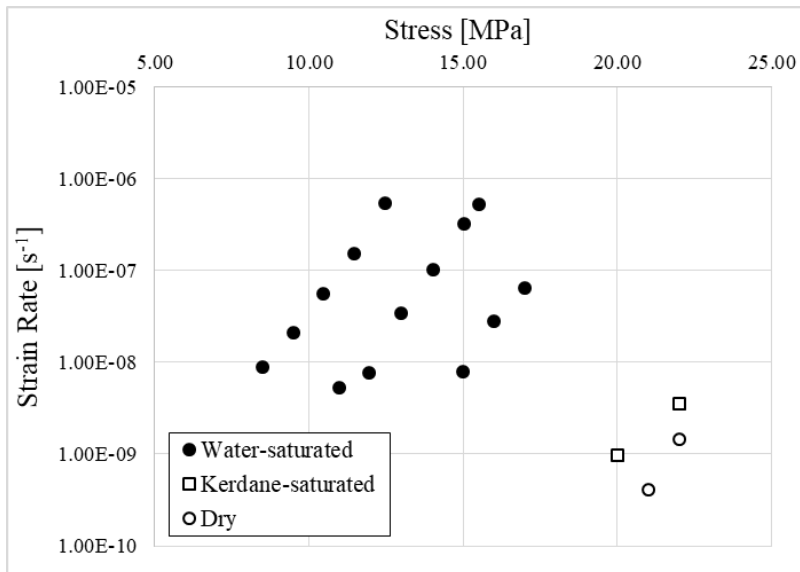
Figure 7.10 Strain-rate vs stress plot of the step-wise creep tests in water-saturated, oil-saturated and dry conditions

125

Figure 7.11 shows the strain-time curves of the 'complete' creep tests performed in water-saturated conditions. All the curves show an initial phase with decreasing strain rate. The strain rate continues to slightly decrease until it reaches a minumum rate. Then, a trend inversion is observed, with an increase of strain rate, that progressivly accelerates until the complete verticalization of the curve (i.e. sample collapse).
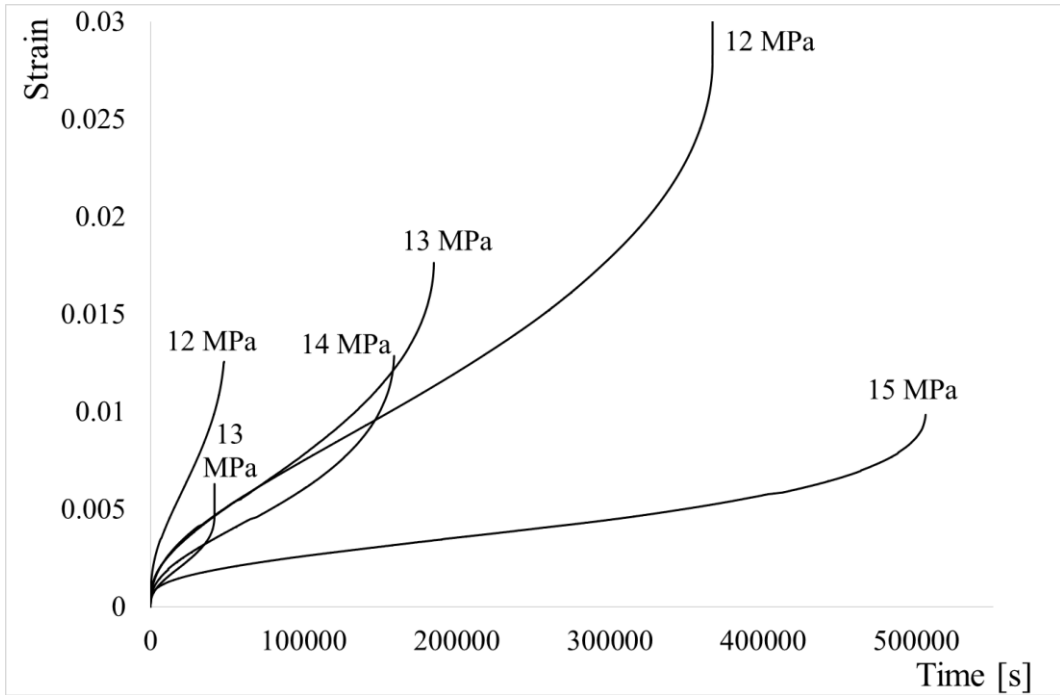
Figure 7.11 Strain-time curves obtained in the creep tests in water-saturated conditions. For each curve, the creep stress is reported.

The data suggest a general inverse linear trend between measured strain rate and the applied stress (i.e. the sample strength, since the applied stress was calibrated on the position of the elastic onset) (Figure 7.12a). However, the results also show the absence of a clear trend between the strain measured during creep (i.e. plastic strain) and other parameters (e.g. strain rate, applied stress, time of failure), i.e. high creep strains are not univocally related to a lower strain rate or to an higher applied stress (Figure 7.12b). The only relationship was observed with the porosity, as shown in Figure 7.12c. A quite regular linear trend between plastic strain and initial porosity can be observed, suggesting a higher propensity of the material to develop plastic strain for higher initial porosities.
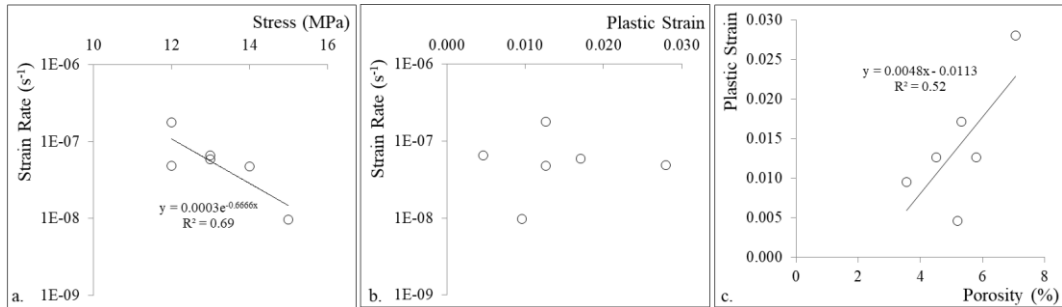
Figure 7.12 Comparison of parameters registered during the creep tests: a. Strain rate against stress; b. Strain rate against plastic strain; c. Plastic strain against sample porosity.

The performed uniaxial tests does not provide a measure of radial strain. Therefore, in order to have an indication on the volumetric behaviour of the material, pre- and post- test porosities of three representative samples were measured. The samples were tested water-saturated in normal strain rate, low strain rate and creep conditions. Tests were stopped in correspondence of early strains, with the aim to observe the behaviour before the complete collapse of the sample produced by a long post-failure deformation (Figure 7.13a).

The porosities were measured with the three-weight method (i.e. dry mass, saturated mass, Archimedes suspended mass). With this method, the possible changes of "geometrical" volume induced by the mechanical tests does not influence the measure.

Even considering a volumetric compression during the elastic phase (i.e. pore closure), the measure of pre- and post-test porosities should allow to distinguish between a clear dilatancy in the post-peak (i.e. opening of tensional cracks) and a general volume decrease, that could be expected with a strain-hardening behaviour (e.g. low strain rate conditions).

Results, reported in Figure 7.13b, highlight an increase of porosity (i.e. volumetric dilatancy) for all the considered situations. The highest dilatancy percentage is registered in correspondence of the "fast" strength test. However, also the test with low strain rate registers a clear increase of porosity (from 4.75% to 5.31%). The creep test, performed with a lower applied stress and stopped in an early stage, show an almost unchanged porosity. Admitting the occurrence of the closure of pores in the early phases of the test, it has to be imagined that during the creep deformation some kind of dilatancy interested the sample.

The existence of a dilatant behaviour in creep conditions in gypsum rock is coherent with the experimental data by Hoxha et al. 2006. Those results showed, indeed, a dilatant behaviour in gypsum samples under creep triaxial compression in presence of high humidity conditions that was considered as an evidence of a damage-like mechanism active in the rock during the creep deformation.
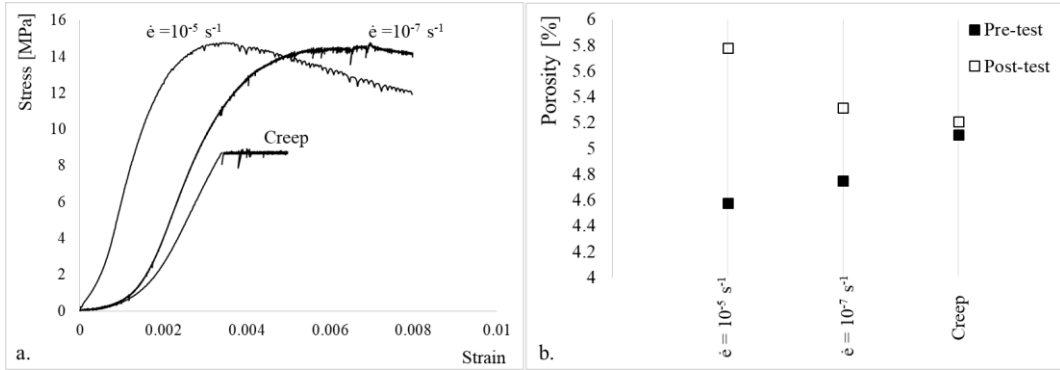
Figure 7.13 a. Stress-strain paths of the samples used for the measure of pre- and post-peak porosities. b. Results of pre- and post-peak porosities measures.

7.4.2   Triaxial loading conditions

Figure 7.14 shows the axial and volumetric strain curves of the triaxial tests in dry (Figures 7.14a) and partially de-saturated conditions (Figure 7.14b). The same curves are re-proposed, as a comparison in Figure 7.14c.

Dry tests (Figures 7.14a) refers to a range of confining pressures from 10 to 100 MPa. Except for sample at Pc=10 MPa, all the curves show a clear strain hardening behaviour. The majority of the tests show, in the hardening part, the presence of stress-drops, similar to the ones observed in uniaxial compression. Despite the strain hardening, the volumetric strain maintains a dilatant character up to very high confining pressures. A dilatancy onset is still observed at Pc=100 MPa.

In presence of water (Figure 7.14b), a clear decrease of strength can be observed for all the considered confining pressures, as testified by the comparison graph in Figure 7.14c. All the curves in the pressure range (between 10 and 80 MPa) describe clear strain hardening and dilatancy. However, in analogy with the behaviour observed for uniaxial compression, the presence of water brings to the disappearance of the stress drops.
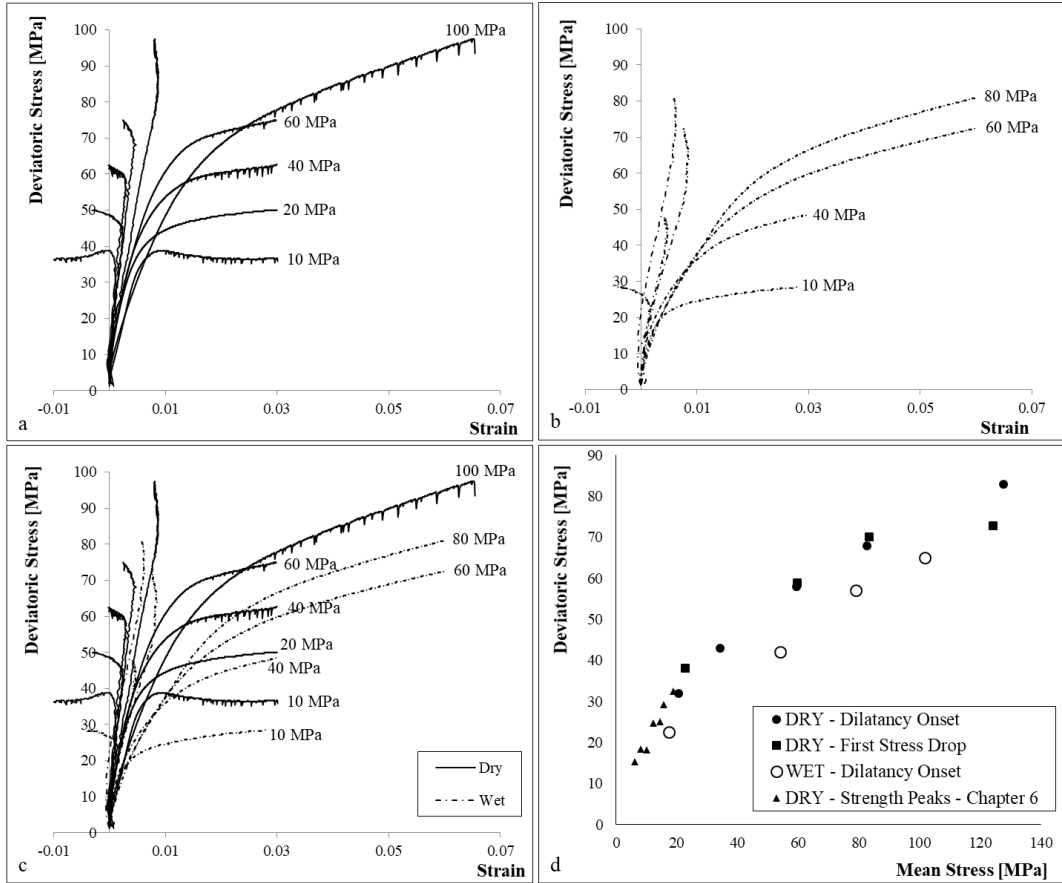
Figure 7.14 a. Triaxial tests in dry conditions. b. Triaxial tests in partially de-saturated samples c. Comparison between graphs in Figures a and b. d. P-q representation of the triaxial tests described in this Chapter and in Chapter 6.

Figure 7.14d sumurizes the results of the triaxial tests in the mean stress – deviatoric stress chart. The yield point was quantified in terms of dilatancy onset and in terms of apperence of the first stress-drop. Both the values are, indeed, easy to be quantified on the stress-strain curves and represent a clear change in the material behaviour. The trend of dry tests draws a well-defined curve, that is in good continuity with the triaxial results described in Chapter 6, despite the difference in sample size. The strength loss due to the water partial saturation is clearly described in the graph in Figure 7.14d for the entire range of pressures.

7.5 Microstructures
7.5.1   Uniaxial Tests
With the aim to investigate the microstructures produced in the material by the compression, a series of mechanical tests was planned to be stopped in an early phase, to preserve the developing structures before the complete failure coalescence.

The microstructures were then analysed preparing thin sections of the central part of the samples.

Standard dry uniaxial compression microstructures were described on the sample reported in Figure 7.15. The early interruption of the test allowed to preserve an incipient failure surface, as testified by the naked-eye macroscopic (Figure 7.15b) and SEM (Figures 7.15c) observations.
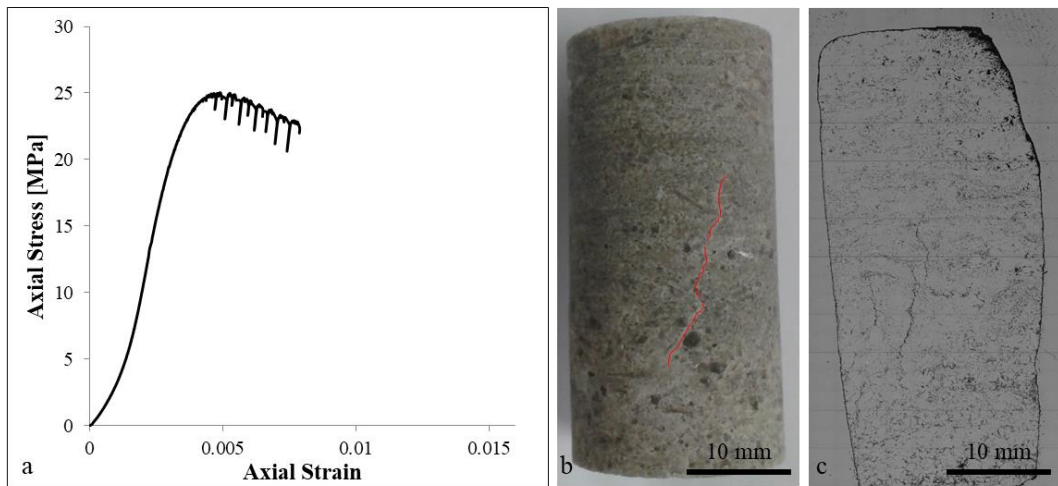
Figure 7.15 a. Stress-strain curve of the sample used for microstructural analysis of dry uniaxial conditions b. Macroscopic appearance of post-failure sample c. General view of the thin section

The not-continuity of this failure surface is confirmed also at a more detailed scale. Figures 7.16a and 7.16b show portions of the rock where the open cracks (in the lower part of the images) are interrupted upward.

The thin section photographs a specific instant of the deformation. Figure 7.16a, in addition to the open crack in the lower part, shows a fine, almost-close crack in the upper part of the image. The image seems to suggest that, if the test had not been interrupted, the lower and the upper cracks would have been coalescing, overcoming the rock bridges that are still present. The presence of a series of parallel micro-cracks within a gypsum crystal in this still-intact rock portion suggests that the coalescence would have been cutting through that grain.

A similar possible evolution can be imagined for Figure 7.16b, where the interruption of the crack continuity seems to be driven by a change in the textural features of the rock (i.e. presence of a layer of finer material).

This kind of failure coalescence "by steps" is coherent with the unstable stress-drop behaviour registered in the mechanical test.

In general, the failure surface appears as a crack with opening of a few tens of μm, with sharp borders, that frequently cuts through the gypsum crystals (e.g. Figure

7.16c) and that is often rimmed by fine-grained material (Figure 7.16d). Some lateral branches, departing from the principal crack, follow the sub-horizontal layering of the branching selenite structure.
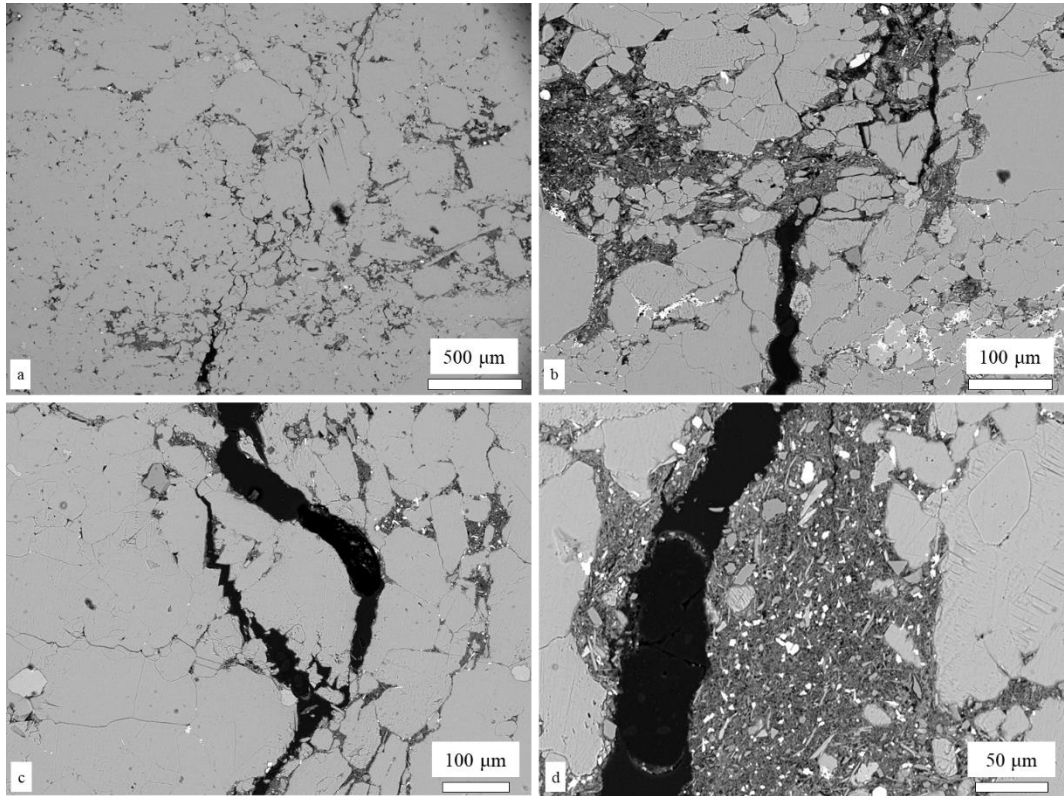
Figure 7.16 SEM micrographs of dry uniaxially loaded sample: a. Failure surface before coalescence b. Failure surface interrupted upward. c. Failure surface cutting through a gypsum crystal b. Failure surface rimmed by the fine-grained material.

The change from dry to water-saturated conditions brings, as said, to a strength decrease of about 50% and to the disappearance of the stress-drops in the strain softening curve. The microstructures produced in water-saturated test conditions were analysed on the sample reported in Figure 7.17. Again, the early stop of the test allows for the recording of the structure before the complete coalescence of the failure. As a matter of fact, in this case, the first sight of the thin section (Figure

7.17c) suggests the absence of clear open cracks that across all (or part of) the sample.
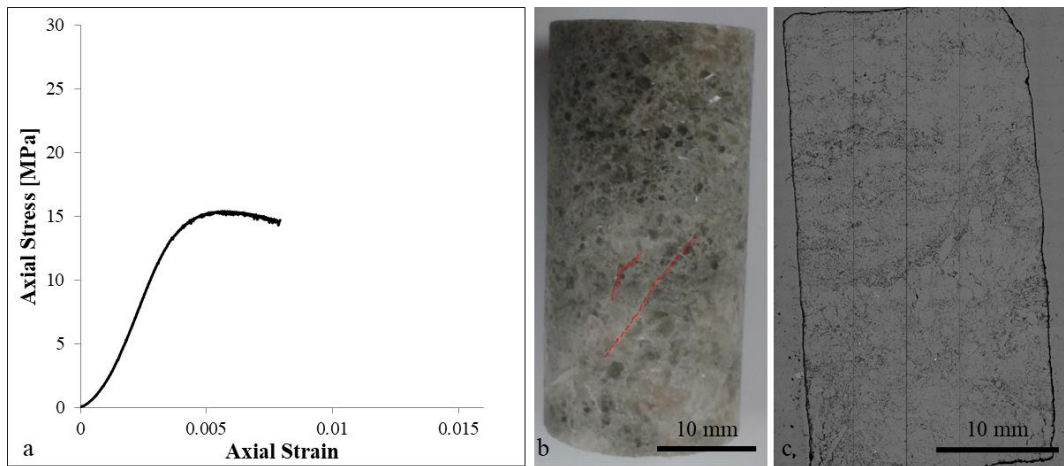
Figure 7.17 a. Stress-strain curve of the sample used for microstructural analysis of water-saturated uniaxial conditions b. Macroscopic appearance of post-failure sample c. General view of the thin section

Figure 7.18, reporting some representative micrographs of the thin section, shows that the principal cracks in the sample corresponds to detachments along the grain boundaries. As instance, Figure 7.18a shows a big gypsum crystal almost completely rimmed by a detachment with respect to the surrounding rock. The cracking propagates, however, also within the crystals, but always following linear parallel paths (i.e. following the mineral cleavage – Figures 7.18b-c) or creating undulate dissolution structures (e.g. Figure 7.18d).
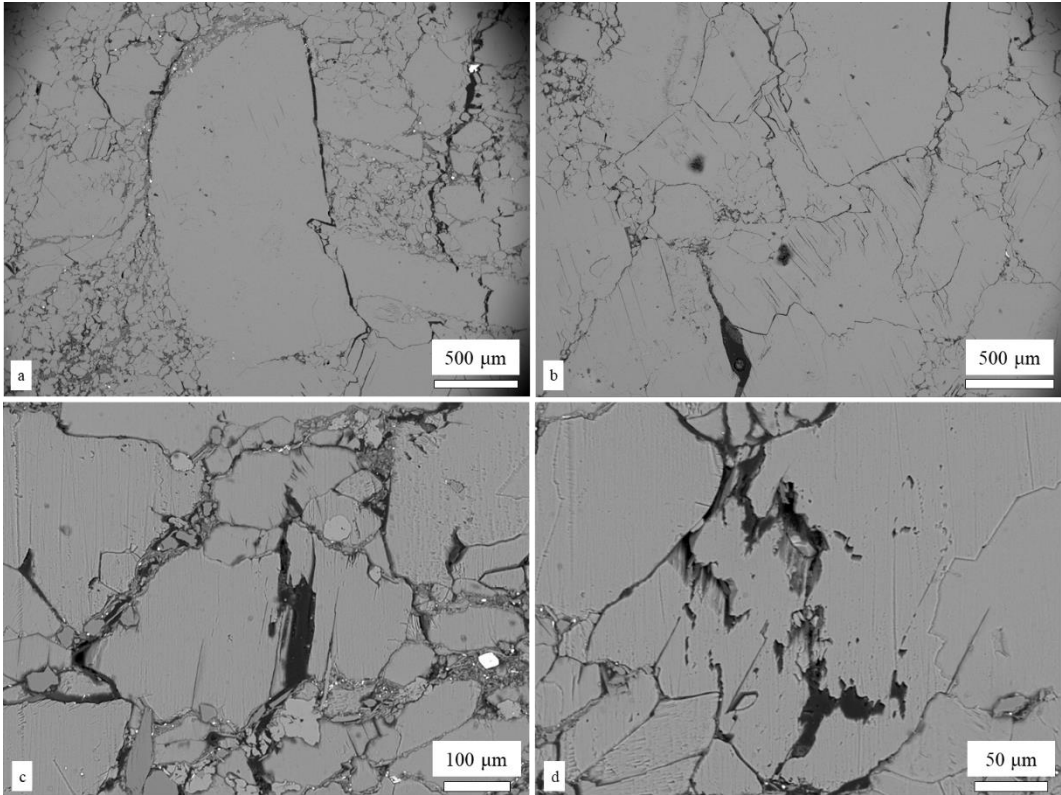
Figure 7.18 a. Detachment of a big gypsum crystal from the surrounding rock b. Straight and parallel cracks within a gypsum crystal in the central part of the sample c. Crack propagation within a gypsum crystal, perfectly straight d. Evidences of dissolution structures within a gypsum mineral

The change of post-peak behaviour in slow-strain rate water-saturated tests suggests the possibility of a time-dependent change of the microstructure. Considering the absence of strain softening in these test conditions, both an early stopped and a long-strained water-saturated tests with slow strain-rate (i.e.$10^{-7}s^{-1}$) were used for microstructural analysis (Figure 7.19a). The former allows for a direct comparison with dry and water-saturated microstructures. The latter aims to provide information about the reasons of the absence of a strain softening behaviour. As can be seen in Figure 7.19, sample of Curve 2 (shown in Figures 7.19b-c), despite the high accommodated strain (i.e. almost 2%), does not show a coalesced failure neither macroscopically nor in the thin section. The thin section shows, on the other hand, the presence of a diffuse fracturing, mainly vertical oriented.
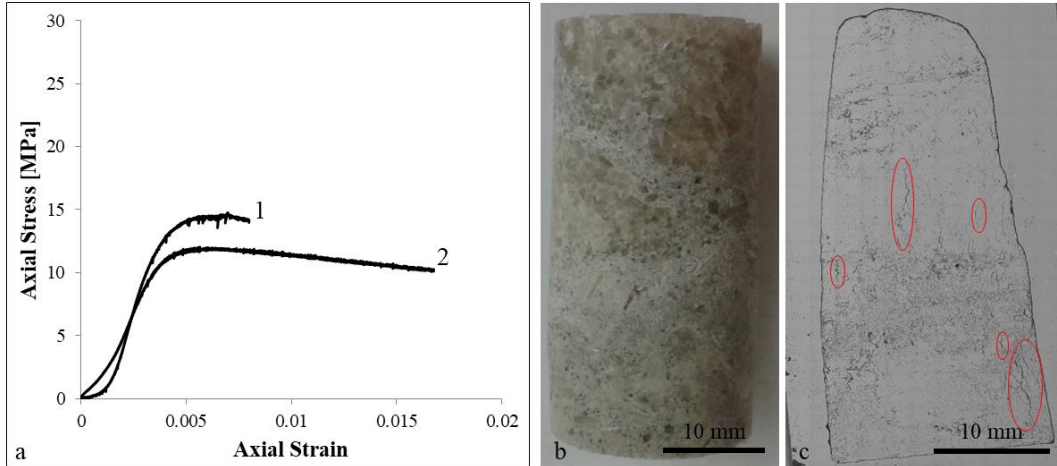
Figure 7.19 Stress-strain curves of the samples used for microstructural analysis of water-saturated slow-strain-rate uniaxial tests b. Macroscopic appearance of post-failure sample of curve 2 c. General view of the thin section of sample of curve 2. The red circles highlight the most evident vertical fractures.

At a more detailed scale, the thin sections show an enhancement of the features already described for the standard water-saturated test, i.e. detachment along grain boundaries (e.g. Figure 7.20a), straight and parallel intra-crystalline cracks, following the mineral cleavage (Figure 7.20b), and irregular dissolution-related structures (Figure 7.20c-d). In particular, the structure reported in Figure 7.20c-d, being oriented almost perpendicular to the applied stress, is likely produced by a phenomenon of pressure solution, due to the enhancement of water-solubility of gypsum for the effect of the compression.
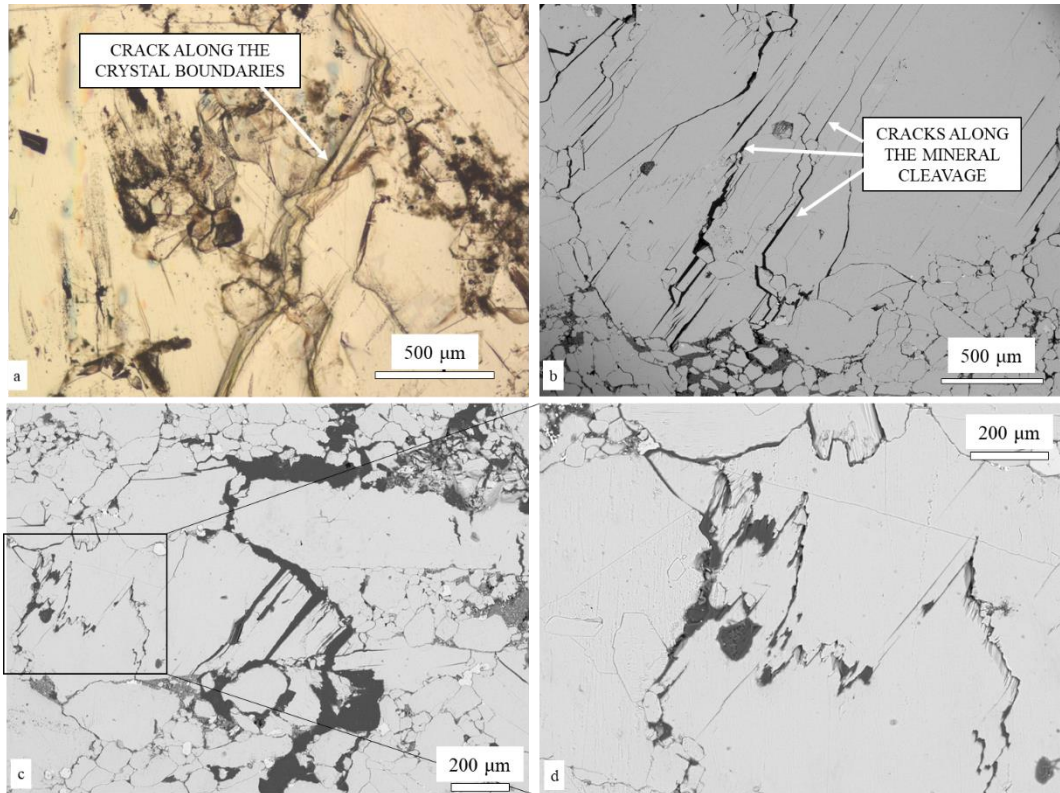
Figure 7.20 a. Sub-vertical opening along the grain boundaries (optical microscope) b. Intra-crystalline cracking along the mineral cleavage (SEM) c. Evidences of detachment along the grains, of intra-crystalline cracking along the mineral cleavage and of surface of pressure solution (SEM) d. Surface of pressure solution (detail of Figure c)

7.5.2 Triaxial Tests

In agreement with the microstructures discussed in Chapter 6, the principal evidence of strain accommodation in the thin sections of triaxially loaded samples is the presence of kinked grains.

As suggested in Chapter 6, the kinking structures imply the hardening of the stress-strain curve because of the finite strain that can be accommodated by a single grain. Once the maximum folding is reached, the energy required to start to kink a new grain is lower than the energy needed to bring the grain to failure. With the increase of confining pressure (e.g. Pc = 40 MPa, Figure 7.21a-b), the kinking becomes denser and the presence of fragile cracking decreases, justifying the more intense hardening registered in the mechanical test.

Figure 7.21c-d, referring to triaxial tests in wet conditions, shows the substantial analogy in microstructures: the kinking of the grains is well-evident also in wet conditions.
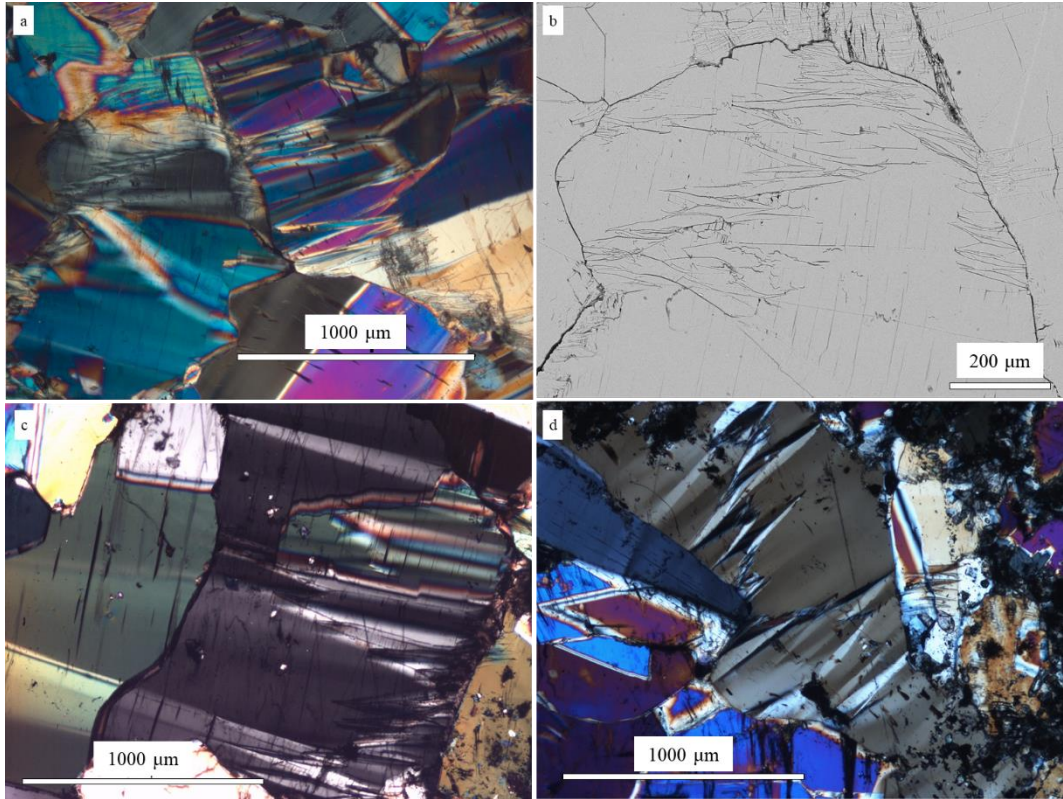
Figure 7.21 a. Intense grain kinking in optical microscope (dry triaxial test at Pc = 40 MPa) b. Detail of kinking structure at SEM (dry triaxial test at Pc = 40 MPa) c-d. Intense grain kinking in optical microscope (wet triaxial test at Pc = 40 MPa)

7.6 Discussion of the results
7.6.1 Water-related weakening mechanism
The experimental program discussed in this Chapter reports on the important influence of water on the mechanical response of gypsum rock. In uniaxial stress conditions, a strength decrease of 50% is observed in presence of water saturation. Despite the difficulties in testing set up, also under triaxial compression a clear decrease of yield point is registered in presence of water for a range of confining pressures between 10 and 100 MPa. Moreover, results show the existence of an intense time-dependent deformation related to the presence of water. In dry conditions or under saturation with an a-polar fluid (i.e. oil), the time-dependent deformation is absent or almost unmeasurable.

The analysis of post-failure microstructures testifies a difference in the prevalent typology of crack opening in dry and water-saturated samples. In dry samples, a clear failure is identified by sharp surfaces, cutting through the grains, with an unstable stepping propagation. Water-saturated samples, on the other hand, show the

prevalence of cracks along the grain boundaries, suggesting an opening for detachment, or along the mineralogical cleavage of the gypsum crystals.

These evidences suggest that the saturating water, filling the pores of the rock, progressively destroys the connections between the gypsum crystals through the dissolution of material at the tip of existing microcracks. In addition, due to the higher solubility of gypsum along the surfaces of the mineral cleavage (010 crystallographic surface), the presence of water in the pores, under the effect of the applied pressure, facilitates the opening of cracks along the mineralogical cleavage.

The weakening of the connections among grains brings to the substitution of the unstable step-wise crack coalescence with a more gradual and "facilitated" failure coalescence. The change of failure coalescence process is also confirmed by the disappearance of the stress drops in the post-peak stress-strain curves.

The enhancement of these wet microstructures (i.e. detachment along grain boundaries and intra-crystalline cracks along the mineralogical cleavage) observed in low-strain-rate samples suggests that the intense time-dependent deformation of the material may be connected to the same over-described dissolution processes that, with longer available times, are more efficient. The opening of tensional cracks along the grain boundaries, already weakened by the action of water, may generate a gradual energy dissipation that inhibits, in the low-strain-rate tests, the crack coalescence and the strain softening. This is also coherent with the dilatant behaviour registered in these test conditions.

In creep conditions, the existence of a direct relationship between plastic creep strain and porosity seems to confirm the importance of water dissolution processes on the material deformation. Higher initial porosities, with higher specific surface areas and higher availability of water intrusion and dissolution, increases the material propensity to develop plastic strain.

The experimental results showed, however, the possibility of creep failure in water-saturated conditions under a static level of stress up to 15% lower than the peak strength.

7.6.2   Triaxial results

The results of triaxial compression tests presented in this Chapter and in Chapter 6 show several analogies with the experimental dataset presented in Brantut et al., 2011. In that study, the investigation of triaxial response of Volterra gypsum brought to the observation of stress drops in the strain hardening curves (similarly to Figure 7.14a, in this Chapter). In addition, the principal element described in the microstructures of triaxial-compressed Volterra gypsum is the presence of kinked grains.

Despite the differences in gypsum typology between Volterra facies and branching selenite facies (Volterra gypsum is a highly-pure alabastrine gypsum facies, with very low porosity – lower than 1.5% – and very fine grain-size – from 10 μm to 200 μm), the mechanical data, compared in the p-q graph in Figure 7.22, show a surprising similarity.
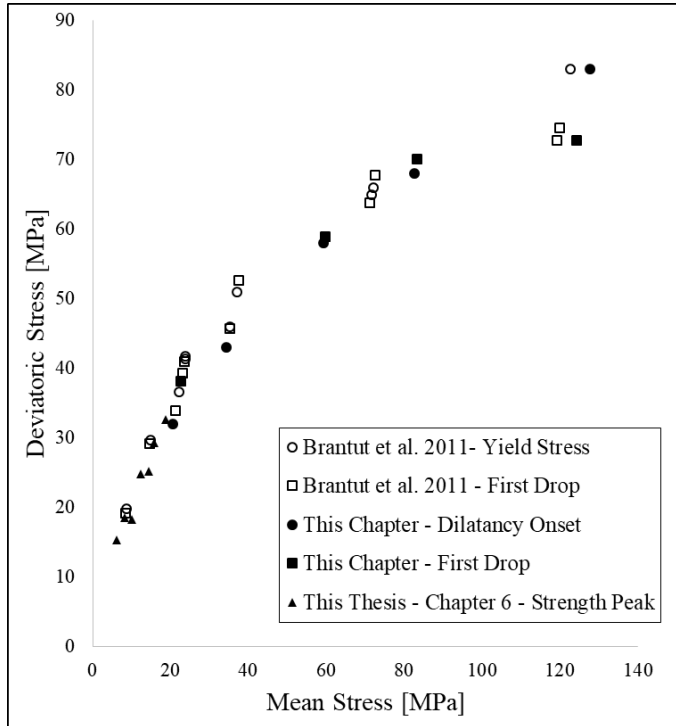
Figure 7. 22 Comparison of triaxial results obtained in this Chapter and in Chapter 5 with the results of Volterra gypsum reported in Brantut et al., 2011

Since the contribute by Brantut et al., 2011 does not include data about the unconfined strength of the material, some additional uniaxial tests (dry and water-saturated) were performed on Volterra gypsum, with the same methodologies and equipment described in this Chapter, to facilitate the comparison with the here presented experimental investigation. The tests returned values of peak strength of Volterra gypsum about twice than in branching selenite gypsum, both in dry and water-saturated conditions.

This suggests that, in presence of a confinement that inhibits the crack coalescence, the influence of the initial microstructure on the final strength is reduced. On the other hand, the homology of strain mechanism (i.e. grains kinking) may control the similarity in the strength results.

Annex 7.1

Sample ID	Length (mm)	Mean Diameter (mm)	Bulk Volume (cm³)	Dry Mass (g)	He-Pycnometer Solid Volume (cm³)	Porosity (%)	Solid Density (g/cm3)	Bulk Density (g/cm3)
1	39.98	19.92	12.45	27.26	11.66	6.38	2.34	2.19
2	40.12	19.88	12.45	27.64	11.83	4.99	2.34	2.22
3	40.10	19.95	12.53	27.44	11.68	6.76	2.35	2.19
4	40.13	19.93	12.52	27.88	11.93	4.67	2.34	2.23
5	40.05	19.94	12.50	27.53	11.77	5.87	2.34	2.20
6	40.08	19.93	12.50	27.88	11.93	4.50	2.34	2.23
7	40.08	19.92	12.48	27.66	11.82	5.35	2.34	2.22
8	40.19	19.91	12.51	27.69	11.83	5.42	2.34	2.21
9	40.16	19.89	12.48	27.34	11.62	6.88	2.35	2.19
10	40.09	19.92	12.49	27.61	11.80	5.58	2.34	2.21
11	40.04	19.93	12.48	27.32	11.65	6.69	2.35	2.19
12	40.09	19.89	12.45	27.57	11.78	5.38	2.34	2.21
13	40.16	19.93	12.52	27.92	11.95	4.56	2.34	2.23
14	40.11	19.92	12.49	28.05	12.02	3.78	2.33	2.25
15	40.18	19.93	12.53	27.68	11.81	5.71	2.34	2.21
16	40.08	19.89	12.45	27.50	11.73	5.80	2.35	2.21
17	40.22	19.92	12.53	27.45	11.72	6.45	2.34	2.19
18	40.29	19.90	12.53	27.59	11.78	5.99	2.34	2.20
19	40.23	19.93	12.55	27.92	11.95	4.77	2.34	2.22
20	40.22	19.93	12.54	27.72	11.83	5.68	2.34	2.21
21	40.25	19.89	12.51	27.85	11.91	4.75	2.34	2.23
22	40.14	19.83	12.39	27.85	11.91	3.90	2.34	2.25
23	40.01	19.88	12.42	27.83	11.84	4.61	2.35	2.24
24	40.09	19.88	12.44	28.03	11.96	3.89	2.34	2.25
25	40.12	19.84	12.40	27.66	11.77	5.11	2.35	2.23
26	40.02	19.87	12.41	27.91	11.96	3.62	2.33	2.25
27	40.08	19.87	12.43	27.91	11.90	4.24	2.34	2.25
28	40.10	19.85	12.41	27.58	11.76	5.23	2.34	2.22
29	40.10	19.90	12.47	27.60	11.77	5.59	2.34	2.21
30	40.12	19.88	12.45	26.82	11.31	9.18	2.37	2.15
31	40.09	19.87	12.43	27.20	11.53	7.20	2.36	2.19
32	40.10	19.90	12.47	27.45	11.62	6.81	2.36	2.20

33	40.11	19.90	12.48	26.99	11.42	8.51	2.36	2.16
34	40.11	19.89	12.46	27.55	11.73	5.86	2.35	2.21
35	40.16	19.90	12.49	27.02	11.38	8.88	2.37	2.16
36	39.98	19.89	12.42	27.23	11.52	7.22	2.36	2.19
37	40.01	19.92	12.47	27.41	11.62	6.77	2.36	2.20
38	40.07	19.92	12.48	27.40	11.58	7.20	2.37	2.20
39	39.98	19.90	12.43	27.16	11.50	7.49	2.36	2.18
40	40.01	19.89	12.43	27.38	11.60	6.70	2.36	2.20
41	40.00	19.88	12.42	27.31	11.57	6.85	2.36	2.20
42	40.04	19.87	12.42	27.17	11.47	7.62	2.37	2.19
43A	40.06	19.91	12.47	27.72	11.82	5.22	2.35	2.22
44A	40.11	19.88	12.45	27.65	11.79	5.31	2.34	2.22
45A	40.06	19.92	12.48	27.29	11.60	7.05	2.35	2.19
46A	40.16	19.93	12.53	28.01	11.99	4.34	2.34	2.23
47A	40.11	19.89	12.47	27.82	11.91	4.50	2.34	2.23
48A	40.16	19.89	12.48	27.86	11.92	4.47	2.34	2.23
49A	40.06	19.93	12.50	27.72	11.84	5.32	2.34	2.22
43	40.07	19.54	12.02	26.72	11.07	7.85	2.41	2.22
44	40.04	19.97	12.54	27.81	11.49	8.37	2.42	2.22
45	40.00	19.96	12.52	28.37	12.00	4.15	2.36	2.27
46	39.94	19.97	12.51	28.36	12.06	3.56	2.35	2.27
47	40.04	19.97	12.54	28.22	11.78	6.08	2.40	2.25
48	39.89	19.97	12.49	28.40	12.07	3.37	2.35	2.27
49	39.98	19.97	12.52	28.10	11.85	5.39	2.37	2.24
50	40.13	19.96	12.56	28.48	12.05	4.05	2.36	2.27
51	40.07	19.97	12.55	28.20	11.88	5.33	2.37	2.25
52	40.00	19.97	12.53	28.15	11.85	5.40	2.38	2.25
53	40.00	19.97	12.53	28.34	11.93	4.79	2.38	2.26
54	40.13	19.97	12.57	28.32	11.93	5.10	2.37	2.25
55	40.08	19.97	12.55	28.39	11.98	4.61	2.37	2.26
56	40.04	19.98	12.55	28.05	11.86	5.52	2.36	2.23
57	40.10	19.97	12.56	28.27	11.91	5.18	2.37	2.25
58	40.07	19.95	12.53	28.31	11.97	4.44	2.37	2.26
59	40.02	19.97	12.53	28.21	11.88	5.19	2.37	2.25
60	40.04	19.97	12.54	28.16	11.87	5.36	2.37	2.25
61	40.10	19.80	12.35	27.06	11.13	9.82	2.43	2.19

62	39.98	19.80	12.31	27.29	11.39	7.51	2.40	2.22
63	40.08	19.90	12.47	27.39	11.40	8.52	2.40	2.20
64	40.05	19.96	12.53	28.48	12.11	3.38	2.35	2.27
65	40.18	19.96	12.57	28.17	11.88	5.55	2.37	2.24
66	40.00	19.97	12.53	28.06	11.84	5.51	2.37	2.24
67	40.15	19.96	12.56	28.18	11.81	5.98	2.39	2.24
68	40.11	19.97	12.56	28.54	12.14	3.35	2.35	2.27
69	40.07	19.96	12.54	28.16	11.91	5.00	2.36	2.25
70	40.12	19.85	12.42	27.63	11.56	6.93	2.39	2.23

Chapter 8

Long-term creep and relative humidity control

The restrictions imposed by the common laboratory practice imply the difficulty to investigate the creep behaviour of rock materials under low applied stresses. The decrease of stress, indeed, generates a non-linear decrease in creep strain rate, requiring the execution of tests over long time periods (i.e. several months or years). For these reasons, the classical experiments on brittle creep in rock focus on a stress range able to induce creep failure in few days or weeks (e.g. Chapter 7).

In order to fill the gap between the classical timescales of laboratory investigation and the everyday practice of safe excavation (i.e. low axial stresses that guarantee the long-term stability), the present Chapter proposes a complementary dataset to Chapter 7, describing an experimental investigation on creep response of branching selenite gypsum under low applied stresses and under the influence of different values of relative humidity. The increase in sample sizes with respect to Chapter 7

allows, moreover, to test a more representative volume of rock. Considering the particular structure of branching selenite rock (with a branched structure periodically repeated at the meso-scale and at the rock-mass scale) a rock sample with a representative volume allows for a good description of the material at the rock-mass scale.

The Chapter also contains a proposal of application of a constitutive model from the scientific literature, with an integration aimed to include the relative humidity as a variable.

8.1 Introduction
The influence of water on the mechanical response of gypsum rock, discussed in Chapter 7 and well-documented in the scientific literature (e.g. Castellanza et al., 2008; de Meer and Spiers, 1999, 1997, 1995; Liang et al., 2012; Salih and Mohammed, 2017; Yilmaz, 2007; Zhu et al., 2019), testifies the drastic reduction of strength and the equally significant increase of creep strain induced by water saturation.

In underground gypsum quarries, high values of relative humidity have often been recorded even in absence of complete water-saturation (e.g. Auvray et al., 2008, 2004). For this reason, Hoxha et al., 2006, 2005 proposed an experimental investigation and a constitutive contribution that relate the long-term creep behaviour of gypsum to the relative humidity. The direct relation of the mechanical response with the relative humidity overcomes the dry-saturated dichotomy, typical of laboratory investigation (e.g. Chapter 7), allowing for a more realistic description of the natural site conditions.

Long-term creep properties of gypsum rock are directly involved in several application fields. Besides the assessment of long-term stability of abandoned or old underground quarries, they cover an important role in the tectonic transports of large areas in orogenetic belts (e.g de Meer and Spiers, 1999). Despite the relevance of this subject, poor experimental data about the long-term creep behaviour of natural gypsum rocks are available in the scientific literature.

With the aim to fill this gap, the present Chapter proposes an experimental investigation of strength and creep of branching selenite gypsum, evaluating the role of relative humidity on both short-term strength and creep behavior. Low level of applied stress (i.e. similar to the stress ranges usually applied on the gypsum pillars in underground environments) were chosen to describe the creep strain over long periods of time. In addition, an experimental-based integration to an available constitutive contribution (Nedjar and Le Roy, 2013) is proposed, aiming to include the role of relative humidity in the model.

8.2 Laboratory investigation
8.2.1 Mechanical tests

Similarly to the tests described in Chapters 5 and 6, **uniaxial short-term strength** tests were performed with a servo-controlled press applying an axial stress with constant strain rate of $10^{-5}s^{-1}$. Both A-type and B-type gypsum samples were considered. The formers (A-type) were tested as prismatic samples, with mean sizes of 100 mm x 50 mm x 50 mm, to facilitate the comparison with the creep tests (performed on cubic samples). The latters, due to the low quality of the rock and the difficulties in the cutting of prismatic shape, were tested as cylinders.

For the **creep**, a specific **test** set-up was designed, in order to guarantee the uniformity of stress conditions over long periods of time (i.e. several months) and to optimize the use of laboratory equipment.
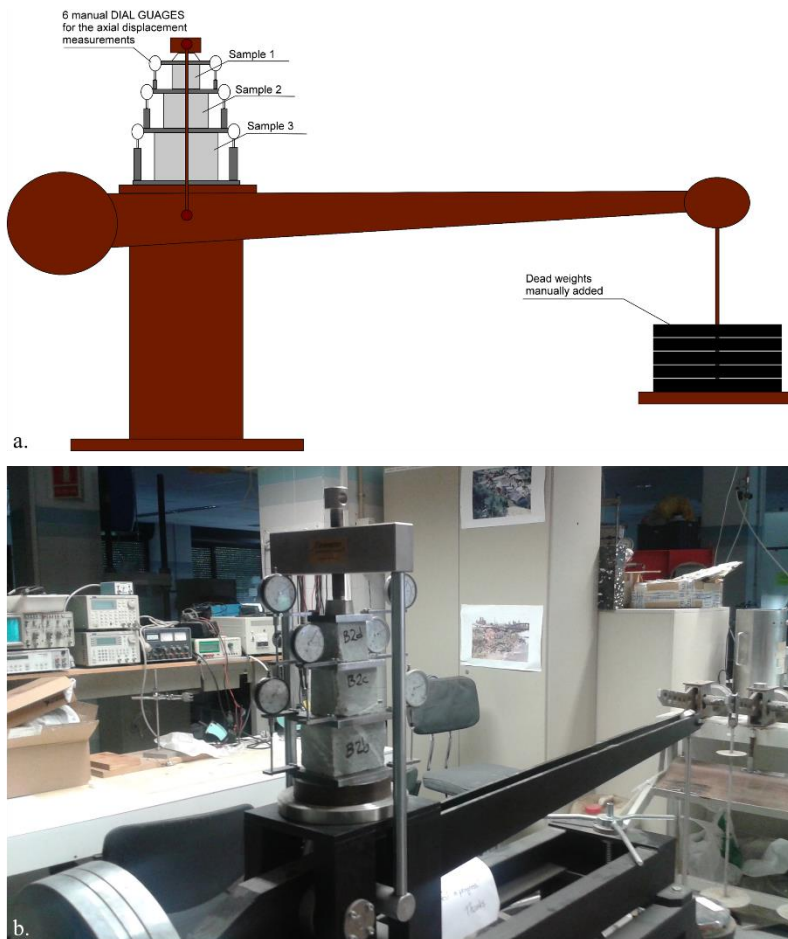
Figure 8.1 General view of the lever system used in the creep tests: scheme (a) and photographic image (b)

The set-up contemplates a lever system that simultaneously applies the load to three cubic gypsum samples with different sizes (Figure 8.1). Since the load distributes on

the different areal surfaces of the samples, the resulting stress applied to each of them is different. Metallic plates separate the samples and transfer the load from one sample to the others. Two dial gauges for each plate measure the axial displacements and give additional information about the uniformity of the strain (i.e. absence of plate rotation) (Figure 8.2).
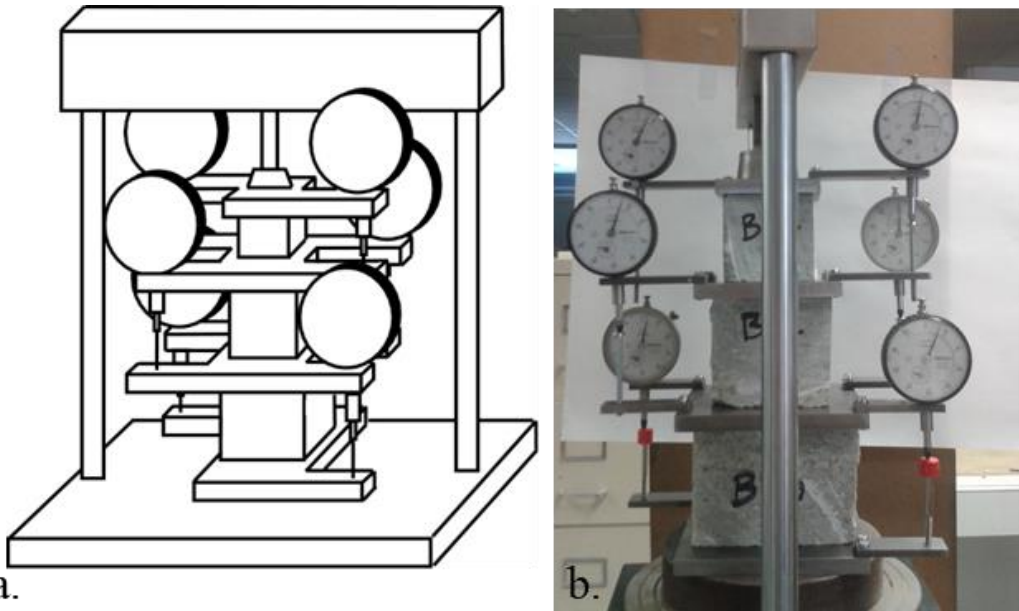
Figure 8.2 Detailed view of the set-up of the creep test: scheme (a) and photographic image (b)

Table 8.1 summarizes the areas of the samples and the correspondent applied stresses. Tests were continued until stable steady state conditions were reached, with the measure of a constant strain rate over time. Since some of the tests are still running at the time this Thesis is written, some of the records in the Table do not include the information about test duration. However, the date of the test beginning is reported, to allow the reader to calculate the time duration of the test at the present day.

Due to the long times required for the tests, only A-type material (more homogeneous and allowing for more repeatable conditions) was tested. The test repeatability of A-type material allowed for the evaluation of the influence of other parameters: considering the relevance of the anisotropy orientation in the quarry assessment (as discussed in Chapter 6), one set of experiments was dedicated to evaluate the influence of the layering orientation on the creep results.

Table 8.1 Sample geometrical features and test conditions of the creep tests. For the creep tests still on-going when this Thesis is written, the information about test duration is replaced by the date of test start.

Creep Tests					
Sample Name	**Sample Area**	**Applied Stress**	**Relative Humidity**	**Test Duration**	**Anisoropy Orientation**
	[mm²]	[MPa]	[%]	[days]	
B2	7708	2.13	50 - not controlled	335	Horizontal
	5596	2.94	50 - not controlled	335	Horizontal
	3976	4.14	50 - not controlled	335	Horizontal
P0	8050	2.04	90	213	Horizontal
	5688	2.89	90	213	Horizontal
	3595	4.57	90	213	Horizontal
P0A	8318	1.98	20	*(started on 13.12.2018)*	Horizontal
	5554	2.96	20	*(started on 13.12.2018)*	Horizontal
	3771	4.36	20	*(started on 13.12.2018)*	Horizontal
P0C	8007	2.11	90	*(started on 11.03.2019)*	Inclined (45°)
	5552	2.96	90	*(started on 11.03.2019)*	Inclined (45°)
	3888	4.23	90	*(started on 11.03.2019)*	Inclined (45°)
P0B	1755	6.30	90	*(started on 20.05.2019)*	Horizontal
	1060	10.43	50 - not controlled	*(started on 20.05.2019)*	Horizontal
	1079	10.24	50 - not controlled	*(started on 20.05.2019)*	Horizontal

In the creep test with the most disadvantageous conditions (i.e. 10 MPa and RH = 90%), a special precaution was taken in view of the possible acceleration and failure of the sample. A metal support was prepared in order to bear the axial load in case of collapse of the sample (Figure 8.3). The height of this metal support is 10% lower than the sample. If, during the test, the sample reaches an axial strain of 10% (i.e. creep failure), the higher plate will touch the metal support and the test will continue on the two lower samples.
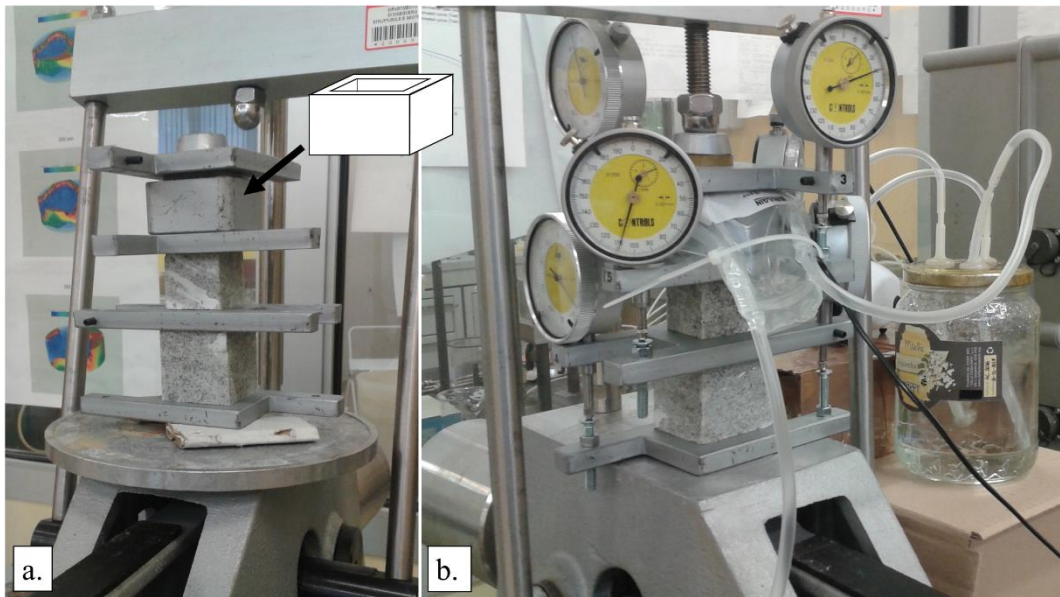
Figure 8.3 Set-up of the creep test with a specific metal support to bear the axial load in case of sample collapse. a. Test set-up before the application of the load. The sample in the higher position is within the metal support. b. Running test. The sample in the higher position and the metal support are within the plastic bag.

8.2.2 Control of relative humidity

Short-term and long-term tests were performed both in free environment and with relative humidity control.

In the first mode, samples are free to equilibrate with the relative humidity of the laboratory (i.e. Laboratory of Soil and Rock Mechanics of the Department of Geotechnical Engineering and Geosciences of UPC, Barcelona and Geotechnical Laboratory of the Department of Structural, Geotechnical and Building Engineering of Polytechnic, Turin). In both the laboratories, the environmental humidity is maintained constant with the help of a system of conditioned air. The measure of humidity over a period of 6 months in Turin laboratory returned values ranging between 38-40% and 50-52%. In Barcelona laboratory, despite a shorter period of monitoring, a range of humidity between 38-40% and 55-57% was measured. A mean value of relative humidity of 45-50% can be therefore attributed to the free tests, but, for the long-term conditions, no assurances of humidity stability is given.

In the second mode, samples were tested within a close environment (i.e. plastic bags), with controlled relative humidity imposed with specific water-salt solutions. Figure 8.4 shows the circuit used to create controlled humidity conditions in short-term and creep tests respectively.
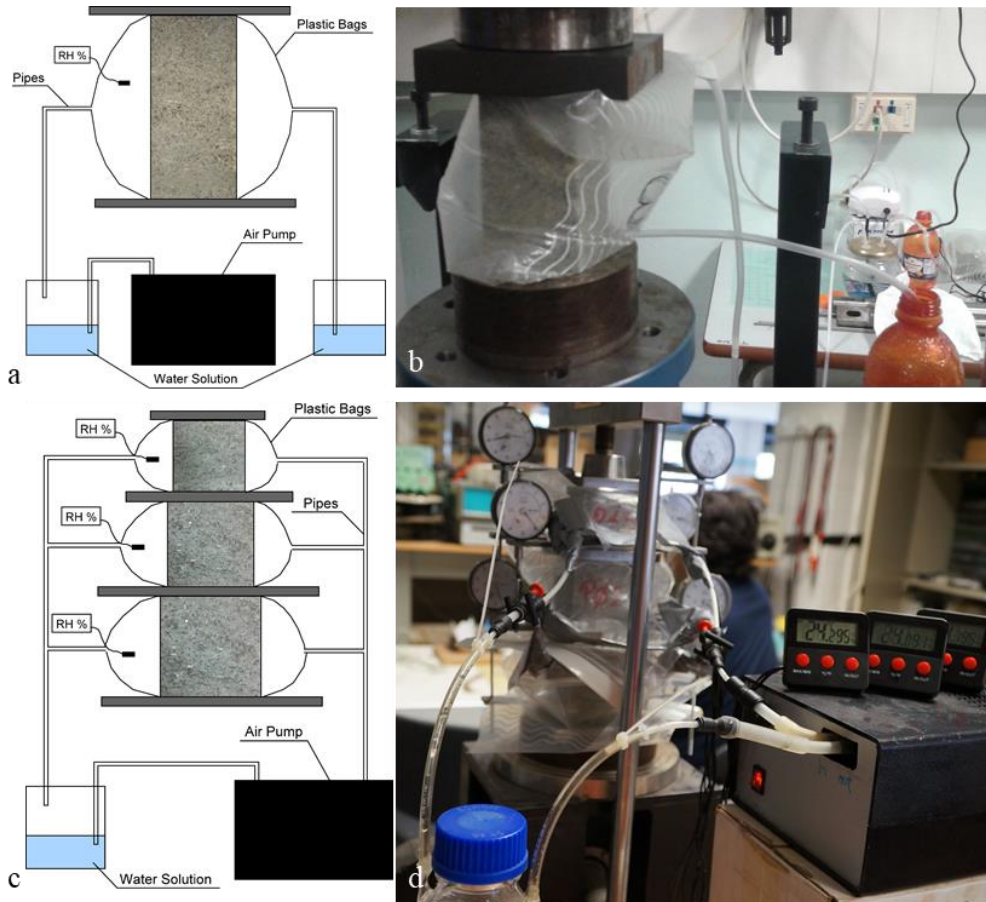
Figure 8.4 a. Scheme of the configuration of the system for the humidity control in the short-term uniaxial strength tests. b. Uniaxial test with humidity control c. Scheme of the configuration of the system for the humidity control in the creep tests. d. Creep test with high relative humidity conditions.

Silicone pipes connect the plastic bags with a close recipient with a water solution oversaturated with a specific salt. At the equilibrium, the salt in solution controls the relative humidity of the environment in contact with the water free surface, following Table 8.2.

Distilled water, with a nominal relative humidity of 100%, was chosen to create conditions of high relative humidity, while an oversaturated Lithium Chlorite solution, with a nominal relative humidity of 11%, was used to impose the low humidity conditions.

The connection of the recipient with an air pump assures the circulation of the atmosphere with the desired relative humidity and the maintenance of equilibrium conditions between the different parts of the circuit. Depending on the type of pump, the exiting air from the bags directly connects with the air pump itself, closing the

circuit (Figure 8.4c), or is directed to a new recipient with the same water solution, to avoid the injection of uncontrolled air (Figure 8.4a).

Before the test start, the circuit was kept active for a minimum of 3-4 days to reach the equilibrium and allow the humidity to permeate the gypsum sample.

Relative humidity was monitored during the test with probe hygrometers. Considering some air dispersion in the system, regular values of relative humidity of 90% and 25% were obtained in high and low humidity tests respectively.

Table 8. 2 Corresponding relative humidity for different saturated salt solutions at a temperature of 20°C and 25°C

Salt	Relative Humidity at 20°C [%]	Relative Humidity at 25°C [%]
Lithium Chloride	11.31 ± 0.31	11.30 ± 0.27
Potassium Acetate	23.11 ± 0.25	22.51 ± 0.32
Magnesium Chloride	33.07 ± 0.18	32.78 ± 0.16
Potassium Carbonate	43.16 ± 0.33	43.16 ± 0.39
Magnesium Nitrate	54.38 ± 0.23	52.89 ± 0.22
Sodium Chloride	75.47 ± 0.14	75.29 ± 0.12
Potassium Chloride	85.11 ± 0.29	84.34 ± 0.26
Potassium Nitrate	94.62 ± 0.66	93.58 ± 0.55
Potassium Sulfate	97.59 ± 0.53	97.30 ± 0.45

The long permanence of the high humidity conditions in a close environment brought, during the creep tests with 90% of relative humidity, to the precipitation of water drops in the bags. At the end of the test, electrical resistivity of this water precipitation was measured. The value (1.8 mS/cm) is coherent with data about gypsum-saturated water solutions, testifying the occurrence of a process of gypsum dissolution in the plastic bags by the precipitated water.

8.3 Results
8.3.1   Effect of Relative Humidity on Short-Term Strength Tests
Figures 8.5a and 8.5b show the comparison of uniaxial short-term tests with different humidity in A-type and B-type gypsum respectively.

As can be seen, in the case of A-type gypsum, a substantial analogy between stress-strain curves in free environment (i.e. RH = 50%) and under low relative humidity (i.e. RH = 25%) can be observed. The results show, on the other hand, a clear decrease in strength and elastic modulus in samples with high humidity conditions (i.e. RH = 90%). The presence of a humid environment causes a decrease in peak strength and an increase in axial strain in correspondence of the peak and the post-peak phase, describing a longer and less sharp softening. Differently from the water saturated tests discussed in Chapter 7, here the strength decrease driven by the high relative humidity does not imply the disappearance of the unstable stress-drops behaviour in the post-peak.

On the other hand, the clear disappearance of the stress-drops is observed for all the B-type tested samples (Figure 8.5b). The high heterogeneity of B-type samples makes difficult to recognize and isolate the influence of an external parameter as the relative humidity. However, despite some outliners, the trend observed for humid A-type samples (i.e. decrease of strength and stiffness with the high relative humidity) can be re-proposed for Figure 8.5b. On the other hand, the samples tested with RH = 25% are extremely dispersed, not allowing for the definition of a trend.
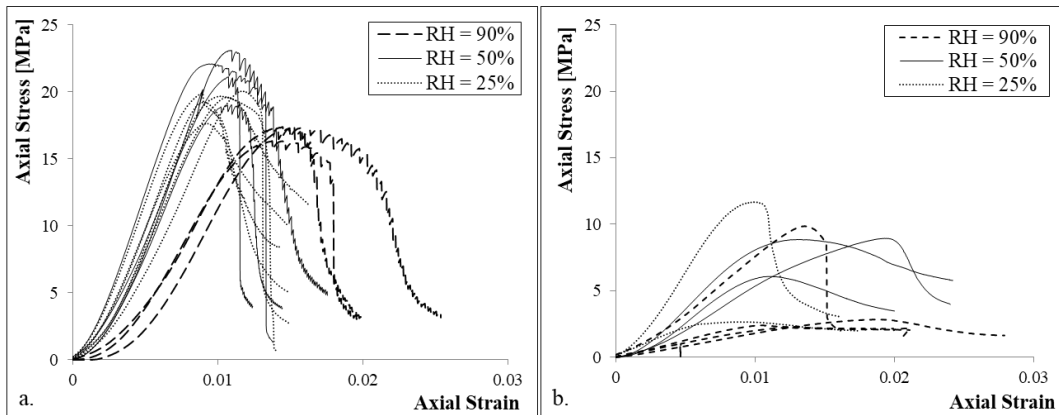
Figure 8.5 Stress-strain curves of short-term uniaxial tests with different humidity conditions in A-type (a) and B-type (b) gypsum samples.

8.3.2   Creep Tests
8.3.2.1 Effect of Relative Humidity

Figures 8.6a, 8.6b, 8.6c show the results of creep tests under high, not-controlled and low humidity conditions respectively. Starting point of the curves is after one hour from the application of the load, in order to nullify the contributions due to the instantaneous deformations.

The difference between Figure 8.6a and Figures 8.6b-c testifies the strong influence of relative humidity on the results. With high relative humidity (Figure 8.6a), the material creep faster, with a higher strain rate recognizable from the very first data.

The curves are regular and well defined, with clear definition of transient and steady state phases of the creep. A clear dependence of the behaviour from the applied stress is observable: samples loaded with 2 and 3 MPa does not show big differences in the measured strain, but samples under 4 MPa and, particularly, 10 MPa clearly shows an increase in measured strain and strain rate. At the time this Thesis is written, any evidence of test acceleration is registered for any of the samples. However, test under applied stress of 10 MPa is still running, not excluding the possibility of an acceleration in the next future.

Figure 8.6 a Creep tests with high humidity conditions. b. Creep tests with environmental humidity conditions c. Creep tests with low humidity conditions.

Samples deformed without humidity control or under low relative humidity (Figures 8.6b-8.6c) show an irregular trend, with highly noisy strain records. Even if an initial transient phase is maintained, the curves br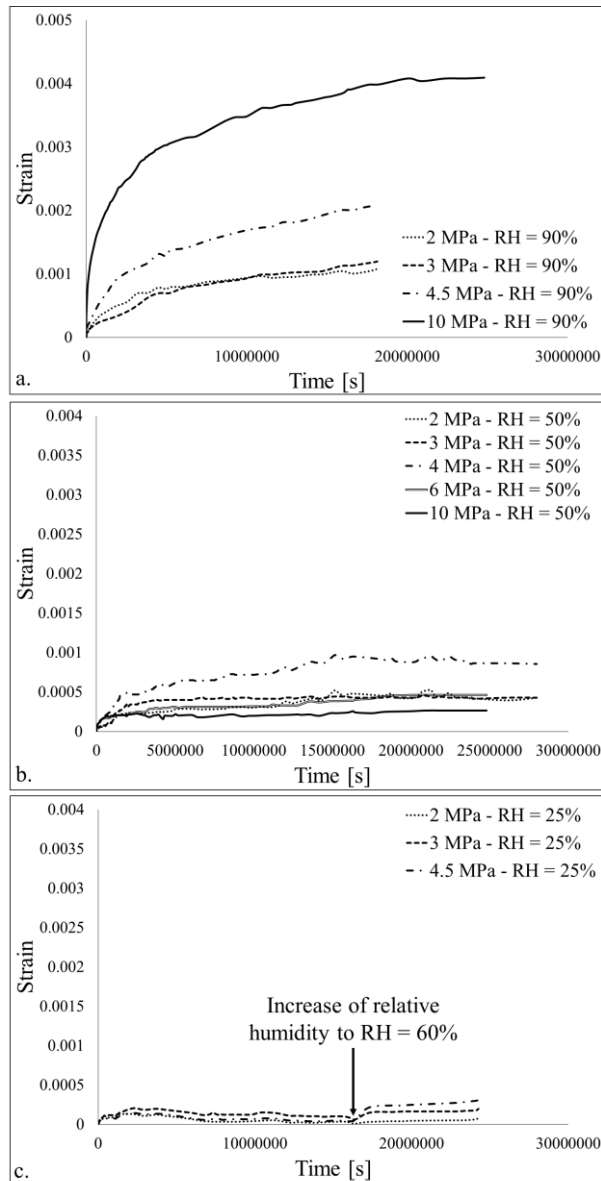iefly reach a condition of absence of creep, i.e. a strain rate too low to be quantifiable. In free environmental conditions (Figure 8.6b), the curves does not identify a clear relationship between applied stress and final strains and strain rates. Samples under 6 MPa and 10 MPa have similar behaviour of sample under 2 MPa. Without the influence of the humidity, an increase in axial stress seems to not necessarily imply an increase in strain rate. The influence of other parameters (e.g. sample variability, temperature, or scale effect, that causes an increase in stiffness with the decrease of sample sizes) is probably more effective than the lonely applied stress.

Tests performed under low relative humidity (Figure 8.6c) register a further decrease in strain rate. In the long-term, the graph highlights a substantial absence of strain. After 190 days, by changing the water solution in the circuit, the relative humidity was increased, imposing RH = 60%. As can be seen, this change in the environmental conditions generates a sudden change in the strain path, with an increase in strain rate, at least for the samples with 3 and 4.5 MPa of applied stress.

The gradual decrease and stabilization of strain rate during the evolution of the test is well described by the graph in Figure 8.7. In the Figure, the strain rates of samples with RH = 90% and free environmental humidity conditions are reported against time in a semi-logarithmic plot. The Figure confirms the difference in behaviour in consequence to the changes in relative humidity and the high noisiness of data recorded in absence of humidity control.
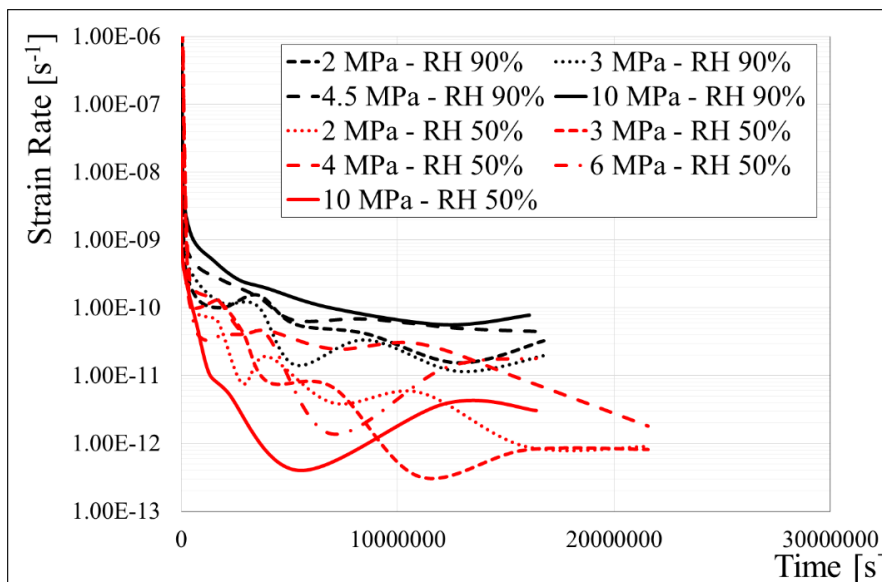
Figure 8.7 Semi-logarithmic plot of strain rate against time of creep data in high and environmental humidity conditions.

8.3.2.2 Effect of Anisotropy Orientation

Figure 8.8a shows the strain – time curves of creep tests on samples with anisotropy planes oriented at 45°. The curves of the tests with equivalent conditions (i.e. stresses = 2, 3, 4 MPa and RH = 90%) but horizontal anisotropy are reported in the graph to facilitate the comparison. Results show very low levels of strain and strain rate in samples deformed with applied stresses of 2 and 3 MPa (i.e. largely lower than in the equivalent samples with horizontal anisotropy). On the other hand, sample with the highest applied stress (4 MPa) starts with similar low strain rates, but, after 24 days, suddenly accelerates, reaching the highest strain rates in the dataset.
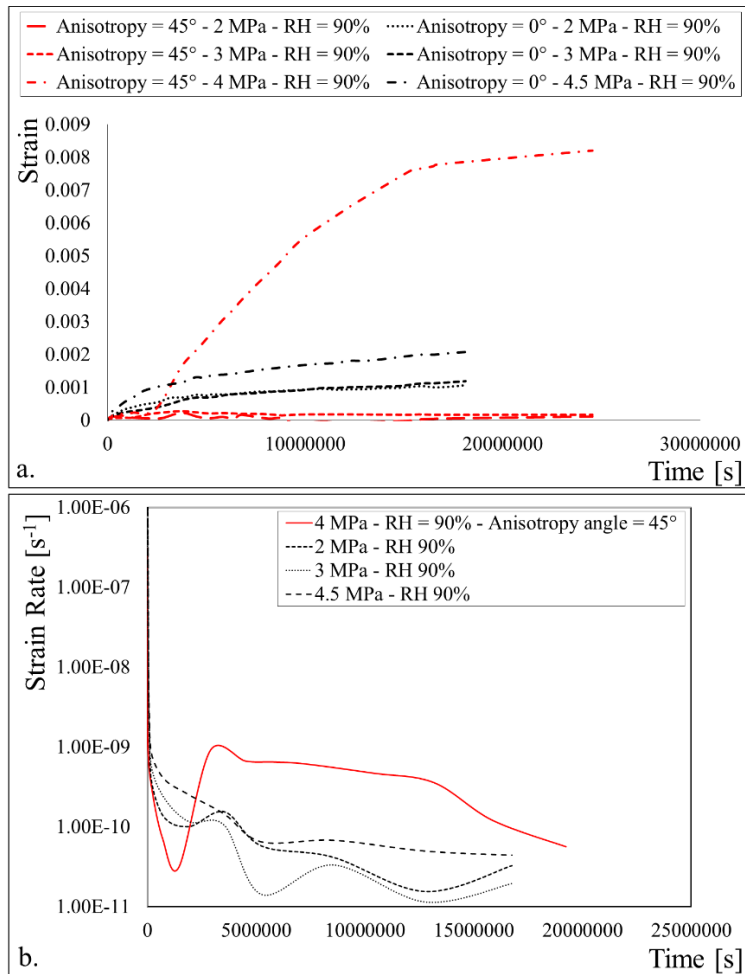
Figure 8.8 a. Results of creep tests on samples with different orientations of the anisotropy. b. Anomalous trend of the sample with inclined anisotropy in the strain-rate vs time chart

Figure 8.8b, showing the strain rate – time plot in semi-logarithmic scale, confirms the anomalous behavior of this sample. The initial trend of decreasing strain rate is drastically interrupted by a sudden increase at time of about $2 \cdot 10^6$ s, that brings the strain rate to a value of $1 \cdot 10^{-9}$ s^{-1}. A new phase of strain deceleration, however, brings

to the new assessment of strain rate to the general mean values of the dataset (between $1 \cdot 10^{-10}$ $1 \cdot 10^{-11}$ s^{-1}).

8.3.3 Constitutive model

Nedjar and Le Roy, 2013 proposed a constitutive model for the uniaxial short-term strength and long-term creep tests in gypsum rock. The model was created and calibrated on the experimental results reported in Moirat et al. 2006 (i.e. creep tests on saccharoid gypsum samples under uniaxial load and water-saturated conditions). It offers an accurate simulation of creep behaviour of gypsum. However, the formulation is calibrated on saturated conditions, not including the relative humidity (or the saturation) as a variable. In order to provide a constitutive contribution able to include the variation of humidity, we propose an integration into the Nedjar and Le Roy, 2013 model.

The original model, consisting on the parameters reported in Table 8.3, can be described, in a one dimension simplified version (used for the here-presented simulations), with the following formulation:

$$\sigma = (1 - D)E(\varepsilon - \varepsilon^{v}) \qquad (1)$$

where σ and ε are axial stress and axial strain, E is the Young modulus and D and ε^{v} are two internal variables describing the damage and the viscous part of the strain respectively. Since the model relies on the definition of these two internal variables, a brief description of the elements that compose them is provided hereafter.

Table 8.3 Parameters of the Nedjar and Le Roy, 2013 model and reference values used for the sensitivity analysis in Figures 8.10, 8.11 and 8.12

	Damage parameters	**Unit of measure**	**Values in the A-type curves at RH=50%**
E	Elastic modulus (Young modulus)	MPa	2900
W	Damage Threshold	MPa	5.5E-3
ζ_1	Parameter of the source of damage	MPa	2250
m_1	Damage exponent component	*Dimensionless*	5
m_2	Damage exponent component	*Dimensionless*	2
m_3	Damage exponent component	*Dimensionless*	1

Viscous strain parameters		Unit of measure	
τ_i *(vector of two elements)*	Relaxation time	h	[83; 2000]
ω_i *(vector of two elements)*	Stiffness factor	*Dimensionless*	[0.21; 0.28]

The first internal variable (damage D) of equation 1 is a scalar between 0 and 1 (where 0 is undamaged and 1 completely damaged). Its formulation remains unmodified in the short-term and long-term behaviour of the material. This means that, once the parameters are defined for the instantaneous behaviour, they can be directly used for the simulation of creep. The definition of damage is controlled by three elements:

1. the function **S(ε)**, describing the **source of the damage**, that depends on the history of total strains. It is defined by the parameter ζ_1, following

$$S(\varepsilon) = \frac{1}{2}\zeta_1\{((\langle\varepsilon_1\rangle^+)^2 + (\langle\varepsilon_2\rangle^+)^2 + (\langle\varepsilon_3\rangle^+)^2\} \qquad (2)$$

where $\langle\varepsilon_n\rangle^+$ is the extensional contribution of the n component of the strain tensor.

2. the '**damage exponent**' m, that depends on three sub-parameters (m_1, m_2 and m_3) and is written as a damage-dependent variable in the form:

$$m(D) = m_1(1 - D)m_2 + m_3 \qquad (3)$$

It controls the evolution of damage and indirectly defines the hardening/softening behaviour of the material.

3. the **damage threshold W**, that controls the initialisation of damage. It is imposed to be $(1 - D)^m S(\varepsilon) \leq W$. When the quantity $(1 - D)^m S(\varepsilon)$ exceeds the threshold (i.e. the inequality $(1 - D)^m S(\varepsilon) < W$ is not verified), the damage D, initialised as 0 at the beginning of the test, starts to increase, following the time derivative, computed as:

$$\dot{D} = \frac{1-D}{mS(\varepsilon)}\dot{S}(\varepsilon) \qquad (4).$$

In the short-term uniaxial test curves, the first point where the equality $(1 - D)^m S(\varepsilon) = W$ is verified corresponds to the elastic onset, when the material behaviour departs from the linear elastic curve. For a fixed value of ζ_1, the parameter W can be therefore determined using the strain value measured in the onset point, where the damage is still 0 and the equality can be written as $S(\varepsilon) = W$.

The second internal variable (viscous strain ε^v) is defined as the sum of a number l of contributions following:

$$\varepsilon^v = \sum_{i=1}^{l} \varepsilon_i^v \qquad\qquad (5)$$

Each i-th element ε_i^v includes an elastic and a viscous contributions, as illustrated in the rheological model (Figure 8.9). The elastic and the viscous parts of the i-th elements are defined by a stiffness parameter (E_i) and a viscosity parameter (η_i) respectively. These material parameters appear in the model in terms of relaxation time ($\tau_i = \eta_i/ E_i$) and stiffness factor ($\omega_i = E/E_i$, where E is the Young modulus). In order to simulate the test progress, the increment of the internal variable ε^v for a small time interval Δt is iteratively calculated with the following equation:

$$\varepsilon_{i,n+1}^v = \varepsilon_{i,n}^v + \frac{\omega_i}{\tau_i}\Delta t(\varepsilon_n - \varepsilon_n^v) - \frac{\Delta t}{\tau_i}\varepsilon_{i,n}^v \qquad\qquad (6)$$

where ε_i^v corresponds to each element of ε^v (for $i=1$,..., l) and n and $(n+1)$ represent two consecutive time instants, where $t_{n+1} - t_n = \Delta t$. Following equation 5, the value of ε^v in each time step is then calculated as the sum of the l contributions ε_i^v.

In our simulation, the number l of contributions was fixed to 2. The viscous strain ε^v, as well as the relaxation time (τ_i) and the stiffness factor (ω_i), are, therefore, vectors of two elements.
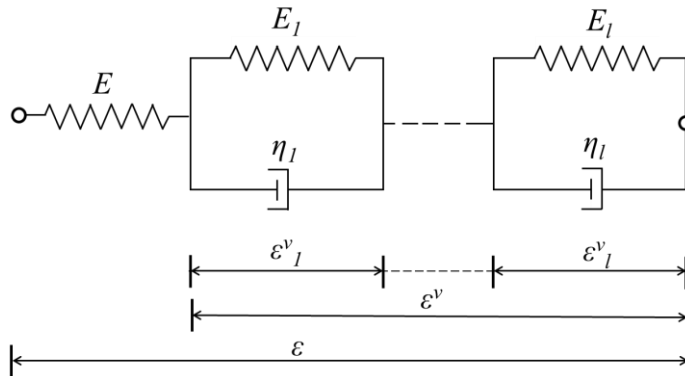

Figure 8.9 One dimensional rheological model by Nedjar and Le Roy, 2013

In order to introduce the humidity variable in the model, a sensitivity analysis was first performed to evaluate the influence of each parameter on the modelled curves. The graphs in Figures 8.10, 8.11, 8.12 show the results of a set of simulations performed using as reference the modelled curves obtained with the set of parameters reported in Table 4. These parameters were calibrated using as reference the stress-strain curves of the uniaxial tests with free environmental relative humidity (with a peak strength of 20 MPa and a correspondent strain of 0.01 – Figure 8.5a). For the creep test, a constant stress of 10 MPa was considered. The graphs, obtained by varying the 8 parameters, one by one, in a certain range, describe the specific influence of each of them on the final curves.

The Young Modulus E (Figure 8.10a-b) is the most effective parameter on both short- and long-term curves. An increase in E tends to increase the strength and decrease the creep propensity of the material.

The damage threshold W and the source of damage parameter ζ_1 (Figures 8.10c-d and e-f) have similar effects, even if inverted. They are, indeed, both involved in the inequality that controls the damage activation $((1 - D)^m S(\varepsilon) \leq W)$. Both parameters affect the UCS curves modifying the position of the onset point and, consequently, the final strength and strain. They also have a visible effect on the creep deformation. It is, however, possible to identify a 'minimum creep curve' corresponding to the absence of damage (i.e. the strains are, for the entire duration of the creep test, too low to overcome of the damage threshold). Below that curve, the effect of all the damage-related parameters is null.
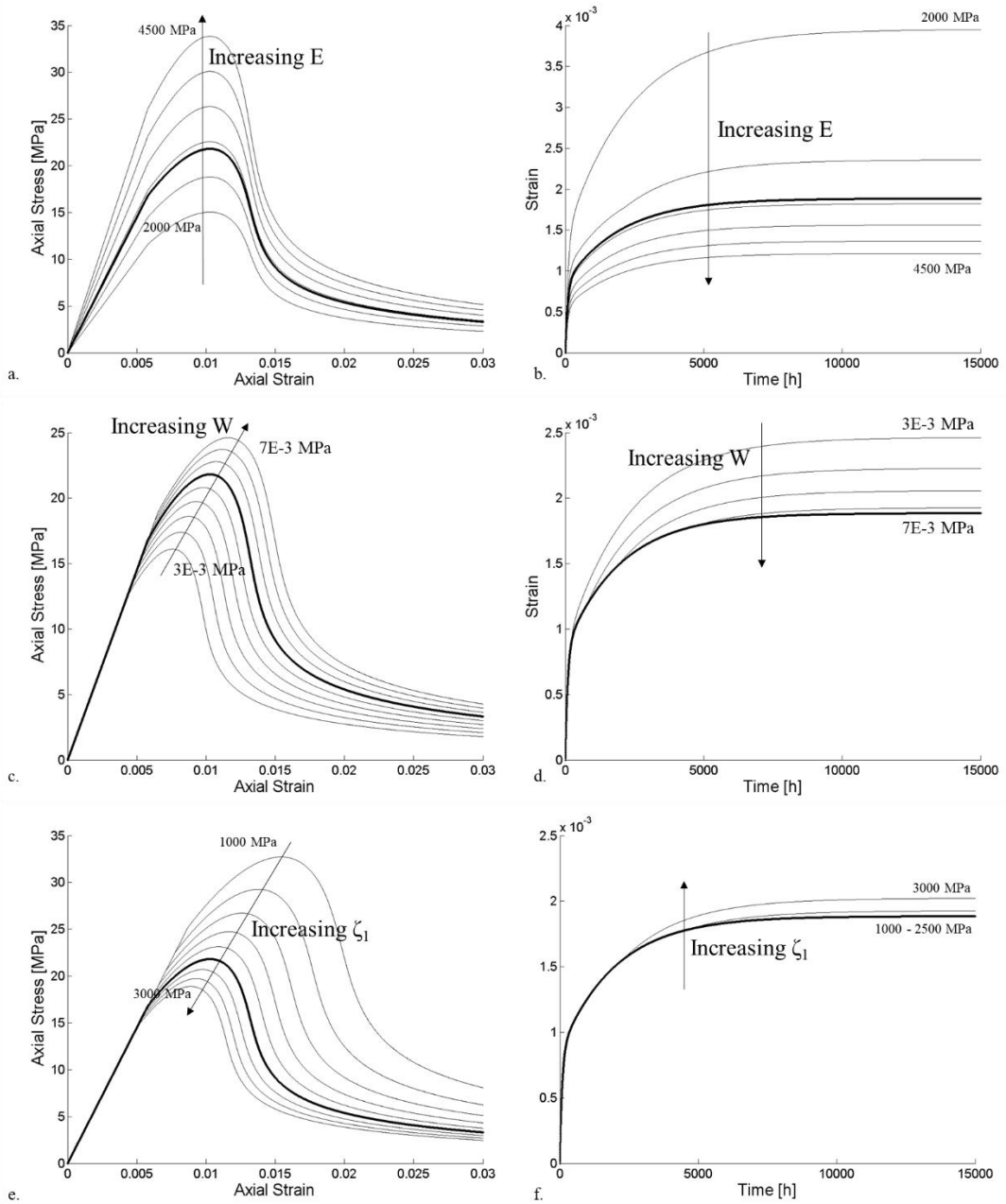
Figure 8.10 Sensitivity analysis of the damage-related model parameters. a-b Effect of the Young Modulus E on the UCS and creep curves. c-d Effect of the damage threshold W. e-f Effect of the source of damage parameter ζ_1. The reference curve (thick line) refers to the parameters in Table 4.

The parameters related with the definition of the m-exponent (m_1-m_2-m_3 – Figure 8.11) are only effective in the short-term regime, changing the shape of the curve. They are, however, ineffective in the long-term regime in the considered stress and strain conditions, since the damage threshold is not overcame during the creep test.

Their effect, indeed, being related to the evolution of damage, is subordinate to the parameters of damage threshold: if the threshold is not exceeded, their effect is null.
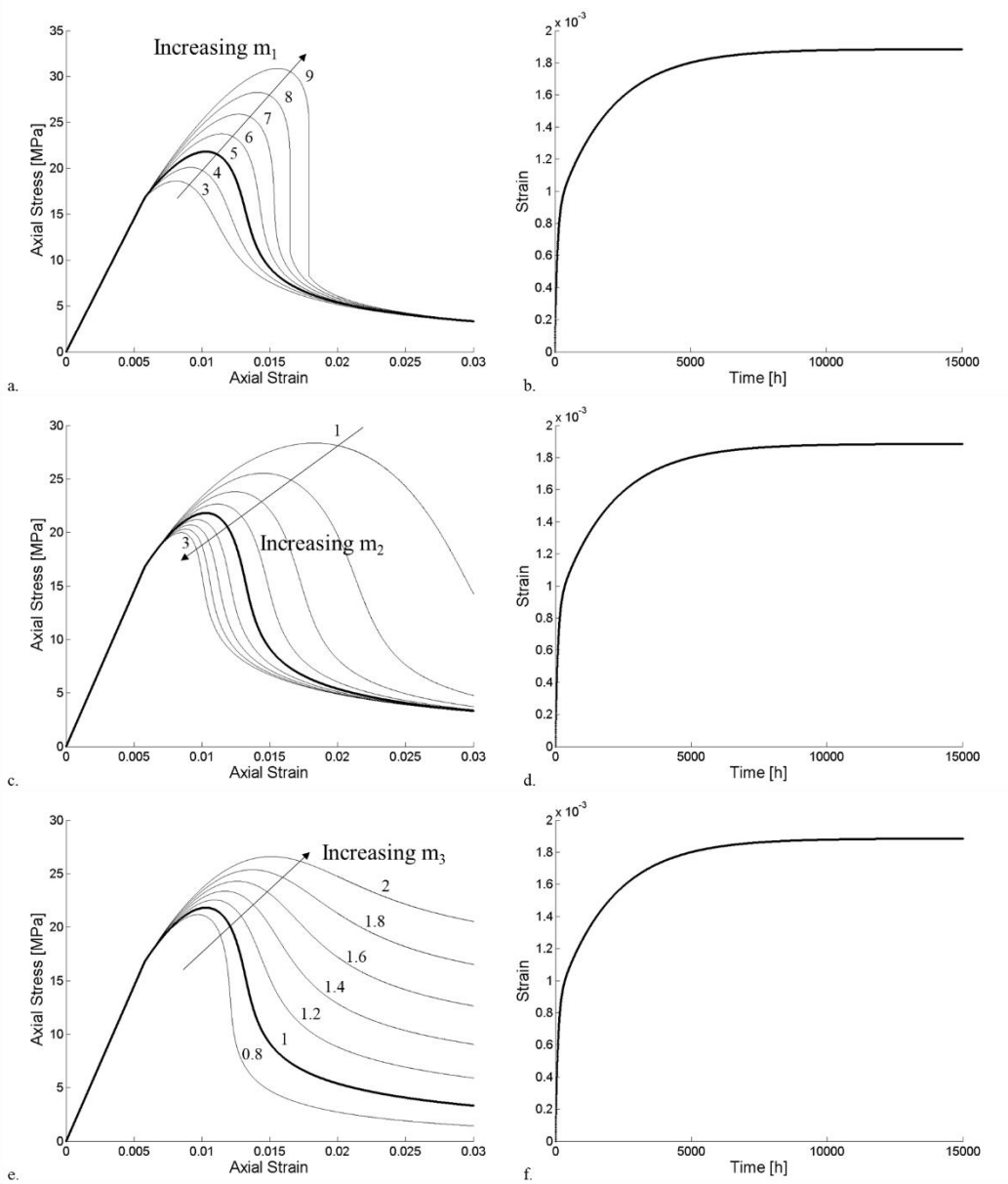
Figure 8.11 Sensitivity analysis of the damage-related model parameters. a-b Effect of m_1. c-d Effect of m_2. e-f Effect of m_3. The reference curve (thick line) refers to the parameters in Table 4.

Since the viscous strain-related parameters (τ and ω) only influence the time-dependent behaviour by definition, the sensitivity analysis on the short-term curves is not reported. Figure 8.12 shows, on the other hand, the influence of an increase in

relaxation time (τ) and stiffness factor (ω) on the creep curves. As can be seen, the relaxation time has the sole effect of changing the shape of the curve (i.e. how fast the transient phase is concluded). The influence of the stiffness factor is more effective, inducing big changes in the measured strains.
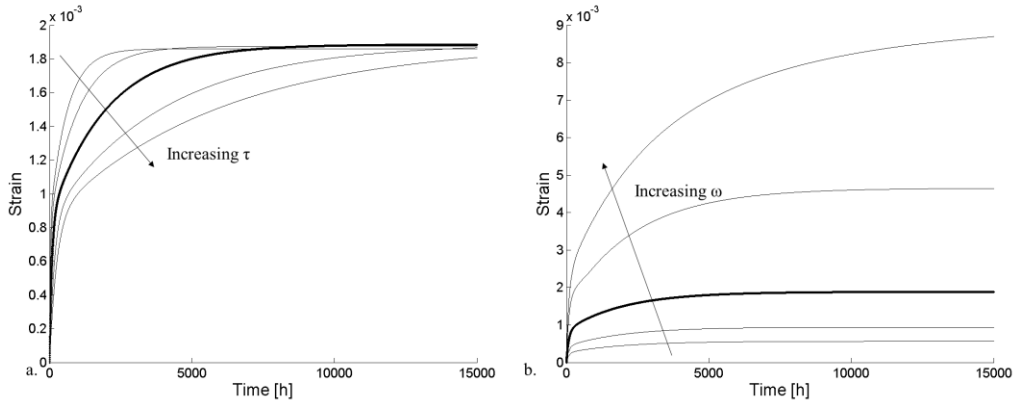
Figure 8.12 Sensitivity analysis of the viscous strain-related model parameters. a. Effect of the relaxation time (τ) on the creep curves. b. Effect of the stiffness factor (ω) on the creep curves. The reference curve (thick line) refers to the parameters in Table 8.3.

Based on these information, the effect of the relative humidity on the experimental results was described by working on the Young Modulus and the Damage Threshold W (i.e. the two most effective parameters on both short-term and long-term curves). Due to the low sensitiveness of short-term behaviour to the changes in relative humidity below 50%, we assumed the existence of a threshold value of relative humidity (that we fixed at RH = 50%, for the absence of further constraints) that triggers the change in the damage mechanism.

Figures 8.13a-b propose the best-fitting curves for the experimental results of short-term tests. Starting from the parameters reported in Table 4, the Young Modulus E and the Damage Threshold W were modified until the best fitting of the all the experimental data was obtained. The final values of E and W are reported in Figures 8.13c-d, as a function of the relative humidity, obtaining two formulations (for A-type and B-type gypsum respectively) that quantify this humidity-related change of damage mechanism. The equations reported in Figures 8.13c-d describe, therefore, how the Young Modulus and the Damage Threshold change if the relative humidity exceeds the threshold of 50%.
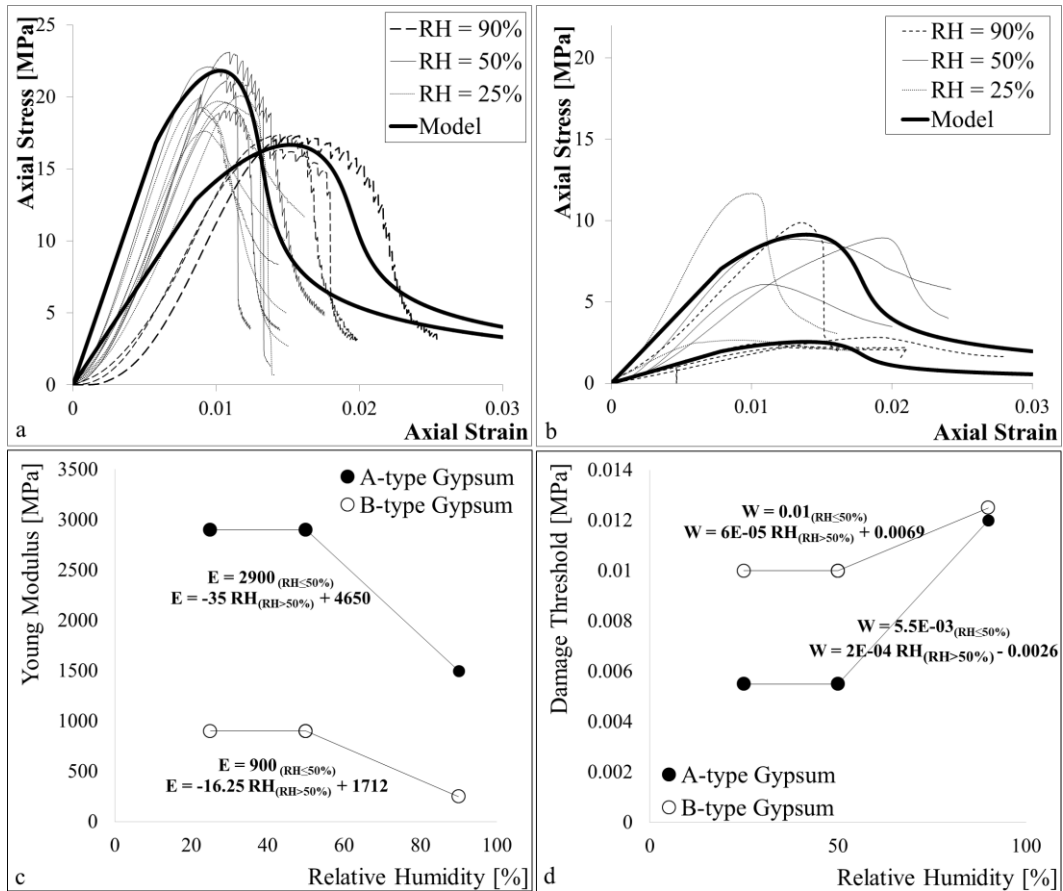
Figure 8.13 Experimental and modelled curves for A-type (a) and B-type (b) gypsum. c. Dependence of the Young Modulus on the relative humidity. d. Dependence of the damage threshold on the relative humidity

Unlike the short-term strength tests, the creep tests registered a certain sensitivity also to the changes in relative humidity below 50%, requiring the introduction of an additional mechanism. Based on the sensitivity analysis in Figure 8.12, the more effective stiffness factor (ω) was selected to simulate this mechanism.

The curve fitting reported in Figure 8.14 follows the relationships proposed in Figure 8.13. In addition, the stiffness factor was adjusted in order to obtain the best possible fitting. In Figure 8.14b (i.e. creep curves in free environmental humidity) values of RH=40% and RH=60% were considered for the tests performed in Turin and in Barcelona laboratory respectively. The final result describes well experimental data, even if in Figure 8.14b some of the curves (e.g. the creep test under 10 MPa) are completely out of trend.

The best fitting values of stiffness factor are reported in Figure 8.15 as a function of the relative humidity, allowing for the definition of a logarithmic dependence equation.
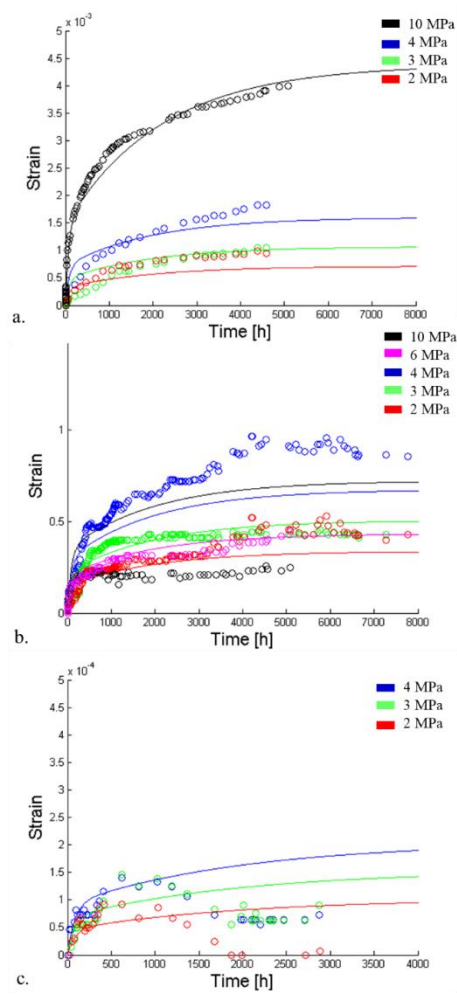
Figure 8.14 Data (dots) and model (lines) creep tests in conditions of high relative humidity (a), free laboratory humidity (b) and low relative humidity (c)
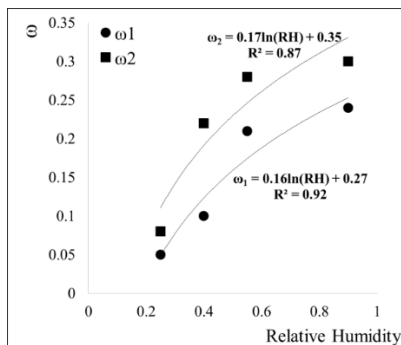
Figure 8.15 Dependence of the stiffness factor on the relative humidity.

8.4 Discussion of the results

The experimental results presented in this Chapter underlined the clear decrease in short-term strength and stiffness of gypsum rock under conditions of high relative humidity. However, the entity of strength reduction (about 25%) is lower than the strength reduction described in Chapter 7 in presence of water saturation (about 50%). In addition, despite the high relative humidity, the post-peak behaviour remains characterized by the presence of an unstable stress-drops behaviour. These evidences seem to suggest that, even if the water molecules in the atmosphere clearly produce an effect on the mechanical response, the absence of water in liquid state does not completely triggers the dissolution effects observed in water-saturated conditions.

The strong influence of relative humidity on the material strength was also observed in B-type samples. Despite the heterogeneity of this material group, the results clearly show a fall of strength to very low values (i.e. 2 MPa).

The test results showed, in all the tests on B-type material, the absence of the stress-drops that seem to characterize the post-peak behaviour of all branching selenite samples in dry conditions. Following the microstructural characterization presented in Chapter 4, B-type material is characterized by the frequent presence of dissolution structures (i.e. microcracks and detachments along the grain boundaries). The similarity of these structures with the ones produced by the coupled effect of water and uniaxial compression in Chapter 7 suggests that the pre-existence of microcracks and dissolution structures in B-type material, besides to be the cause of its lower strength, may also imply the not-development of the unstable step-wise failure coalescence process.

The presence of high relative humidity strongly influences also the creep response of the material (only tested for A-type samples). With relative humidity of 90%, the creep tests registered strain rates of one order of magnitude higher than the equivalents in free-environmental humidity for the entire test duration.

Chapter 9

From the sample-scale to the site-scale: some discussion on the scale effect and general conclusions

The present PhD Thesis proposed an investigation of the mechanical behaviour of gypsum rock under the influence of material features and external parameters. In particular, the Thesis focused on the material heterogeneity and anisotropy, on the weakening effect of water and on the time-dependent response. The research dealt with the gypsum facies called 'branching selenite', poorly investigated despite its strategical importance in stratigraphic reconstructions and orebody evaluation all over the Mediterranean basin.

Aim of this Chapter is to provide a review of the obtained results, introducing some considerations on the scale effect and contextualizing the laboratory results in the framework of underground excavation.

9.1 Summary of the results and scale effect

9.1.1 Material heterogeneity

The results of the physical-chemical characterization presented in Chapter 4 suggested that branching selenite gypsum has a primary variability that is consequence of the macroscale structure (i.e. big "branches" of coarse gypsum immersed into the finer-grained gypsiferous matrix). The mesoscale features of the rock (i.e. the size distribution of the crystals, the porosity and the mineralogical composition) depend on the position of the sample in this structure (e.g. within the branches of coarser gypsum or in the surrounding material, with higher or lower concentration of coarser lenses).

The microstructural analyses highlighted, in addition to this primary heterogeneity, the evidences of a worsening of some portions of the rock for effect of water dissolution processes. The data suggest, indeed, that the long permanence of karst water in portions of the rock-mass have been producing changes in the microstructure, opening microcracks, big pores and structures of detachment along the grain boundaries.

Figure 9.1 proposes a schematization of a hypothetical branching selenite gypsum layer that aims to show the distribution in the rock-mass of these heterogeneities (both primary and water-induced). The internal organization of the gypsum layer is controlled by the presence of the elongated gypsum branches, that influence both the material heterogeneity and the anisotropy orientation. The scheme reports five tunnels in different relationships with the rock structure, to exemplify some typical situations.
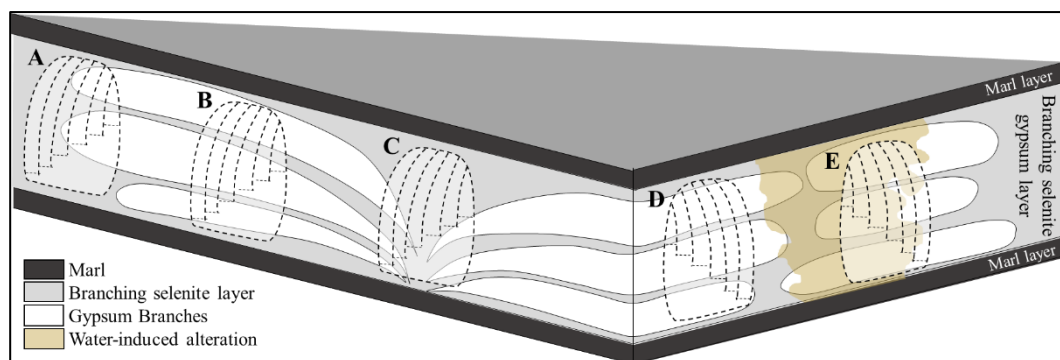
Figure 9.1 Schematic representation of the branching selenite structure. The scheme includes 5 hypothetical tunnels in different position of the structure. Tunnel A is peripheral with respect to the origin of the branches. The rock in that point will be finer and with lower gypsum content. Tunnel B is narrow to the branches origins, with a consequent coarser grain size and higher gypsum content in the rock. Tunnel C is in correspondence of the origin of the branches. In this position, the orientation of the layering is inclined. Tunnel D, differently from tunnels A-B-C, is oriented perpendicular to the elongation of the branches. Tunnel E is in correspondence of a karst area, with water-induced modification of the rock microstructure.

Tunnel A is in a peripheral position with respect to the nucleation point of the branches. In this position, the gypsum lenses are smaller and the rock is characterized by a predominant fine matrix, creating a situation similar to Figure 9.2a. Tunnel B, on the other hand, is near to the branches origin. In this case, the rock is coarser and has higher gypsum content. The rock appearance could be, therefore, more similar to Figure 9.2b. In addition to this primary variability, Figure 9.1 exemplifies the possibility of a local development of karst dissolution (tunnel E). In these conditions, a microstructural worsening of rock properties has to be expected.

Figure 9.2 Excavation faces in underground tunnels in branching selenite gypsum with different macro-textural features. a. Small gypsum nodules in a predominant fine matrix. b. Big coarse gypsum branches with lower concentration of finer matrix.

The overall heterogeneity of the material was schematized, in the framework of the Thesis, with the definition of two end-members (A-type and B-type gypsum, describing respectively a good quality material, with compact structure, fine grain size and low porosity, and a poorer material, with coarse grain size, layering mainly

consisting of phyllosilicate minerals and microstructures related to water dissolution).

The characterization presented in Chapter 5 showed that this material heterogeneity results in a significant variability of the mechanical response. Uniaxial short-term tests returned strength ranges of 12-20 MPa and 5-10 MPa for A-type and B-type gypsum respectively.

In the framework of underground excavations, the consideration of the material heterogeneity assumes, therefore, a fundamental role for the stability assessment. In the drift portions where B-type material is prevalent (e.g. in presence karst phenomena, as in tunnel E in Figure 9.1), a mean strength value, representative of the entire rock body, would be largely overestimated, creating serious risk scenarios. On the other hand, the size of underground pillars mainly composed of good quality material (A-type gypsum) may be overestimated if a mean value of strength is considered.

The results of mechanical tests showed an additional distribution of the strength parameters along the vertical of the gypsum layer. Figure 9.3 shows the distribution of strength values (in terms of Point Load Strength Index Is_{50}) against the layer thickness for two of the drilled cores investigated in the Thesis. The drilled cores refer to rock portions with prevalent A-type and B-type features respectively. As can be seen, in both the cases the strength parameter decreases at the top and at the bottom of the layer.
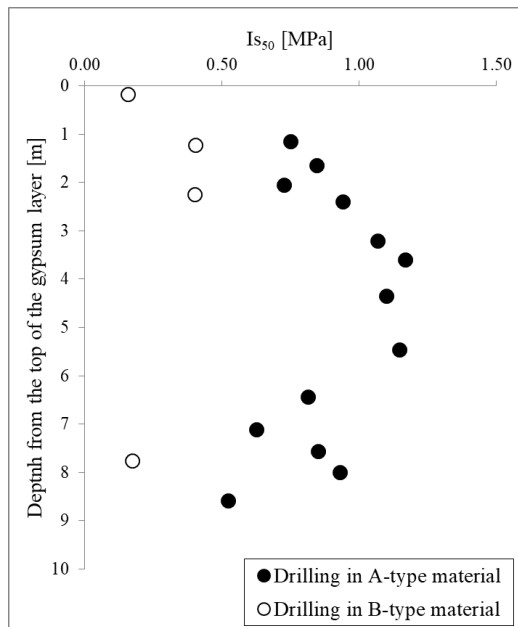

Figure 9.3 Distribution of Strength Index (from Point Load tests) along the layer thickness in two representative drillings

This strength distribution reflects the gradual transition of sedimentary conditions at the beginning and at the end of the gypsum cycle. The change of paleo environmental conditions from more humid (i.e. marl deposition), to arid (i.e. gypsum precipitation) to new humid conditions is gradual. As a consequence, the bottom and the top of the gypsum layers are often characterized by transitional features (e.g. coarser grain size, higher marl content) that may cause the softening of mechanical response.

This sedimentary-induced softening of mechanical strength may generate structural problems to the overall stability of underground excavation, since the top and the bottom of the layer usually correspond to weak structural elements (e.g. tunnel roof and floor portions).

9.1.2 Anisotropy orientation

The schematization of the rock body proposed in Figure 9.1 exemplifies another potential risk factor due to the branching selenite structure: the change of orientation of the anisotropic layering. As described in the Figure, despite the mean horizontal orientation of the gypsum branches in tunnels A and B, the structure defines a moderate to very inclined orientation of the layering in correspondence of the nucleation point (tunnel C). As shown by the experimental results presented in Chapter 6, the orientation of mesoscale anisotropy (layering) strictly controls the mechanical response and, in particular, the process of crack coalescence. Intermediate angles of anisotropy, with weak surfaces orientated almost parallel to the final angle of failure, facilitate the failure coalescence, reducing the bulk strength of the material. Hence, the stratigraphic configuration of tunnel C may create disadvantageous conditions for the tunnel stability.

In addition, DIC analysis on samples with horizontal anisotropy testified the easier failure propagation in parallel direction to the rock lineation (i.e. linear orientation of gypsum crystals and nodules). This lineation is, again, a consequence of the orientation of the gypsum branches. As shown in the zoomed scheme in Figure 9.4, indeed, the gypsum branches are elongated in parallel direction to the red dashed lines.
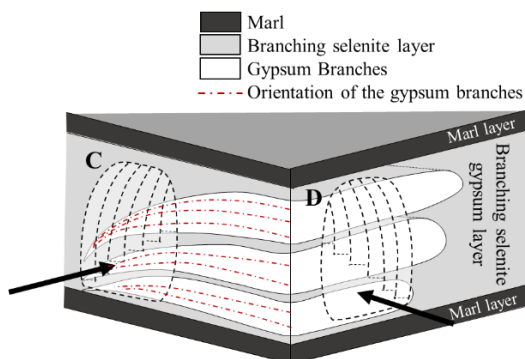

Figure 9.4 Detail of Figure 9.1, showing the relationship between branches orientation and tunnels direction.

In Figures 9.1 and 9.4, the orientation of tunnels have, therefore, different relationships with the branches elongation direction: tunnels A, B and C are parallel, tunnels D and E are perpendicular. The interaction between these two oriented elements may influence the general stability of the quarry.

9.1.3 Weakening effect of water and relative humidity

As discussed in Chapter 2, the existence of a water-related worsening of the mechanical properties of gypsum rock is largely documented in the scientific literature. The gypsum-water interaction triggers a weakening mechanism that is largely more effective than the simple mechanical effect due to the presence of a fluid (i.e. overpressure).

Underground gypsum bodies are often water saturated or partially-saturated. The excavation of underground tunnels usually requires de-watering operations (e.g. pumping). Even when liquid water is not present, the atmosphere of the underground drifts may have high relative humidity that triggers the water-gypsum interaction mechanisms.

The mechanical tests described in Chapter 7 showed a decrease of gypsum strength of 50% in water saturated conditions. The additional experimental investigation presented in Chapter 8 underlined a clear decrease in strength and stiffness also in presence of high relative humidity (i.e. RH higher than 90%), while low or absent changes in the mechanical response were observed for relative humidity ranging between 50% and 25%.

Results of Chapter 8 also showed how the effect of water worsening on intrinsic low-quality material (e.g. B-type gypsum) may create very disadvantageous mechanical conditions, with peak strength values of only 2 MPa.

The mechanical and microstructural evidences suggested the existence of a weakening mechanism based on the progressive dissolution of gypsum along the grain boundaries. This dissolution process, propagating from the pores and microcracks edges, brings to an important reduction of the bulk strength of the rock, since the tensional strength of the intra-crystalline connections drastically falls. Under the effect of an external applied stress, the water further intrudes the rock pores and generates additional cracks along the grain boundaries and within the crystals, following the mineral cleavage along the 010 crystallographic surface.

This kind of weakening effect is not only related to the uniaxial stress conditions. Triaxial tests (reproducing stress configurations generally more common in the real site frameworks) registered a clear decrease of yield point in presence of water. Even when the behaviour becomes completely strain hardening and the failure coalescence

is completely replaced by plastic structures (i.e. grain kinking), the weakening effect of water is still evident.

9.1.4   Time dependent behaviour

Experimental results presented in Chapter 7 and Chapter 8 showed the existence of an intense time-dependent deformation in branching selenite gypsum, subjected to the presence of water. In water-saturated conditions, creep failure was observed after short times (i.e. few days) under stress levels correspondent to 85% of the peak strength. The record of creep strains of 0.4% and strain rate of $1\cdot10^{-10}$ s^{-1} over a period of 6 months was registered under an applied stress of 10 MPa (about 60% of the peak strength) in conditions of high relative humidity (RH = 90%).

Chapter 8 proposed a constitutive contribution that models the short-term and long-term response of gypsum in uniaxial stress conditions. The model was adapted from the scientific literature to include the relative humidity as a variable, allowing for a realistic representation of the underground natural conditions, where, even in absence of complete water saturation, different ranges of relative humidity may be registered.

The time-dependent deformation and failure of rocks has a specific relevance in underground quarries, where the stress configuration implies the presence of static loads on the pillars over long time (several years or even decades). After the end of active exploitation, the conditions of long-term stability may be further compromised by the interruption of the pumping operations, involved in the dewatering of gypsum orebody during the exploitation. The consequent restoring of groundwater level brings to the new saturation of the rock mass, creating the environmental conditions that maximize the time-dependent deformations in gypsum rock. Furthermore, the flow of fresh water, potentially under-saturated in sulphates, could trigger important dissolution processes on the free surfaces of the drifts, worsening the mechanical quality of the material.

9.2 Future Research

The Thesis provided a physical-chemical and mechanical characterization of branching selenite gypsum facies. The macroscale texture and structure of the material, with specific features of heterogeneity and anisotropy, was considered in order to propose an evaluation of the influence on the mechanical response. The additional influence of water, relative humidity and time factor was evaluated and considered in a wide experimental investigation.

Possible extensions of this work may include the development of a micro-mechanical modeling of the mechanisms of water-induced softening and time-dependent deformation of gypsum rock, with a numerical simulations of the effect of water dissolution.

Another interesting development of this research may include the application of the presented methodologies to the investigation of other gypsum facies and other evaporitic rocks (e.g. anhydrite). As instance, the presence in the northwestern Italian Alps of big volumes of evaporitic rocks (gypsum and anhydrite rocks, traditionally ascribed to the Triassic age) may require an attentive investigation for the possible implications of mechanical response on tunneling and civil infrastructures.

References

Chapter 1

Auvray, C., 2003. Vieillissement et comportement rhéologique du gypse (PhD Thesis). Unpublished.

Auvray, C., Homand, F., Sorgi, C., 2004. The aging of gypsum in underground mines. Eng. Geol. 74, 183–196. https://doi.org/10.1016/j.enggeo.2004.03.008

Castellanza, R., Nova, R., Orlandi, G., 2010. Evaluation and remediation of an abandoned gypsum mine. J. Geotech. Geoenvironmental Eng. 136, 629–639. https://doi.org/10.1061/(ASCE)GT.1943-5606.0000249

Lugli, S., Manzi, V., Roveri, M., Schreiber, C.B., 2010. The Primary Lower Gypsum in the Mediterranean: A new facies interpretation for the first stage of the Messinian salinity crisis. Palaeogeogr. Palaeoclimatol. Palaeoecol. 297, 83–99. https://doi.org/10.1016/j.palaeo.2010.07.017

Sadeghiamirshahidi, M., Vitton, S.J., 2019. Laboratory Study of Gypsum Dissolution Rates for an Abandoned Underground Mine. Rock Mech. Rock Eng. 52, 2053–2066. https://doi.org/10.1007/s00603-018-1696-6

Van Driessche, A.E.S., Stawski, T.M., Kellermeier, M., 2019. Calcium sulfate precipitation pathways in natural and engineering environments. Chem. Geol. 119274. https://doi.org/10.1016/j.chemgeo.2019.119274

Wang, J.-A., Shang, X.C., Ma, H.T., 2008. Investigation of catastrophic ground collapse in Xingtai gypsum mines in China. Int. J. Rock Mech. Min. Sci. 45, 1480–1499. https://doi.org/10.1016/j.ijrmms.2008.02.012

Xia, K., Chen, C., Zhou, Y., Liu, X., Zheng, Y., Pan, Y., 2019. Catastrophe Instability Mechanism of the Pillar-Roof System in Gypsum Mines Due to the Influence of Relative Humidity. Int. J. Geomech. 19, 06019004. https://doi.org/10.1061/(ASCE)GM.1943-5622.0001378

Chapter 2

Alonso, E. e., Ramon, A., 2013. Heave of a railway bridge induced by gypsum crystal growth: field observations. Géotechnique 63, 707–719. https://doi.org/10.1680/geot.12.P.034

Alonso, E.E., Sauter, S., Ramon, A., 2015. Pile groups under deep expansion: a case history. Can. Geotech. J. 52, 1111–1121. https://doi.org/10.1139/cgj-2014-0407

Alonso, E. E., Berdugo, I.R., Ramon, A., 2013. Extreme expansive phenomena in anhydritic-gypsiferous claystone: the case of Lilla tunnel. Géotechnique, 63(7), 584–612 http://doi.org/10.1680/geot.12.P.143

Auvray, C., Homand, F., Sorgi, C., 2004. The aging of gypsum in underground mines. Eng. Geol. 74, 183–196. https://doi.org/10.1016/j.enggeo.2004.03.008

Bing, D., Guicheng, H., Zhijun, Z., 2018. A Numerical Research on Crack Process of Gypsum Containing Single Flaw with Different Angle and Length in Uniaxial Loading [WWW Document]. Shock Vib. https://doi.org/10.1155/2018/2968205

Bobet, A., Einstein, H.H., 1998. Fracture coalescence in rock-type materials under uniaxial and biaxial compression. Int. J. Rock Mech. Min. Sci. 35, 863–888. https://doi.org/10.1016/S0148-9062(98)00005-9

Bonetto, S. 2006 "Il gesso: da risorsa economica a patrimonio culturale del Monferrato. Aggiornamento tecnico, metodologie operative e ipotesi di riuso dei siti di cava dimessi." Doctorate Thesis, Politecnico di Torino. Unpublished.

Brantut, N., Schubnel, A., Guéguen, Y., 2011. Damage and rupture dynamics at the brittle-ductile transition: The case of gypsum. J. Geophys. Res. Solid Earth 116. https://doi.org/10.1029/2010JB007675

Castellanza, R., Gerolymatou, E., Nova, R., 2008. An Attempt to Predict the Failure Time of Abandoned Mine Pillars. Rock Mech. Rock Eng. 41, 377–401. https://doi.org/10.1007/s00603-007-0142-y

Castellanza, R., Nova, R., Orlandi, G., 2010. Evaluation and remediation of an abandoned gypsum mine. J. Geotech. Geoenvironmental Eng. 136, 629–639. https://doi.org/10.1061/(ASCE)GT.1943-5606.0000249

Čebašek, T.M., Frühwirt, T., 2018. Investigation of creep behaviours of gypsum specimens with flaws under different uniaxial loads. J. Rock Mech. Geotech. Eng. 10, 151–163. https://doi.org/10.1016/j.jrmge.2017.11.002

Chen, Z., Sucech, S., Faber, K.T., 2010. A hierarchical study of the mechanical properties of gypsum. J. Mater. Sci. 45, 4444–4453. https://doi.org/10.1007/s10853-010-4527-z

Craker, W.E., Schiller, K.K., 1962. Plastic deformation of gypsum. Nature 193, 672–673. https://doi.org/10.1038/193672a0

de Meer, S., Spiers, C.J., 1999. Influence of pore-fluid salinity on pressure solution creep in gypsum. Tectonophysics 308, 311–330.

de Meer, S., Spiers, C.J., 1997. Uniaxial compaction creep of wet gypsum aggregates. J. Geophys. Res. Solid Earth 102, 875–891. https://doi.org/10.1029/96JB02481

de Meer, S., Spiers, C.J., 1995. Creep of wet gypsum aggregates under hydrostatic loading conditions. Tectonophysics, Influence of Fluids on Deformation Processes in Rocks 245, 171–183. https://doi.org/10.1016/0040-1951(94)00233-Y

Fan, C., Teng, H.H., 2007. Surface behavior of gypsum during dissolution. Chem. Geol. 245, 242–253. https://doi.org/10.1016/j.chemgeo.2007.08.007

Heidari, M., Khanlari, G.R., Torabi Kaveh, M., Kargarian, S., 2012. Predicting the Uniaxial Compressive and Tensile Strengths of Gypsum Rock by Point Load Testing. Rock Mech. Rock Eng. 45, 265–273. https://doi.org/10.1007/s00603-011-0196-8

Hoxha, D., Giraud, A., Homand, F., 2005. Modelling long-term behaviour of a natural gypsum rock. Mech. Mater. 37, 1223–1241. https://doi.org/10.1016/j.mechmat.2005.06.002

Hoxha, D., Homand, F., Auvray, C., 2006. Deformation of natural gypsum rock: Mechanisms and questions. Eng. Geol. 86, 1–17. https://doi.org/10.1016/j.enggeo.2006.04.002

Lacidogna, G., Accornero, F., Carpinteri, A., 2019. Influence of snap-back instabilities on Acoustic Emission damage monitoring. Eng. Fract. Mech., Application of Acoustic Emission Techniques in Fracture Mechanics 210, 3–12. https://doi.org/10.1016/j.engfracmech.2018.06.042

Liang, W., Yang, X., Gao, H., Zhang, C., Zhao, Y., Dusseault, M.B., 2012. Experimental study of mechanical properties of gypsum soaked in brine. Int. J. Rock Mech. Min. Sci. 53, 142–150. https://doi.org/10.1016/j.ijrmms.2012.05.015

Liu, Z., Zheng, H., Li, M., 2019. Experimental Research on Creep Failure Characteristics of Gypsum Rock Based on Rock Longitudinal Wave Velocity. Geotech. Geol. Eng. 37, 1515–1522. https://doi.org/10.1007/s10706-018-0704-7

Meng, T., Xiangxi, M., Donghua, Z., Hu, Y., 2018. Using micro-computed tomography and scanning electron microscopy to assess the morphological evolution and fractal dimension of a salt-gypsum rock subjected to a coupled thermal-hydrological-chemical environment. Mar. Pet. Geol. 98, 316–334. https://doi.org/10.1016/j.marpetgeo.2018.08.024

Mirwald, P.W., 2008. Experimental study of the dehydration reactions gypsum-bassanite and bassanite-anhydrite at high pressure: indication of anomalous behavior of H(2)O at high pressure in the temperature range of 50-300 degrees C. J. Chem. Phys. 128, 074502. https://doi.org/10.1063/1.2826321

Moiriat, D., Potherat, P., Massieu, E., Durville, J.-L., 2006. Données expérimentales sur le fluage du gypse saccharoïde en condition saturée. Rev. Fr. Géotechnique 3–10. https://doi.org/10.1051/geotech/2006115003

Nedjar, B., Le Roy, R., 2013. An approach to the modeling of viscoelastic damage. Application to the long-term creep of gypsum rock materials: LONG-TERM CREEP OF GYPSUM ROCK. Int. J. Numer. Anal. Methods Geomech. 37, 1066–1078. https://doi.org/10.1002/nag.1138

Papadopoulos, Z., Kolaiti, E., Mourtzas, N., 1994. The effect of crystal size on geotechnical properties of Neogene gypsum in Crete. Q. J. Eng. Geol. 27, 267–273.

Ramon, A., Alonso, E. E., 2013. Heave of a railway bridge: modelling gypsum crystal growth. Géotechnique 63, 720–732. https://doi.org/10.1680/geot.12.P.035

Ramon, A., Alonso, E.E., 2018. Heave of a Building Induced by Swelling of an Anhydritic Triassic Claystone. Rock Mech. Rock Eng. 51, 2881–2894. https://doi.org/10.1007/s00603-018-1503-4

Ramon, A., Alonso, E.E., Olivella, S., 2017. Hydro-chemo-mechanical modelling of tunnels in sulfated rocks. Géotechnique 67, 968–982. https://doi.org/10.1680/jgeot.SiP17.P.252

Roy, M.G., Rao, K.S., 2015. Analysis of creep behaviour of soft rocks in tunneling. Presented at the ISEG-EGNM.

Sagong, M., Bobet, A., 2002. Coalescence of multiple flaws in a rock-model material in uniaxial compression. Int. J. Rock Mech. Min. Sci. 39, 229–241. https://doi.org/10.1016/S1365-1609(02)00027-8

Salih, N., and A. Mohammed, 2017. Characterization and Modeling of Long-Term Stress–Strain Behavior of Water Confned Pre-saturated Gypsum Rock in Kurdistan Region, Iraq. Rock Mech. Geotech. Eng. 9. https://doi.org/doi:10.1016/j.jrmge.2017.03.009

Schreiber, B.C., Tabakh, M.E., 2000. Deposition and early alteration of evaporites. Sedimentology 47, 215–238. https://doi.org/10.1046/j.1365-3091.2000.00002.x

Shen, B., Stephansson, O., Einstein, H.H., Ghahreman, B., 1995. Coalescence of fractures under shear stresses in experiments. J. Geophys. Res. Solid Earth 100, 5975–5990. https://doi.org/10.1029/95JB00040

Singh, R.N., Eksi, M., 1987. Rock characterization of gypsum and marl. Min. Sci. Technol. 6, 105–112. https://doi.org/10.1016/S0167-9031(87)90543-3

Tang, Y., Gao, J., Liu, C., Chen, X., Zhao, Y., 2019. Dehydration Pathways of Gypsum and the Rehydration Mechanism of Soluble Anhydrite γ-CaSO4. ACS Omega 4, 7636–7642. https://doi.org/10.1021/acsomega.8b03476

Wong, L.N.Y., Einstein, H.H., 2009a. Crack coalescence in molded gypsum and carrara marble: Part 1. macroscopic observations and interpretation. Rock Mech. Rock Eng. 42, 475–511. https://doi.org/10.1007/s00603-008-0002-4

Wong, L. N. Y., Einstein, H.H., 2009b. Crack Coalescence in Molded Gypsum and Carrara Marble: Part 2—Microscopic Observations and Interpretation. Rock Mech. Rock Eng. 42, 513–545. https://doi.org/10.1007/s00603-008-0003-3

Yilmaz, I., 2010. Influence of water content on the strength and deformability of gypsum. Int. J. Rock Mech. Min. Sci. 47, 342–347. https://doi.org/10.1016/j.ijrmms.2009.09.002

Yilmaz, I., 2007. Differences in the geotechnical properties of two types of gypsum: alabastrine and porphyritic. Bull. Eng. Geol. Environ. 66, 187–195. https://doi.org/10.1007/s10064-006-0055-0

Yılmaz, I., Sendır, H., 2002. Correlation of Schmidt hardness with unconfined compressive strength and Young's modulus in gypsum from Sivas (Turkey). Eng. Geol. 66, 211–219.

Yu, W.D., Liang, W.G., Li, Y.R., Yu, Y.M., 2016. The meso-mechanism study of gypsum rock weakening in brine solutions. Bull. Eng. Geol. Environ. 75, 359–367. https://doi.org/10.1007/s10064-015-0725-x

Zhu, C., Xu, X., Liu, W., Xiong, F., Lin, Y., Cao, C., Liu, X., 2019. Softening Damage Analysis of Gypsum Rock With Water Immersion Time Based on Laboratory Experiment. IEEE Access 7, 125575–125585. https://doi.org/10.1109/ACCESS.2019.2939013

Zucali, M., Barberini, V., Chateigner, D., Ouladdiaf, B., Lutterotti, L., 2010. Brittle plus plastic deformation of gypsum aggregates experimentally deformed in torsion to high strains: Quantitative microstructural and texture analysis from optical and diffraction data. Geol. Soc. Lond. Spec. Publ. 332, 79-98. doi:10.1144/SP332.6. https://doi.org/10.1144/SP332.6

Chapter 3

Bonetto, S., Fiorucci, A., Fornaro, M., Vigna, B., 2008. Subsidence hazards connected to quarrying activities in a karst area: the case of the Moncalvo sinkhole event (Piedmont, NW Italy). Est. J. Earth Sci. 57, 125. https://doi.org/10.3176/earth.2008.3.01

Bonetto, S., Fornaro, M., 2005. Subsidence events related to natural conditions and gypsum quarrying activity in the Monferrato area (Piedmont, NW Italy). Presented at the In Proceedings of MAEGS14 - 14th Meeting of the Association of European Geological Societies, Torino, 19-23 September 2005, pp. 61-62, -, p. .

CIESM, 2008. The Messinian Salinity Crisis from mega-deposits to microbiology - A consensus report.

Clari P, Dela Pierre F, Novaretti A, Timpanelli M. Late Oligocene Miocene sedimentary evolution of the critical Alps-Apennine junction: The Monferrato area, Northwestern Italy. Terra Nova 1995;7: 144-52.

Dal Cin, M., Del Ben, A., Mocnik, A., Accaino, F., Geletti, R., Wardell, N., Zgur, F., Camerlenghi, A., 2016. Seismic imaging of Late Miocene (Messinian) evaporites from Western Mediterranean back-arc basins. Pet. Geosci. 22, 297–308. https://doi.org/10.1144/petgeo2015-096

Dela Pierre, F., Bernardi, E., Cavagna, S., Clari, P., Gennari, R., Irace, A., Lozar, F., Lugli, S., Manzi, V., Natalicchio, M., Roveri, M., Violanti, D., 2011. The record of the Messinian salinity crisis in the Tertiary Piedmont Basin (NW Italy): The Alba section revisited. Palaeogeogr. Palaeoclimatol. Palaeoecol. 310, 238–255. https://doi.org/10.1016/j.palaeo.2011.07.017

Dela Pierre, F., Natalicchio, M., Lozar, F., Bonetto, S., Carnevale, G., Cavagna, S., Colombero, S., Sabino, M., Violanti, D., 2016. The northernmost record of the Messinian salinity crisis (Piedmont basin, Italy). Geol.F.Trips 8, 58.

Geostudio, 2018. Cava di gesso in sotterraneo "Franca" sita in località "Pietra" del Comune di Calliano (AT). Technical report.

Lugli, S., Manzi, V., Roveri, M., Schreiber, C.B., 2010. The Primary Lower Gypsum in the Mediterranean: A new facies interpretation for the first stage

of the Messinian salinity crisis. Palaeogeogr. Palaeoclimatol. Palaeoecol. 297, 83–99. https://doi.org/10.1016/j.palaeo.2010.07.017

Piana F, Polino R. Tertiary structural relationships between Alps and Apennines: The critical Torino Hill and Monferrato area, Northwestern Italy. Terra Nova 1995;7:138–43.

Rouchy, J.M., Caruso, A., 2006. The Messinian salinity crisis in the Mediterranean basin: A reassessment of the data and an integrated scenario. Sediment. Geol., The Messinian Salinity Crisis Revisited 188, 35–67. https://doi.org/10.1016/j.sedgeo.2006.02.005

Roveri, M., Flecker, R., Krijgsman, W., Lofi, J., Lugli, S., Manzi, V., Sierro, F.J., Bertini, A., Camerlenghi, A., De Lange, G., Govers, R., Hilgen, F.J., Hübscher, C., Meijer, P.Th., Stoica, M., 2014. The Messinian Salinity Crisis: Past and future of a great challenge for marine sciences. Mar. Geol., 50th Anniversary Special Issue 352, 25–58. https://doi.org/10.1016/j.margeo.2014.02.002

Vigna, B., D'Angeli, I., Fiorucci, A., Waele, J.D., 2017. Hydrogeological flow in gypsum karst areas: some examples from northern Italy and main circulation models. Int. J. Speleol. 46. https://doi.org/<p>https://doi.org/10.5038/1827-806X.46.2.2095</p>

Vigna, B., Fiorucci, A., Banzato, C., Forti, P., De Waele, J., 2010. Hypogene gypsum karst and sinkhole formation at Moncalvo (Asti, Italy). Z. Für Geomorphol. Suppl. Issues 54, 285–306. https://doi.org/10.1127/0372-8854/2010/0054S2-0015

Chapter 4

Buscombe, D., 2013. Transferable wavelet method for grain-size distribution from images of sediment surfaces and thin sections, and other natural granular patterns. Sedimentology 60, 1709–1732. https://doi.org/10.1111/sed.12049

Giesche, H., 2006. Mercury porosimetry: A general (practical) overview. Part. Part. Syst. Charact. 23, 9–19. https://doi.org/10.1002/ppsc.200601009

Heilbronner, R., Keulen, N., 2006. Grain size and grain shape analysis of fault rocks. Tectonophysics, Deformation mechanisms, microstructure and rheology of rocks in nature and experiment 427, 199–216. https://doi.org/10.1016/j.tecto.2006.05.020

Jutzeler, M., Proussevitch, A.A., Allen, S.R., 2012. Grain-size distribution of volcaniclastic rocks 1: A new technique based on functional stereology. J. Volcanol. Geotherm. Res. 239, 1–11. https://doi.org/10.1016/j.jvolgeores.2012.05.013

Porta, J., 1998. Methodologies for the analysis and characterization of gypsum in soils: A review. Geoderma 87, 31–46. https://doi.org/10.1016/S0016-7061(98)00067-6

Romero, E., Simms, P.H., 2008. Microstructure Investigation in Unsaturated Soils: A Review with Special Attention to Contribution of Mercury Intrusion

Porosimetry and Environmental Scanning Electron Microscopy. Geotech. Geol. Eng. 26, 705–727. https://doi.org/10.1007/s10706-008-9204-5

Schneider, C.A., Rasband, W.S., Eliceiri, K.W., 2012. NIH Image to ImageJ: 25 years of image analysis [WWW Document]. Nat. Methods. https://doi.org/10.1038/nmeth.2089

Chapter 5

ASTM D2845-08, 2008. Standard Test Method for Laboratory Determination of Pulse Velocities and Ultrasonic Elastic Constants of Rock. West Conshohocken, Pennsylvania, USA.

ASTM D5731 - 07, 2007. Standard Test Method for Determination of the Point Load Strength Index of Rock and Application to Rock Strength Classifications. West Conshohocken, Pennsylvania, USA.

ASTM D 3148 - 02, 2002. Standard Test Method for Elastic Moduli of Intact Rock Core Specimens in Uniaxial Compression. West Conshohocken, Pennsylvania, USA.

ASTM D 4543 – 01, 2001. Standard Practices for Preparing Rock Core Specimens and Determining Dimensional and Shape Tolerances. West Conshohocken, Pennsylvania, USA.

ASTM D5731-95, 1995. Standard Test Method for Determination of the Point Load Strength Index of Rock. West Conshohocken, Pennsylvania, USA.

Atapour, H., Mortazavi, A., 2018. The influence of mean grain size on unconfined compressive strength of weakly consolidated reservoir sandstones. J. Pet. Sci. Eng. 171, 63–70. https://doi.org/10.1016/j.petrol.2018.07.029

Basu, A., Kamran, M., 2010. Point load test on schistose rocks and its applicability in predicting uniaxial compressive strength. Int. J. Rock Mech. Min. Sci. 47, 823–828. https://doi.org/10.1016/j.ijrmms.2010.04.006

Baud, P., Exner, U., Lommatzsch, M., Reuschlé, T., Wong, T.-F., 2017. Mechanical behavior, failure mode, and transport properties in a porous carbonate. J. Geophys. Res. Solid Earth 122, 7363–7387. https://doi.org/10.1002/2017JB014060

Bieniawski, Z.T., 1975. The point-load test in geotechnical practice. Eng. Geol. 9, 1–11. https://doi.org/10.1016/0013-7952(75)90024-1

Broch, E., Franklin, J.A., 1972. The point-load strength test. Int. J. Rock Mech. Min. Sci. 9, 669–676. https://doi.org/10.1016/0148-9062(72)90030-7

Butel, N., Hossack, A., Kizil, M.S., 2014. Prediction of in situ rock strength using sonic velocity.

Chau, K.T., Wong, R.H.C., 1996. Uniaxial compressive strength and point load strength of rocks. Int. J. Rock Mech. Min. Sci. Geomech. Abstr. 33, 183–188. https://doi.org/10.1016/0148-9062(95)00056-9

Cheung, C.S.N., Baud, P., Wong, T.-F., 2012. Effect of grain size distribution on the development of compaction localization in porous sandstone. Geophys. Res. Lett. 39. https://doi.org/10.1029/2012GL053739

Çobanoğlu, İ., Çelik, S.B., 2008. Estimation of uniaxial compressive strength from point load strength, Schmidt hardness and P-wave velocity. Bull. Eng. Geol. Environ. 67, 491–498. https://doi.org/10.1007/s10064-008-0158-x

Colombero, C., Comina, C., Umili, G., Vinciguerra, S., 2016. Multiscale geophysical characterization of an unstable rock mass. Tectonophysics 675, 275–289. https://doi.org/10.1016/j.tecto.2016.02.045

Eberhardt, E., Stimpson, B., Stead, D., 1999. Effects of Grain Size on the Initiation and Propagation Thresholds of Stress-induced Brittle Fractures. Rock Mech. Rock Eng. 32, 81–99. https://doi.org/10.1007/s006030050026

Fener, M., Kahraman, S., Bilgil, A., Gunaydin, O., 2005. A Comparative Evaluation of Indirect Methods to Estimate the Compressive Strength of Rocks. Rock Mech. Rock Eng. 38, 329–343. https://doi.org/10.1007/s00603-005-0061-8

Fredrich, J.T., Evans, B., Teng-Fong, W., 1990. Effect of grain size on brittle and semibrittle strength: implications for micromechanical modelling of failure in compression. J. Geophys. Res. 95, 10,907-10,920.

Handin, J., Hager, R.V., 1957. Experimental Deformation of Sedimentary Rocks Under Confining Pressure: Tests at Room Temperature on Dry Samples. AAPG Bull. 41, 1–50.

Hardy, S.J., 1997. The point load test for weak rock in dredging applications. Int. J. Rock Mech. Min. Sci. 34, 295.e1-295.e13. https://doi.org/10.1016/S1365-1609(97)00063-4

Hatherly, P., Medhurst, T., Sliwa, R., Turner, R., 2005. A rock mass assessment procedure based on quantitative geophysical log analysis of coal measure sequences. Explor. Geophys. 36, 112–117. https://doi.org/10.1071/EG05112

Hatzor, Y.H., Palchik, V., 1998. A microstructure-based failure criterion for Aminadav dolomites. Int. J. Rock Mech. Min. Sci. 35, 797–805. https://doi.org/10.1016/S0148-9062(98)00004-7

Hatzor, Y.H., Palchik, V., 1997. The influence of grain size and porosity on crack initiation stress and critical flaw length in dolomites. Int. J. Rock Mech. Min. Sci. 34, 805–816. https://doi.org/10.1016/S1365-1609(96)00066-6

Heidari, M., Khanlari, G.R., Torabi Kaveh, M., Kargarian, S., 2012. Predicting the Uniaxial Compressive and Tensile Strengths of Gypsum Rock by Point Load Testing. Rock Mech. Rock Eng. 45, 265–273. https://doi.org/10.1007/s00603-011-0196-8

ISRM, 1985 "Suggested Method for Determining Point Load Strength".

JahanGer, Z.K., Ahmed AA. 2013. Correlation Between Point Load Index And Very Low Uniaxial Compressive Strength Of Some Iraqi Rocks. Aust. J. Basic Appl. Sci. 7, 216–229.

Kahraman, S., Gunaydin, O., 2009. The effect of rock classes on the relation between uniaxial compressive strength and point load index. Bull. Eng. Geol. Environ. 68, 345–353. https://doi.org/10.1007/s10064-009-0195-0

Kahraman, S., Gunaydin, O., Fener, M., 2005. The effect of porosity on the relation between uniaxial compressive strength and point load index. Int. J. Rock Mech. Min. Sci. 42, 584–589. https://doi.org/10.1016/j.ijrmms.2005.02.004

Karaman, K., Kesimal, A., 2015. Correlation of Schmidt Rebound Hardness with Uniaxial Compressive Strength and P-Wave Velocity of Rock Materials. Arab. J. Sci. Eng. 40, 1897–1906. https://doi.org/10.1007/s13369-014-1510-z

Klein, E., Baud, P., Reuschlé, T., Wong, T., 2001. Mechanical behaviour and failure mode of bentheim sandstone under triaxial compression. Phys. Chem. Earth Part Solid Earth Geod. 26, 21–25. https://doi.org/10.1016/S1464-1895(01)00017-5

Lawrence, W., Emery, J., Canbulat, I., 2013. Geotechnical roof classification for an underground coal mine from borehole data. Coal Oper. Conf.

Li, D., Wong, L.N.Y., 2013. Point Load Test on Meta-Sedimentary Rocks and Correlation to UCS and BTS. Rock Mech. Rock Eng. 46, 889–896. https://doi.org/10.1007/s00603-012-0299-x

McNally, G.M., 1990. The prediction of geotechnical rock properties from sonic and neutron logs. Explor. Geophys. 21, 65–71. https://doi.org/10.1071/EG990065

Olsson, W.A., 1974. Grain size dependence of yield stress in marble. J. Geophys. Res. 79, 4859–4862. https://doi.org/10.1029/JB079i032p04859

Oyler, D.C., Mark, C., Molinda, G.M., 2010. In situ estimation of roof rock strength using sonic logging. Int. J. Coal Geol. 83, 484–490. https://doi.org/10.1016/j.coal.2010.07.002

Palchik, V., 1999. Influence of Porosity and Elastic Modulus on Uniaxial Compressive Strength in Soft Brittle Porous Sandstones. Rock Mech. Rock Eng. 32, 303–309. https://doi.org/10.1007/s006030050050

Palchik, V., Hatzor, Y.H., 2004. The Influence of Porosity on Tensile and Compressive Strength of Porous Chalks. Rock Mech. Rock Eng. 37, 331–341. https://doi.org/10.1007/s00603-003-0020-1

Sabatakakis, N., Koukis, G., Tsiambaos, G., Papanakli, S., 2008. Index properties and strength variation controlled by microstructure for sedimentary rocks. Eng. Geol. 97, 80–90. https://doi.org/10.1016/j.enggeo.2007.12.004

Salah, H., Omar, M., Shanableh, A., 2014. Estimating Unconfined Compressive Strength of Sedimentary Rocks in United Arab Emirates from Point Load Strength Index. J. Appl. Math. Phys. 02, 296–303. https://doi.org/10.4236/jamp.2014.26035

Sharma, P.K., Singh, T.N., 2008. A correlation between P-wave velocity, impact strength index, slake durability index and uniaxial compressive strength.

Bull. Eng. Geol. Environ. 67, 17–22. https://doi.org/10.1007/s10064-007-0109-y

Singh, S.K., 1988. Relationship among fatigue strength, mean grain size and compressive strength of a rock. Rock Mech. Rock Eng. 21, 271–276. https://doi.org/10.1007/BF01020280

Singh, T.N., Kainthola, A., A, V., 2012. Correlation Between Point Load Index and Uniaxial Compressive Strength for Different Rock Types. Rock Mech. Rock Eng. 45, 259–264. https://doi.org/10.1007/s00603-011-0192-z

Skinner, W.J., 1959. Experiments on the Compressive Strength of Anhydrite.

Tsiambaos, G., Sabatakakis, N., 2004. Considerations on strength of intact sedimentary rocks. Eng. Geol. 72, 261–273. https://doi.org/10.1016/j.enggeo.2003.10.001

Ulusay, R., Türeli, K., Ider, M.H., 1994. Prediction of engineering properties of a selected litharenite sandstone from its petrographic characteristics using correlation and multivariate statistical techniques. Eng. Geol. 38, 135–157. https://doi.org/10.1016/0013-7952(94)90029-9

UNI EN 1926-2007. 2007. "Natural Stone Test Methods - Determination of Uniaxial Compressive Strength."

Vasanelli, E., Colangiuli, D., Calia, A., Sbartaï, Z.-M., Breysse, D., 2017. Combining non-invasive techniques for reliable prediction of soft stone strength in historic masonries. Constr. Build. Mater. 146, 744–754. https://doi.org/10.1016/j.conbuildmat.2017.04.146

Vasconcelos, G., Lourenço, P.B., Alves, C.A.S., Pamplona, J., 2008. Ultrasonic evaluation of the physical and mechanical properties of granites. Ultrasonics 48, 453–466. https://doi.org/10.1016/j.ultras.2008.03.008

Wang, Y., Li, X., 2015. Experimental study on cracking damage characteristics of a soil and rock mixture by UPV testing. Bull. Eng. Geol. Environ. 74, 775–788. https://doi.org/10.1007/s10064-014-0673-x

Wong, R.H.C., Chau, K.T., Wang, P., 1996. Microcracking and grain size effect in Yuen Long marbles. Int. J. Rock Mech. Min. Sci. Geomech. Abstr. 33, 479–485. https://doi.org/10.1016/0148-9062(96)00007-1

Yasar, E., Erdogan, Y., 2004. Correlating sound velocity with the density, compressive strength and Young's modulus of carbonate rocks. Int. J. Rock Mech. Min. Sci. 41, 871–875. https://doi.org/10.1016/j.ijrmms.2004.01.012

Zel, I.Y., Ivankina, T.I., Levin, D.M., Lokajicek, T., 2015. Application of a modified method of ultrasonic measurements for determination of elastic moduli of rocks. Crystallogr. Rep. 60, 537–545. https://doi.org/10.1134/S1063774515040239

Chapter 6

Blaber, J., Adair, B., Antoniou, A., 2015. Ncorr: Open-Source 2D Digital Image Correlation Matlab Software. Exp. Mech. 55, 1105–1122. https://doi.org/10.1007/s11340-015-0009-1

Brantut, N., Schubnel, A., Guéguen, Y., 2011. Damage and rupture dynamics at the brittle-ductile transition: The case of gypsum. J. Geophys. Res. Solid Earth 116. https://doi.org/10.1029/2010JB007675

Chu, T.C., Ranson, W.F., Sutton, M.A., 1985. Applications of digital-image-correlation techniques to experimental mechanics. Exp. Mech. 25, 232–244. https://doi.org/10.1007/BF02325092

Ferrero, A.M., Migliazza, M.R., 2009. Theoretical and numerical study on uniaxial compressive behaviour of marl. Mechanics of Materials 41,561–572. https://doi.org/10.1016/j.mechmat.2009.01.011

Lugli, S., Manzi, V., Roveri, M., Schreiber, C.B., 2010. The Primary Lower Gypsum in the Mediterranean: A new facies interpretation for the first stage of the Messinian salinity crisis. Palaeogeogr. Palaeoclimatol. Palaeoecol. 297, 83–99. https://doi.org/10.1016/j.palaeo.2010.07.017

Nguyen, T.L., Hall, S.A., Vacher, P., Viggiani, G., 2011. Fracture mechanisms in soft rock: Identification and quantification of evolving displacement discontinuities by extended digital image correlation. Tectonophysics 503, 117–128. https://doi.org/10.1016/j.tecto.2010.09.024

Pan, B., Asundi, A., Xie, H., Gao, J., 2009. Digital image correlation using iterative least squares and pointwise least squares for displacement field and strain field measurements. Opt. Lasers Eng. 47, 865–874. https://doi.org/10.1016/j.optlaseng.2008.10.014

Peters, W.H., Ranson, W.F., 1982. DIGITAL IMAGING TECHNIQUES IN EXPERIMENTAL STRESS ANALYSIS. Opt. Eng. 21, 427–431. https://doi.org/10.1117/12.7972925

Stirling, R.A., Simpson, D.J., Davie, C.T., 2013. The application of digital image correlation to Brazilian testing of sandstone. Int. J. Rock Mech. Min. Sci. 60, 1–11. https://doi.org/10.1016/j.ijrmms.2012.12.026

Vend Roux, G., Knauss, W.G., 1998. Submicron deformation field measurements: Part 2. Improved digital image correlation. Exp. Mech. 38, 86–92. https://doi.org/10.1007/BF02321649

Vitone, C., Viggiani, G., Cotecchia, F., Hall, S.A., 2013. Localized deformation in intensely fissured clays studied by 2D digital image correlation. Acta Geotech. 8, 247–263. https://doi.org/10.1007/s11440-013-0208-9

Yang, G., Cai, Z., Zhang, X., Fu, D., 2015. An experimental investigation on the damage of granite under uniaxial tension by using a digital image correlation method. Opt. Lasers Eng. 73, 46–52. https://doi.org/10.1016/j.optlaseng.2015.04.004

Zhang, H., Huang, G., Song, H., Kang, Y., 2012. Experimental investigation of deformation and failure mechanisms in rock under indentation by digital

image correlation. Eng. Fract. Mech. 96, 667–675.
https://doi.org/10.1016/j.engfracmech.2012.09.012

Zucali, M., Barberini, V., Chateigner, D., Ouladdiaf, B., Lutterotti, L., 2010. Brittle plus plastic deformation of gypsum aggregates experimentally deformed in torsion to high strains: Quantitative microstructural and texture analysis from optical and diffraction data. Geol. Soc. Lond. Spec. Publ. 332, 79-98. doi:10.1144/SP332.6. https://doi.org/10.1144/SP332.6

Chapter 7

Brantut, N., Baud, P., Heap, M.J., Meredith, P.G., 2012. Micromechanics of brittle creep in rocks. J. Geophys. Res. Solid Earth 117. https://doi.org/10.1029/2012JB009299

Brantut, N., Heap, M.J., Meredith, P.G., Baud, P., 2013. Time-dependent cracking and brittle creep in crustal rocks: A review. J. Struct. Geol. 52, 17–43. https://doi.org/10.1016/j.jsg.2013.03.007

Brantut, N., Schubnel, A., Guéguen, Y., 2011. Damage and rupture dynamics at the brittle-ductile transition: The case of gypsum. J. Geophys. Res. Solid Earth 116. https://doi.org/10.1029/2010JB007675

de Meer, S., Spiers, C.J., 1999. Influence of pore-fluid salinity on pressure solution creep in gypsum. Tectonophysics 308, 311–330.

de Meer, S., Spiers, C.J., 1997. Uniaxial compaction creep of wet gypsum aggregates. J. Geophys. Res. Solid Earth 102, 875–891. https://doi.org/10.1029/96JB02481

de Meer, S., Spiers, C.J., 1995. Creep of wet gypsum aggregates under hydrostatic loading conditions. Tectonophysics, Influence of Fluids on Deformation Processes in Rocks 245, 171–183. https://doi.org/10.1016/0040-1951(94)00233-Y

Gasc-Barbier, M., Chanchole, S., Bérest, P., 2004. Creep behavior of Bure clayey rock. Appl. Clay Sci. 26, 449–458. https://doi.org/10.1016/j.clay.2003.12.030

Heap, M.J., Baud, P., Meredith, P.G., 2009. Influence of temperature on brittle creep in sandstones. Geophys. Res. Lett. 36. https://doi.org/10.1029/2009GL039373

Hoxha, D., Homand, F., Auvray, C., 2006. Deformation of natural gypsum rock: Mechanisms and questions. Eng. Geol. 86, 1–17. https://doi.org/10.1016/j.enggeo.2006.04.002

Liang, W., Yang, X., Gao, H., Zhang, C., Zhao, Y., Dusseault, M.B., 2012. Experimental study of mechanical properties of gypsum soaked in brine. Int. J. Rock Mech. Min. Sci. 53, 142–150. https://doi.org/10.1016/j.ijrmms.2012.05.015

Yilmaz, I., 2010. Influence of water content on the strength and deformability of gypsum. Int. J. Rock Mech. Min. Sci. 47, 342–347. https://doi.org/10.1016/j.ijrmms.2009.09.002

Zhu, C., Xu, X., Liu, W., Xiong, F., Lin, Y., Cao, C., Liu, X., 2019. Softening Damage Analysis of Gypsum Rock With Water Immersion Time Based on Laboratory Experiment. IEEE Access 7, 125575–125585. https://doi.org/10.1109/ACCESS.2019.2939013

Chapter 8

Auvray, C., Homand, F., Hoxha, D., 2008. The influence of relative humidity on the rate of convergence in an underground gypsum mine. Int. J. Rock Mech. Min. Sci. 45, 1454–1468. https://doi.org/10.1016/j.ijrmms.2008.02.008

Auvray, C., Homand, F., Sorgi, C., 2004. The aging of gypsum in underground mines. Eng. Geol. 74, 183–196. https://doi.org/10.1016/j.enggeo.2004.03.008

Castellanza, R., Gerolymatou, E., Nova, R., 2008. An Attempt to Predict the Failure Time of Abandoned Mine Pillars. Rock Mech. Rock Eng. 41, 377–401. https://doi.org/10.1007/s00603-007-0142-y

de Meer, S., Spiers, C.J., 1999. Influence of pore-fluid salinity on pressure solution creep in gypsum. Tectonophysics 308, 311–330.

de Meer, S., Spiers, C.J., 1997. Uniaxial compaction creep of wet gypsum aggregates. J. Geophys. Res. Solid Earth 102, 875–891. https://doi.org/10.1029/96JB02481

de Meer, S., Spiers, C.J., 1995. Creep of wet gypsum aggregates under hydrostatic loading conditions. Tectonophysics, Influence of Fluids on Deformation Processes in Rocks 245, 171–183. https://doi.org/10.1016/0040-1951(94)00233-Y

Hoxha, D., Giraud, A., Homand, F., 2005. Modelling long-term behaviour of a natural gypsum rock. Mech. Mater. 37, 1223–1241. https://doi.org/10.1016/j.mechmat.2005.06.002

Hoxha, D., Homand, F., Auvray, C., 2006. Deformation of natural gypsum rock: Mechanisms and questions. Eng. Geol. 86, 1–17. https://doi.org/10.1016/j.enggeo.2006.04.002

Liang, W., Yang, X., Gao, H., Zhang, C., Zhao, Y., Dusseault, M.B., 2012. Experimental study of mechanical properties of gypsum soaked in brine. Int. J. Rock Mech. Min. Sci. 53, 142–150. https://doi.org/10.1016/j.ijrmms.2012.05.015

Moirat, D., Potherat, P., Massieu, E., Durville, J.L., 2006. Experimental data on creep of the saccharoid gypsum in saturated condition. Rev. Fr. Géotechnique 115, 3–10.

Nedjar, B., Le Roy, R., 2013. An approach to the modeling of viscoelastic damage. Application to the long-term creep of gypsum rock materials: LONG-

TERM CREEP OF GYPSUM ROCK. Int. J. Numer. Anal. Methods Geomech. 37, 1066–1078. https://doi.org/10.1002/nag.1138

Salih, N., and A. Mohammed, 2017. Characterization and Modeling of Long-Term Stress–Strain Behavior of Water Confned Pre-saturated Gypsum Rock in Kurdistan Region, Iraq. Rock Mech. Geotech. Eng. 9. https://doi.org/doi:10.1016/j.jrmge.2017.03.009

Yilmaz, I., 2007. Differences in the geotechnical properties of two types of gypsum: alabastrine and porphyritic. Bull. Eng. Geol. Environ. 66, 187–195. https://doi.org/10.1007/s10064-006-0055-0

Zhu, C., Xu, X., Liu, W., Xiong, F., Lin, Y., Cao, C., Liu, X., 2019. Softening Damage Analysis of Gypsum Rock With Water Immersion Time Based on Laboratory Experiment. IEEE Access 7, 125575–125585. https://doi.org/10.1109/ACCESS.2019.2939013